Swansea University
Prifysgol Abertawe

Small Scale Testing of Nickel-Based Superalloys Produced by ALM

Hani Hilal

BEng (First Hons)

Submitted to Swansea University in fulfilment of the requirements for the Degree of Doctor of Engineering

Swansea University

February 2021

DECLARATION

This work has not previously been accepted in substance for any degree and is not being concurrently submitted in candidature for any degree.

Signed 

Date 26/02/2021

STATEMENT 1

This thesis is the result of my own investigations, except where otherwise stated. Where correction services have been used, the extent and nature of the correction is clearly marked in a footnote(s).

Other sources are acknowledged by footnotes giving explicit references. A bibliography is appended.

Signed 

Date 26/02/2021

STATEMENT 2

I hereby give consent for my thesis, if accepted, to be available for photocopying and for inter-library loans **after expiry of a bar on access approved by the Swansea University.**

Signed 

Date 26/02/2021

Abstract

Nickel-based superalloys exhibit an impressive range of mechanical properties, from high temperature strength and toughness to excellent oxidation and corrosion resistance. It is for these reasons that they are heavily incorporated in a wide range of industrial sectors, particularly the aerospace industry where they are extensively utilised within the combustor and turbine section of a holistic gas turbine engine, where temperatures often reach arduous conditions. Although nickel-based superalloys are typically manufactured using traditional cast and wrought methodologies, the aerospace industry is becoming increasingly interested in the use of alternative manufacturing methods in an attempt to further drive gas turbine development through weight reduction and increased Turbine Entry Temperatures (TET). As such, interest regarding the use of near-net shape manufacturing technologies such as Additive Layer Manufacturing (ALM) has risen in parallel, but concerns have arisen given the metallurgical complexity of the process and the prevalence of phenomena such as anisotropic behaviour, residual stressing and structural integrity.

This thesis has investigated the influence of key process parameters and variables on the mechanical and microstructural behaviour of the two-contrasting nickel-based superalloys, CM247LC and IN718. A novel miniaturised mechanical testing method, Small Punch (SP), in combination with in-depth material characterisation techniques was implemented on a series of Laser Powder Bed Fusion (LPBF) variants of differing build orientation and parameter selections. In addition to this, a robust analytical methodology was employed on a series of LPBF variants in order to ascertain process parameters' influence on melt pool profile and both alloys relative propensity for defect formation. The findings of this work will help further the understanding of parameter selection and support a key development strategy being implemented by Rolls-Royce plc. regarding the safe incorporation of additive components into service.

Contents Page

Acknowledgements

Throughout the tenure of my project, I have been extremely blessed to be the beneficiary of ongoing supervision and support from colleagues, friends, family members and professional institutions.

I would firstly like to express my sincere gratitude to Professor Robert Lancaster, who has been heavily involved in my project and professional development over the last 4 years, providing invaluable technical expertise and acumen. I'd also like to thank Dr Spencer Jeffs, who in the early years of my doctorate aided and assisted with mechanical testing alongside providing technical and practical guidance in the laboratory setting.

I would also like to thank my funders, the Materials and Manufacturing Academy (M2A) who have supported me through the European Social Fund and my industrial sponsors Rolls-Royce plc. The provision of materials and supporting information from Rolls-Royce plc. is gratefully acknowledged and I would like to express particular recognition to Dr Dave Stapleton, Dr Gavin Baxter and John Boswell at Rolls-Royce plc., whose continued involvement, guidance and technical support throughout my project has been greatly appreciated.

Additionally, I'd like to thank Swansea University's College of Engineering and particularly the Institute of Structural Materials (ISM), who in unprecedented and challenging times have continued to provide me with the facilities and platform to develop as a professional engineer. Facilities include the Swansea Materials Research and Testing Ltd (SMaRT) where all mechanical tests were performed and the Advanced Imaging of Materials (AIM) laboratory, which was funded in part by EPSRC (EP/M028267/1), The European Regional Development Fund through the Welsh Government (80708) and the Sêr Solar project via the Welsh Government. I'd like to thank Professor Mark Whittaker, Professor Martin Bache, Julie Palmer and John Morgan who over the years have continuously supported the postgraduate students presiding within the ISM and moreover, I'd like to give gratitude to the ISM's workshop technicians David Beckett, Emyr Rees and Paul McGowan, who have continuously provided their skilled expertise on numerous occasions.

Finally, I would like to dedicate my thesis to all of my friends, family and particularly my parents, who have always pushed me to work hard and not sell myself short. I'm incredibly blessed to have you all in my life and I do not take it for granted.

Publications Relating to this Thesis

Journal Publications

H. Hilal, R. Lancaster, S. Jeffs, J. Boswell, D. Stapleton and G. Baxter, "The Influence of Process Parameters and Build Orientation on the Creep Behaviour of a Laser Powder Bed Fused Ni-based Superalloy for Aerospace Applications," Materials, vol. 12, no. 9, 2019. DOI: 10.3390/ma12091390.

H. Hilal, R. Lancaster, D. Stapleton and G. Baxter, "Investigating the Influence of Process Parameters on the Structural Integrity of an Additively Manufactured Nickel-Based Superalloy," Metals, vol. 9, no. 11, 2019. DOI: 10.3390/met9111191

Conference Publications

H. Hilal, R. Lancaster, S. Jeffs, L. Ednie, J. Boswell, D. Stapleton and G. Baxter, "High temperature mechanical deformation of an additive manufactured nickel based superalloy using small scale test methods," 5th International Small Sample Test Techniques Conference, 2018. DOI: 10.5334/uproc.21

Conference Presentations

Oral Presentations

H. Hilal, R. Lancaster, S. Jeffs, L. Ednie, J. Boswell, D. Stapleton and G. Baxter, "High temperature mechanical deformation of an additive manufactured nickel based superalloy using small scale test methods," 5th International Small Sample Test Techniques Conference, 10-12th July 2018.

H. Hilal, R. Lancaster, D. Stapleton and G. Baxter, "Investigating the Influence of Process Parameters on the Structural Integrity of an Additively Manufactured Nickel-Based Superalloy," The Annual International Solid Freeform Fabrication Symposium, 12-14th August 2019.

Poster Presentations

H. Hilal, R. Lancaster, S. Jeffs, D. Stapleton, J. Boswell, G. Baxter, "Small Scale Testing of Ni-based Superalloys Produced by ALM", in M2A Annual Conference, 25th April 2017.

H. Hilal, R. Lancaster, S. Jeffs, D. Stapleton, J. Boswell, G. Baxter, "Small Scale Testing of Ni-based Superalloys Produced by ALM", Rolls-Royce plc Strategic Partnership Conference, 10-12th July 2017.

H. Hilal, R. Lancaster, S. Jeffs, D. Stapleton, J. Boswell, G. Baxter, "Small Scale Testing of Ni-based Superalloys Produced by ALM", in M2A Annual Conference, 27th March 2018.

H. Hilal, R. Lancaster, S. Jeffs, D. Stapleton, J. Boswell, G. Baxter, "Small Scale Testing of Ni-based Superalloys Produced by ALM", in M2A Annual Conference, 30th April 2019.

H. Hilal, R. Lancaster, S. Jeffs, D. Stapleton, J. Boswell, G. Baxter, "Small Scale Testing of Ni-based Superalloys Produced by ALM", Rolls-Royce plc Strategic Partnership Conference, 13-15th May 2019.

Nomenclature

AB	As-Built
ACARE	Advisory Council for Aviation Research and Innovation in Europe
ALM	Additive Layer Manufacturing
ASTM	American Society for Testing and Materials
BCT	Body-Centred Tetragonal
C	Material Constant
CAD	Computer Aided Design
CC	Conventionally Cast
CoP	Code of Practice
C_p	Specific Heat Capacity
DED	Directed Energy Deposition
DLD	Directed Layer Deposition
d_m	Punch Head Displacement at the Maximum Load
DOE	Design of Experiments
DS	Directionally Solidified
E^*	Energy Density
E_0^*	Normalised Equivalent Energy Density
EASA	European Aviation Safety Agency
EBM	Electron Beam Melting
EBSD	Electron Backscatter Diffraction
EDM	Electrical Discharge Machining
EDS	Energy Dispersive Spectroscopy
ESU	Effective Structural Unit
F	SP Load
FAA	Federal Aviation Authority
FCC	Face Centred Cubic
FEA	Finite Element Analysis
F_{Max}	Maximum Load
FOD	Foreign Object Damage
F_y	Yield Load
GBA	Grain Boundary Angle
h	Hatch Spacing
h^*	Normalised Hatch Spacing
h_0	Initial Thickness of the Specimen

HAGB	High Angle Grain Boundaries
HAZ	Heat Affected Zone
HIP	Hot Isostatic Pressing
HP	High Pressure
HSHT	Higher Solution Heat Treatment
HT	Heat Treatment
IPF	Inverse Pole Figure
l	Layer Height
l^*	Normalised Layer Height
LAGB	Low Angle Grain Boundaries
LAM	Localised Average Misorientation
LMP	Larson-Miller Parameter
LP	Low Pressure
LPBF	Laser Powder Bed Fusion
LVDT	Linear Variable Displacement Transducer
m	Material Constant
MSFC	Marshall Space Flight Centre
NASA	National Aeronautics and Space Administration
NMI	Non-Metallic Inclusions
Ø	Diameter
PBF	Powder Bed Fusion
PMZ	Partially Melted Zone
PPB	Prior Particle Boundaries
q	Beam Power
q^*	Normalised Power
R	Receiving hole radius
r	Radius of the punch head
rB	Beam Radius
RF	Recrystallisation Fraction
RT	Room Temperature
SEM	Scanning Electron Microscopy
SHT	Solution Heat Treatment
SLM	Selective Laser Melting
SP	Small Punch
SPC	Small Punch Creep
SPF	Small Punch Fatigue

SPT	Small Punch Tensile
T	Temperature
T_0	Initial Powder Bed Temperature
TBC	Thermal Barrier Coating
TCP	Topologically Close-Packed
TET	Turbine Entry Temperature
t_f	Time to Failure
T_m	Melting Temperature
UTS	Ultimate Tensile Strength
v	Beam Velocity
v^*	Normalised Beam Velocity
VAR	Vacuum Arm Remelting
VIM	Vacuum Induction Melting
A_q	Surface Absorptivity
α_1	Material Constant
α_2	Material Constant
β_1	Material Constant
β_2	Material Constant
δ	Delta
γ	Gamma
γ'	Gamma Prime
γ''	Gamma Double Prime
λ	Thermal Conductivity
$\dot{\varepsilon}_m$	Minimum Creep Rate
θ	Theta
η	Thermodynamic Efficiency
ρ	Density
q_{in}	Heat In
q_{out}	Heat Out
σ	Stress
σ_{UTS}	Ultimate Tensile Strength
σys	Yield Strength
δm	Minimum Deflection Rate

List of Figures

List of Tables

Chapter 1 – Introduction

1.1 Background

Nickel-based superalloys display an impressive range of mechanical properties from high temperature strength to excellent oxidation and corrosion resistance. It is for these reasons that they are heavily exploited in a wide range of industrial sectors, in particular the aerospace industry which incorporates them within the combustor and exhaust region of the gas turbine engine. Given the ever-increasing demands from regulatory commissions and governing bodies such as the European Aviation Safety Agency (EASA) and Federal Aviation Authority (FAA) for reduction in CO_2 and NO_x emissions, the aerospace industry and Rolls-Royce plc. have put a major emphasis on gas turbine development, in particular from a materials perspective. As such, alternative means for component manufacture and repair prove to be of significant importance and an area of research that has risen in parallel.

Additive Layer Manufacturing (ALM) is a near-net shape manufacturing technology first developed in the late 1970s and has since undergone major advancements driven primarily by the medical industry. Given its tremendous upside and numerous advantageous characteristics from the manufacture of highly intricate components not feasible through alternative methods to very little material wastage, the aerospace sector has become increasingly interested in its exploitation given its scope for design freedom. As such, a need for detailed understanding of the process from a materials perspective has become paramount given concerns regarding the metallurgical complexity of the process and consequential phenomena such as structural integrity, residual stressing and anisotropic behaviour.

Given the ever increasing interest in additive based technologies, an understanding as to the laser powder bed fusion (LPBF) process is required for the next generation of ALM built nickel-based superalloys. As such, the investigation of process parameters, key variables and post processing treatments takes precedent and shall support a key development strategy that is being developed globally by Rolls-Royce plc. for gas turbine technologies.

1.2 Overview and Scope of the Thesis

This thesis consists of nine chapters as described below:

The first chapter includes the background information, scope of research and the aims and objectives of this study. The second chapter consists of a comprehensive overview of the gas turbine engine, nickel-based superalloys, additive manufacturing and the application of the miniaturised mechanical testing methodology, small punch, for mechanical properties assessment. This chapter provides an overall review of the published literature and provides context as to why this work has been carried out. The third chapter covers all the experimental equipment and methodologies utilised in this thesis, outlining the materials manufactured, sample extraction and the metallurgical preparation procedures for the microscopy and small scale testing techniques employed.

The results of the thesis are presented in four separate chapters with respect to the work packages provided by Rolls-Royce plc., followed by a general discussion and comparison between the alloys evaluated. Chapter 4 provides the experimental results generated through the small-scale mechanical testing and in-depth microstructural characterisation methodologies conducted on a variety of LPBF CM247LC variants. These process variants encompassed two distinct changes in build orientation and the employment of five distinct parameter sets from within CM247LC's anticipated process window. Chapter 5 presents the quantitative approach incorporated on an array of LPBF CM247LC variants, which comprised of changes in normalised beam speed, power and energy density. The melt track profiles of these variants were numerically assessed in combination with defect analysis and correlated to the parameter selection implemented. Chapter 6 showcases the results produced by the application of small-scale mechanical testing techniques in combination with detailed microstructural assessments on a series of LPBF IN718 variants. These variants included two changes in build orientation, alongside the employment of five generic parameter sets. Chapter 7 displays the results formed from the statistical assessment applied to a collection of LPBF IN718 variants, which consisted of changes in normalised beam speed, power and energy density. Melt track profiles were quantitatively assessed alongside defect analysis and correlated to changes in parameter deposition.

The results presented in Chapters 4 – 7 are discussed in Chapter 8 in relation to the entire scope of the study, where comparisons are drawn with regards to the similarities and differentiations of the mechanical and microstructural behaviour between the two alloys investigated. Finally, Chapter 9 provides the concluding remarks with regards to the main research findings from this thesis, alongside recommendations for future work.

1.3 Aims and Objectives

The general aims and objectives of this research were to further the understanding as to the influence of process parameters and variables on the microstructural and mechanical behaviour of the two contrasting nickel-based superalloys CM247LC and IN718 manufactured through LPBF. This work would inherently help facilitate Rolls-Royce plc.'s high temperature applications team and their ongoing efforts with regards to the safe introduction of additively manufactured components into service, with advancements being streamlined towards the development of gas turbine technology through both increasing temperature capability and driving weight reduction.
The specific research objectives of this work is as follows:

- To conduct a literature overview and highlight the benefit of utilising the small scale testing technique small punch to rapidly assess and characterise an abundance of process parameters and variables.

- To employ the small punch testing methodology in conjunction with microstructural characterisation techniques to assess the mechanical response of LPBF CM247LC and IN718 variants and further the understanding of process variables influences on the behaviour of CM247LC and IN718.

- To assess the effect of changes in process parameters on both melt track profile and the structural integrity of LPBF CM247LC and IN718 variants, gauging an understanding as to each alloy's respective propensity for defect formation.

- To compare and contrast the similarities and contradictions in the relationships observed between LPBF CM247LC and IN718 over a range of process parameters and variables.

Chapter 2 – Literature Review

2.1 The Gas Turbine Engine

2.1.1 History

In modern day society, the aviation industry plays a pivotal role by providing fast, reliable and affordable transportation across the globe from both a commercial and civil standpoint. These revolutions are widely attributed to the development of the gas turbine engine, the innovation for which started with a French engineer by the name of René Lorin, who patented a jet propulsion system in 1913. However, given the state of materials technology at the time, from both a manufacturing and heat resistance perspective, it proved unfeasible and challenging. It wasn't until 1930 that Sir Frank Whittle was granted a patent for the application of a gas turbine as a propulsive jet system. Then 11 years' later this concept was successfully realised with the completion of its maiden flight [1]. Fast forward to today, this premise has formed the basis of the modern day holistic gas turbine engine, one of the 20th century's greatest technological feats. It is thought that within the civil aerospace sector for a market leader such as Rolls-Royce plc., there are over 3300 engines currently in service worldwide at any one time [2], with one example being the Trent XWB as illustrated in Figure 2.1.

Figure 2.1. The Rolls-Royce Trent XWB engine [3].

2.1.2 Basic Principles

The holistic gas turbine engine works primarily on the principle of Newton's 3rd law of motion, 'for every action there is an equal and opposite reaction', where gas is forced through the turbine in one direction creating an equal reactionary 'thrust' in the opposed direction [4]. The open-cycle process is initiated with the intake of air through the first of four main stages via fan blades as shown in Figure 2.2. From there, the air is passed through a series of rotating and stationary aerofoils where it is chopped and compressed to a significant degree; in some engines this can be almost up to 40 times [5]. Following its compression, the air is introduced to the combustion chamber in conjunction with fuel which is

continuously injected and ignited, leading to an explosion of hot air that burns ~ 2000°C. This air is then forced through to the turbine section where stator vanes direct the gas flow into rotary blades which in turn are connected to turbine discs that drive the turbine, converting kinetic energy into mechanical energy [6].

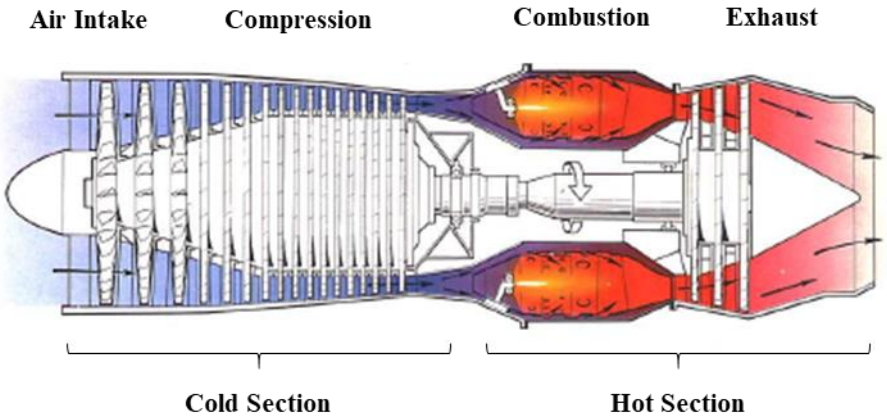

Figure 2.2. Schematic of the holistic gas turbine engine, adapted from [1].

From a thermodynamic standpoint, the open cycle process, otherwise known as the Brayton cycle, can be illustrated in two forms as shown in Figure 2.3a and b, the first being the relation of temperature to entropy and the second, pressure to volume. This is represented in 4 stages as discussed and illustrated. Stages 1-2 represent the initial air intake at atmospheric conditions (T_1, P_1) the pressure increase consequent to isentropic compression. Stages 2-3 highlight the temperature increase at constant pressure, where stages 3-4 represent the isentropic expansion of air and pressure drop following combustion. Stages 4-1 depict the heat ejection at the end of the cycle process [7].

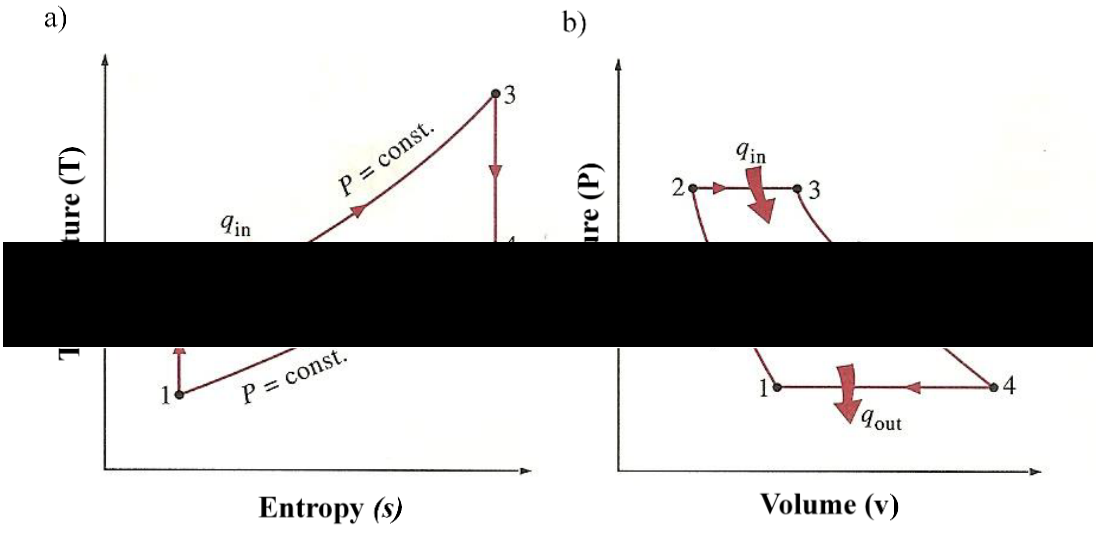

Figure 2.3. The ideal Brayton cycle in relation to a) temperature and entropy and, b) pressure and volume [7].

The understanding of this thermodynamic cycle is essential as it can be utilised to improve engine efficiency. When expressing the terms empirically, a key understanding of where design considerations can have a major impact on such efficiencies is illustrated, with thermodynamic efficiency, η, defined as follows.

$$\eta = 1 - \frac{q_{out}}{q_{in}} = 1 - \frac{C_p(T_4 - T_1)}{C_p\,(T_3 - T_2)} = 1 - \frac{T_1(\frac{T_4}{T_1} - 1)}{T_2(\frac{T_3}{T_2} - 1)} \quad (1)$$

Where *Cp* is the specific heat of the gas, q_{out} is the heat out ($T_4 - T_1$) and q_{in} is the heat in ($T_3 - T_2$).

Given the fact that stages 1-2 and 3-4 are isentropic, $P_2 = P_3$ and $P_4 = P_1$ and thus

$$\frac{T_2}{T_1} = \frac{P_2^{\frac{k-1}{k}}}{P_1} = \frac{P_3^{\frac{k-1}{k}}}{P_4} = \frac{T_3}{T_4} \quad (2)$$

$$\eta_{th} = 1 - \frac{1}{\frac{T_4}{T_3}} \quad (3)$$

Considering the expression for thermodynamic efficiency shown in Equation 3, it is evident that both T_3 and T_4 are the key controlling factors. Since it can be difficult to influence turbine exit temperature, Turbine Entry Temperature (TET) is of notable interest and can be manipulated relatively easily with changes in fuel to air ratio. However, the challenge arises in producing materials that can withstand such harsh conditions [8]. The following section will give an overview as to the material selection within individual sections of the holistic gas turbine engine.

2.1.3 Materials Selection

2.1.3.1 Fan Blades

As mentioned, the first section of the gas turbine is the fan inlet section, where cool air is drawn into the engine. Given the temperatures it is subjected too, the need for high temperature performance is not necessary. However, the possibility for foreign object damage (FOD), such as bird strikes, and corrosion, in the form of dust and rain, and becomes prominent and as such the need for corrosion resistance and toughness takes precedent. In addition to these service demands, centrifugal loading of ~100 tonnes in conjunction with vibrations also need to be considered and as such titanium alloys, in particular Ti-64 (Ti-6Al-4V) are predominantly utilised for this section given their high strength to weight ratio, corrosion resistance and fatigue performance.

2.1.3.2 Compressor

Following on from the fan intake, the air is passed through to the compressor section which is made of a series of rotors and stators. Given ideal gas law, the increase in air pressure comes with an apparent increase in temperature, meaning that there is a continuous rise in the stresses and temperatures that the components are subjected too. As such, the compressor is often categorised into two sections, referred to as the low pressure (LP) and high pressure (HP) compressors respectively. For the early stages within a LP compressor where temperatures reach ~300°C, titanium and in particular Ti-64 is utilised. However, as temperatures increase to up to ~ 450°C, stronger alloys with higher temperature capabilities such as Ti-6246 (Ti-6Al-2Sn-4Zr-6Mo) are exploited. For new generation jet engines, it is often the case that temperatures go beyond 450°C and surpass that of titanium's capabilities. In these instances, nickel-based superalloys such as Inconel 718, Udimet 720 and RR1000 are employed.

2.1.3.3 Combustor

Post compression, this air is introduced to the combustion chamber in conjunction with fuel, where it is ignited and raised to over 2000°C. This sudden change in temperature leads to major expansion, creating a momentum that generates thrust. Nickel-based superalloys such as C263 and Haynes 282 are now more prominent, given their high strength, excellent corrosion resistance and high temperature capabilities. However, the components in this section suffer significant in-service challenges as temperatures often exceed that of the metals' temperature capabilities. To combat this, the utilisation of ceramic Thermal Barrier Coatings (TBCs) and the introduction of cold air to the combustion chamber through cooling channels is incorporated.

2.1.3.4 Turbine

Once this generation of thrust and momentum is achieved following the expansion and direction of hot air, the turbine which consists of a series of rotors and stators is turned. This turbine is attached to the shaft which connects the rear of the gas turbine to the frontal fan and compressor section, allowing the engine to be a self-reciprocating process that takes in more air. Similar to that of the combustor section, hot air ~1700°C is present which will often exceed the materials' capabilities. As such, TBCs are applied in order to provide a protective layer and cool air that bypasses the combustor section and is bled into the turbine section. Given the harsh environment from both a temperature and stress perspective, nickel-based superalloys provide the most suitable basis of physical and mechanical properties for these applications. For safety critical components such as rotatives, high strength single crystal systems such as CMSX-4 are utilised. An illustrated overview as to material selection within the gas turbine engine is shown below in Figure 2.4.

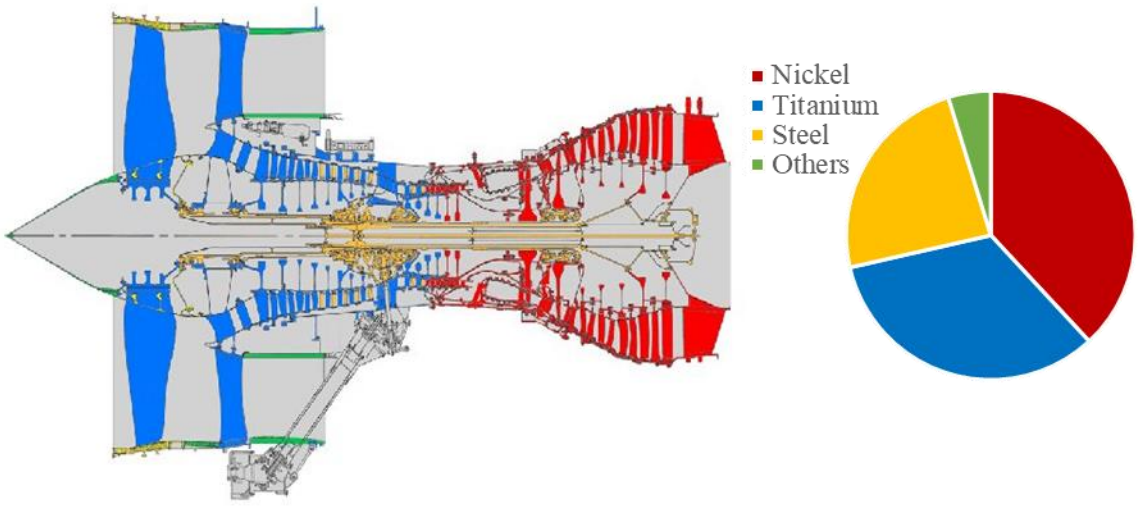

Figure 2.4. Materials selection within the holistic gas turbine engine, adapted from [9].

2.1.4 Material Developments

2.1.4.1 Driving Factors

Since the introduction of the gas turbine, there have been ongoing efforts to increase research and development to match its ever-evolving requirements. The major driving forces for material development are primarily two fold; economic and environmental.

From an economic standpoint, Rolls-Royce plc. is a longstanding multidisciplinary engineering company that was established in 1904 and today remains one of the largest engine manufacturers in the aerospace sector. In order to maintain that position and compete within the marketplace, further enhancements in engine efficiency both in the form of weight reduction and fuel burn become ever imperative [10]. In addition to the commercial viewpoint, environmental considerations and advancements need to be made in order to meet the ever increasing demands of regulatory commissions and governing bodies such as the Federal Aviation Authority (FAA) and European Aviation Safety Agency (EASA) for NOx, CO_2 and noise pollution. Since 1950, there has been a 4x reduction in noise pollution and a 70% reduction on fuel burn, but a report published by the House of Commons in 2011 using data issued by the Department for Transport states that it expects air travel in the UK alone to increase two fold as illustrated in Figure 2.5 [11] [12]. However, given the emergence of the COVID-19 pandemic in late 2019, civil aviation has been significantly reduced consequent to the introduction of travel restrictions that of which contradict the projections, with the long term impact on the aviation sector being unknown at this point in time [13].

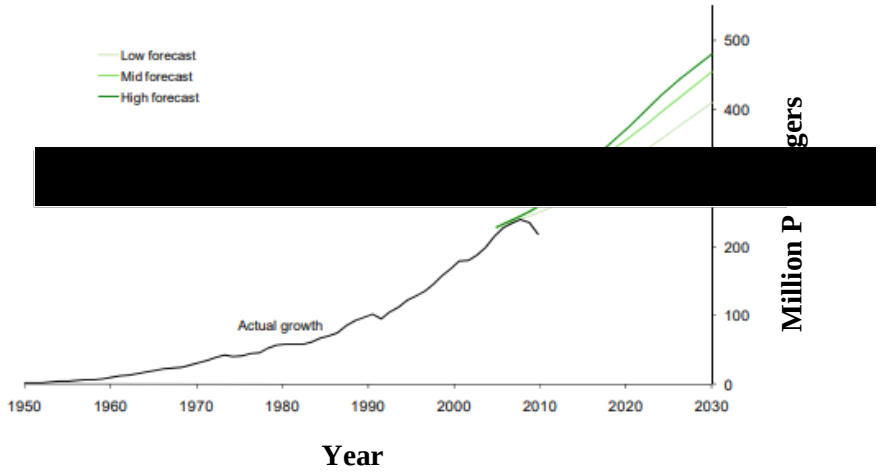

Figure 2.5. Forecasted air traffic demand published by the Department for Transport in 2009 [12].

The Advisory Council for Aviation Research and Innovation in Europe (ACARE) has made targets regarding emissions entitled FlightPath 2050, where technologies and procedures can allow for major reductions by the year 2050. It is expected that there will be a 75% reduction in CO_2 emissions and a 90% reduction in NO_x emissions per passenger kilometre [14].

2.1.4.2 Turbine Entry Temperatures

Given the driving factors associated with gas turbine technology as previously discussed, the desire for higher fuel efficiencies whilst maintaining safety from a commercial aspect takes priority. As shown previously, the best way to improve thermodynamic efficiency is to increase its TET and as such this has been the basis for major advancements in alloy development, manufacturing techniques and the application of cooling mechanisms and TBCs as shown in Figure 2.6.

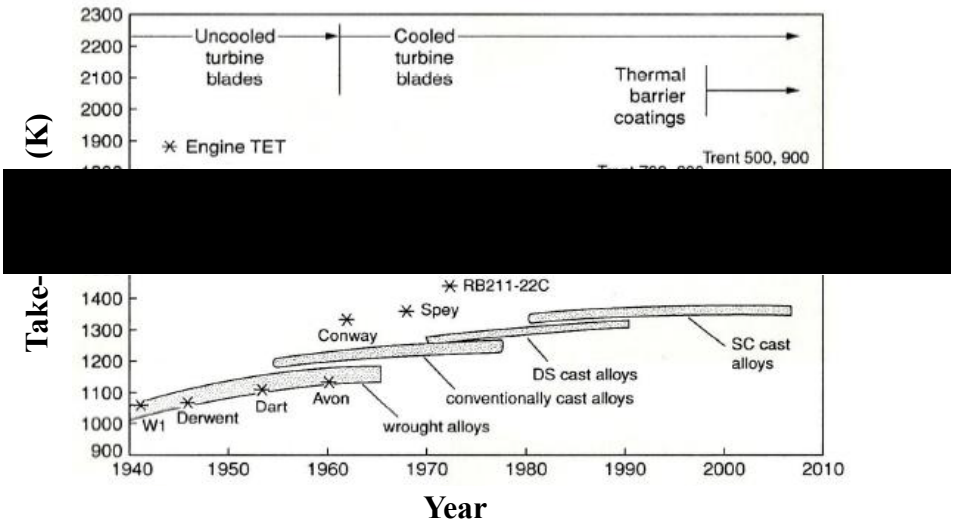

Figure 2.6. TETs consequent to development in nickel-based superalloys in terms of alloy design, manufacturing technology and the introduction of blade cooling and TBCs between 1994-2010 [4].

Given the driving factors mentioned, the need for material development for higher temperature applications in particular is of great importance. As such, a key and detailed understanding of nickel-based superalloys is necessary. The following section will give an overview on the evolution and utilisation of nickel-based superalloys.

2.2 Nickel-Based Superalloys

2.2.1 Introduction

Nickel (atomic number 28, atomic weight 58.71), is a highly abundant transition metal utilised in a wide range of industrial applications over the past 4 decades, from aerospace and power generation to even more aggressive environments such as nuclear and chemical processing plants [15]. The crystallographic structure of the metal in pure form is FCC (face centred cubic) and exhibits both impressive physical and mechanical properties in comparison to other structural metals. The melting temperature of pure nickel is 1455°C, which represents the absolute limit for temperature capability of alloyed variations. In addition, nickel is an extremely dense metal in comparison to other structural metals, with a density of 8908kg/m^3 (Titanium 4505kg/m^3 and Aluminium 2700kg/m^3) as illustrated in Table 2.1. Nickel's main asset over other structural metals however is that it retains mechanical properties such as strength, ductility and toughness at higher temperatures. It is these characteristics alongside an excellent resistance to oxidation/corrosion, fatigue crack growth and creep strain accumulation that have led to nickel being heavily alloyed and engineered for industrial application, specifically within the aerospace industry [16] [17].

Table 2.1. Physical and mechanical properties of structural materials in pure form, adapted from [18].

Properties	**Titanium**	**Aluminum**	**Iron**	**Nickel**
Melting Point (°C)	1665	660	1535	1455
Density (Kg/m^3x10^3)	4.505	2.70	7.86	8.908
Tensile Strength (MPa)	440	80	340	450
Elongation to Failure (%)	29	47	39	47

As mentioned, Ni-based superalloys offer an impressive range of mechanical properties from high temperature strength and toughness to oxidation and corrosion resistance. It is worth noting however that these mechanical properties vary as a result of both chemical composition and material processing, as these factors majorly influence key microstructural features and subsequently mechanical properties. These microstructural features include grain sizing and structure, dendrite arm spacing,

gamma prime volume fraction and the presence of various secondary phases such as carbides and borides [19] [20] [21]. Through years of engineering, both compositions and process parameters have been amended to allow Ni-based superalloys to tolerate average temperatures of ~1050°C with occasional hot spots reaching temperatures as high as 1200°C [22] where high temperature mechanical deformation mechanisms such as creep are prominent [23]. The high temperature capabilities of Ni-based superalloys allow them to be used for a range of gas turbine components that are often subjected to arduous temperatures for long periods of time such as disc rotors [24], combustor cans [25] and turbine blades [26]. The following section will give an overview to alloying additions and how those can be used to influence and control microstructural evolution.

2.2.2 Microstructure and Chemistry

Although the major constituent of these superalloys is nickel, many cast alloys contain up to a 40 wt% of a combination of typically 5-10 other elements [27]. More complex alloy design with up to 15 alloying additions can be fabricated through powder processing [28], which will be discussed later in further depth. Alloying additions are an essential aspect of alloy design as they can be used to influence the presence and prominence of phases present within the microstructure. Ni-based superalloys primarily consist of the 3 phases, gamma (γ), gamma prime (γ') and MC carbides [29]. It is worth noting however that in specific cases, additional phases such as gamma double prime (γ'') and topologically close-packed (TCP) phases can be present [30]. Figure 2.7 gives an overview of the alloying additions typically associated with nickel.

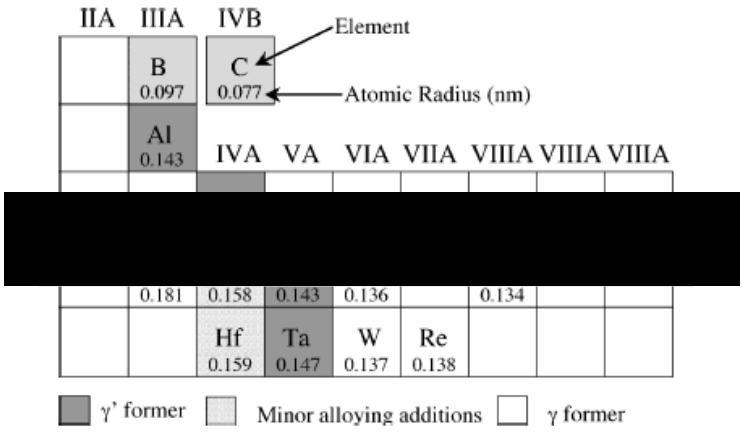

Figure 2.7. Alloying additions typically used in Ni-based superalloys and their relative positions within the period table [15].

2.2.2.1 Gamma and Gamma Prime

The γ phase is a continuous matrix of FCC structured nickel in which other phases reside. Within this matrix there are additions of elements exhibiting similar atomic radii (0.124-0.125nm) such as Co, Fe, Cr, Ru, Mo, Re and W. These additions contribute to the austenitic γ phase through a stabilisation mechanism. The γ' phase is the secondary precipitate, consisting of an ordered $L1_2$ crystal

structure of typically Ni_3Al, as shown in Figure 2.8. It is worth noting however that other alloying additions of similar atomic radii to Al (0.143-0.147nm) such as Ti, Ta and Nb can also contribute to the formation and strengthening of this phase. Both Ni and Al consist of FCC crystal structures, resulting in a significant degree of directional covalent bonding in each unit cell. In addition, the FCC crystal structure results in Ni-Al bonding rather than Ni-Ni or Al-Al bonding, displaying a strong degree of 'chemical order'. Furthermore, γ' precipitates give rise to a precipitation strengthening mechanism, where small, hard intermetallic particles are present within the disordered FCC γ matrix giving rise to impeded dislocation movement. Subsequently, the yield strength of nickel superalloys is primarily a function of various γ' characteristics including inter-particle distance, volume fraction of the particles and particle sizing alongside dislocation interaction.

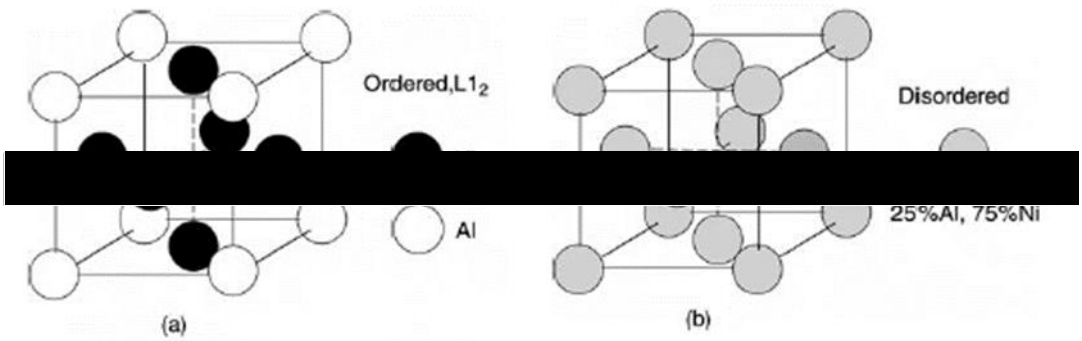

Figure 2.8. Ni and Al atom arrangement for both ordered and disordered FCC structures [9].

This precipitation strengthening process consequently results in γ' being a key strengthening phase within Ni-based superalloys and a key area of interest during microstructural evolution. γ' is formed through the cooling of a supersaturated solid solution of γ below the equilibrium solvus temperature and it is worth noting that both the solidus and solvus temperatures vary for different alloys. The sizing of this precipitate will dictate the location, distribution and frequency of this phase and as a result is typically defined into three subcategories: primary, secondary and tertiary γ' based on their size and location [31]. An overview of their size and microstructural coherency is given in Figure 2.9.

- Primary γ' is 1-5μm in size and is as a result not coherent with the γ matrix. Given this, they typically form along grain boundaries.
- Secondary γ' is 100-400nm in size and is as a result coherent with the γ matrix, precipitating out of the matrix upon quenching from solution heat treatments above 1000°C for specific alloys.
- Tertiary γ' is 5-50nm in size and is again as a result coherent with the γ matrix, precipitating out of the matrix upon quenching from solution heat treatments below 900°C for specific alloy systems.

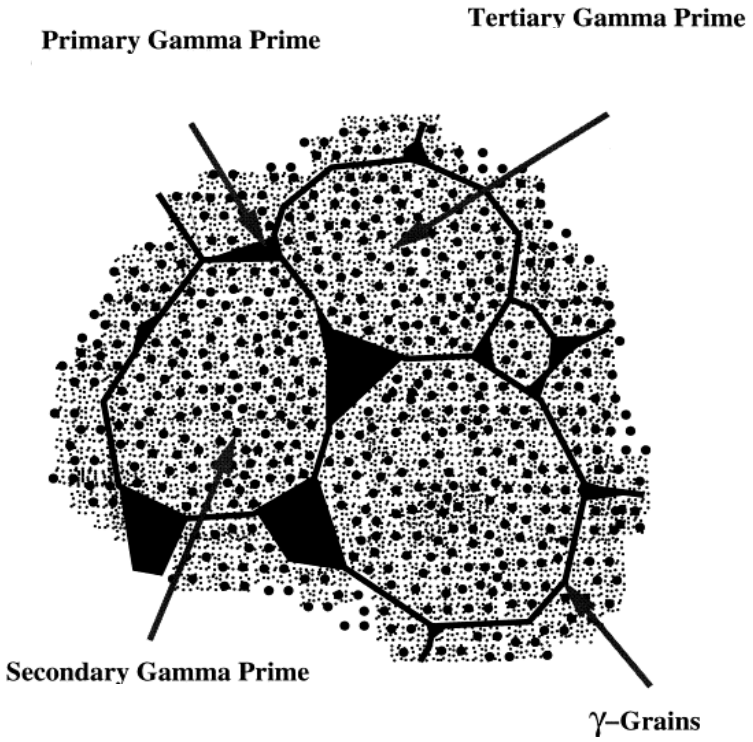

Figure 2.9. Primary γ' formed along grain boundaries alongside secondary and tertiary γ' which reside within the γ matrix, adapted from [32].

2.2.2.2 Carbides and Borides

Carbides form along γ grain boundaries when carbon, with concentrations up to 0.2wt%, combines with small additions of alloying elements such as Ti, Ta and Hf to form a primary MC, where M represents the metal atom. This occurs as a result of carbon's high affinity for these elements. Although the influences of carbide formation on mechanical properties are not yet fully understood, there is evidence to suggest both beneficial and detrimental effects. Thus, their formation is used as a method of controlling grain structure and enhancing creep performance through the reduction of stress accumulation at grain boundaries whilst impeding dislocation movement [33]. Furthermore, carbides can be used to restrain detrimental elements that also sit on grain boundaries. In addition, carbon, boron and hafnium can also combine with small additions of Cr or Mo to form borides along γ grain boundaries, which also gives rise to creep resistance through the same microstructural mechanisms as demonstrated by Chen et al [34]. Although it is worth noting that carbides are far more frequent and prominent and their morphologies vary substantially as a consequence to varying degrees of aging and the extent of alloying additions such as carbon and boron [35]. It is noted that higher carbon contents generally lead to more complex morphologies such as secondary and tertiary dendrite arms. It is also worth mentioning that these primary carbides can decompose into other variations such as $M_{23}C_6$, M_6C and M_3B_2 during heat-cycles, which is dependent on their original composition and the alloying additions present [36]. An illustration of such variations like MC and $M_{23}C_6$ situated along the grain boundary in the nickel superalloy MAR-M247 is shown in Figure 2.10.

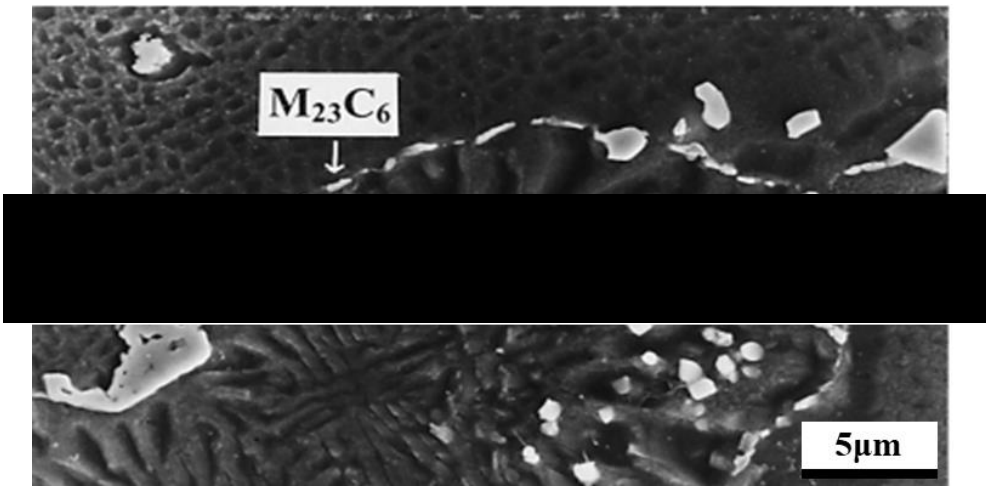

Figure 2.10. MC and $M_{23}C_6$ carbides situated on grain boundaries in Mar-M247 [37].

2.2.2.3 Gamma Double Prime and Delta Phase

Within specific nickel-based superalloys which use high quantities of Nb such as IN718 and IN706, the primary strengthening phase is not *γ'* but instead a body-centred tetragonal (BCT) ordered phase known as gamma double prime (γ'') (see Figure 2.11). Typically consisting of the composition Ni_3Nb and sometimes Ni_3V, this BCT crystal structure results in lattice mismatch with the surrounding FCC matrix leading to high coherency strains and 'order hardening' [38].

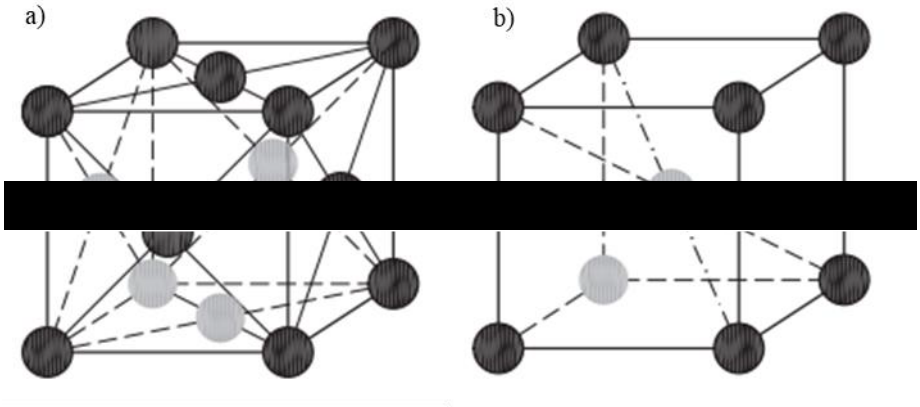

Figure 2.11. Schematics illustrating a) face centred cubic crystal structure and b) body centred tetragonal crystal structure [39].

It is worth noting however that γ'' is typically used to strengthen nickel-based superalloys at lower temperatures up to <650°C as γ'' is metastable and can thus transform into undesirable thermodynamically stable delta (δ) phases under thermal exposure [40]. However, δ phases are incoherent with the γ matrix and in specific cases such contents can strengthen the matrix and inhibit grain growth during heat treatments, which can be subsequently exploited. However, in typical cases, the precipitation of this phase is at the expense of γ'' and thus leads to an apparent decrease in strength. An example of δ phase precipitation in IN718 in both needle and globule form is shown in Figure 2.12.

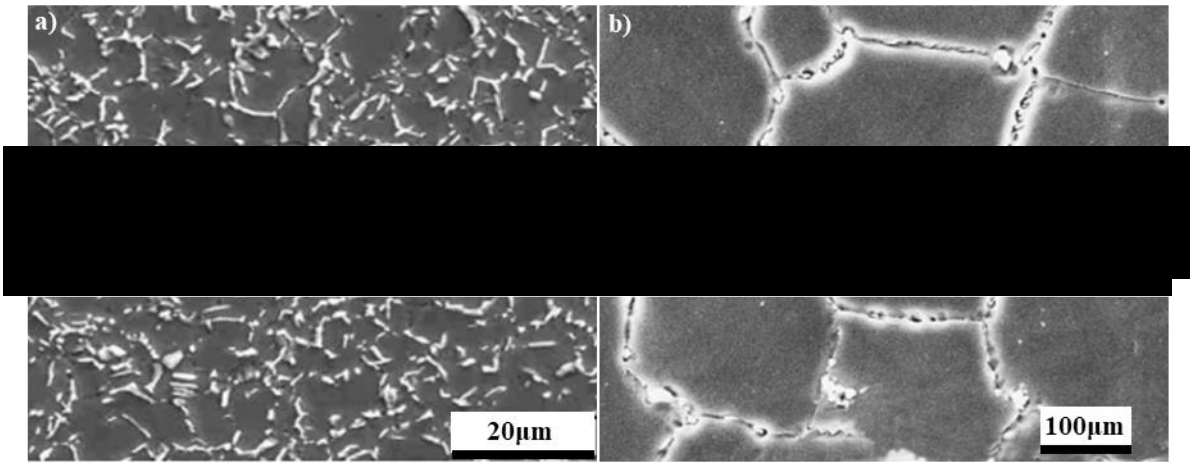

Figure 2.12. a) delta phase distribution within IN718 post heat treatment [41] b) delta phase populating the grain boundaries of IN718 [42].

2.2.2.4 Laves Phase (Topologically Close-Packed)

High amounts of Fe, Cr, Mo, W and Re initiate the precipitation of an undesired brittle intermetallic topologically close-packed (TCP) phase known as Laves as shown in Figure 2.13. This occurs as of consequence to Nb, Si, and Mo segregation and consists of a number of key characteristics such as high uniform packing density and non-metallic directional bonding, which can significantly degrade mechanical properties [43]. In addition to the brittle nature of Laves phases, given the inherent chemical segregation of Nb, it has been shown that the presence of Laves phase can lead to Nb depletion both within the γ and γ'' phases and thus degrade their precipitation strengthening effect in a similar manor to δ phasing.

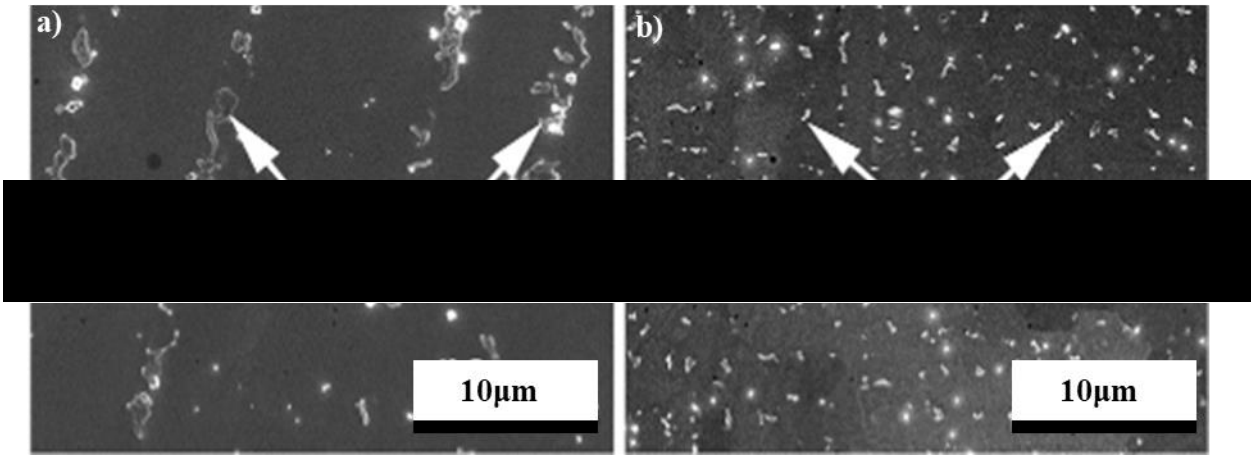

Figure 2.13. Laves phases with different morphologies and distributions dependant on variables within the manufacturing route [44].

2.2.2.5 Further Alloying Additions

Despite the presence of alloying additions influencing the phases which are present in the final alloy, it is worth considering that given the usage of Ni-based superalloys within the gas turbine engine, they will often face challenges from an environmental degradation perspective. In particular, for low altitude flights over seas, deserts and volcanic regions can lead to the ingestion of contaminant particles, giving rise to forms of hot corrosion [45] [46]. As a result of this, alloy designers combat these degradation mechanisms through the alloying additions of Cr, Y and La, which can significantly improve both oxidation and corrosion resistance. Within alloying chemistry, the presence of some elements and trace contaminants such as Si, P and in particular S can become prevalent and are often detrimental [21] [47]. Given their incoherency with the γ matrix, they are likely to segregate and form lower melting points on grain boundaries, aiding intergranular cracking [48]. It is therefore worth noting that the alloying additions of minor elements such as Hf and Zr that can form stable sulphides become indispensable, as they can reduce the influence of embrittlement from trace elements remaining in solid solution.

2.2.3 Alloy Design and Application

As mentioned in the previous section, alloying additions and chemistry play a pivotal role in the formation and presence of phases within Ni-based superalloys, which subsequently dictate physical and mechanical properties. The following section will give a brief introduction and insight into the alloy designs of both CM247LC and IN718, the alloys utilised within this study.

2.2.3.1 CM247LC

CM247LC is a nickel-based superalloy developed by the Cannon Muskegon Corporation in the late 1970s as a low carbon alternative to MAR-M247 [49]. It was originally designed with the intention for directionally solidified turbine blade applications within the gas turbine engine given its high temperature capabilities and coarsened grain structure, lending itself favourably to creep resistance [50].

Table 2.2. CM247LC alloy composition by weight %.

C	**Cr**	**Ni**	**Co**	**Mo**	**W**	**Ta**
0.07	8	Bal.	9	0.5	10	3.2
Ti	**Al**	**B**	**Zr**	**Hf**	**Si**	**S**
0.7	5.6	0.015	0.01	1.4	0.03	15ppm

CM247LCs high temperature capabilities come as of direct consequence to the high proportions of γ' formers being present in the material's composition as shown in Table 2.2, comparative to most nickel-based superalloys. This can subsequently lead to an astonishingly high γ' prime volume fraction

of roughly 50-60%. As previously mentioned, the precipitation strengthening effect that γ' imposes is the key strengthening mechanism within Ni-based superalloys, however given the extremely high volume fraction witnessed this can be at the expense for ductility and weldability as will be discussed later on. In an attempt to alleviate these unfavourable effects with resistance to high temperature mechanical deformation mechanisms in mind, the reduction of elements such as S (15ppm) and Si (0.03wt%) were imposed in an attempt to minimise the presence of grain boundary cracking. Furthermore, the presence of sulphide stabilisers such as Zr and Hf were included in an attempt to combat this mechanism. Additionally, a reduction in carbon content of 0.07%wt was imposed in order to adjust for the coarsened grain structure and minimise the volume fraction of grain boundaries observed in directionally solidified structures and to reduce the presence of coarsened, detrimental MC carbides at these grain boundaries.

Given CM247LC's specific tailoring towards directional solidification, the influence of the manufacturing route and any post processing treatments on the various mechanical properties has been well investigated. Kim et al [51] has highlighted the influence of the casting procedure on grain structure for both Conventionally Cast (CC) and Directionally Solidified (DS) CM247LC and their inherent differences in tensile properties over a range of temperatures as shown in Figure 2.14. It is shown in Figure 2.14a that DS CM247LC displays a greater ultimate tensile strength (UTS) than that of CC CM247LC whereas Figure 2.14b also further emphasised the importance of solution heat treatments and aging over standalone aging treatments, given its ability to improve high temperature elongation and consequently, high temperature tensile performance as shown in Figure 2.15.

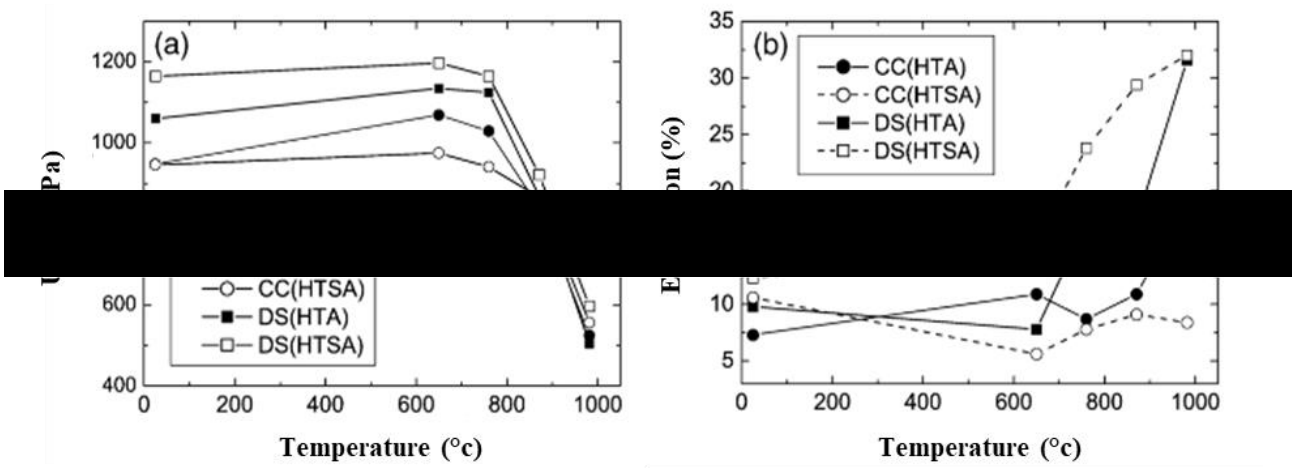

Figure 2.14. Influence of casting procedure on a) ultimate tensile strength (UTS) and b) % elongation of CM247LC over a range of temperatures [51].

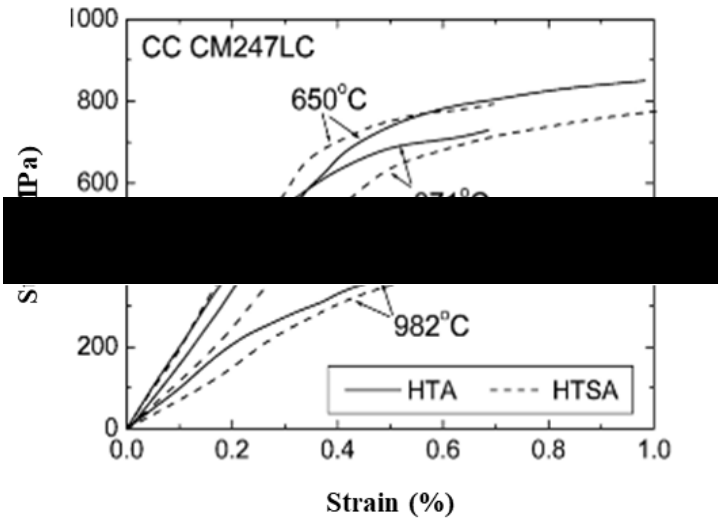

Figure 2.15. Influence of heat treatments on the tensile properties of conventionally cast CM247LC [51].

2.2.3.2 IN718

Inconel 718 was originally designed in the late 1950s by the International Nickel Company and displays an impressive range of mechanical properties from high strength to excellent ductility and weldability [52] [53]. It is for these reasons, alongside relatively low cost achieved through low Co and high Fe contents (17.62wt%), that IN718 has lent itself as a competitive choice for a wide range of industrial applications, specifically within the aerospace sector where it has been heavily exploited in the gas turbine engine for temperature applications up to ~650°C [54] [55]. The alloy's composition is presented in Table 2.3.

Table 2.3. IN718 alloying nominal composition by weight %.

C	**Cr**	**Ni**	**Mo**	**Mn**	**Nb**
0.024	18.84	Bal.	3.08	0.02	5.23
Ti	**Al**	**Fe**	**Si**	**S**	**P**
0.95	0.53	17.62	0.06	0.002	0.003

Given its relatively low volume fraction of γ' formers such as Al and Ti (0.53wt% and 0.93wt% respectively) and high Nb contents (5.23wt%) as indicated, the formation and prevalence of Ni_3Nb becomes apparent. As consequence, IN718 is primarily strengthened by the formation of the metastable γ'' at a volume fraction of approximately 20% [56], which under thermal exposure over 650°C can

transform into the undesirable thermodynamically stable δ phase as previously mentioned. This transformation is typically associated with the loss of γ'', strength and it is for this reason that IN718 is limited to applications up to 650°C. Furthermore, given the high ductility apparent with low γ' volume fractions, tighter controls over detrimental alloying additions such as Si and S are not necessary as demonstrated (0.06 wt% and 0.002 wt % respectively). El-Bagoury et al [57] demonstrated the effects of heat treatments in order to manipulate the size and morphology of γ'' whilst being able to homogenise chemical segregation and thus dissolve δ phases.

2.2.4 Processing Routes

Ni-based superalloys are traditionally manufactured through wrought and cast methodologies given its scalability. However, there is ongoing research into the use of alternative means such as powder processing metallurgy, both of which have numerous advantageous and limitative characteristics. The choice of route is generally dictated by the desired application of the component and alloy chemistry. Alloys such as IN718 that have a relatively low level of Al, Ti and Nb are usually formed through ingot metallurgy given the relatively low cost implications associated with this process. Powder metallurgy routes on the other hand are used for highly complicated alloys as previously mentioned at an expense for higher costs. A brief outline of cast and wrought methodologies alongside powder metallurgy is given below.

2.2.4.1 Wrought Alloys

Casting is an ancient process that dates back to 3200 B.C and is thus subject to 5000 years of technological advances [58]. It is the process in which molten metal flows by gravity or force into a mould where it solidifies in the shape of the mould cavity and thus is used to form either a complex desired shape, or an ingot which will be subsequently reworked through rolling, forging or extrusion [59]. Per year, over 100 million tonnes of cast and wrought material is manufactured [60] given both its reliability and scalability and as a result it is heavily utilised as the primary source of fabrication for Ni-based superalloy components within the aerospace sector.

For basic component geometries, the use of an initial ingot that can be further plastically deformed offers significant simplicity. For the aerospace industry in particular, standard ingot metallurgy incorporates the use of a series of melting processes such as vacuum induction melting (VIM), electro-slag remelting and vacuum arc remelting (VAR) in order to remove low melting point trace contaminants and evenly distribute and minimise the contamination of non-metallic inclusions (NMI). These 3 melting processes result in the production of a high quality ingot suitable for aerospace applications which will then undergo multiple plastically deforming operations, primarily forging in order to produce a billet with a maximum diameter of 10".

2.2.4.2 Casting Alloys

For fairly complex geometries, the utilisation of casting processes with complex mould cavities becomes necessary. Although there are 90+ forms of casting technologies worldwide, they can be primarily categorised through several criteria such as reusability of the mould and the method in which the molten metal flows into the mould cavity [61]. Sand casting is one example of the process in which an expendable sand mould is utilised in order to shape the molten liquid. Once the molten liquid enters the mould through gravity it is subject to cooling and solidification, after which the mould is broken off. Within this method, further processing may be required in regards to the machining of excess material trimmings as well as surface treatments given sands implications on surface roughness [62]. Die casting on the other hand is the process in which molten liquid is forced between dies and can be performed in a variety of forms, which include gravity, low pressure and high pressure. Upon cooling and solidification, the die opens and the casting is removed, however further processing to remove additional material trimmings such as flow offs and flash is removed [63]. Given the lack of dimensional accuracy and additional processing techniques needed to improve surface finish for both sand and die casting, they are not considered appropriate for the manufacture of safety critical components. Therefore, the utilisation of investment casting takes precedent, where wax patterns in the desired shape of the casts are fabricated and coated with a refractory material to form a mould. From there, the wax is melted away and the remaining mould is filled, mass-producing components of high dimensional accuracy and surface finish [64].

2.2.4.4 Alternative Routes

Although cast and wrought methodologies have numerous advantageous aspects, they are suspect to limitations. As such, the aerospace industry in particular is becoming increasingly interested in the use of alternate manufacturing routes such as powder metallurgy in order to facilitate the production of highly intricate components, which gives increasing scope both in regards to mechanical and alloy design.

Powder processing also begins with the use of VIM in a refractory crucible, which is subsequently re-melted and fed into an inert gas atomisation procedure, leading to the formation of powder. The resulting powder formed is screened through a sieving process; removing any large NMIs beyond a certain threshold and ultimately improving the cleanliness of the process [65]. As previously mentioned with VIM, there are concerns as to the presence of NMI as a result of direct contact with the refractory crucible. NMIs such as alumina and other ceramics exhibit different thermal expansion coefficients, leading to the formation of undesired microstructural abnormalities during solidification. Once screened, the powder is then consolidated, loaded into a can, degassed and sealed which is

subjected to Hot Isostatic Pressing (HIP) consolidation. Powder processing gives a lower concentration of undesired inclusions and higher chemical homogeneity at a trade-off for cost. However, given the different nature and recent emergence of powder processing routes, there are different challenges and unknown phenomena. One example of this is chemical inhomogeneity, where powder particles have shown elemental segregation along the surface through the formation of oxide films (<50nm deep). In addition, during thermomechanical processes such as HIPing, carbon diffuses to the surface of the particles, forming a network of oxycarbides known as prior particle boundaries (PPBs), which have been shown to reduce fatigue life [66].

The following section will give an overview as to the utilisation of powder processing for near net shape manufacturing technologies.

2.3 Additive Layer Manufacturing

2.3.1 Introduction

Additive Layer Manufacturing (ALM) is a near-net shape fabrication technique that utilises high-energy heat sources such as electron beams and lasers to build components layer by layer with the use of a computer aided design (CAD) [67]. ALM first emerged into industry in the late 1980s with the invention of stereo-lithography, an innovative technology that incorporated the use of a laser to solidify ultraviolet sensitive photopolymers in conjunction with a 3D model [68]. This concept sparked the interest of numerous industrial sectors, leading to its further development throughout the 1990s and 2000s [69], with the medical industry in particular leading the way, fabricating numerous medical devices from blood vessels and prosthetics to fully functional organs [70]. Within the last decade, the aerospace industry has become increasingly interested in exploiting ALM for both component repair and fabrication [71].

2.3.2 Additive Manufacturing Processes

The additive manufacturing of materials and specifically metallic alloys can be subcategorised into two particular methodologies; Directed Energy Deposition (DED) and Directed Layer Deposition (DLD) [72]. DED is a material deposition process in which stock, wire or powder, is solidified on a specified surface with both high accuracy and potentially high deposition rates [73]. As a result of this, blown powder, one of the most notable DED technologies, has been implemented within the aerospace industry for repairing components damaged by foreign objects within service, with one key example application being blisk (bladed disk) repair [74]. During blown powder, metallic powders are blown coaxially into the laser beam where these powders melt on the targeted surface and then solidify when cooled, forming bonds. Despite the advantageous characteristics of this process, blown powder does face significant drawbacks and challenges. These include poor surface finish, low powder efficiency and geometric limitations [75].

The key primary example of DLD technology is Powder Bed Fusion (PBF), a manufacturing technology that offers the ability to produce highly intricate components with very little to no material wastage. Thin layers of powder (approximately 0.1mm), are spread over the build platform and melted using a high energy heat source (electron or laser) in order to fabricate a sliced layer of CAD data. From there a roller is used as a recoating mechanism, laying down powder on top of each scanning area, allowing further layers or cross-sections to be repeatedly added layer by layer using pistons until a full 3D component is manufactured as depicted in Figure 2.16. Powder not taken up during the process is removed and subsequently recycled [76].

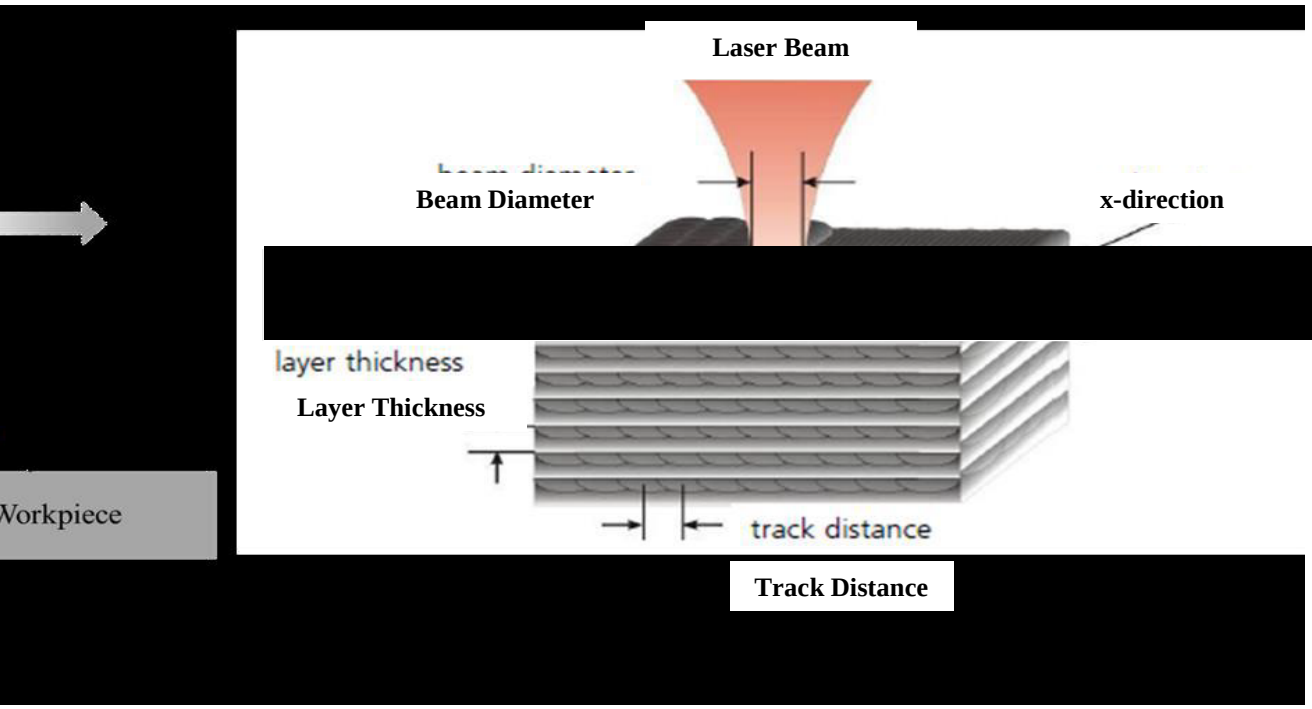

As mentioned, PBF processes typically employ either an electron or laser beam as a heating source and are thus referred to as either electron beam melting (EBM) or laser powder bed fusion (LPBF). The employment of different heating sources inherently bears implications on the configuration of the process and as such each process offers different advantageous characteristics and limitations. EBM is performed within a vacuum where the advantages of this include the reduction of impurities and internal stresses alongside higher energy capabilities due to a narrower beam diameter. However, these advantages come as a trade-off, with drawbacks including the cost implications of a vacuum, long dead times in-between production and its limitation to materials that are conductive [78]. LPBF on the other hand uses a laser beam as a primary heat source with a continuous argon stream and is often referred to as selective laser melting (SLM), which offers numerous advantages in comparison to EBM. Laser melting processes are highly flexible regarding material developments, offering the possibility to work with finer powders and produce higher geometrical complexity [79].

ALM processes offer significant advantages over conventional cast and wrought methodologies with the major premise being the ability to produce components of high geometrical complexity not

possible using traditional casting techniques. This is of particular interest to the aerospace industry as it lends itself well to the driving factors in materials development discussed in section 2.1.4, where the ability to produce components with high geometrical intricacy can drive weight reduction through advances in engine architecture and design [80] [81]. In addition to this, the implementation of complex internal features such as cooling channels can give rise increased temperature capabilities [82].

2.3.3 Process Parameters and Variables

Given the advantageous characteristics of LPBF, the aerospace industry has become ever more attentive in exploiting such technology for component manufacture in an attempt to drive advancements in the gas turbine engine as mentioned previous. However, given the metallurgical complexity of the process, concerns arise regarding structural integrity as a result of process dependant phenomena. Consequently, a key understanding of the process parameters, variables and their influence on the formation of stress raising features has risen in parallel.

It is evident in literature that process variables such as heat sources, powder bed temperatures and component geometries alongside process parameters such as beam velocity, power, hatch spacing and layer thickness has been the subject of ongoing research. However, given the sheer volume of possible variations of combined parameters and their interactions, the assessment of these metrics influence proves rather difficult. There is a general unanimity in ALM literature that utilises energy density as a good forecaster for material density and microstructural characteristics [83] [84], although there has been criticism as to its effectiveness [85] [86] for reasons which will be discussed later. This concept is shown from a volumetric standpoint in Equation 4, utilising the key process parameters beam power (q), beam speed (v), hatch spacing (h) and layer height (l).

$$E^* = \frac{q}{v\,h\,l} \tag{4}$$

Where beam power (q) is in watts, beam speed (v) is in meters per second and both hatch spacing (h), layer height (l) are in meters, leading to energy density (E^*) being joules per cubic meter.

Given the complexities regarding the abundance of process parameters as discussed, methods have been developed in order to establish more simplified approaches of data interpretation. Ion et al [87] developed the initial normalised process map approach as a means of visually representing this information and puts forward the concept that the two dimensionless groups of parameters, namely beam power (q^*) and beam velocity (v^*), which should be considered in regards to the thermal cycle at any point within the material. Where A_q is the surface absorptivity, r_B is the beam radius, λ and α are the thermal conductivity and diffusivity of the alloy being processed and T_m and T_0 are the respective melting and initial powder bed temperatures of the material.

$$q^* = \frac{A_q}{[r_B \lambda (T_m - T_0)]} \tag{5}$$

$$v^* = \frac{v r_B}{a} \tag{6}$$

Thomas et al [88] further adapted this approach by incorporating additional ALM process variables such as *l* and *h*. As shown in the cross sectional schematic of the melted zone of material in Figure 2.17, $2r_B l$ gives an approximation of the area of material melted**.** It is stated that if the energy used for a unit length of track is q/v, then the energy per unit volume in order to raise the material to the critical temperature T_m is $q/2vlr_B$. This dimensionless energy term can be expressed as shown in Equation 7**.**

Hatch spacing was considered within this study as a key consideration as it controls the level of overlay between neighbouring melt pools. High *h* is economically beneficial as it'll reduce build times and is therefore a key consideration from an industrial perspective, however, it also runs the risk of lack of full material consolidation and consequently the formation of voidage. Narrower *h* on the other hand eliminates this issue given the prominence of overlapping tracks and remelting, at a cost for time.

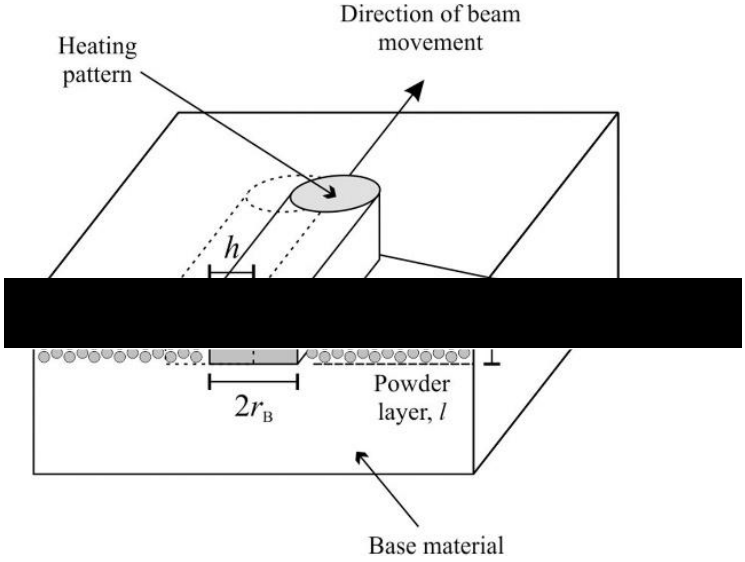

Figure 2.17. Schematic representation of melting zone for LPBF [88].

$$E^* = \frac{q^*}{v^* l^*} = \left[\frac{Aq}{2vlr_B}\right]\left[\frac{1}{0.67pC_p(T_m - T_0)}\right] \tag{7}$$

$$h^* = \frac{h}{r_B} \tag{8}$$

By incorporating these process variables numerically in conjunction with existing literature over a wide range of alloying systems such as titanium, nickel and steel, Thomas et al [88] developed the normalised process map as shown in Figure 2.18 as a means for visually representing the process window. A logarithmic scale of E^* is compared directly with $1/h^*$, which is used as a ranking tool and ordinate scale to measure the degree of hatch spacing relative to the beam diameter. It is worth noting the significantly narrow processing window for CM247LC, which is typically associated with high γ' nickel superalloys as shown below in Figure 2.19. This is as of consequence to the increased mechanism associated with γ', at a trade-off for ductility. Considering that ALM is a multi-pass welding process with cooling rates of up to ~ 10^6 K/s [89], structural integrity issues become a concern in terms of high residual stressing and dislocation activity, thus making the ALM of these alloys and the alleviation of such issues particularly challenging. An overview of the parameters utilised within the normalised process map is given below in Table 2.4.

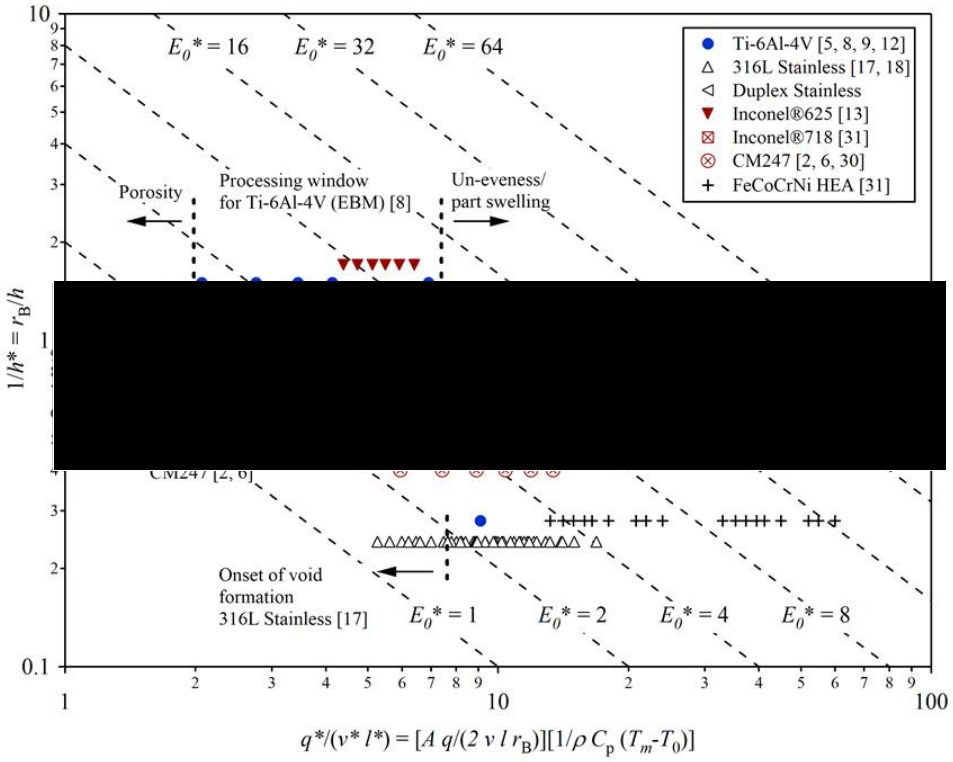

Figure 2.18. Normalised process map for a range of ALM alloying systems [88].

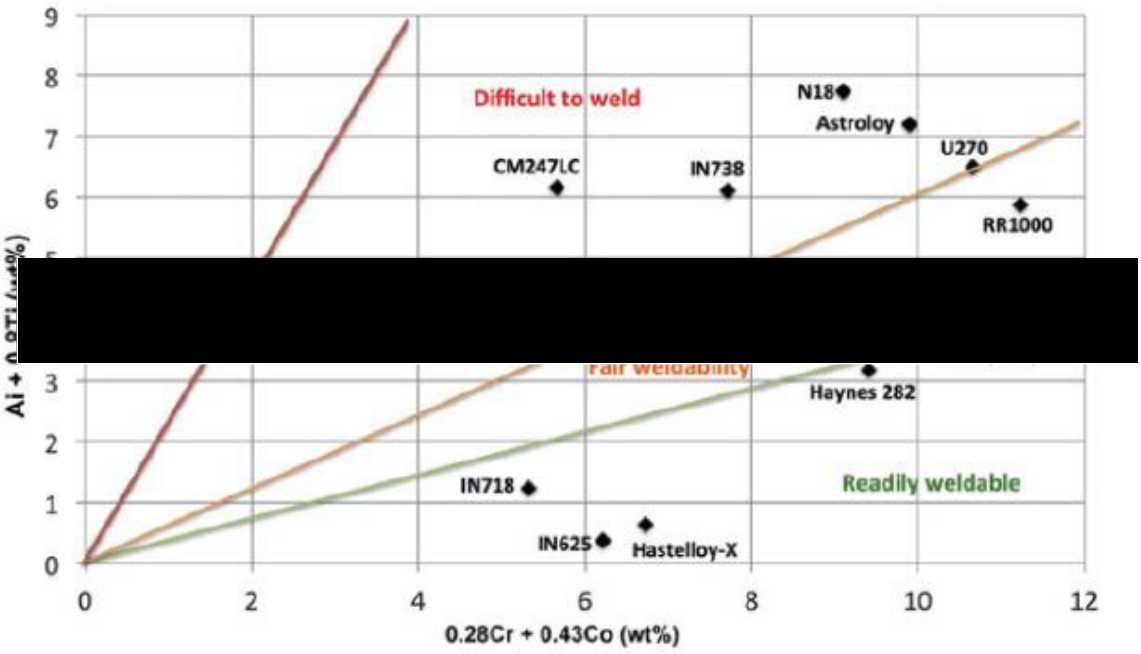

Figure 2.19. Weldability of Ni-based superalloys in relation to γ /γ' content [90].

Table 2.4. Process and material variables that contribute to process parameters.

Notation	Process Variables & Material Properties	Units	Notation	Process Variables & Material Properties	Units
A	Surface Absorptivity	-	q	Power	W
C_p	Specific Heat Capacity	$J\ kg^{-1}\ K^{-1}$	q*	Normalised Power	-
E_0*	Normalised Equivalent Energy Density	-	rB	Beam Radius	M
h	Hatch Spacing	m	T_m	Melting Temperature	K
h*	Normalised Hatch Spacing	-	T_0	Initial Powder Bed Temperature	K
l*	Layer Height	m	v	Beam Velocity	ms^{-1}
ρ	Density	$kg\ m^{-3}$	V*	Normalised Beam Velocity	-

Carter et al [91] has highlighted how the extremities of the process window can lead to the formation of microstructural defects and abnormalities for high γ' nickel alloys such as CMSX486. In this study, variations in nominal energy density (not including thickness) and the influence of parameters such as *q* on structural integrity were investigated, with low powers giving rise to lack of material consolidation. As energy is increased and the material's *E** threshold is surpassed, full material consolidation and the initiation of grain boundary cracking occurs. Further increases in *E** leads to higher, more excessive cracking and in some cases keyholing as will be discussed in Section 2.3.5. This is highlighted in Figure 2.20.

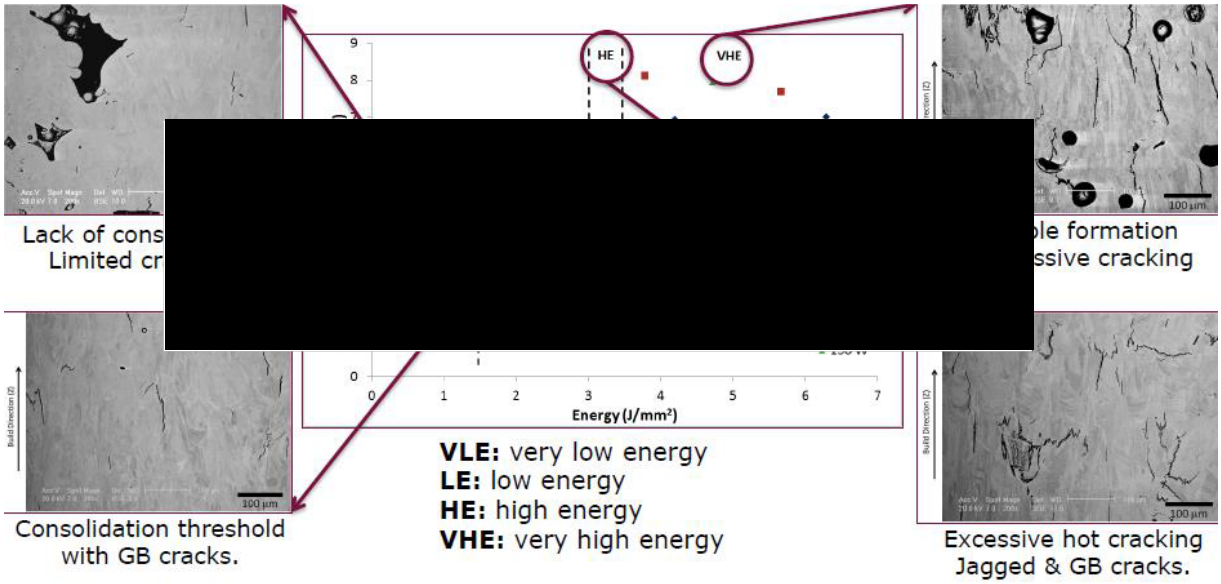

Figure 2.20. Cracking density against nominal energy density for CMSX486 with resulting microstructural defects [91].

Carter has further demonstrated similar mechanisms within CM247LC [92], highlighting the importance of *E** and in particular the minimum *E** threshold from a structural integrity standpoint. Lower *E** lead to a lack of material consolidation with limited cracking as shown in Figure 2.21 and as *E** increases past the material's consolidation threshold, cracking appears to generally increase until a certain point where it seemingly levels off, as highlighted in Figure 2.22. It is worth noting the level of scatter and variability for cracking density appears to be significantly more prevalent at higher powers comparative to low powers, highlighting the challenges associated with using the simplified *E** as a quantitative metric. Nevertheless, the degree of variance is likely to be consequential to the large degree of parameters and variants within the ALM process, many of which could innately impact beam-material interaction dynamics, once again highlighting the difficulties in characterising and interpreting process parameters.

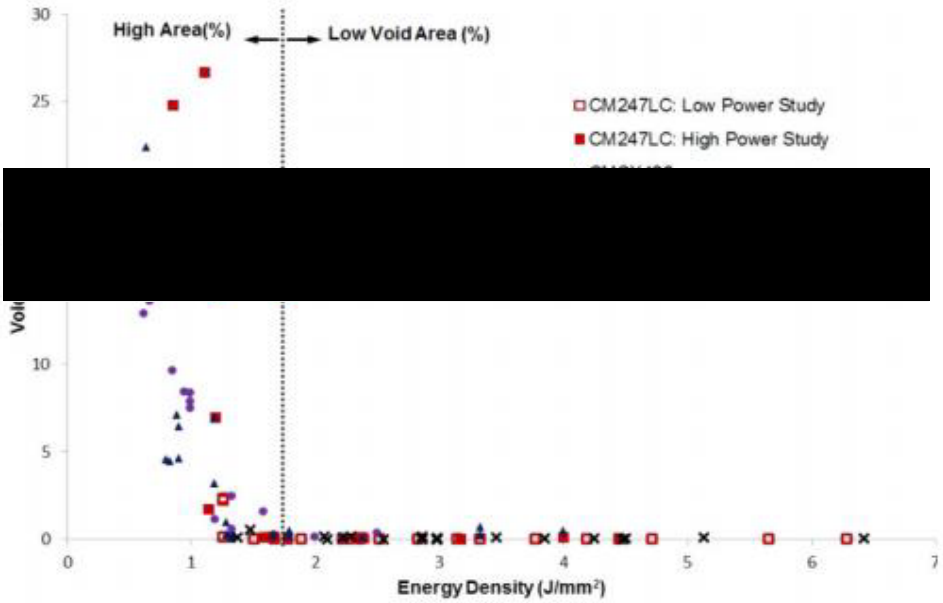

Figure 2.21. Influence of energy density on void formation for several LPBF nickel superalloys [92].

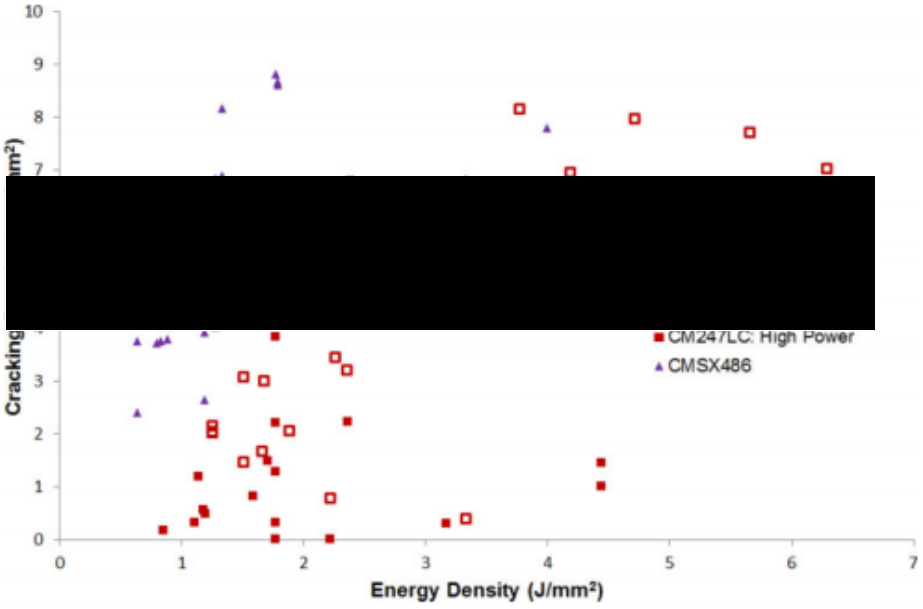

Figure 2.22. Influence of energy density on cracking density for CM247LC and CMSX486 [92].

On the contrary to CM247LC, IN718 is widely accepted to be a fairly weldable alloy given its γ' content and as such lends itself well to ALM [53]. Subsequently, IN718 is considered to have a wide process window with little to no cracking being encountered. One study found that the build process parameters had minimal influence on the resulting mechanical properties providing that the materials relative density is in fact ~ 99% as shown by Huang et al [93]**.** This study does note however the pivotal role process parameters play on both the key strengthening precipitates, γ' and γ'' and detrimental δ phase, with higher energy outputs increasing the average dendrite arm spacing and δ volume fraction**.** Despite the relatively wide process window of IN718, research has suggested that process parameters

do play a role on porosity levels as illustrated by Kumar et al [94] in Figure 2.23, where increases in *v* promotes relatively higher levels of porosity and increases in *E**, emphasising the inverse effect.

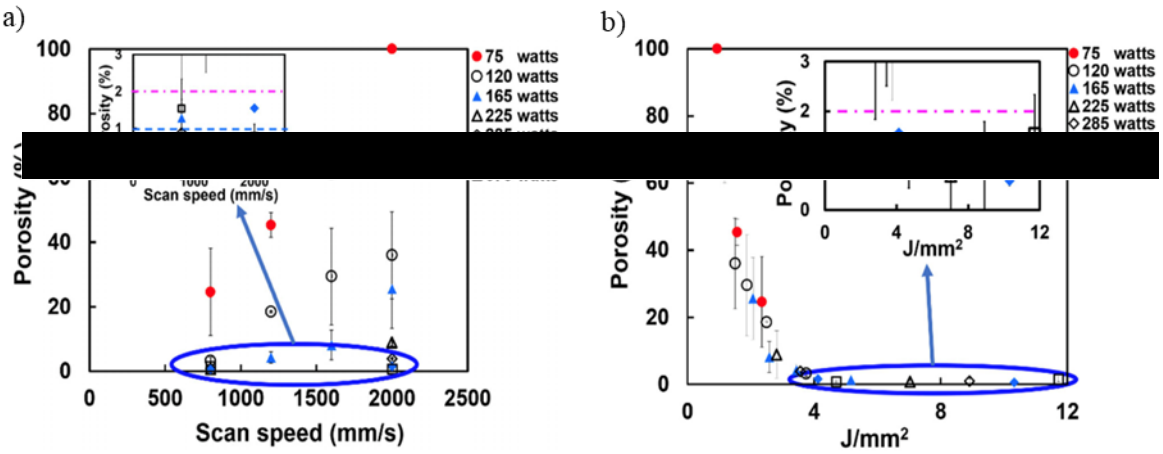

Figure 2.23. Porosity volume fraction in relation to a) beam scan speed b) energy density [94].

It is suggested that despite the weldability and relatively high density of IN718, process parameters do play a role in porosity mechanisms. However, it is suggested that this is as of consequence to their influence on melt pool shape and dimension which consequently play a more dominant role in dictating both the level and shape of porosity. Given this, a further understanding of the influence of process parameters on melt pool dimension and shape is required. The following section will give an indication as to the nucleation, growth and grain structures observed within ALM as previously eluded too as well as the influence of process parameters on melt pool dynamics and its implications on microstructure and structural integrity.

2.3.4 Microstructural Evolution

Given the layer upon layer nature of the process, ALM is subject to epitaxial grain growth and cooling mechanisms that offer different metallurgical characteristics to that of traditional casting methodologies. In the initial layers, high cooling rates are achieved through contact with the substrate leading to the formation of a fine grain structure as a result of shorter growth times being available [95] [96]. However, as layer height increases and contact with previously heated layers become prominent, slower cooling rates lead to the formation of coarser and eventually elongated grains subsequent to competitive grain growth as indicated in Figure 2.24**.** The direction of grain growth is typically aligned to the {001} direction and is dictated by the melt pool shape and size, with the grains growing from the boundary towards the centre of the melt pool as shown in Figure 2.25. In the case of LPBF, melt pools are traditionally long and shallow with variances dictated by process parameters, giving further indication as to the existence of a downwards heat flow.

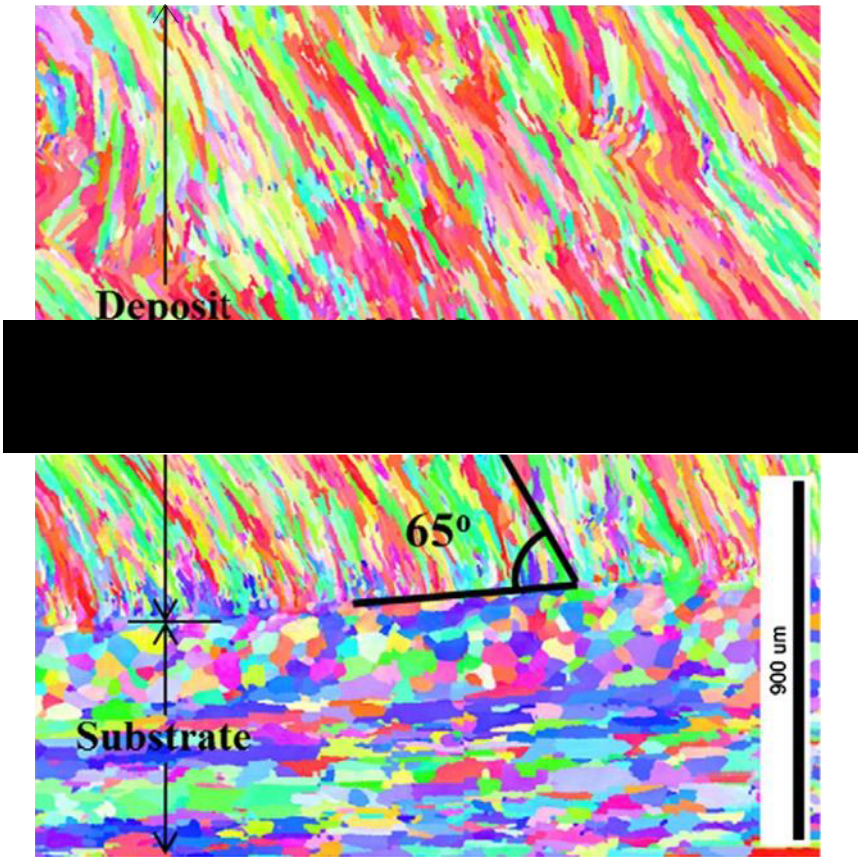

Figure 2.24. EBSD texture mapping of the evolving microstructure within LPBF AlSi10Mg alloy [97].

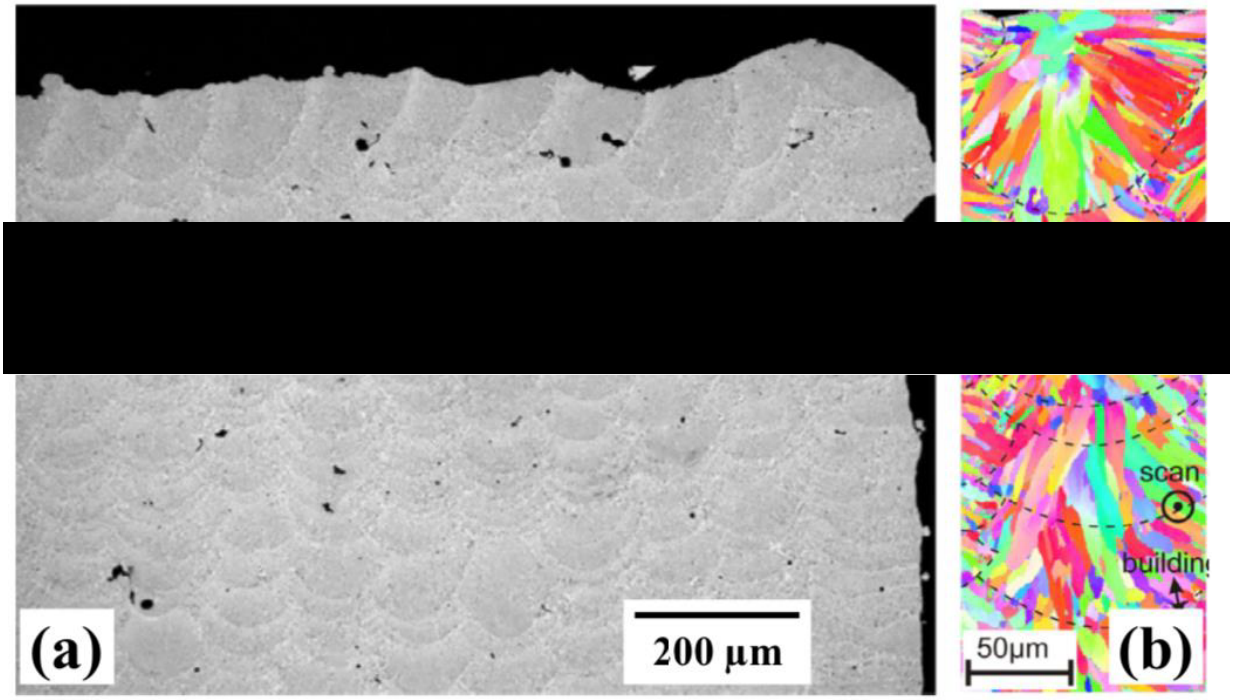

Figure 2.25. a) SEM of existing melt tracks within LPBF AlSi10Mg alloy b) corresponding EBSD texture mapping of melt tracks showing internal grain growth within the molten pool [98].

Given the fact that melt pools act as the origin for grain growth and are dictated by process parameters, there have been ongoing efforts to characterise melt pools as they give insight into the consistency of the process. This has even been continued to the extent where it is included in the Marshall Space Flight Centre's (MSFC) technical standard and specification for controlling LPBF metallurgical processes [99] which acts as a subsidiary to the National Aeronautics and Space Administration (NASA).

White et al [100] utilised a semi empirical, statistical approach to quantifiably ascertain the impact of process parameters on melt pool profiles within a LPBF AlSi10Mg alloy. Microscopic analysis, as shown in Figure 2.26, was conducted in conjunction with manual measurements to gauge the impact on both track depth and width. It was shown that both power and scan speed are 'primary parameters' for influencing melt pool depth, as shown in Figure 2.27, with a linear asymptotic correlation being observed between energy density and track depth. This paper also found that *h** and *l** can impact track width, where track coalescence and pairing can occur given their interactions with previously deposited layers.

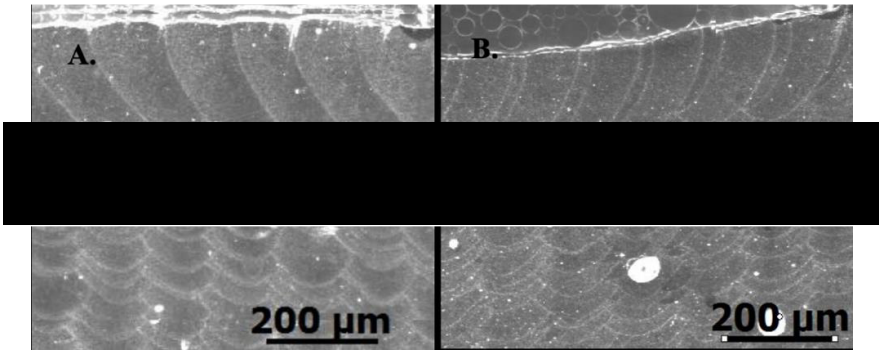

Figure 2.26. Microscopy of AlSi10Mg melt tracks fabricated with the LPBF process [100].

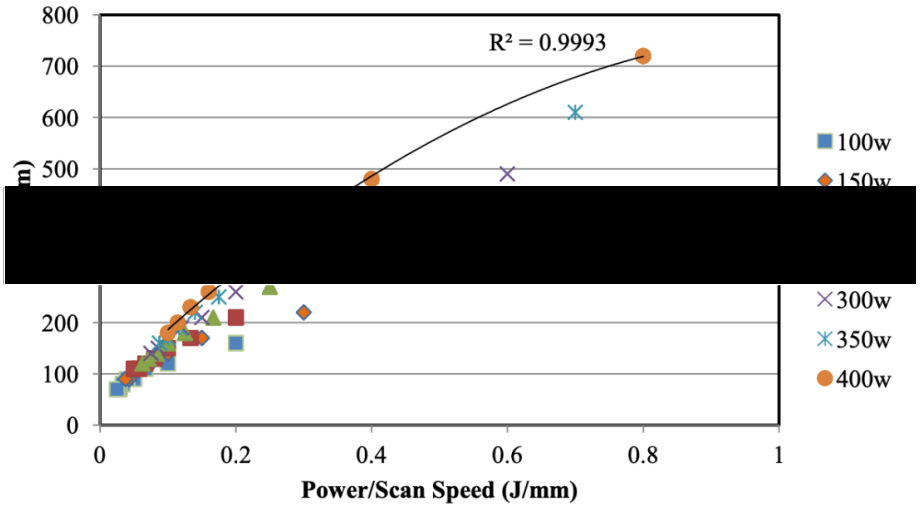

Figure 2.27. Track depth vs power/scan speed over a series of powers for LPBF AlSi10Mg alloy [100].

Given the cost/time implications associated with ALM and the challenges characterising melt pools in multi-weld passes, research has looked at the characterisation of single bead fabrications as shown by Gong et al [101]. SLM variants in beam speed/power and their inherent impact on melt pool geometries were investigated as shown in Figure 2.28, which has provided useful insight as to how parameters such as hatch spacing can be down-selected in accordance with track sizing.

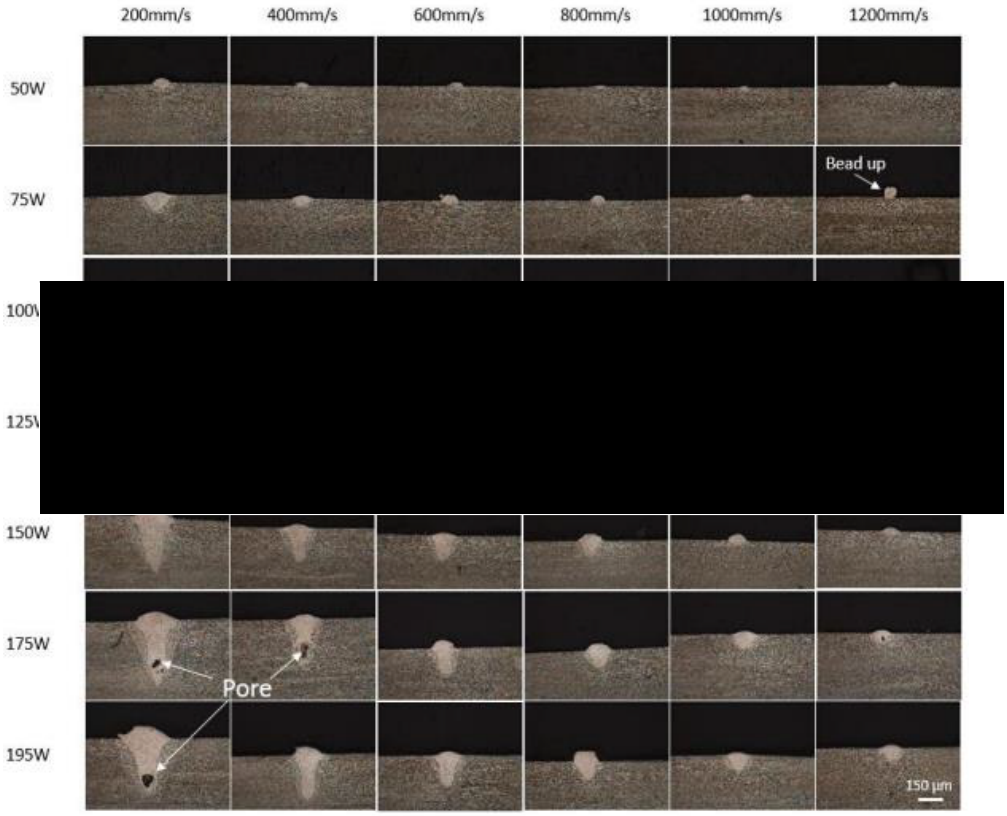

Figure 2.28. Melt pool profiles with variations in beam speed and power [101].

Numerous papers have highlighted further challenges associated with characterising melt pool profiles and as such have utilised modelling processes and in-situ characterisation technologies for high speed imaging. Guo et al [102] in particular noted and revealed the differing rates of energy absorption under a constant input energy density, giving rise to melt pool variation which further validates work done by Bertoli et al [86], suggesting that volumetric energy density can fail to capture melt pool physics in some instances.

The grain structure formed during solidification significantly affects its mechanical properties and thus negatively impacts its resistance to high temperature mechanical deformation mechanisms. The following section will give an overview as to how the metallurgical complexity of these cooling characteristics can lead to the formation of undesired defects unique to the LPBF process.

2.3.5 Material Defects

Given the metallurgical complexity of the manufacturing process as previously discussed, ALM is privy to unique defects and process phenomena not seen in alternate manufacturing routes. The following section will give an overview as to these characteristics, their causes and measures that can be taken to alleviate such issues.

2.3.5.1 Porosity

In a similar manner to cast and wrought methodologies, porosity is a commonly occurring defect that is noticeably observed in ALM built components. It is well documented and hypothesised that there are multiple mechanisms of formation that consequently change their size, frequency and distribution. One of the most noted mechanisms for porosity formation is that of keyholing, where high energy densities lead to the transition from a conduction to keyhole welding mode. This is typically characterised by a deep and narrow weld, which consequently gives rise to internalised reflections of the laser which intrinsically converts to heat. As this process develops, these keyholes become unstable and collapse leading to entrapped vapour and subsequently the formation of large, highly spherical pores, examples of which can be seen in Figure 2.29. Given the existence of this phenomenon, much work has gone into characterising this transition through various means. An example of this is shown by Philo et al [103], who employed pragmatic continuum level modelling in combination with over 60 single line experiments.

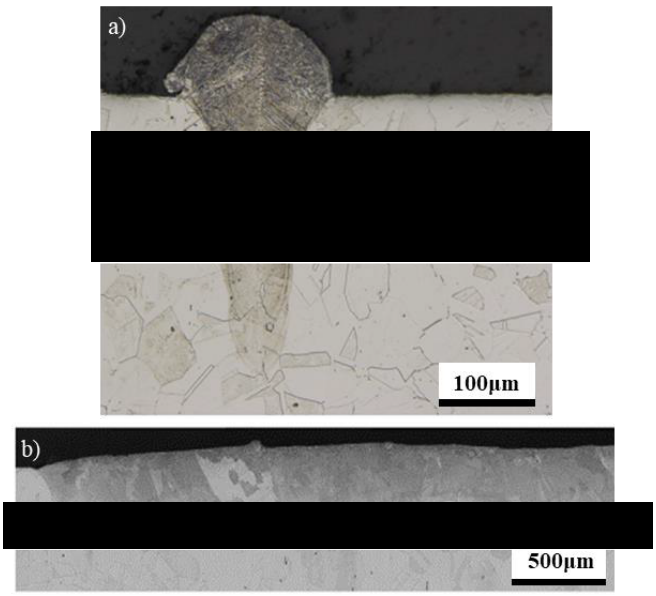

Figure 2.29. a) keyhole formation from excessively high energy density in a 316L stainless steel fabricated by LPBF b) large spherical porosity consequent to keyholing within bulk material [104].

In addition to entrapped vapour, additional gas entrapment mechanisms as a result of hollow powder particles can form during the gas atomisation process. During gas atomisation, liquid metal is

interrupted and subjected to a high velocity gas flow (nitrogen or argon). In some cases, this gas can become entrapped within the powder during formation, which when melted within the LPBF process can lead to the formation of spherical pores. What's more, the incorporation of gas shielding environments during the powder bed process through the introduction of an inert gas such as nitrogen or argon can become entrapped within the liquid molten pool as shown in Figure 2.30a.

Furthermore, when energy densities aren't sufficient enough to penetrate previously deposited layers, defects such as a lack of fusion become more prominent. This insufficient penetration causes a lack of cohesion between layers and subsequently, elongated voids as shown in Figure 2.30b. Given their morphology, these are more likely to be stress concentrating features and as such result in a significant reduction in mechanical performance.

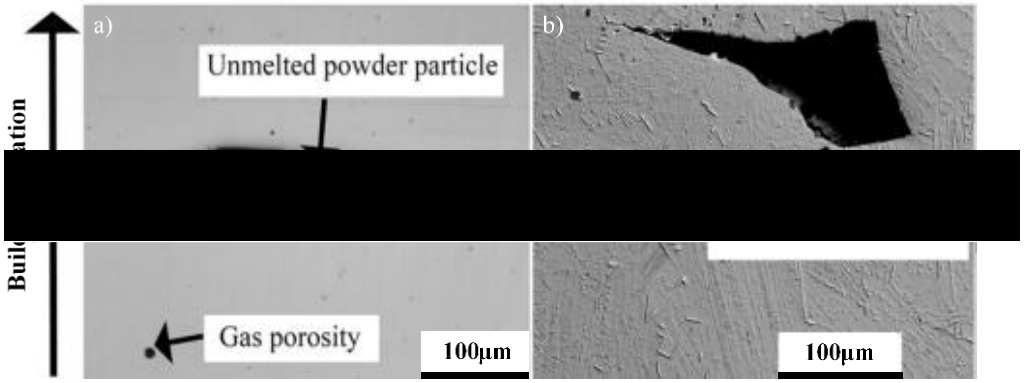

Figure 2.30. a) Gas porosity and unmelted powder particle in IN718 b) lack of fusion defect in IN718 [105].

2.3.5.2 Cracking

Considering the unique thermal characteristics of layer upon layer deposition as discussed, ALM is subject to multiple mechanisms of cracking, some of which are similar to that of welding. Solidification cracking in particular is prominent in highly strengthened nickel superalloys such as CM247LC and CMSX486, where the solidifying deposit contracts and shrinks at a different rate to that of the previously deposited layer [95] [106]. As such, a tensile force is generated which can often exceed the material's strength and consequently, grain boundary cracking ensues.

In addition to solidification cracking, liquation cracking is a commonly occurring mechanism within the welding of nickel superalloys given the large difference between the liquidus and solidus temperatures, leading to the existence of a large partially melted zone (PMZ). For nickel superalloys, fast heating to temperatures below the liquidus temperature can lead to the liquidation of low melting point precipitates such as carbides and when the PMZ undergoes a tensile load as a result of contraction

mechanisms similar to that of solidification cracking, these regions can act as stress raisers [95] [106]. Examples of liquation cracking in both cast and ALM material is shown in Figure 2.31.

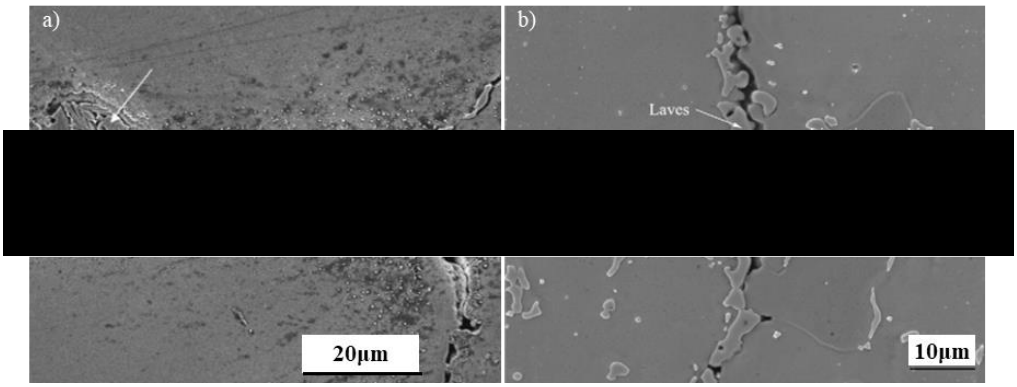

Figure 2.31. SEM image highlighting the prevalence of liquated HAZ zones around a welding crack in a) cast IN738 and b) laser melting deposited IN718 [107] [108].

2.3.5.3 Residual Stress

As mentioned, ALM is subject to a directional thermal gradient and heat flux which not only has implications on anisotropic grain growth but cooling and contraction mechanisms associated with defect formation. One mechanism which has major implications on mechanical performance is that of residual stressing, which results from liquid molten metal coming in contact with previously deposited layers or substrates which are inherently cooler. Subsequently, an abrupt thermal gradient and exceptionally high cooling rate occurs, which can cause high levels of plastic strain accumulation [109] and thus have numerous negative implications such as inaccurate dimensional tolerances, geometric distortion and the exacerbation of previously existing defects [110].

2.3.5.4 Selective Vapourisation

Studies have emphasised that during ALM, the loss of alloying additions and consequently the lack of uniform chemical homogeneity becomes apparent. This takes place as a result of selective vapourisation mechanisms, in particular for low melting point elements such as aluminium and magnesium which have been shown by Brice et al for titanium and aluminium alloying systems [111] [112], an example of which is shown in Figure 2.32. It is noted by Debroy et al [113] that the loss of such elements occurs at the surface of these high temperature liquid molten pools, although chemical depletion occurs throughout the entire volume of the melt pool, meaning that the surface area-to-volume ratio is the key considerable. Considering this and the influence on microstructural development previously mentioned, a detailed understanding of melt pool geometries and temperature fields is evident.

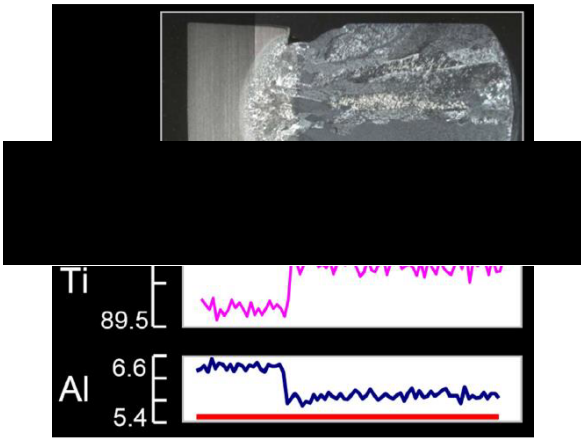

Figure 2.32. Aluminium depletion and an increase in titanium concentration along the build height of a Ti-6Al-4V sample fabricated by LPBF [114].

2.3.6 Mechanical Testing of ALM

In industry today, the understanding as to the mechanical performances of newly developed materials whether it be by means of alloy design or manufacturing route are imperative for establishing suitability in respect to specific applications and in-service conditions. The traditional approach to mechanical property assessment is the use of conventional uniaxial testing methodologies, where generic specimen geometries are utilised for the high temperature tensile testing of metallic materials in accordance with ISO 6892-2:2018 [115] and the uniaxial creep testing of metallic materials in accordance with ISO 204:2018 [116]. Although these methods are internationally recognised and provide the fundamental basis for mechanical property assessment over a wide range of industries, certain circumstances can highlight their limitations where the implementation of small scale testing methodologies prove to be beneficial.

One of the most significant advantages of the ALM process is to produce highly intricate components not feasible through traditional cast and wrought methodologies. Given this, the use of traditional test specimen geometries can be considered somewhat restrictive and may not be entirely representative of the mechanical properties of a finalised component. Moreover, the fabrication of geometrically complex features such as lattice structures [117] or thin wall architectures [118] [119] may not provide enough bulk material for the extraction of standard test specimen geometries. Furthermore, additive processes are subject to epitaxial grain growth mechanisms and consequently they have highly transient microstructures [120] as detailed in Section 2.3.4. Given the nature of conventional testing specimens, traditional uniaxial testing may not prove sensitive enough to detect the discrete microstructural changes inherent to ALM and as such small scale testing methodologies provide value with regards to localised mechanical property assessment. Finally, given the metallurgical complexity of ALM and the abundance of process parameters and variables as outlined in Section 2.3.3,

the implementation of small scale testing methodologies as a means for rapid mechanical property characterisation proves not only to be economically beneficial given the cost implications of powder metallurgy routes as explored in in Section 2.2.4, but also given the accelerated test times as highlighted by Hosemann et al [121].

In order for LPBF components to be utilised within the aerospace sector, a detailed understanding of the microstructural evolution and variation of mechanical properties throughout the substrate, initial layers and developing structure is required. Given the metallurgical complexity of ALM and its inherent abundance of process parameters and variables, this thesis will look to employ the miniaturised small scale testing methodology Small Punch (SP) as a means for rapid validation and mechanical property assessment. The following section will give an overview of SP, detailing its successful utilisation for characterising a range of advanced materials over numerous industrial sectors.

2.4 Small Punch Testing

2.4.1 Introduction

Small Punch (SP) testing is a small scale testing procedure developed in the nuclear industry by Manahan in the early 1980s in order to generate mechanical property data from small volumes of material, both in and out of service [122] [123]. Given the positive implications of localised mechanical testing, numerous industrial sectors attempted to implement this methodology into their testing procedures, however there was a halt to this movement given concerns regarding the correlation of data to traditional uniaxial testing methodologies. It wasn't until the 1990s where SP testing underwent its resurgence after being successfully utilised in order to ascertain high temperature creep properties [124]. It has since been incorporated over a wide range of industrial sectors and material systems, offering the distinctly unique ability to characterise localised regions of material where evolving microstructures are prominent such as welded joints [125] [126] and complex piping systems [127] [128]. Subsequently, SP testing has been exploited by the aerospace industry for the mechanical assessment and characterisation of advanced materials such as ALM components, where traditional methodologies may not be possible given the nature of highly intricate components and their subsequent geometry restrictions [129].

Within this work, SP testing will be incorporated as a means of mechanical property assessment and hence utilised as an effective tool for ranking and rapid validation; demonstrating the influence of ALM's key process variables, the material discontinuities they produce and ultimately their adverse effects on mechanical performance. The following section will give an overview as to the basic principles of SP testing and the manners in which they can be conducted.

2.4.2 Test Setup & Data Interpretation

SP testing consists of subjecting a miniature, thin, disc shaped specimen, typically 8-9.5mm diameter and 500μm ±5μm thickness to a 2-2.5mm diameter indenter, the material of which is dependent on both testing conditions and the material on which the test is being applied. The indenter or 'punch' can be driven into the specimen in several manners dependant on the desirable information intended, as will be discussed further on, however the general consensus is that the disc be circumferentially clamped between an upper and lower die as presented in Figure 2.33.

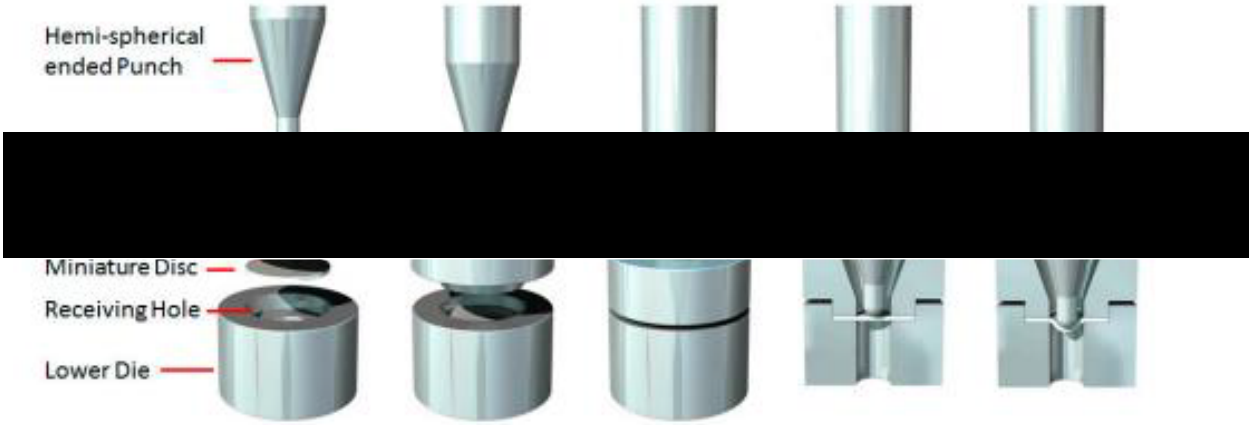

Figure 2.33. Schematic illustrating circumferential clamping of specimen within the test setup [130].

From a specimen preparation perspective, cylindrical rods are typically removed from larger pieces of material by electrical discharge machining (EDM), which are subsequently turned down to 8-9.5mm diameter and sliced into sections of reasonable thickness, 1-2mm. These disc sections are then ground down on both faces through a series of successively finer grit papers until the desired thickness of 500μm ±5μm is achieved with a 1200 grit finish. Prior to testing, the disc is measured both centrally and at four other locations in order to ensure that the specimen uniformly falls within the ASTM E3205-20 standard [131].

2.4.2.1 Small Punch Tensile

For Small Punch Tensile (SPT), the indenter is driven into the specimen under a constant displacement, generating a biaxial tension and subsequently, tensile like deformation. Given the compressive fashion in which the load is applied, electric-screw test frames are typically utilised with the force required to punch through the specimen being recorded as a function of the material's deflection. The small disc like specimen is circumferentially clamped between an upper and lower die, with the upper die possessing a circular aperture in order to allow the puncher to pass through and impose force. The lower die also contains a receiving hole, typically 4mm in diameter, in accordance with the dimensions stated in ASTM E3205-20 [131], in which the sample will plastically deform through and emerge during testing. From a test monitoring perspective, it is also worth noting that the specimens' deflection is recorded with a Linear Variable Displacement Transducer (LVDT) that is

placed in contact with the underside of the disc, opposite to the point of contact from the punch tip. This is necessary in order to ensure correct force compliance and intimate measurement of the material's deformation. An illustrated overview of SPT can be seen below in Figure 2.34. An example of results generated from SPT testing on a range of steel alloys is illustrated in Figure 2.35.

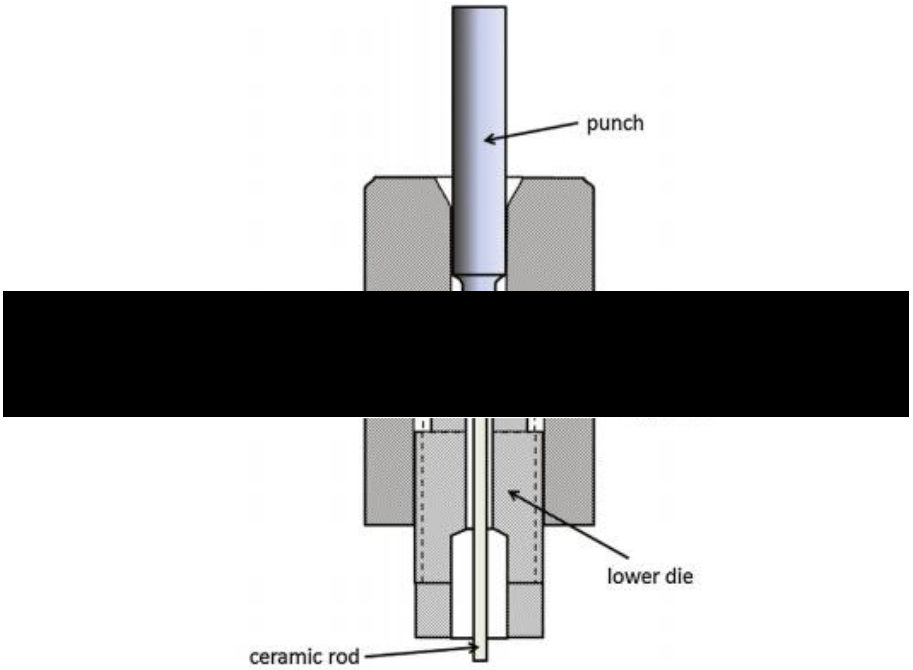

Figure 2.34. A schematic representation for a typical small punch tensile setup [132].

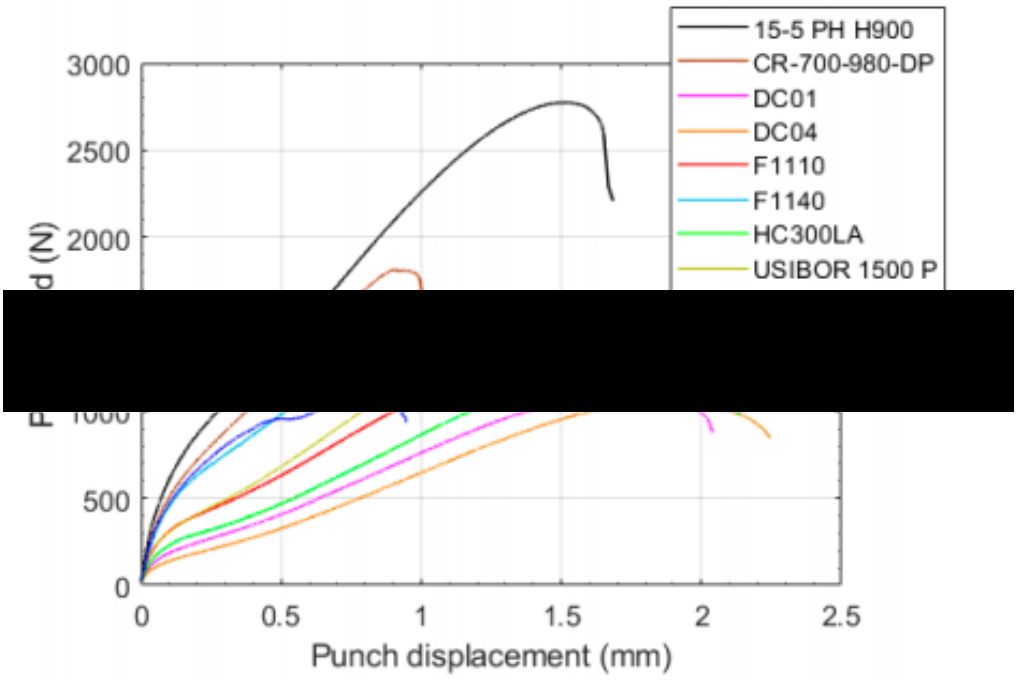

Figure 2.35. SPT results on a range of steel alloys [133].

2.4.2.2 Small Punch Creep

In an almost identical manner to SPT, in a Small Punch Creep (SPC) test, the indenter is driven into the specimen under a constant static load. These tests are performed in a 'dead-weight' testing frame with the disc also being circumferentially clamped between the upper and lower die. It is imperative that over clamping should be prevented as it will help to reduce any issues related to thermal expansion which could subsequently influence data generation, affecting both the accuracy and repeatability of the test. In both SPT and SPC, high temperatures are introduced to the system using either digitally controlled furnaces or induction heating system. For SPC, it is also recommended that an inert gas environment be introduced in order to prevent oxidation effects.

Once the specimen is under load, the deformation of the disc is monitored and recorded from both the top and bottom surfaces of the disc using LVDTs. The first transducer is positioned just below the loading pan, parallel to the loading axis, with the second transducer being in contact with underside of the disc, similar to SPT, through the use of a SiO_2 quartz rod that is fed through the lower die. An average value of these displacements are recorded and displayed on the SPC curve in relation to time. The high temperatures induced during SPC are also monitored and recorded throughout testing using thermocouples, the main of which is placed in contact with the sides of the disc. There is the option for an additional thermocouple, located within the upper die although it is neither a necessity nor standard practice. A typical SPC setup is shown below in Figure 2.36 with an example of the results generated shown in Figure 2.37.

Post testing, results are characterised and displayed graphically using time-displacement curves. Within these curves there are the recognised stages of creep deformation (primary, secondary and tertiary) similar to that of traditional uniaxial testing, but with considerably different deformation mechanisms. The primary region is dictated through the initial elastic bending period as to when the disc firstly undergoes load. Once yielding occurs, the onset of plastic deformation and what is referred to in some literature as 'steady-state' creep occurs through membrane stretching dictated by the biaxial stress induced by through the puncher. Once the disc is suspect to considerable thinning through necking, it approaches the tertiary stage where failure is imminent. It is worth noting that within the last decade, there have been on-going efforts to standardise both SPT and SPC alongside the European Code of Practice (CoP) [134], leading to the development of the ASTM International Standard Test Method for Small Punch Testing of Metallic Materials [131].

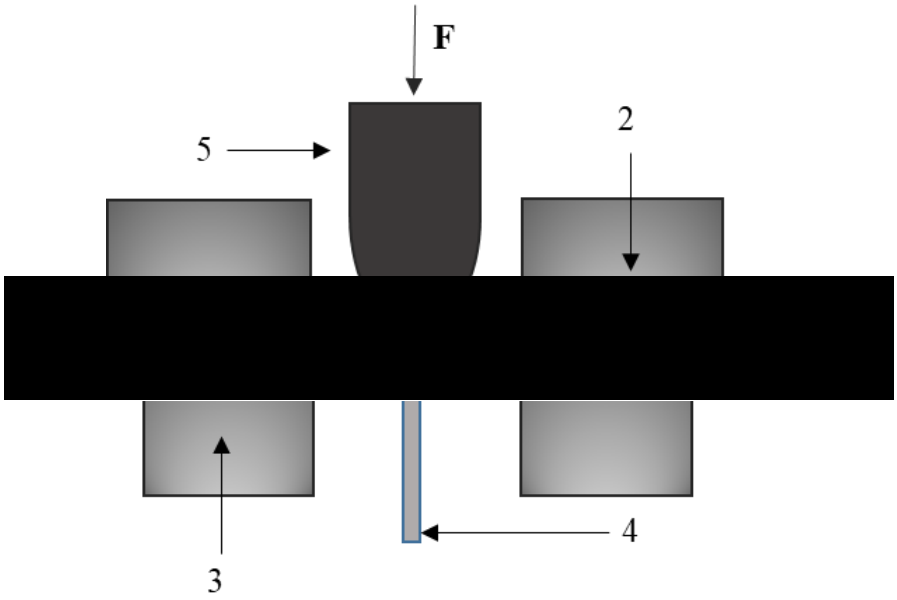

1. Small Punch Disc
2. Upper Die
3. Lower Die
4. Transducer Quartz Rod
5. Punch

Figure 2.36. A schematic representation of a typical small punch creep setup, recreated from [135].

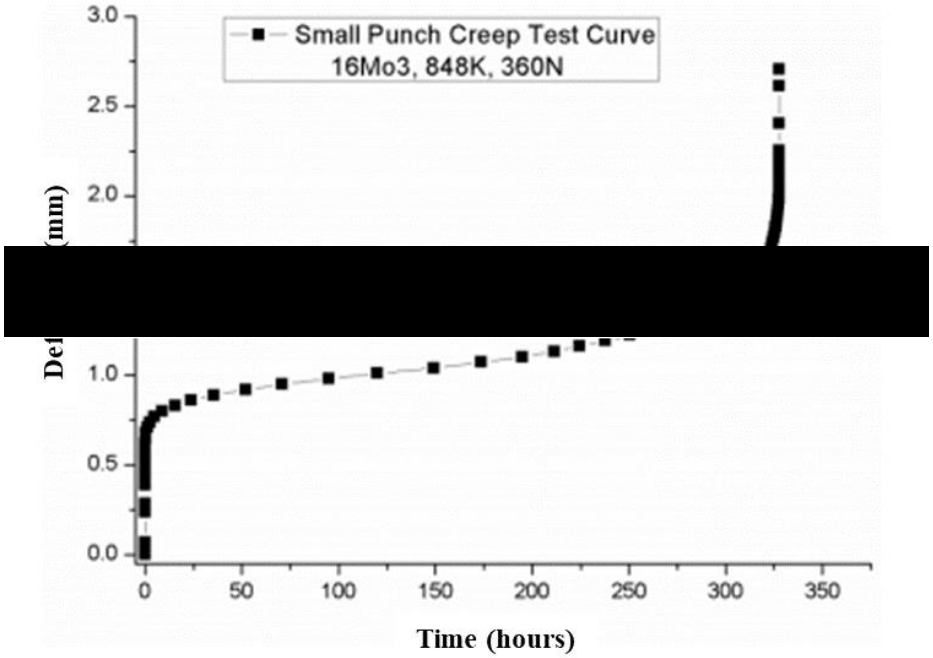

Figure 2.37. SPC results the steel alloy 16Mo3 [136].

2.4.2.3 Small Punch Fatigue

Given the advancements made in both SPT and SPC and their successful incorporation over a wide range of industrial sectors, research in more recent years has recognised the need for applying stress/load in a cyclic fashion, representing fatigue deformation that is often seen as the primary causation for failures within service. This has heralded the development of the Small Punch Fatigue (SPF) test, where efforts have been made to replicate the loading regimes that can often be seen within conventional fatigue loading, with different setups being incorporated for compressive loading ratios (R > 0), positive loading regimes (R = 0.1) and fully reversed loading cycles (R = -1) [137]. An example of the SPF results generated from this test setup on Ti-6Al-4V can be seen below in Figure 2.38.

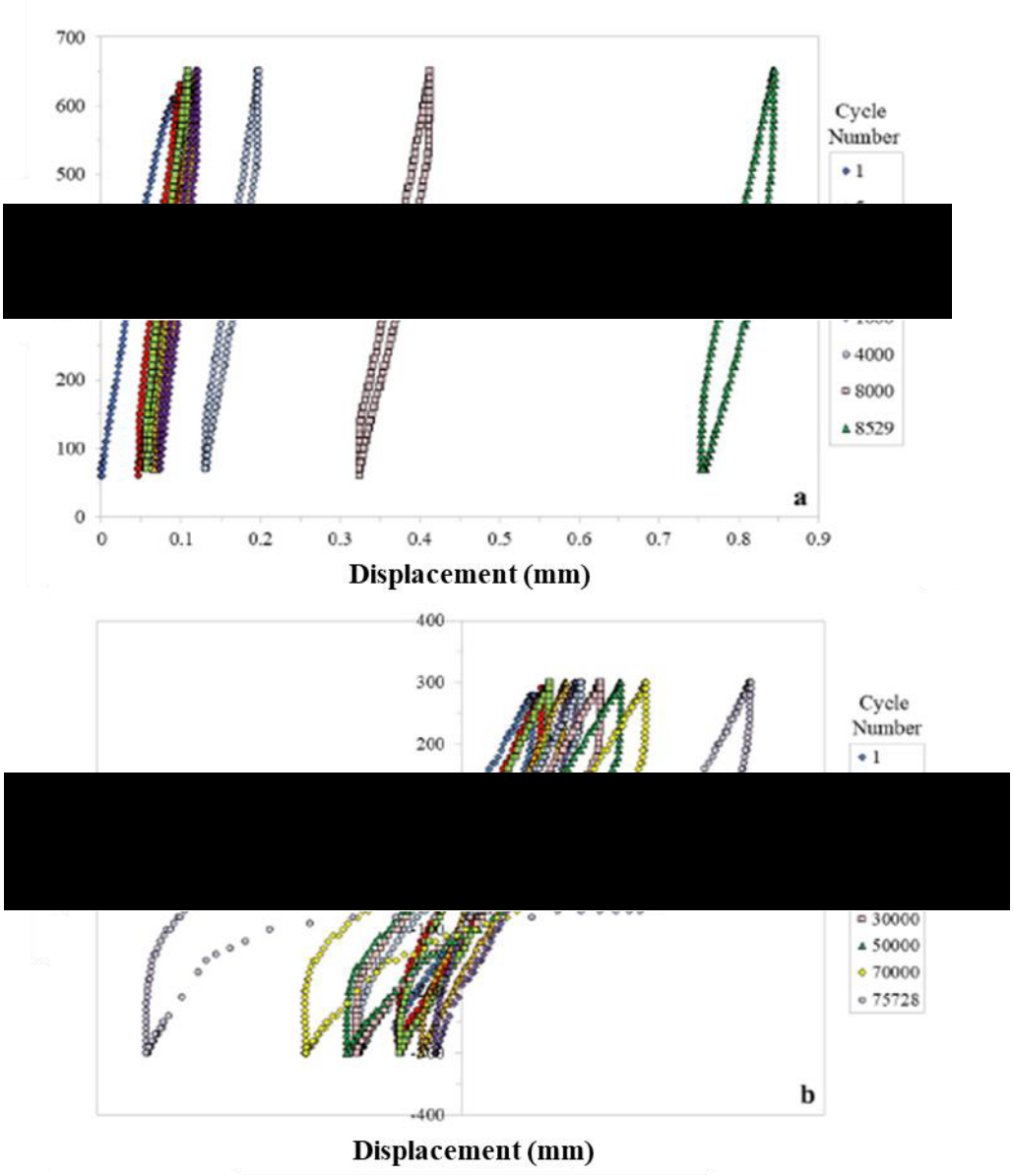

Figure 2.38. SPF testing on Ti-6Al-4V specimens at 20°C, a) R = 0.1 b) R = -1 [138].

Despite SPF not being utilised within this study, it further highlights the robust and versatile nature of small scale testing methodologies such as SP. All these manners of testing are indicative and somewhat representative of the nature that traditional uniaxial testing methods are conducted in, with ongoing research looking into data correlation between the two [139]. The following section will give an overview as to the ongoing work regarding correlation to uniaxial data.

2.4.3 Small Punch to Uniaxial Correlation

Traditional uniaxial based mechanical testing methodologies provide the foundational basis and understanding of material properties. However, given the numerous advantageous features of small punch testing and the ability to assess mechanical properties from limited volumes of material, ongoing efforts have been made to establish an empirical correlation to uniaxial data. The following section will give some contextual insight as to some of the existing correlation work.

2.4.3.1 Small Punch to Uniaxial Tensile

When considering the multiaxial nature of small punch testing, direct correlation to traditional uniaxial stress parameters such as yield strength (σys) and ultimate tensile strength (σ_{UTS}) proves to be challenging given the evolving stress state and change in cross sectional area inherent to the testing technique. As such, the generic $\sigma = F/A$ relationship becomes unsuitable and alternative methodologies originating from the load - displacement curves produced by the testing technique, as shown in Figure 2.39, need to be considered.

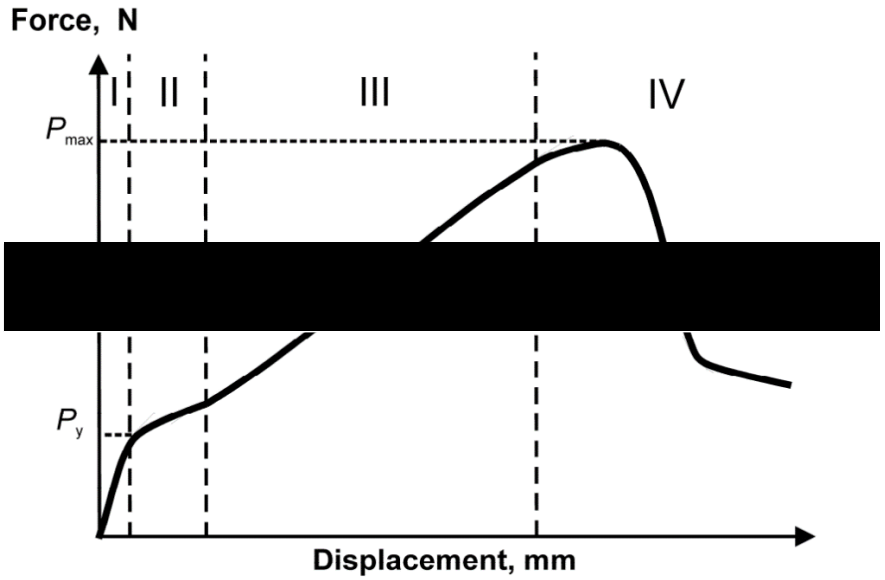

Figure 2.39. Load – Displacement curve produced by SPT testing technique [140].

In order to correlate to and predict the traditional uniaxial stress parameters discussed, loading criteria which relates to these mechanical properties such as yield load (F_y) and maximum load (F_{Max}) must be determined, with F_{Max} being simplistic to identify as it is represented in the maximum point of the load – displacement curve. F_y on the other hand is more difficult to differentiate as it illustrates the change from elastic to plastic deformation and has as such been the subject of numerous investigations where multiple methodologies have been proposed. Early work by Norris et al [141] employed a linear trendline coinciding and overlapping the initial elastic gradient of the load – displacement curve, where the point at which these two lines diverge being considered the yielding point. However, modernised approaches have employed more sophisticated methodologies as critically evaluated by Garcia et al [142] such as the offset methodology and the bilinear two tangent methodology developed by Mao et al [143], of which is considered as the go to methodology in the ASTM E3205-20 standard [131].

For yield strength, there appears to be a general consensus in the literature [144] [145] [146] that a linear relationship exists between σ_{ys} and F_y, which in turn is divided by the square of the initial thickness of the specimen (h_0), as shown in Equation 9. Here, the α_1 and α_2 terms represent material constants derived through existing uniaxial data.

$$\sigma_{ys} = \alpha_1 \frac{F_y}{{h_0}^2} + \alpha_2 \tag{9}$$

For ultimate tensile strength correlation however, there appears to be some disagreement, where the initial outlook was similar to as previously proposed, with F_{Max} being divided by the initial disc thickness squared (h_0^2) to represent σ_{UTS} as shown in Equation 10, with β_1 and β_2 once again representing material constants. However, some literature appeared to contradict this notion [147] and as such the equation was modified in order to take into account the punch head displacement at the maximum load (d_m), as represented in Equation 11 [148].

$$\sigma_{UTS} = \beta_1 \frac{F_{Max}}{{h_0}^2} + \beta_2 \tag{10}$$

$$\sigma_{UTS} = \beta'_1 \frac{F_{Max}}{{h_0}^2 d_n} + \beta'_2 \tag{11}$$

Davies et al [149] demonstrated the application of these empirical correlations on both cast and LPBF variants for C263 where uniaxial data was available, with Figure 2.40 presenting the relationships between yield stress and F_e/h_0^2 and the relationship between ultimate tensile strength (UTS) and F_m/h_0^2.

For both correlations, a high coefficient of determination (> 0.85) was showcased, demonstrating a significant relationship between SP load and uniaxial stresses for both cast and LPBF C263. As such, correlation coefficients were calculated and established, but these were revealed to be both highly material and temperature dependent.

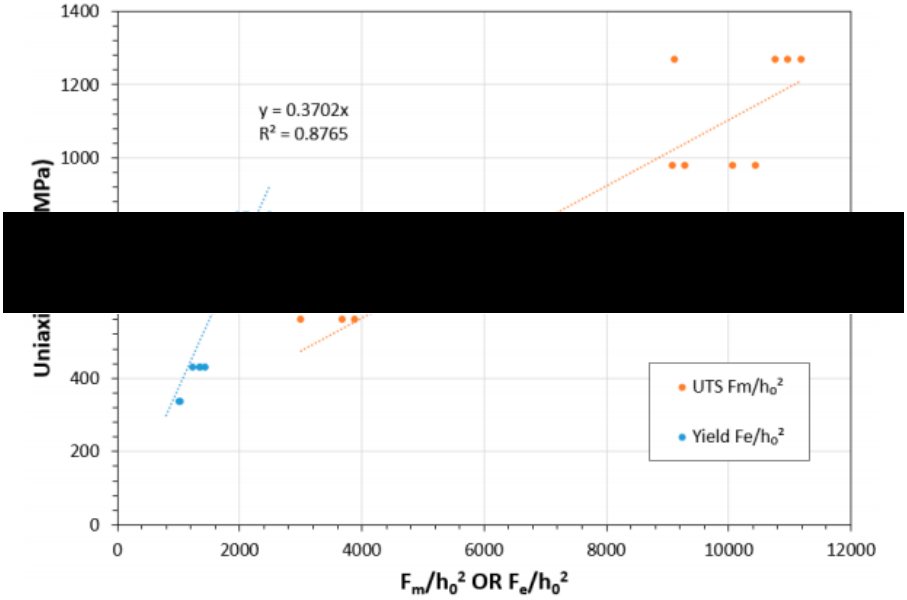

Figure 2.40. Yield Stress vs. F_e/h_0^2 and UTS vs. F_m/h_0^2 for C263 variants [149].

2.4.3.2 Small Punch to Uniaxial Creep

The origins and correlation of small punch to uniaxial creep data was initiated with the Chakrabarty membrane stretch model offered in 1970 [150], which has formed the fundamental basis and understanding between central deflection and strain within the small punch creep test. This model provided the framework for the most widely recognised empirical correlation method to date, that is the k_{SP} method, which essentially acts as a correlation factor to determine uniaxial creep stress from SPC data. This methodology is represented below in Equation 12, where F is the SP load, σ is the applied stress in a uniaxial test, *R* is the receiving holes radius, *r* is the radius of the punch head and h_0 is the thickness of the disc. As such the k_{SP} method has been successfully applied to several material systems including CMSX-4 [151], P91 [152] and P92 steels [125].

$$\frac{F}{\sigma} = 3.33 k_{SP} R^{-0.2} r^{1.2} h_0 \tag{12}$$

However, despite the promise found within previous literature, the k_{SP} method was not without its limitations. The utilisation of a material constant can provide difficulty in the instances where there is no uniaxial data to complement SPC data, resulting in an approximation. Furthermore, considering that the Chakrabarty membrane stretch model is for materials that display significant plasticity and

ductility, it is proved inadequate for more brittle materials that display cracking behaviour during the early stages of loading. This has been well demonstrated by Lancaster et al [153] for γ TiAl 45-2-2 at elevated temperatures, given titanium aluminide's relatively low ductility where the influence of Von Mises and worst principal stress take precedent. It was highlighted that in brittle materials, cracking appeared to initiate directly below the punch head during the initial loading contact, whereas for ductile materials cracking imitated around the periphery of the punch head at a later stage. This will be discussed later in further detail but given the apparent breakdown, alternative methods of correlation have been considered.

The Monkman-Grant approach is a well-established prediction model that is formed off the apparent relationship between time to failure (t_f) and minimum creep rate ($\dot{\varepsilon}_{\mathrm{m}}$). Given its successful demonstration across uniaxial testing [154], it has been the subject of modifications for application towards SPC, where $\dot{\varepsilon}_{\mathrm{m}}$ is replaced with minimum deflection rate ($\dot{\delta_m}$) as shown in Equation 13. The material constant terms within this equation (*m* and *C)* are derived empirically using linear regression and thus the comparison and relationship of $\dot{\varepsilon}_{\mathrm{m}}$ to $\dot{\delta_m}$ is represented in Equation 14. An example of the utilisation of the Monkman-Grant approach on P92 steels is demonstrated in Figure 2.41.

$$\log t_f = m \log \delta_m = C_s \tag{13}$$

$$\dot{\varepsilon} = 10^{C - C_{s/m}} \dot{\delta_m} \tag{14}$$

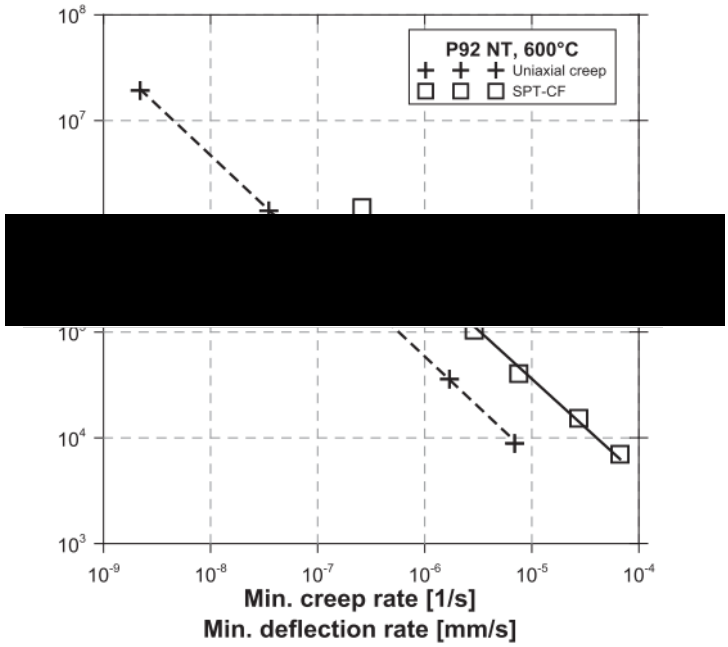

Figure 2.41. Correlation of uniaxial and SPC results through the Monkman-Grant relationship in P92 steel [155].

The Larson-Miller Parameter (LMP) is a widely recognised methodology for predicting the lifetime of a material subjected to creep deformation through derivations of the Arrhenius equation, which is well recognised in literature [154]. A correlation between temperature (T) and time to failure (t_f) is embodied below in Equation 15. In this instance, C is the material constant.

$$LMP = T(C + log_{t_f}) \tag{15}$$

The linear relationship observed relating LMP to uniaxial stress can also be obtained through linear regression as demonstrated by Andres et al [156] when stress is substituted with an applied SPC load, and a correlation factor can be applied to achieve the same relationship and therefore ascertain creep predictions as shown in Figure 2.42.

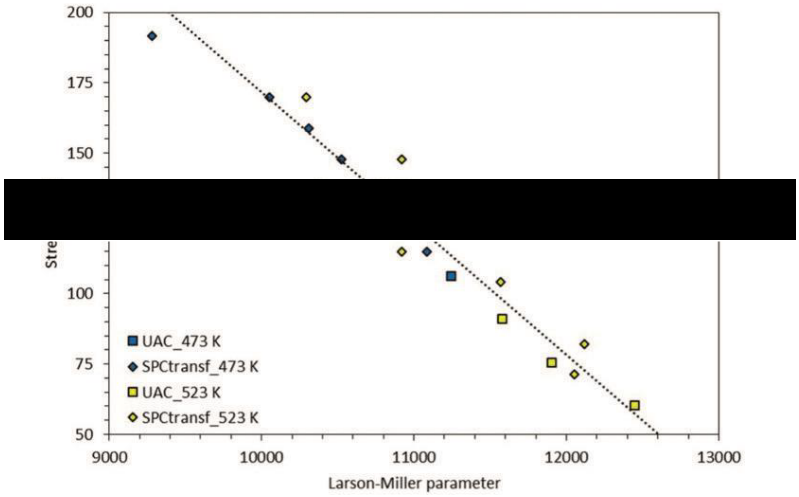

Figure 2.42. Uniaxial and SPC comparisons for AZ31 alloy using the LMP [156].

In more recent times, the Wilshire methodologies have provided a modernised approach to creep lifing and the extrapolation of short-term uniaxial creep data for lifing predictions given the existent breakdown of the power-law equations observed at higher temperatures for more complex alloying systems as highlighted by Whittaker et al [157]. Within this prediction methodology, the assumption made is that dislocation movements aided by diffusion are the dominant mechanism and this approach has successfully been applied in determining creep lives from short-term uniaxial data. Given this, Jeffs et al [158] effectively utilised this methodology by replacing stress with SP load, similar to the LMP approach previously discussed. This approach was employed on CMSX-4 with its abundance of uniaxial creep data as demonstrated in Figure 2.43, where a good agreement was observed between the predictive methodology and the existing data. In addition to single crystal systems, a modified version of the Wilshere equations has been effectively used by Davies et al [159] as shown in Figure 2.44 to determine the long term creep lives of the polycrystalline nickel-based superalloy C263 both in cast and ALM form.

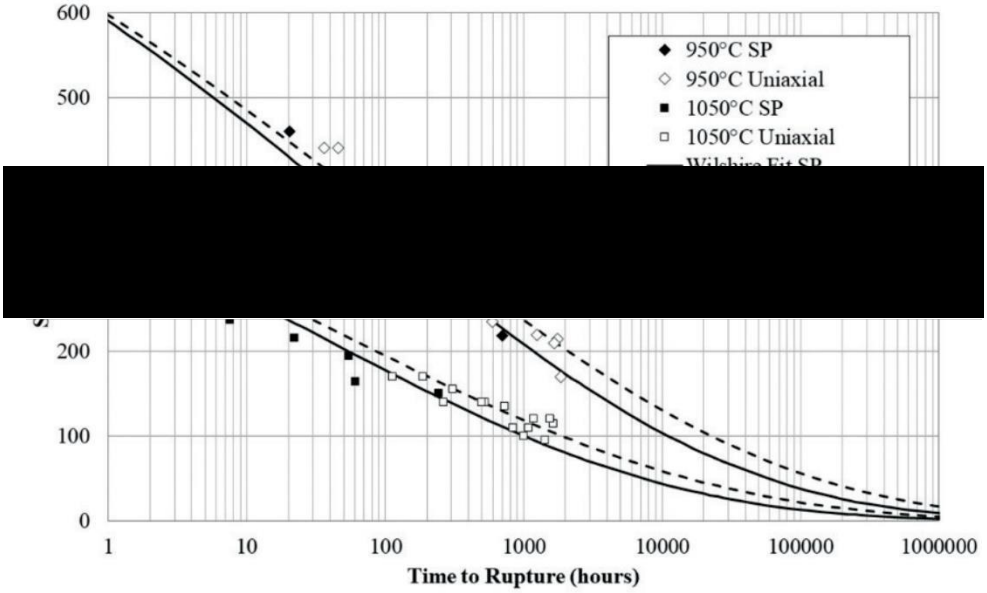

Figure 2.43. Uniaxial and SPC data for CMSX-4 with lifing predictions formed from the Wilshere equations [158].

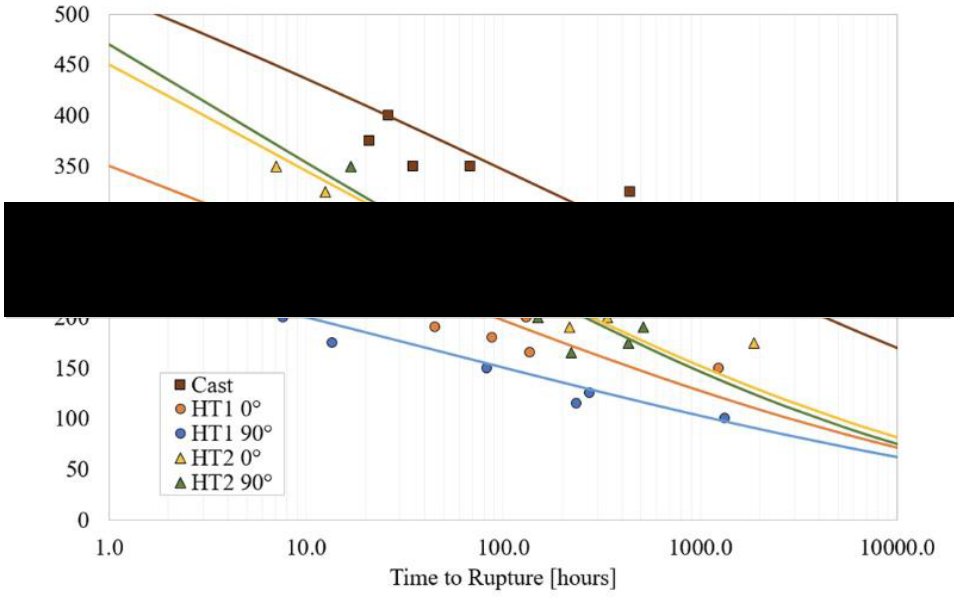

Figure 2.44. Load vs Time to Rupture Plots for SPC tests carried out on cast and LPBF variants of C263, alongside modified Wilshere equation predictions [159].

As discussed, the limitations of simplistic approaches such as the k_{SP} have been noted, specifically with regards to its breakdown for brittle materials subjected to high temperature conditions such as titanium aluminides. Given the previous framework for numerical modelling and the use of Finite Element Analysis (FEA) on SPC behaviour over a range of alloying systems [160] [161] through uniaxial creep data, Lancaster et al [153] incorporated this methodology to predict SP creep in the highly brittle γ-Ti-45Al2Mn-2Nb as previously mentioned. Material parameters consistent with the theta (θ)

projection technique developed by Evans [162] are produced from uniaxial creep data and applied to small punch boundary conditions. An axisymmetric model consisting of 900 CAX4 elements was developed in Abaqus using a *CREEP subroutine in order to correspond with the testing geometries apparent in the SP test technique as shown in Figure 2.45. The top and bottom surfaces of the circumferentially clamped regions being considered rigid with a rough contact being assumed with a coefficient of friction of 0.35.

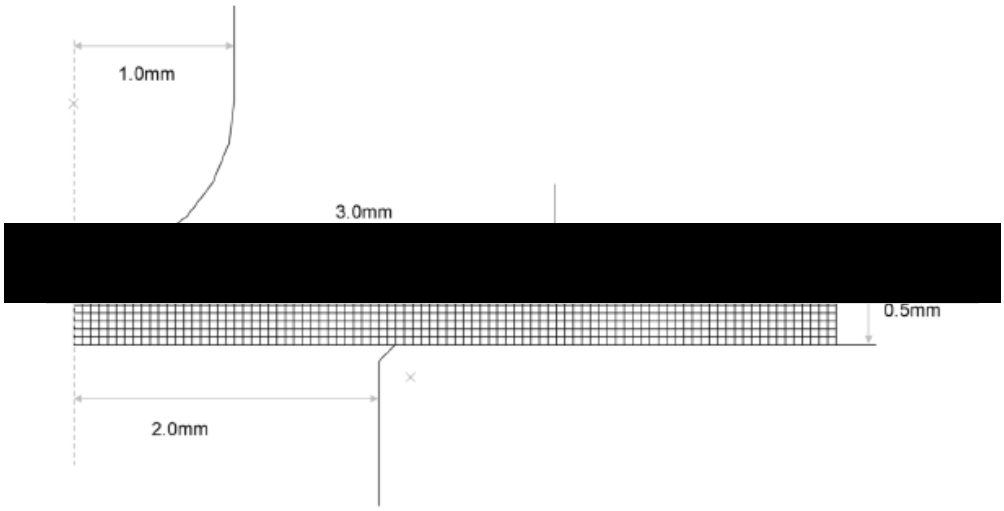

Figure 2.45. Axisymmetric model coinciding with SP testing geometry [153].

The stress states analysed from this model showcased the evolution of the stress apparent in SP testing, where high compressive stresses adjacent to the punch head were confirmed in the initial stages, leading to high radial, hoop and inherently maximum principal stresses to be observed and form on the underside of the disc. As displacement and penetration of the punch head continued to ensue, the stress fields appeared to change with peak stresses decreasing and moving away from the centre of the disc and this appears to be seemingly more evident in ductile materials as will be discussed. Thinning also became evident which inherently further accelerated displacement rate. Given the evolution of stress states during the test, SP tests appeared to showcase different shaped curves comparative to uniaxial approaches as shown by the predictions in Figure 2.46a. The predictions of both the evolving stress states and testing appeared to show a strong fit to both fractography (as will be discussed in the following section) and the experimental data shown in Figure 2.46b over a range of loading conditions; both of which innately provide greater confidence in an understanding of the underlying mechanisms intrinsic to SP.

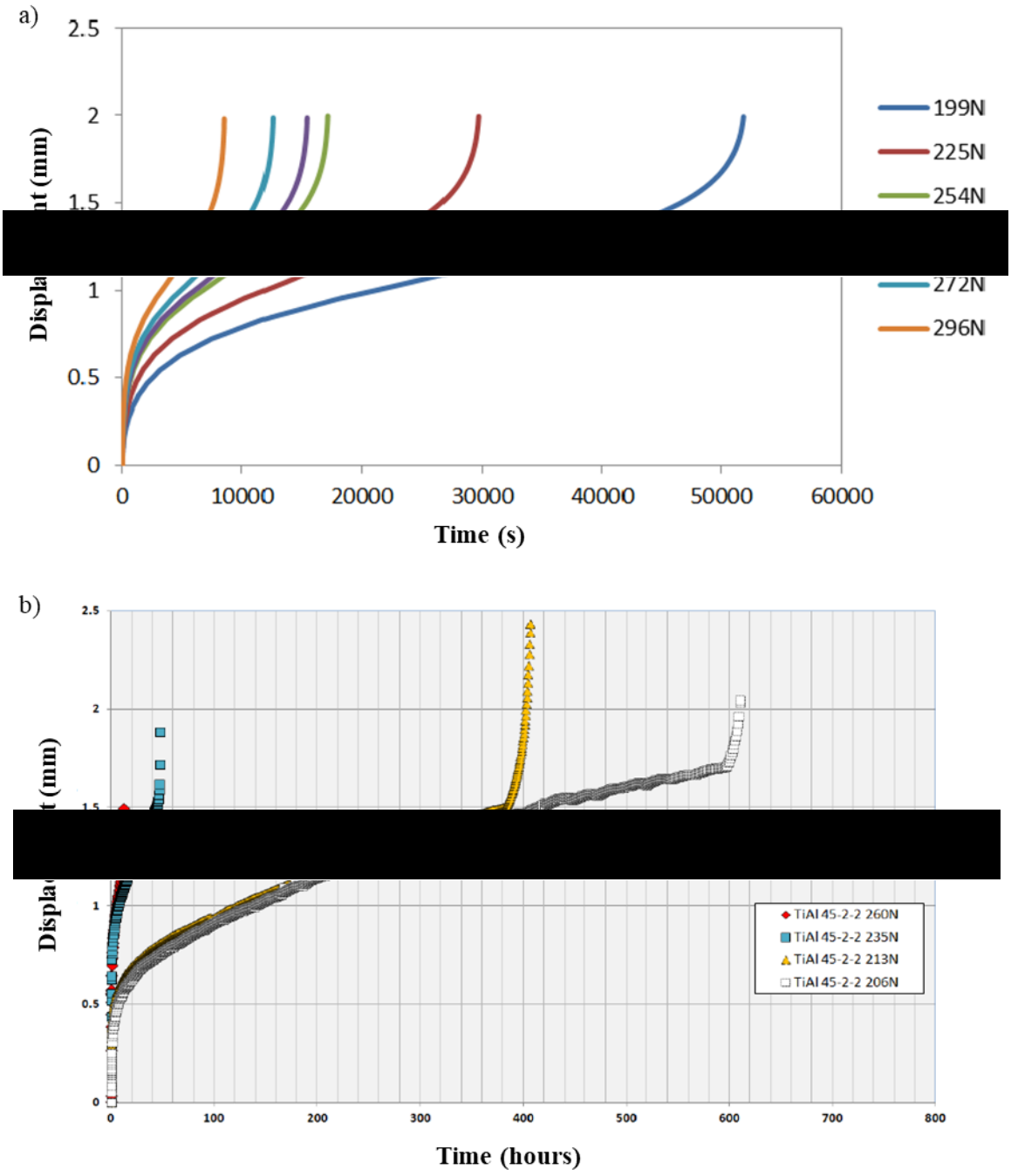

Figure 2.46. a) Predicted SPC Time - Displacement curves at 700°C and b) Time – Displacement curves for SPC testing on γ-Ti-45Al2Mn-2Nb at 750°C [153].

Although this thesis will not look to correlate SP testing to uniaxial data given the limited material availability consequent to the abundance of parameter sets and cost implications of powder metallurgy-based routes, the correlation work outlined provides some demonstrated validity for the testing methodology. This thesis will rather look to effectively employ small punch testing as a ranking tool for rapid validation over a range of LPBF process parameters and variants for two nickel-based superalloys.

2.4.4 Small Punch Fractography

The analysis and investigation of material fractography and more specifically fracture surfaces has been utilised within numerous industrial sectors in order to help gauge an understanding of a materials' failure characteristics. During SPC, fracture typically occurs through one of the two primary failure modes; brittle and ductile.

Brittle fractures are an instantaneous, catastrophic event in which materials fail with very little or no prior plastic deformation. In the case of SP, radial cracking emerges from the central point of the disc where maximum principal stresses are at their highest given the lack of elastic flow stress, appearing in a 'starfish' manner in which the severity of embrittlement is readily apparent as illustrated in Figure 2.47(a-c). In contrast to this, ductile failures are a relatively slow phenomenon, where energy is absorbed during the onset of plastic deformation. In this case of SP, fracture typically occurs around the head of the punch where membrane stretching is prominent and is dictated by Von Mises stress, leading to crack propagation along its circumference indicating that the maximum stress is not located at the centre of the disc. This is most ruddily described in the SP community as 'moon and crescent' fracture as illustrated in Figure 2.47(d-f), where the level of ductility in the material can be readily observed and compared.

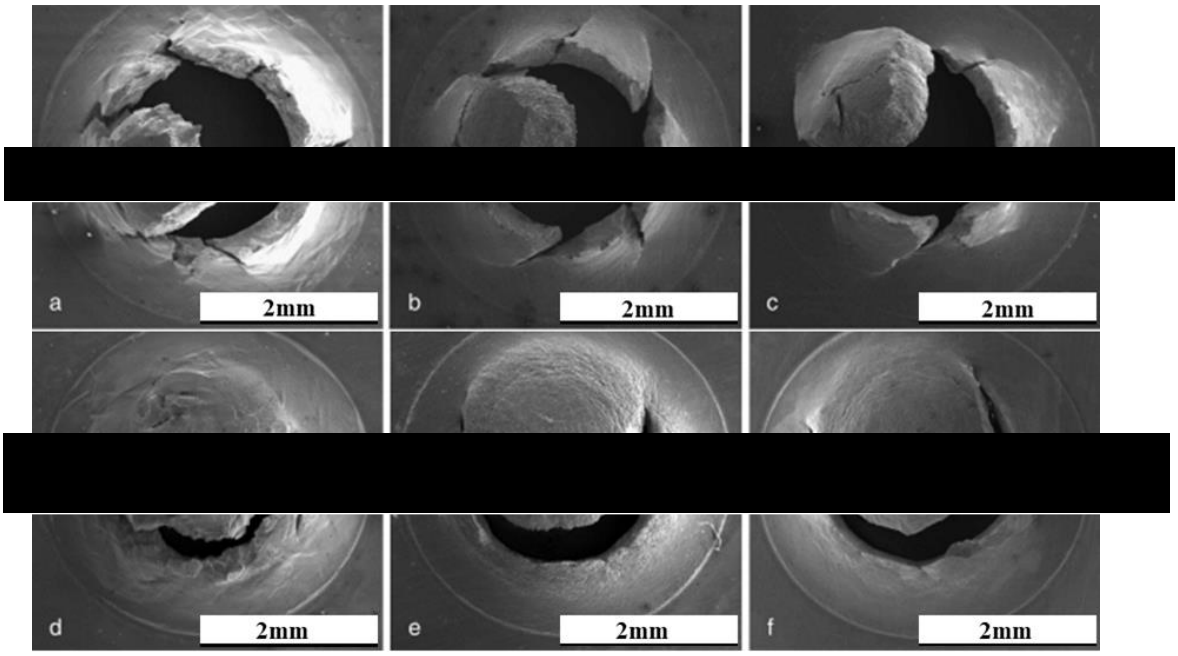

Figure 2.47. SP fractography of Ti-6Al-4V showing levels of embrittlement (a, b and c) and ductility (d, e and f) post rupture [163].

2.4.5 Small Punch Testing of Advanced Materials

Considering the demonstrated validity of this miniaturised testing method and the ongoing efforts to seek standardisation, its use for the characterisation of advanced materials has become prominent in recent years. SP testing has been successfully applied to a wide range of alloying systems across numerous industrial sectors. However, for the aerospace industry in particular, they have been effectively utilised as a means of mechanical characterisation of alloying systems that are extensively used within the gas turbine engine such as titanium, nickels and steel.

SPT has been successfully employed to characterise and mechanically assess polycrystalline Ni-based superalloys in an effort to draw both comparisons and intermediate conclusions as to the influence of manufacture by different means, namely traditionally wrought & cast methodologies, in comparison to ALM [149]. Davies et al employed SPT at both RT and 780°C to effectively rank a series of C263 variants including cast and LPBF variants of differing build orientation and post processing treatments, as shown in Figure 2.48. It was highlighted at both temperature conditions that differentiations in mechanical performance were observed which were subsequently investigated through microstructural analysis, with highly anisotropic microstructures consequent to changes in build orientation being evident with a standard solution heat treatment (SHT) but seemingly alleviated with a higher solution heat treatment (HSHT). Despite this, both LPBF variants appeared to showcase a greater resistance to biaxial deformation than that of traditional cast material which was suggested to be consequent to the increased volume fraction of grain boundaries apparent and the bimodal nature of the grain size in the cast material In addition to this, a noticeable discrepancy in the mechanical performances of the variants subjected to the two differing heat treatments was highlighted through SPT, where energy dispersive spectroscopy (EDS) picked up discrete changes in chemical segregation and particularly the dissolution of γ' formers in the SHT material comparative to the HTST equivalent. When considering the results discussed and the distinct changes in performances observed, SP was demonstrated to be a sensitive testing technique that is effective at characterising discrete microstructural changes.

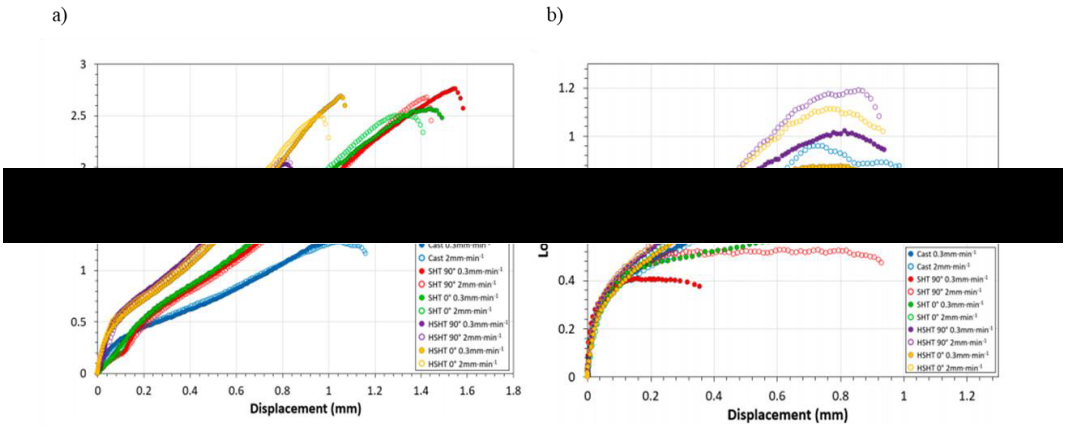

Figure 2.48. SPT employed on a series of cast and LPBF C263 variants at a) RT and b) 780°C [149].

As discussed, once of the significant benefits of the SP testing technique to a wide range of industrial sectors is the discrete sampling nature and ability to mechanically assess localised regions of microstructure. This was exploited to characterise the locational dependency of mechanical properties within a model aerofoil, as shown by Hurst et al [164] and indicated below in Figure 2.49.

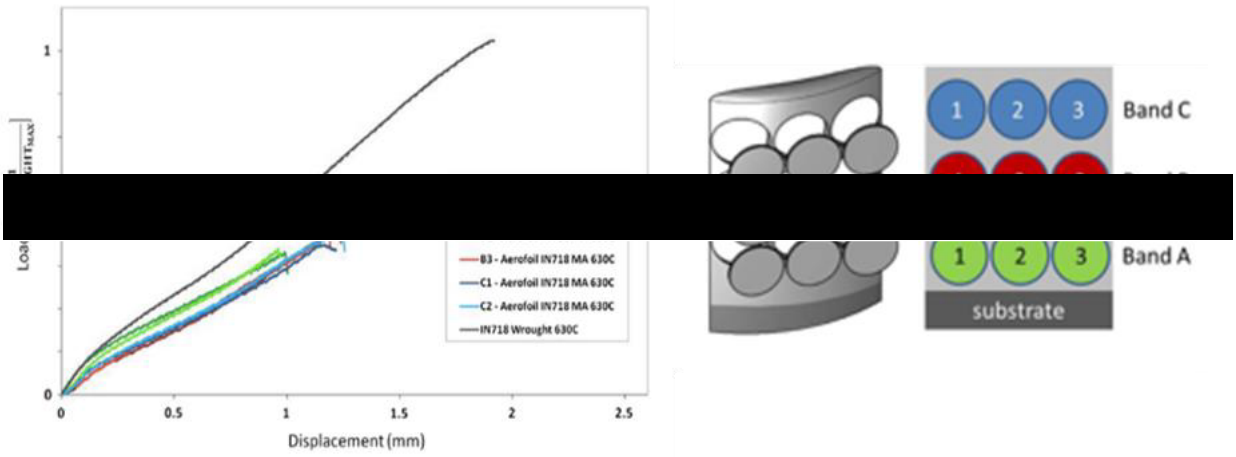

Figure 2.49. a) SP specimen sampling from a DED IN718 model aerofoil b) SPT results of location dependency from aerofoil and wrought material [164].

This paper highlighted two key points in regards to DED IN718 with the first being that there is clear influence of the manufacturing process on the mechanical performance of the material which has been discussed in previous sections. The second is the subtle variation in mechanical performance that is subsequent to the location within the aerofoil component given the anisotropic and evolving grain structures further shown in Figure 2.50a and b. It is highlighted in this study that the deposited layers close to the substrate formed by DLD displayed a weaker response in comparison to the mid-region or the tip of the aerofoil, despite the elongation and coarsening of grain structures apparent. Although it is reasonable to assume the performance would be dominated by the well acknowledged Hall-Petch theory [165], an understanding as to the underlying microtextural influences and their influence is needed as shown, where textural development consequent to the directional heat flow in ALM processes is evident. This paper has subsequently further emphasised the difficulty in ascertaining these influences on mechanical properties using traditional laboratory uniaxial specimens and thus the advantageous aspects of miniaturised testing methods.

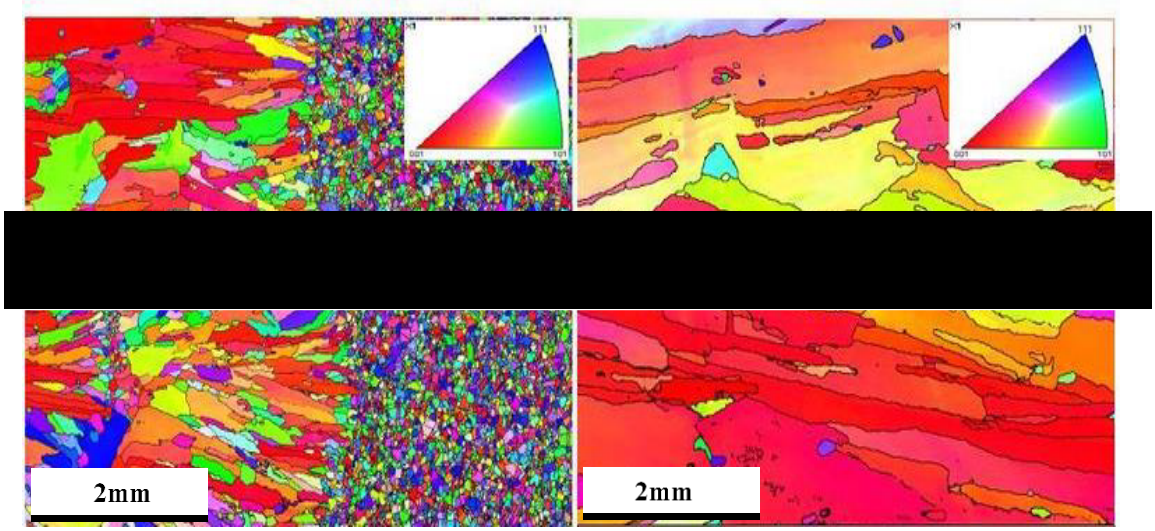

Figure 2.50. EBSD IPF X maps of evolving microstructure from substrate to aerofoil tip highlighting the evolution of grain structure and texture [164].

Furthermore, in addition to the evolution of microstructures with increasing layer height, the influence of orientation effects on mechanical performance was also a key area of interest within this study. It was underlined, as indicated in Figure 2.51, that there was a significant enhancement in tensile performance if the load was applied parallel to the axis of build epitaxy (ST). Conversely, when the load was applied perpendicular to the axis of build epitaxy (T & L), there was a noteworthy reduction in tensile performance. These results can additionally give insight as to how miniaturised mechanical testing methods such as SPT can be exploited to establish, underline and quantify the impact that metallurgical mechanisms associated with ALM have on mechanical performance [164].

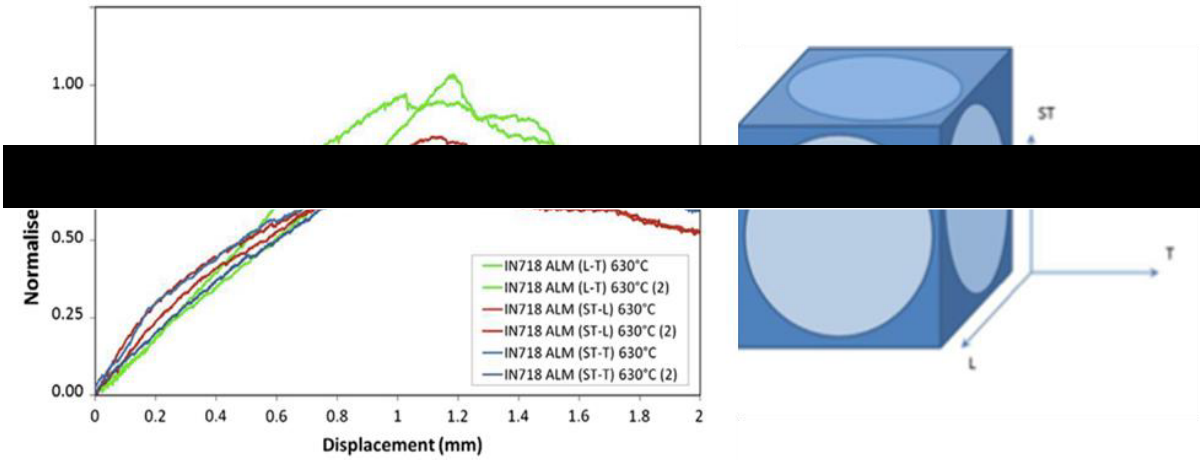

Figure 2.51. SPT results for ALM IN718 for differing loading axis in relation to build epitaxy [164].

As previously mentioned, Zhao et al [125] has successfully demonstrated the application of SPC to ascertain mechanical properties from localised regions of in-service material for complex piping systems, where welded regions give rise to the presence of heat affected zones (HAZ). Figure 2.52a, has shown the utilisation of SPC to characterise both the base and welded regions of material over a range of stresses, whilst Figure 2.52b emphasises the pivotal role that both grain structure and loading conditions have on creep deformation. It was underlined that coarsened grain structures in particular display a superior resistance to creep deformation given that the mechanism of failure is grain boundary dominated and typically intergranular.

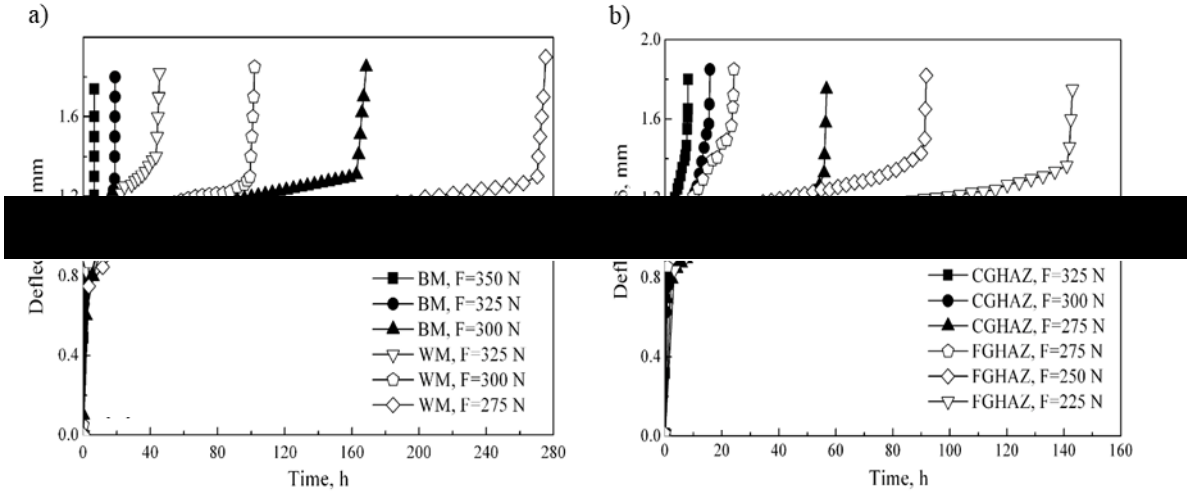

Figure 2.52. SPC testing of both fine-grained and coarse-grained material under different loading conditions [125].

SPC has previously been employed to characterise advanced high temperature materials such as Ni-based superalloys considering the nature of their application within the gas turbine engine. Jeffs et al [151] demonstrated this with the use of SPC on 2nd generation single crystal systems such as CMSX-4 as underlined in Figure 2.53a & b, where a series of tests were carried out at different loads (190-400N) and temperatures (950-1150°C). It was shown, as emphasised in Figure 2.53a, that as load was increased, a direct relationship with resistance to high temperature mechanical deformation was observed, as to be expected. The same can be said for temperature as shown in Figure 2.53b, where an increase in temperature is also shown to further accelerate creep deformation. The use of this miniaturised testing method in conjunction with microstructural analysis proved to be successful in characterising the evolution of mechanisms such as rafting under loading, as shown in Figure 2.54. One of the major points this further emphasises and supports is the existence of biaxial loading conditions within SP testing, as the rafted microstructures form perpendicular to the loading axis.

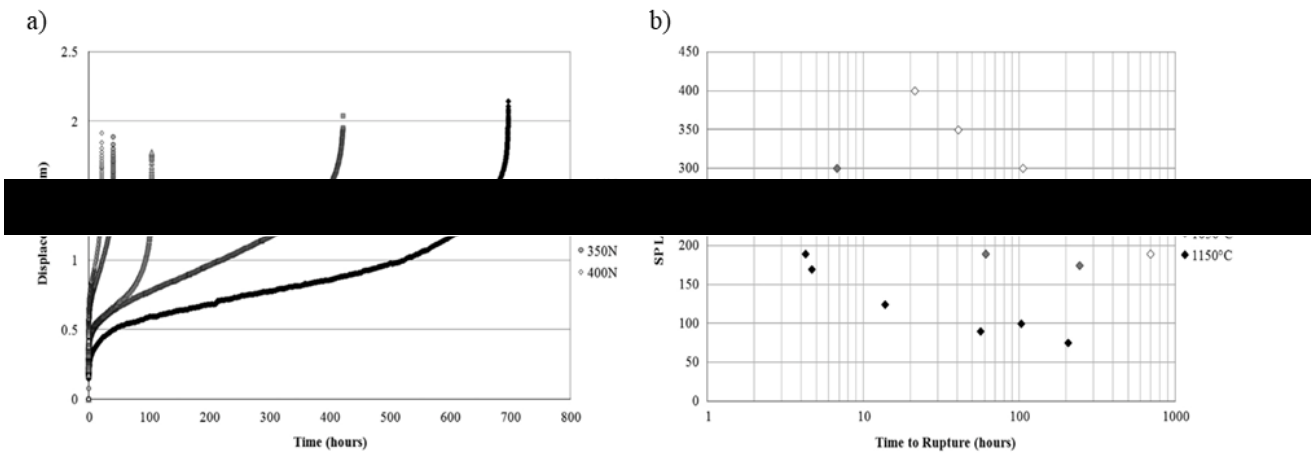

Figure 2.53. a) SPC testing at 950°C for a range of applied loads, b) load vs time to rupture plots for a range of temperatures (950-1150°C) on CMSX-4 [151].

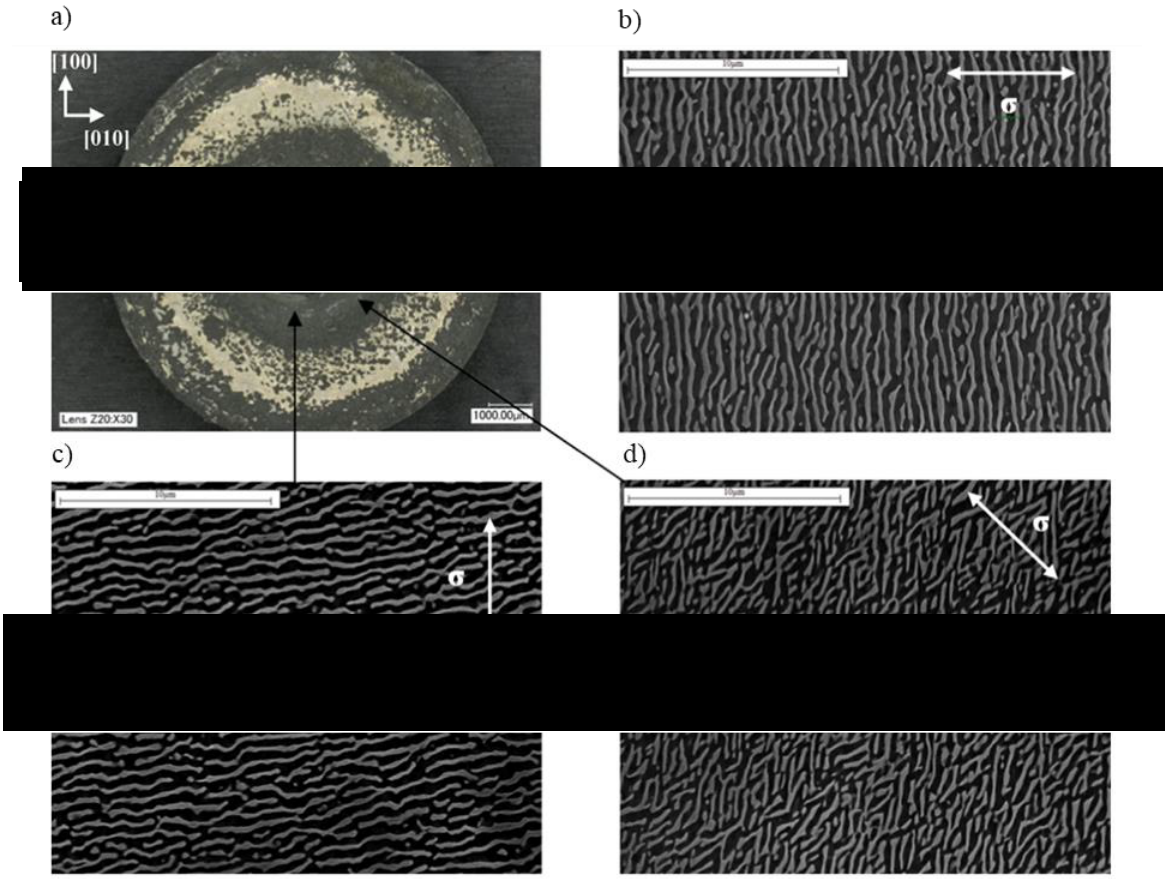

Figure 2.54. a) Ruptured specimen post creep failure with corresponding microstructural imaging that highlights rafting in relation to loading direction b c) & d) [151].

In addition to single crystal systems, Jeffs et al [129] has demonstrated the effectiveness of using SPC to characterise advanced polycrystalline nickel systems, in particular directly comparing and contrasting wrought C263 against LPBF variants of differing build orientations as shown in Figure 2.55a & b. It is shown that both the manufacturing route and the build orientation drastically impact the material's resistance to creep deformation as a result of the significant changes in microstructural features, further highlighting the metallurgical complexity of the ALM process in comparison to traditional cast and wrought methodologies given the intrinsic anisotropic grain structure present. The influence of build orientation on grain sizes and morphologies are depicted in Figure 2.56b & c, which was hypothesised to be the main explanatory factor for the severe changes in mechanical performance, as creep deformation is a grain boundary dominated mechanism. Although these results concur with the anisotropic trends seen in previous literature [130] [166], given the biaxial state apparent as previously discussed, it is suggested that the need for further research becomes necessary.

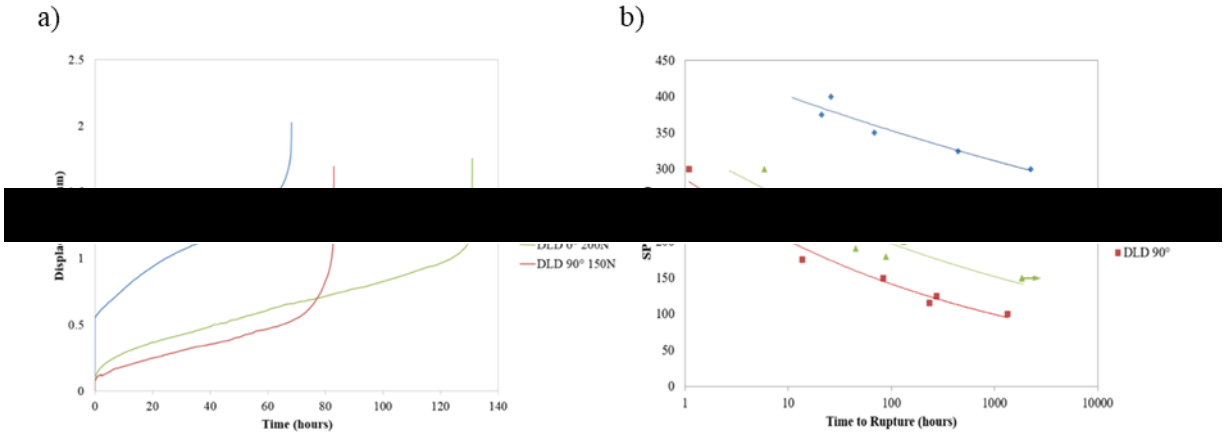

Figure 2.55. SPC results for directly comparing a) cast vs DLD variants and b) SP Load vs Time to Rupture for C263 [129].

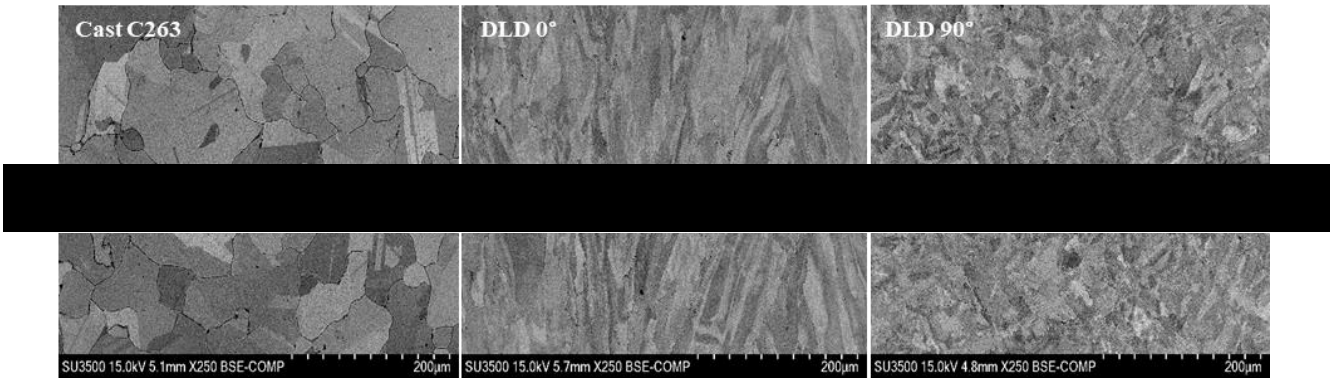

Figure 2.56. C263 manufactured by different means a) cast, b) DLD 0º build orientation and c) DLD 90º build orientation [129].

Davies et al [149] [159] furthered this line of research on C263, by combining both the utilisation of SPC in conjunction with material characterisation microscopy techniques to ascertain and characterise the impact of variations in build orientation and post processing treatments. In this study, a series of LPBF variants of 0° and 90° build orientations were exposed to two different heat treatment regimens, one which was previously defined and one found in literature [167]. It was found that SP test results did in fact coincide with the anisotropic trends previously discussed, however it was observed that post processing routes, in particular high temperature solution treatments could be utilised to alleviate such issues by effectively reducing texture and the presence of elongated grains. The impact of these changes are significantly evident in Figure 2.44, where a change in SPC behaviour is observed for HT1 0° and 90°, contradicting that of the higher temperature solution heat treatment (HT2), where minimal change is noticed when comparing the 0° and 90° orientations. The individual SPC tests for HT2 0° are given as an example in Figure 2.57, where increasing load appears to accelerate creep deformation as to be expected.

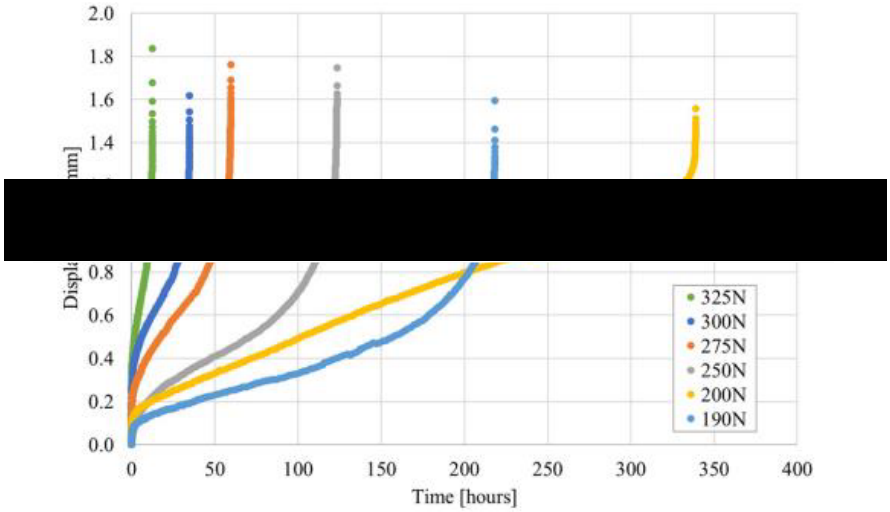

Figure 2.57. C263 SPC curves for HT2 0° at 780°C tested at different loading regimes [159].

Furthermore, this study was able to highlight not only the impact of heat treatments on anisotropic grain structures, but it's bearing on grain boundary strengthening precipitates such as carbides, which are considered to be of significant importance to grain boundary dominated mechanisms such as creep as previously mentioned. This paper highlighted two key points with regards to carbides, the first being that despite the same heat treatment, the manufacturing route appears to have a major influence on carbide characteristics. This is inherent of the rapid cooling mechanisms associated with ALM in comparison to that of casting processes, where limited time within the liquidus region would lead to fine dispersions of Ti and Al segregates within the γ matrix as shown in Figure 2.58a. Higher temperature solution heat treatments were shown to support the development of MC + M_6C carbides as apparent in Figure 2.58b, with the Ti and Al segregates previously mentioned being no longer apparent through both solid-state diffusion into the γ matrix or contribution to the carbide formation.

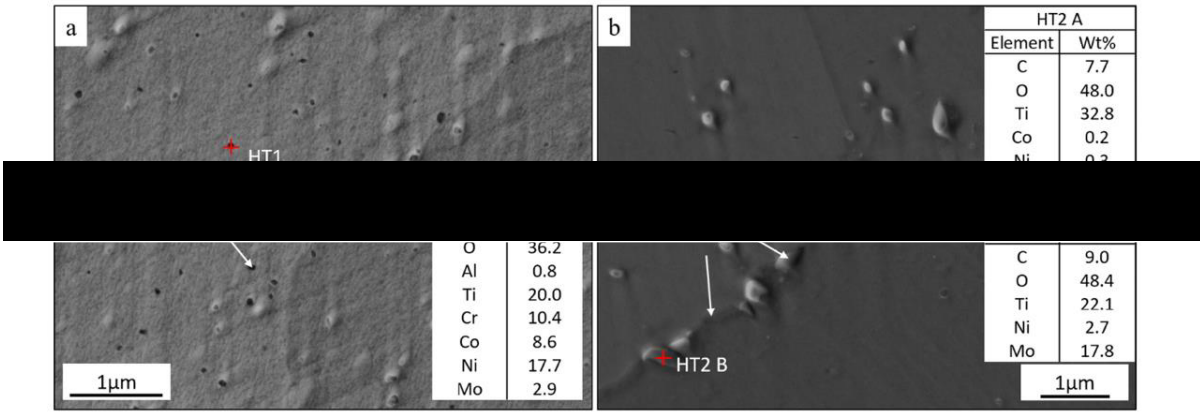

Figure 2.58. Micrographs and elemental analysis of C263's a) HT1's Ti and Al dispersions suspended within the γ matrix b) HT2's MC and M_6C carbides from higher temperature solution heat treatments [159].

2.5 Summary

Nickel-based superalloys showcase an impressive ability to retain mechanical properties at high temperatures alongside excellent oxidation and corrosion resistance. It is for these reasons that they are incorporated in a wide range of industrial sectors, specifically the aerospace industry where they are extensively utilised within the holistic gas turbine engine. Given the increasing demands of the civil aviation sector from both an environmental and economical perspective, the aerospace industry has a continuous need to drive gas turbine development through both increased temperature capability and weight reduction. It is therefore becoming increasingly interested in the use of alternative manufacturing and repair technologies, with research in near net shape technologies such as ALM rising in parallel.

Given the complex nature of ALM processes and the large abundance of parameters and variables apparent, the use of miniaturised testing procedures that can discretely sample material proves to be a useful methodology. As discussed, miniaturised testing methods have been successfully utilised in order to ascertain mechanical properties from small volumes of advanced materials from both the nuclear and aerospace sector. In conjunction with microscopy and in-depth material characterisation methods, previous work at Swansea University has effectively implemented small scale testing methods to characterise single crystal nickel systems alongside metallurgically complex polycrystalline alloys such as LPBF C263.

This study will look to incorporate SPC and SPT alongside in-depth material characterisation methodologies to characterise LPBF variants of polycrystalline nickel-based superalloys which contain high γ' contents such as CM247LC and low γ' alloy such as IN718. The premise behind this work will be to gauge a further understanding as to how process parameters and variables impact changes in microstructural features and thus mechanical performance.

Chapter 3 – Materials and Methodology

In this study, the influence of key process parameters and variables on the mechanical and microstructural behaviour of two contrasting LPBF nickel-based superalloys CM247LC and IN718 was investigated. An assortment of LPBF variants was provided in four separate work packages by Rolls-Royce plc. with key distinct differentials in each Design of Experiments (DOE) being employed. The initial sections of this chapters will introduce the materials, general procedures, equipment and experimental test setups utilised within this study. The latter sections will specifically detail the sample extraction, parameter deposition and testing matrixes utilised within each respective DOE.

3.1 Materials

3.1.1 CM247LC

The LPBF CM247LC variants provided by Rolls-Royce plc. were fabricated using gas atomised CM247LC virgin powder produced by ATI Metals, with a powder particle size distribution of 15.00 - 50.00µm, a mass flow rate of 13.72s/50g and an apparent density of 4.65g/cm^3. Microscopic observations were provided by Rolls-Royce plc. and can be observed below in Figure 3.1, alongside the chemical composition specification for the powder as shown in Table 3.1. All CM247LC variants within this study were manufactured using the EOS M280 on a generic stainless steel build plate with a preheated powder bed of 80°C, with a continuous laser mode being applied in collaboration with a standard stripe hatching strategy, where 67° rotations were incorporated between layers.

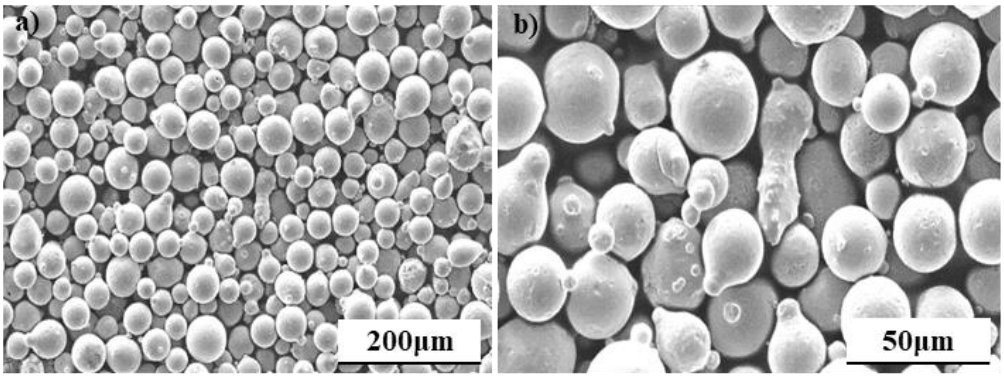

Figure 3.1. SEM observations of CM247LC gas atomised powder used in this study (courtesy of Rolls-Royce plc.)

Table 3.1. Chemical composition specifications of gas atomised CM247LC powder by weight %.

Ni	Cr	Co	Al	Ta
Bal	8.00 – 8.50	9.00 – 9.50	5.40 – 5.80	3.10 – 3.40
Mo	Ti	Hf	B	W
0.50 – 0.60	0.60 – 0.90	1.20 – 1.60	0.01 – 0.02	9.30 – 9.70

3.1.2 IN718

The LPBF IN718 variants provided by Rolls-Royce plc. were fabricated using gas atomised IN718 virgin powder produced by Carpenter Additive, with a powder particle size distribution of 15.00 - 45.00µm, a mass flow rate of 9.47s/50g and an apparent density of 3.81g/cm^3. Microscopic observations can be observed below in Figure 3.2, alongside the chemical composition specification for the powder as represented in Table 3.2. All IN718 variants within this study were manufactured using the EOS M290 on a generic stainless steel build plate with a preheated powder bed of 80°C, with a continuous laser mode being applied in collaboration with a standard stripe hatching strategy, where 67° rotations were incorporated between layers.

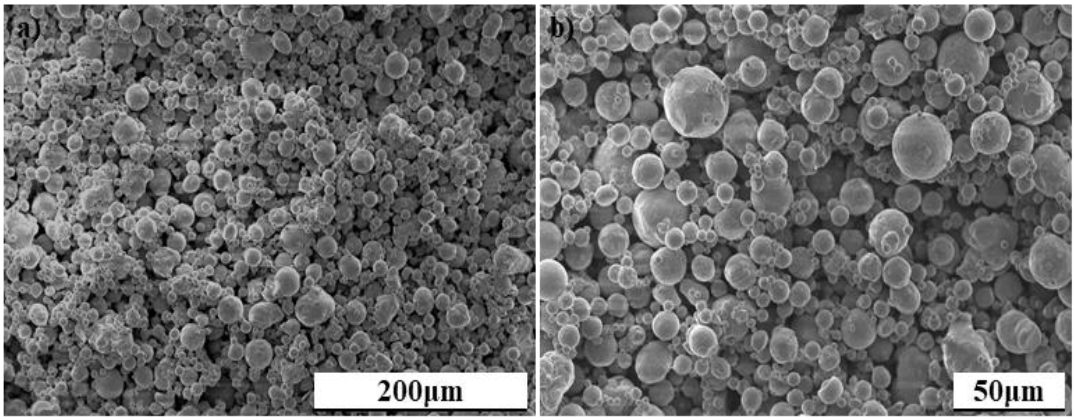

Figure 3.2. SEM observations of IN718 gas atomised powder used in this study.

Table 3.2. Chemical composition specifications of gas atomised IN718 powder by weight %.

C	Cr	Ni	Mo	Mn	Nb
0.08	17 - 21	50 - 55	2.80 - 3.30	0.35 (max)	4.75 - 5.50
Ti	Al	Fe	Si	S	P
0.65 - 1.15	0.2 - 0.8	Bal	0.35 (max)	0.015 (max)	0.015

3.2 General Methodologies, Equipment and Test Setup

The application of small scale mechanical testing methodologies in combination with microscopy based techniques was utilised in this study to assess the impact of changes across key process parameters and variables on mechanical properties, microstructural features and structural integrity. This section will outline the metallurgical preparation procedures for both microstructural analysis and small punch testing, the optical and electron microscopies operated and the miniaturised mechanical testing methodologies employed.

3.2.1 Metallurgical Preparation for Microscopy Analysis

LPBF CM247LC and IN718 were subjected to their own respective series of grinding, polishing and chemical etching procedures. Samples were hot mounted in a conductive phenolic resin, bakelite, and subject to the general grinding and polishing procedures for each alloy as outlined in Tables 3.3 and 3.4, where the ATA SAPHIR 520 was used. Following each step, the samples were washed with water and ethanol. Post polishing, CM247LC was washed with acetone or ethanol to remove the OP-S polishing media employed and then submerged in a high concentration Kalling's reagent (5 grams $CuCl_2$, 100ml HCl and 100ml ethanol) for approximately 10 seconds at room temperature. IN718 was immediately subjected to a swab of lower concentration Kalling's reagent (diluted in distilled water), where a general figure of 8 motion was applied to subside the OP-S polishing media and expose the material surface for approximately 30 seconds at room temperature. For particle analysis, post chemical etching a re-polish was utilised using Step 4 outlined in each alloys' polishing procedure. For fractography imaging, fracture surfaces were cleaned using acetone and distilled water in an ultrasonic bath for 15 minutes.

Table 3.3. Metallographic grinding and polishing procedures for CM247LC.

	Step 1	**Step 2**	**Step 3**	**Step 4**
Base	Piano-120	Largo	Dac	MD-Chem
Media	Water	DiaPro Allegro Largo	DiaPro Dac	OP-S (0.04 micron)
Force (N)	25	25	25	20
Speed (rpm)	300	150	150	150
Time (min)	1	4	5	7-8

Table 3.4. Metallographic grinding and polishing procedures for IN718.

	Step 1	**Step 2**	**Step 3**	**Step 4**
Base	Piano-120	Largo	Dac	MD-Chem
Media	Water	DiaPro Allegro Largo	DiaPro Dac	OP-S (0.04 micron)
Force (N)	25	25	25	20
Speed (rpm)	300	150	150	150
Time (min)	1	6	10	15

3.2.2 Metallurgical Preparation for Small Punch Testing

Ø9.5mm discs of different thicknesses were extracted from the fabricated material as will be outlined in each respective work package section. These discs were subject to a series of sequential grinding procedures using the ATA SAPHIR 360, where grades of silicon carbide papers of increasing grit were consecutively employed as shown in Table 3.5. The discs were held in contact with the grinding media using a bespoke jig with a 9.5mm diameter bore, with the thickness of each disc being monitored at intervals during the grinding process using a calibrated digital micrometre, in order to ensure uniformity. The dimensional accuracies of the discs subjected to testing all conformed to the ASTM E3205-20 standard for small punch testing specifications of a 0.5mm thickness, with tolerances of ± 0.005mm [131].

Table 3.5. Grinding procedure for small punch disc preparation.

Stage	Grit	Sample Thickness	RPM
I	60	> 1mm	300
II	500	> 0.6mm	300
III	1200	< 0.6mm	300

3.2.3 Optical Microscopy

Optical Microscopy was conducted on all LPBF CM247LC and IN718 process variants to capture microstructural features using both the ZEISS Smartzoom 5 and ZEISS Axio Observer. Operating software controls were utilised on both systems to in order to optimise the resolution, brightness and contrast of each image to correspond to the features desired for observation. In addition to this, stitched high resolution imaging was incorporated on numerous process variants as will be detailed later, where an initial low magnification image was acquired using a black and white contrasting coalescence. From there, a meshed grid of tiles was applied over the desired range for acquisition and a heightened magnification of 200x was selected. Autofocusing points were deliberated and determined at various points throughout the sample before the image was acquired.

3.2.4 Scanning Electron Microscopy

Scanning Electron Microscopy (SEM) was employed on a selection of the LPBF CM247LC and IN718 process variants in order to observe and capture the microstructural changes consequent to process parameter selection. The Hitatchi SU3500 was utilised in this study, where mounted samples were loaded onto a motorised stage and introduced to a vacuumed environment. Both secondary electron and backscattered electron contrasting imaging methods were used in this study, where

software controls were utilised in order to change an array of settings including accelerating voltage, working distance and spot size. Image focus, brightness and contrast were optimised to heighten the resolution and clarity of the desired microstructural feature.

3.2.5 Energy Dispersive Spectroscopy

Energy Dispersive Spectroscopy (EDS) was applied within this study on both CM247LC and IN718 to provide chemical mapping analysis. For all EDS maps incorporated in this study, the Oxford Instruments X-Max^{N} System was utilised in collaboration with the AZtec software platform system to provide chemical mapping. A large aperture with an accelerating voltage of 20KV, working distance of ~ 10mm, spot size of 60 and a process time of 4 was selected so that a dead time of between 15 - 40% was achieved.

3.2.6 Electron Backscatter Diffraction

Electron Backscatter Diffraction (EBSD) scans were widely used within this work on both LPBF CM247LC and IN718 to characterise grain sizes and morphology, alongside providing an array of mapping techniques for microstructural characterisation and textural analysis. All EBSD scans generated in this study were completed using the Oxford Instruments NordlysMax^{3} in collaboration with the AZtec software platform. Process settings did vary across scans in order to heighten 'hit rate', but generally a large aperture was selected with an accelerating voltage of 25KV, working distance of 15 - 25mm and a spot size of 90-100 being employed. For all CM247LC scans, a 200x magnification with a step size of 0.25 – 0.50μm was utilised for data acquisition and for all IN718 scans, a 250x magnification with a step size of 0.50μm was employed for data acquisition. All EBSD scans within this study were ensured to have a solution volume fraction rate of > 85%. The EBSD scans conducted were exported to the Oxford Instruments HKL Channel 5 format for subsequent analysis, where a variety of mapping techniques were used.

3.2.7 Small Punch Creep Setup

Small Punch Creep (SPC) testing was performed on a variety of LPBF variants for both CM247LC and IN718 in this study, as will be outlined in the subsequent sections. Specimens were prepared in order to concur with ASTM E3205-20 [131] as defined previously in Section 3.22, where a bespoke, high temperature, 'dead-weight' testing frame developed at Swansea University [151] as shown in Figure 3.3 was used to conduct these tests. The specimen was circumferentially clamped between an upper and lower die, which was centrally aligned to the above loading pan as illustrated, where a receiving hole of Ø4mm exposes the top surface of the disc to a Ø2mm hemispherical alumina punch head. Two Type-N thermocouples were fed through drilled holes in the upper die in order to

maintain contact with the specimen and monitor test temperatures, which were secured in place using Nimonic wiring. Temperature tolerances of ± 3°C were maintained throughout all SPC tests. Two linear variable displacement transducers (LVDTs) were employed in this test setup in order to measure deformation from both sides of the specimen, where one was placed in contact with a SiO_2 quartz rod fixed to the bottom face of the disc to record deflection and the other in contact with the above loading pan to monitor displacement on the top surface. A ceramic tube surrounded the upper and lower die in order to encapsulate the argon introduced to the system in order to prevent the influence of oxidation or corrosion, with a single zone split digital furnace surrounded the entire setup in order to apply heat.

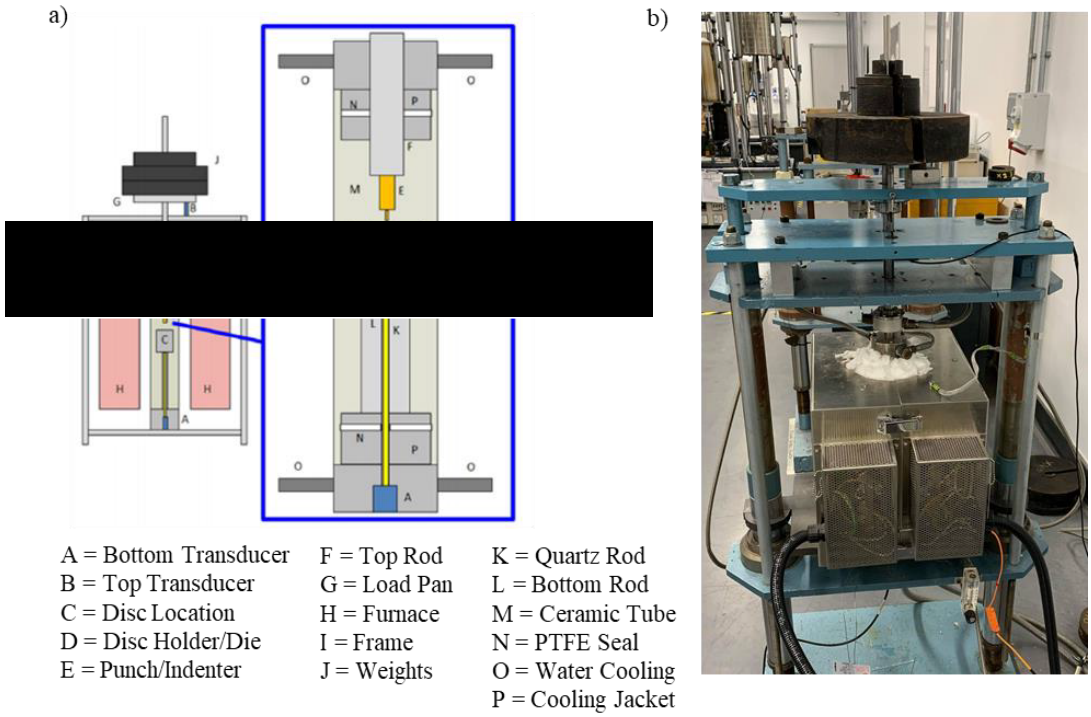

Figure 3.3. Bespoke SPC setup a) schematic illustration [151] b) completed test setup.

3.2.8 Small Punch Tensile Setup

Small Punch Tensile (SPT) testing was applied to a variety of LPBF variants for both CM247LC and IN718, where testing was conducted at both room and elevated temperatures. Specimens were prepared in accordance with ASTM E3205-20 [131] as detailed in Section 3.22 and circumferentially clamped in a bespoke jig assembly developed at Swansea University [168], where the specimen was circumferentially clamped between an upper and lower die which comprised of a circular aperture of Ø4mm. The circumferentially clamped specimen was then encased in a cylindrical housing block and grub screw, in order to ensure central axial alignment of the disc to the testing frame's cross head and loading collar. From there, a Ø2.5mm hemispherical Nimonic-90 punch head was introduced perpendicularly to the specimen alongside a pin pusher and vertically aligned with respect to the testing frame. An overall representation of this jig assembly is illustrated in Figure 3.4, where it's relation to

the general testing frame and loading collar is illustrated in Figure 3.5. In order to monitor test temperatures, an N-type thermocouple was introduced to the bottom face of the disc through a hollow SiO_2 quartz rod and placed in contact with the bottom face of the disc to monitor test temperature. Temperature tolerances of ± 3ºC were maintained throughout all SPT tests. Additionally, this quartz rod was in contact with an LVDT in order to monitor deflection from the bottom face of the disc. A second LVDT was located within the testing frame's cross head, from which displacement values were recorded. A dual-zone split furnace encapsulated the test set up to apply temperature.

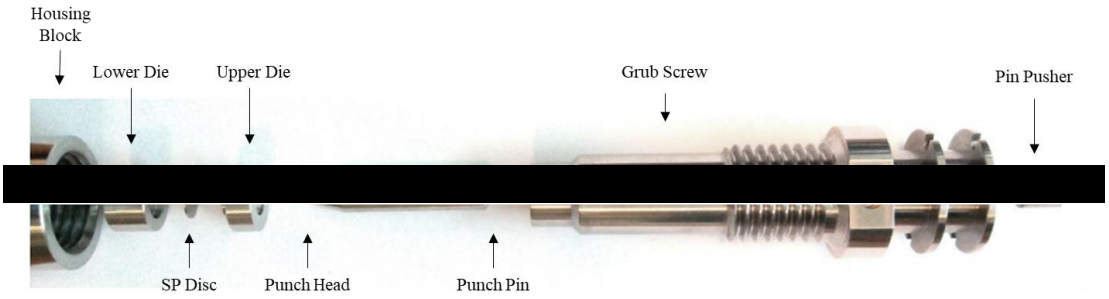

Figure 3.4. Bespoke SPT jig assembly apparatus developed at Swansea University [168].

Figure 3.5. SPT setup a) Zwick / Roell Z5.0 hydraulic testing frame, b) quartz rod and c) loading collar introduced to pin punch during high temperature test.

A wide range of equipment has been utilised in this study in order to effectively characterise the microstructural features and mechanical properties inherent to differing LPBF process variants. The following section will detail each respective individual work package for both alloys, which will include the material supplied by Rolls-Royce plc., the sectioning and sample extraction from the fabricated material implemented within this study and the methodologies employed to characterise them, both mechanically and microstructurally.

3.3 Small Scale Testing & Microstructural Characterisation of CM247LC

A series of LPBF variants of CM247LC were fabricated within this section with changes in build orientation and parameter sets being considered. 28 coupons were manufactured, with 14 iterations of 30° orientations comprising of 5 differing parameter sets, the distinctions of which will be outlined later. Parameter Set 1 was fabricated 6 times, with Parameter Sets 2-5 being fabricated twice. The remaining 14 coupons comprised of the same make up to the 30° orientations mentioned, but with a 90° build orientation imposed. An overall representation of this can be seen in Figure 3.6, where a CAD schematic recreated from pictures of the fabricated architecture is shown. The coupons were removed from the build plate by Rolls-Royce plc. using electrical discharge machining (EDM), and provided in Ø9.5mm discs extracted from the distinct locations on each coupon as shown in Figure 3.7. The top disc was subject to a series of hot isostatic pressing (HIP) and heat treatment (HT) procedures as will be discussed and provided for mechanical testing and analysis.

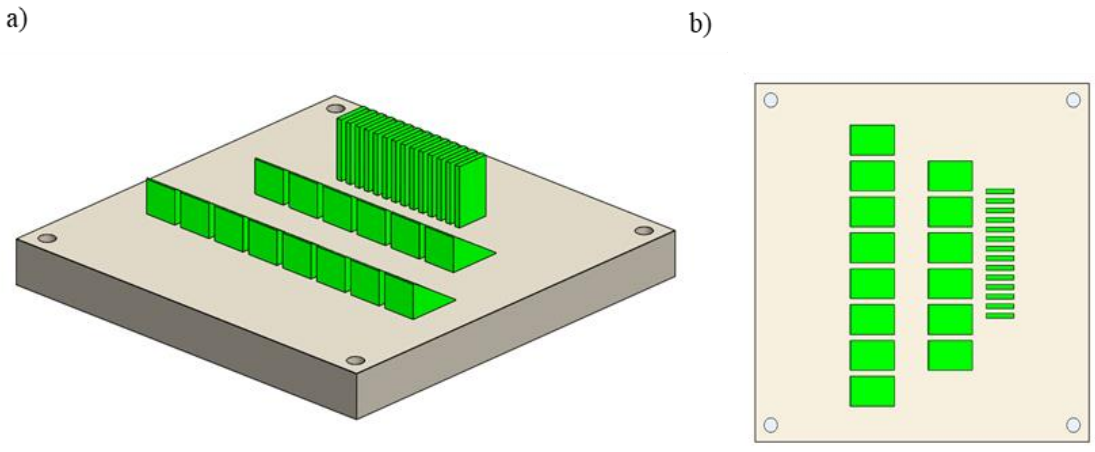

Figure 3.6. Recreated CAD schematic of 30° and 90° coupons fabricated within this work package.

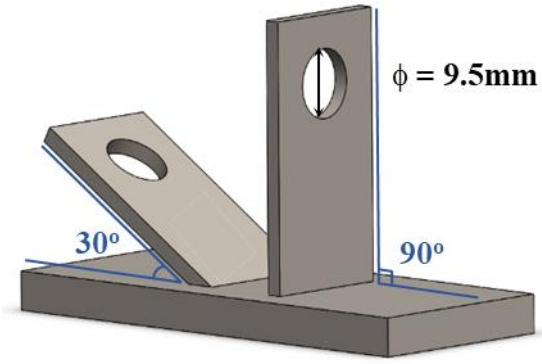

Figure 3.7. Sampling of SP specimens from LPBF CM247LC coupon architectures.

As mentioned, 5 parameter sets were employed in this work package for each respective orientation. These parameter sets were designed and based off of the small processing window for CM247LC, highlighted in the normalised process map as discussed in Section 2.3.3, and incorporated changes in beam settings and the hatch spacing. Diagonal isopleths were utilised in order to indicate varying degrees of equivalent energy densities. An overall representation of the normalised process parameter sets is shown in Figure 3.8, with the parameter conditions summarised in Table 3.6.

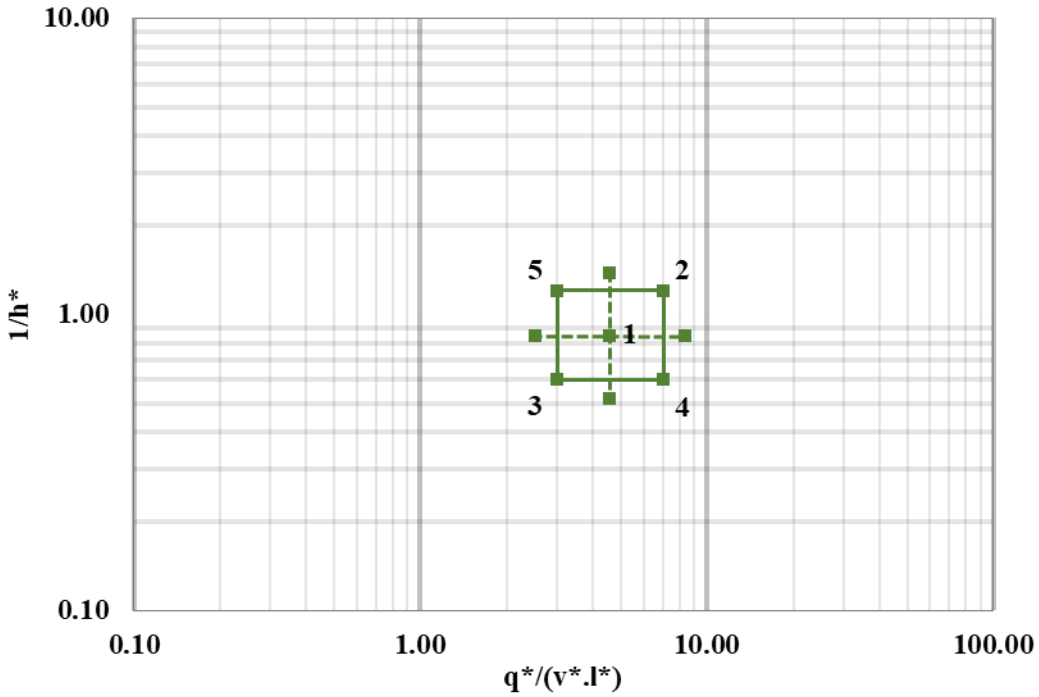

Figure 3.8. Parameter selection from within the normalised process window.

Table 3.6. Parameter set summary with regards to normalised beam settings, hatch spacing and equivalent energy density.

Parameter Set	***q**/(*v**.l*)**	**1/*h****	***E****
1	Medium	Medium	Medium
2	High	High	High
3	Low	Low	Low
4	High	Low	Medium
5	Low	High	Medium

The post processing conditions employed as outlined previously were based on an optimised post processing procedure provided by Canon-Muskegon for directionally solidified CM247LC which was subsequently published by Erickson et al [169], which comprised of 3 primary stages. An initial bespoke low temperature HIPing stage at 1220°C, 143MPa was employed for 2 hours, followed by a solution heat treatment conducted at 1250°C for 4 hours, which was proceeded with an 870°C ageing treatment over 16 hours. An overall representation and summary of this process is showcased below in Figure 3.9 and detailed in Table 3.7.

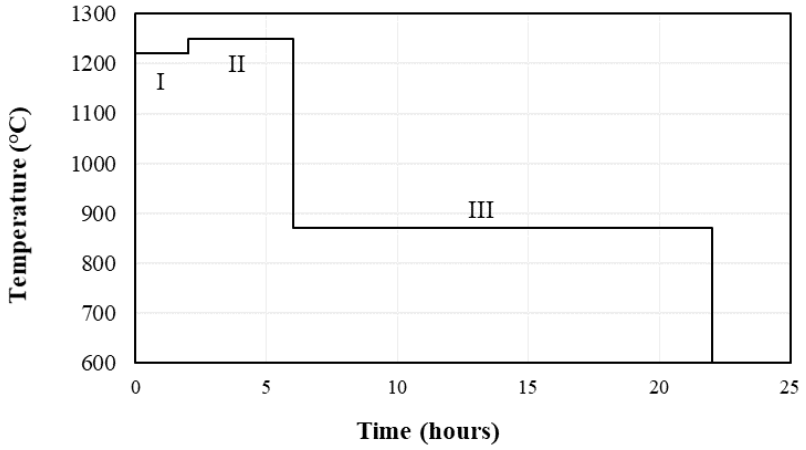

Figure 3.9. Post processing routes employed on LPBF CM247LC variants within this work package.

Table 3.7. Processing conditions for each stage of post processing route.

Stage	Processing Route	Temperature (°C)	Pressure (MPa)	Time (Hours)
I	HIPing	1220	143	2
II	Solution HT	1250	-	4
III	Aging HT	870	-	16

The Ø9.5mm discs extracted previously were ground from 2.4mm thickness to 0.5mm ± 0.005mm in according with ASTM E3205-20 [131] using the methodology outlined in Section 3.22 and subject to SPC, as detailed in Section 3.27. A summary of the samples tested and the testing matrix employed are provided below in Table 3.8. Given the nature of the grinding procedure detailed and the fine tolerances imposed by ASTM E3205-20 [131], some specimens were over ground and out of specification for testing. Post rupture, the specimens were cleaned for fractography in an ultrasonic bath and imaged using electron microscopy. Following this, the samples were mounted upside down in a conductive phenolic mounting resin with the circumferentially clamped region of the disc exposed for the preparation procedures and chemical etching procedures outlined in Section 3.21. They were imaged and analysed using electron microscopy, EDS and EBSD.

Table 3.8. Testing conditions employed during SPC testing and results explored in this study.

Specimen ID	Temperature (°C)	Load (N)	Comments
30°, Parameter Set 1, Build 1	950	150	
30°, Parameter Set 1, Build 2	950	150	
30°, Parameter Set 1, Build 3	950	150	
30°, Parameter Set 1, Build 4	950	150	Void Test
30°, Parameter Set 1, Build 5	950	150	
30°, Parameter Set 1, Build 6	950	150	
30°, Parameter Set 2, Build 1	950	150	Ground too thin.
30°, Parameter Set 2, Build 2	950	150	
30°, Parameter Set 3, Build 1	950	150	
30°, Parameter Set 3, Build 2	950	150	
30°, Parameter Set 4, Build 1	950	150	
30°, Parameter Set 5, Build 1	950	150	
30°, Parameter Set 5, Build 2	950	150	
90°, Parameter Set 1, Build 1	950	150	
90°, Parameter Set 1, Build 2	950	150	
90°, Parameter Set 1, Build 3	950	150	Argon loss during cool down.
90°, Parameter Set 1, Build 4	950	150	
90°, Parameter Set 1, Build 5	950	150	
90°, Parameter Set 1, Build 6	950	150	
90°, Parameter Set 2, Build 1	950	150	
90°, Parameter Set 2, Build 2	950	150	Ground too thin.
90°, Parameter Set 3, Build 1	950	150	Ground too thin.
90°, Parameter Set 3, Build 2	950	150	
90°, Parameter Set 4, Build 1	950	150	Ground too thin.
90°, Parameter Set 4, Build 2	950	150	
90°, Parameter Set 5, Build 1	950	150	Void Test
90°, Parameter Set 5, Build 2	950	150	

3.4 Melt Track and Defect Analysis in CM247LC

In this section, 2 separate builds comprising of 24 LPBF variants of CM247LC were fabricated. The first build produced samples in cubic form with an underpinning pyramid support structure. The process parameters incorporated changes in normalised beam speed, hatch spacing, power and energy density as outlined in Table 3.9. This build was left to remain in the as-built (AB) condition. The second build comprised of the same back to back LPBF variants in rod form, which were subjected to HIPing treatment on the build plate, utilising the same process conditions employed in the previous work package (1220°C, 143MPa for 2 hours). Overall CAD schematics of these builds including trimetric and top plane views are illustrated in Figure 3.10.

Table 3.9. Linearly normalised parameter sets employed for both cube and rod manufacture.

Sample ID	Speed	Hatch Spacing	Power	E*
1	0.51	2	1	0.98
2	0.51	2	1	0.98
3	0.40	2	1	1.25
4	0.40	2	1	1.25
5	0.31	2	1	1.61
6	0.31	2	1	1.61
7	0.65	2	2	1.54
8	0.65	2	2	1.54
9	0.51	2	2	1.96
10	0.51	2	2	1.96
11	0.41	2	2	2.44
12	0.41	2	2	2.44
13	0.83	2	3	1.81
14	0.83	2	3	1.81
15	0.65	2	3	2.31
16	0.65	2	3	2.31
17	0.52	2	3	2.88
18	0.52	2	3	2.88
19	1.00	2	4	2.00
20	1.00	2	4	2.00
21	0.81	2	4	2.47
22	0.81	2	4	2.47
23	0.63	2	4	3.17
24	0.63	2	4	3.17

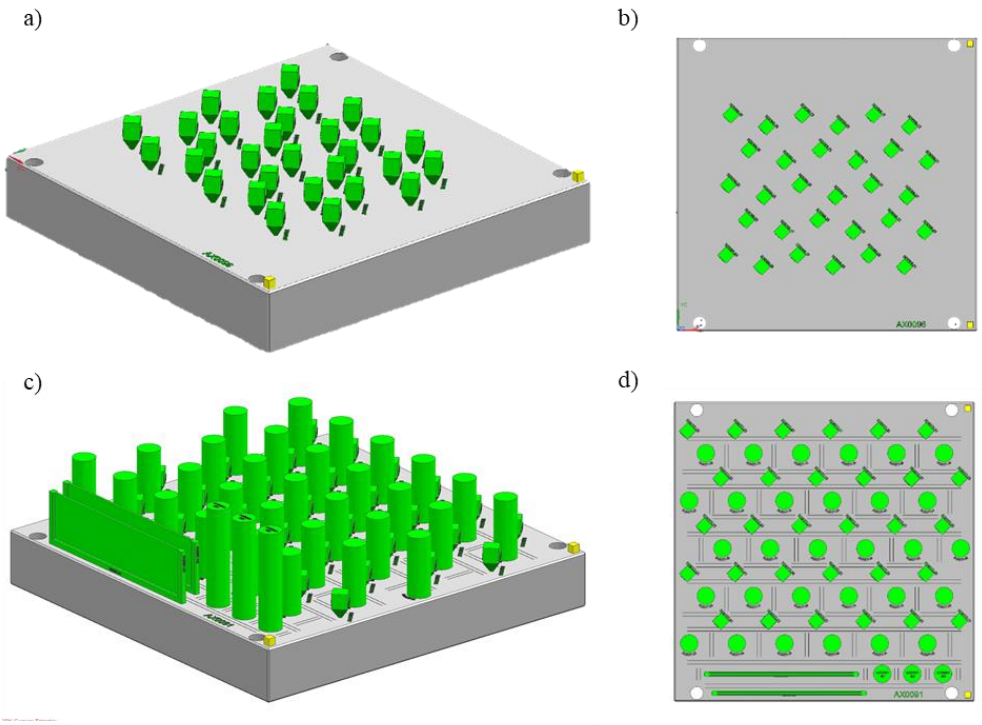

Figure 3.10. CAD schematics of cubes fabricated a) trimetric view b) top plane view, and rods fabricated c) trimetric view and d) top plane view (provided by Rolls-Royce plc.).

The AB cubes were removed from the build plate using a hammer and chisel at the base of the support structure, and were sectioned in 2 manners as illustrated in Figure 3.11 using the Struers Secotom-10 precision cutter with an Aluminum Oxide cutting wheel. The first sectioning was applied perpendicular to and above the pyramid support structure, the offcut of which was used for defect analysis as will be discussed. The second sectioning procedure was taken perpendicular to the scanning lines to reveal melt track profiles. Both offcuts were mounted in Bakelite with their faces revealed and subjected to the polishing and chemical etching procedures outlined for CM247LC in Section 3.21. The cut intended for defect analysis was repolished using step 4 after the chemical etch as previously discussed.

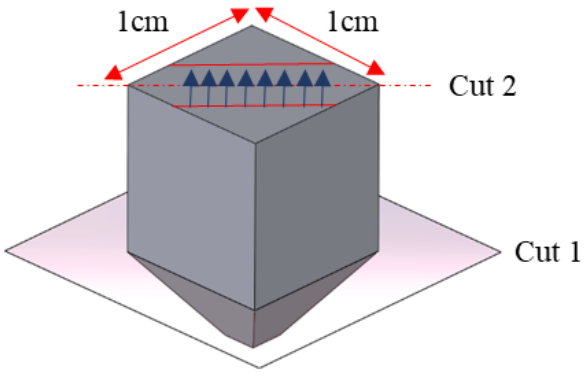

Figure 3.11. Sectioning methodology for the LPBF AB cubes.

As mentioned in Section 3.23, stitched optical microscopy using the ZEISS Smartzoom 5 was conducted on these polished samples in order to facilitate defect analysis using ImageJ, where an initial measurement coinciding with the optical microscope's scale bar is taken in order to set a scaling measurement and correlate distance to pixels. From there, an overlaid square was employed on the materials cross section to exclude the material's edges and any boundaries between the material and mounting resin as shown in Figure 3.12a. The image was then converted to a 32-bit type image and thresholded to represent the defects presiding within the material, with examples demonstrated in Figures 3.12b & c. The analysis particle function was employed with the sizing limit set to $2\mu m^2$ - ∞, with raw data being generated for statistical analysis. The data was split in order to approximately differentiate between porosity and alternative defects, with a circularity of 0.5 being considered the determinative criteria, where data with a circularity ≥ 0.5 was considered porosity and data with a circularity of < 0.5 was considered as an alternative defect. In CM247LC, the alternative defects manifested predominantly appeared to be in the form of microcracking and is therefore referred to as such. Quantitative criterion such as percentage area, feature count and average feature size were evaluated and correlated to parameter selection.

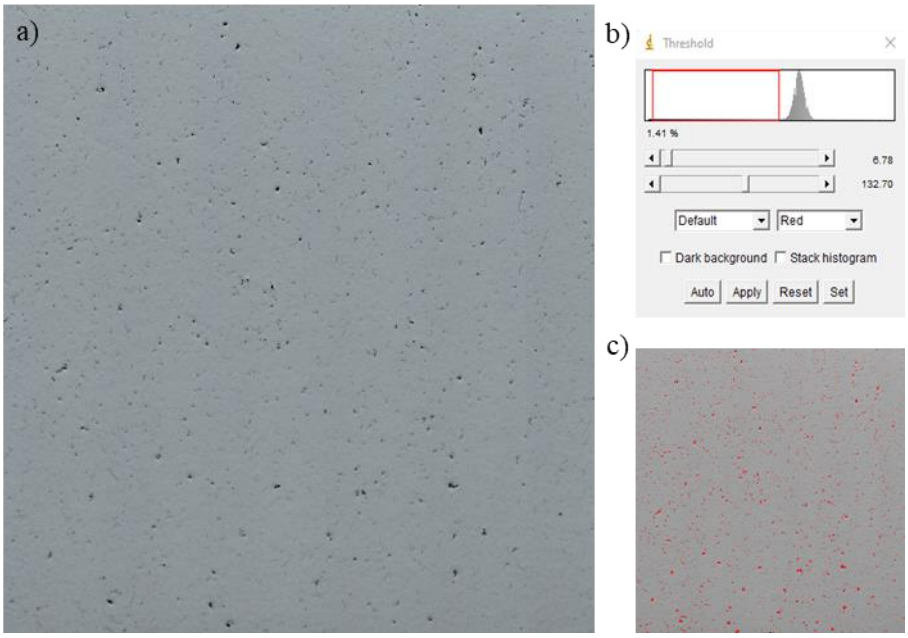

Figure 3.12. ImageJ data analysis example a) ZEISS Smartzoom 5 stitched optical micrograph of an LPBF CM247LC variant, b) thresholding setup and c) examples of threshold to reveal and represent density related issues.

The second cuts that were mounted, polished and chemically etched were utilised to quantitatively assess melt pool profiles. A series of images were taken across the top layer of the material in order to capture these melt pools for each respective variant and were analysed using ImageJ. Once again, an initial measurement was taken with the corresponding scale bar in order to set a scaling

and relate distance to pixels. From there, manual measurements for both track height and width were taken using the methodology demonstrated in Figure 3.13, where for track height, measurements were taken from the minimum point of the melt track's circumference to the surface of the material. For track width, a vertical line was considered from the minimum point of the solidified melt pool to the material's surface, and the distance from this line perpendicularly to where the melt pool's circumference intersected the material's surface was measured. This measurement was doubled with the assumption that the tracks consisted of a uniform geometry. For all variants considered in the analysis, a region of 50-70 melt track measurements for both height and width were taken, and were correlated against parameter selection.

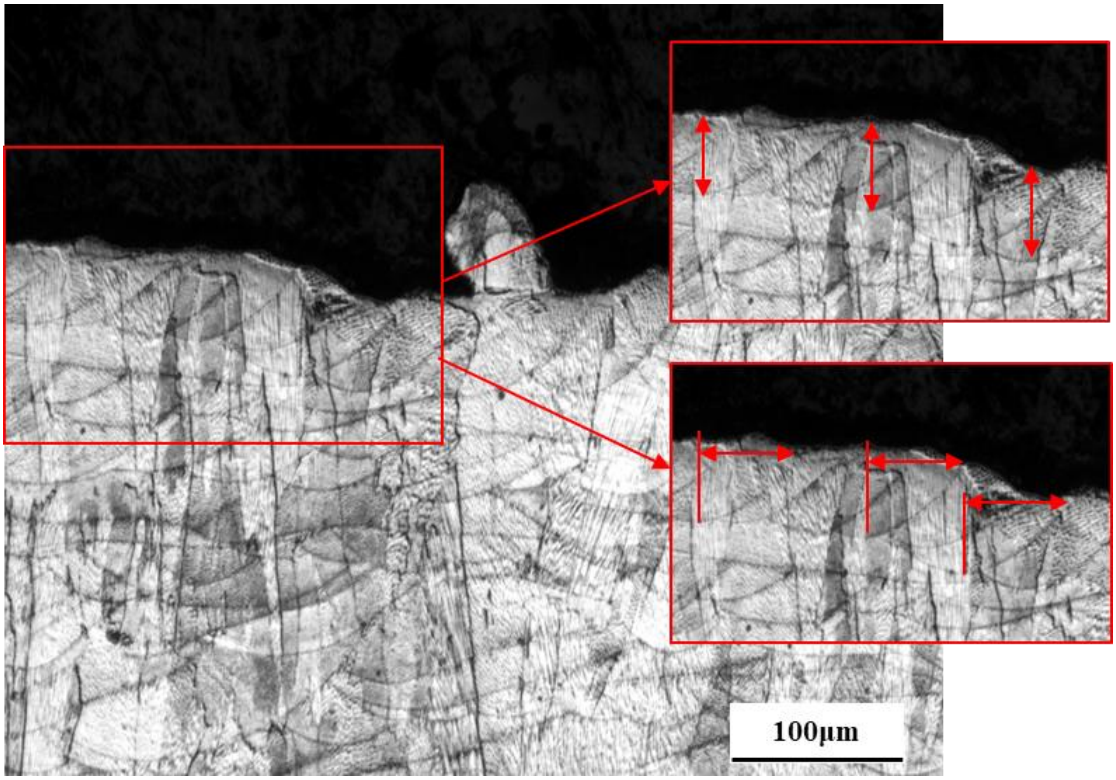

Figure 3.13. Methodology applied for measuring melt track height and width on a LPBF CM247LC variant.

The HIPed rods (Ø1.5cm, 4cm height) were provided on build plates sectioned post HIP by Rolls-Royce plc., with variants displaying varying degrees of macrocracking consequent to HIPing. Optical microscopy images were taken from a top and side view, where measurements were conducted using ImageJ for the macrocracking evident as depicted in Figure 3.14. A single measurement was taken for crack depth alongside 5 measurements for crack width which were consequently averaged, the values of which were related to parameter deposition. Post measurement, 7 parameter variants were selected for furthered analysis through SPT, as will be discussed.

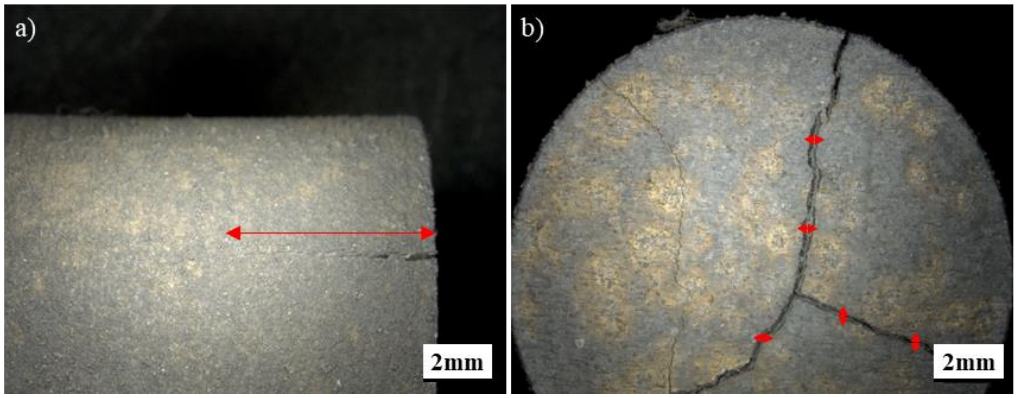

Figure 3.14. Methodology applied for measuring the apparent macrocracking in the HIPed rods, a) crack depth, b) average crack width.

7 parameter variant's rods (samples 1, 3, 5, 9, 18, 19 & 23) were selected which consisted of low, medium and high variations in normalised beam speed, beam power and energy density. These rod's diameters were turned down using a Sealey SM27 Metalworking Lathe from 15mm to 9.5mm diameters and sectioned perpendicularly to the build direction at 1.5cm off the base plate in order to sample SP specimens as shown in Figure 3.15. Several cuts were made using the Struers Secotom-10 precision cutter with an Aluminum Oxide cutting wheel in order to sample 3 SP discs, which were subsequently run through the SP specimen preparation procedures outlined in Section 3.22. The bottom two discs were used for SPT as described in Section 3.28, where the bottom disc was utilised for room temperature SPT and the middle disc for high temperature SPT. These test conditions are summarised in Table 3.10. The top disc was used for SPC testing as described in Section 3.27 with the testing conditions employed showcased in Table 3.11.

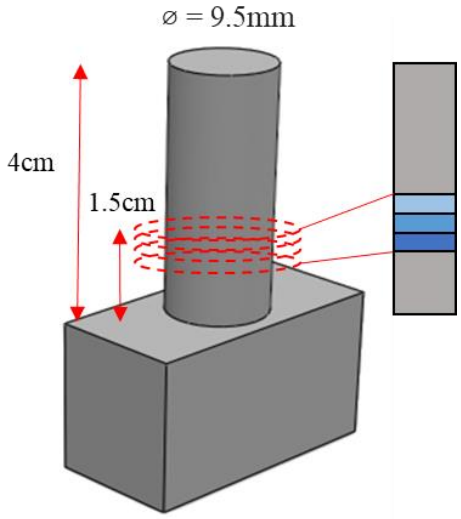

Figure 3.15. Sampling methodology for SP discs from HIPed CM247LC rods (not drawn to scale).

Table 3.10. Testing conditions employed during SPT testing.

Specimen ID	Temperature (°C)	Displacement Rate ($mm.min^{-1}$)	Comments
SPT01	RT	0.5	None.
SPT03	RT	0.5	None.
SPT05	RT	0.5	None.
SPT09	RT	0.5	None.
SPT18	RT	0.5	None.
SPT19	RT	0.5	None.
SPT23	RT	0.5	None.
SPD01	950	0.5	Cracked prematurely during circumferential clamping.
SPD03	950	0.5	None.
SPD05	950	0.5	None.
SPD09	950	0.5	None.
SPD18	950	0.5	None.
SPD19	950	0.5	None.
SPD23	950	0.5	None.

Table 3.11. Testing conditions employed during SPC testing.

Specimen ID	Temperature (°C)	Load (N)	Comments
SPC01	950	150	SP sample displayed signs of cracking pre clamping.
SPC03	950	150	None.
SPC05	950	150	None.
SPC09	950	150	None.
SPC18	950	150	None.
SPC19	950	150	None.
SPC23	950	150	None.

3.5 Small Scale Testing & Microstructural Characterisation of IN718

A series of LPBF variants of IN718 were manufactured within this section with changes in build orientation and parameter sets once again being considered. 22 thin plate architectures were manufactured in line with the original build schematic shown Figure 3.16, 6 of which were built with a 30° orientation comprising of 2 distinct parameter sets, which were repeatedly built 3 times each. It is important to note that 4 of the 30° builds shown in the original CAD schematic were discontinued consequent to fabrication issues, as highlighted in the top plane view represented in Figure 3.16b. The remaining 16 thin plate architectures were manufactured in the 90° orientation, comprising of 5 separate parameter sets, of which the first 3 consisted of changes in energy density. The remaining 2 parameter sets consisted of undisclosed 'baseline' parameter sets for IN718 and CM247LC. An overall summary of the parameter sets incorporated in this work package is represented in Table 3.12.

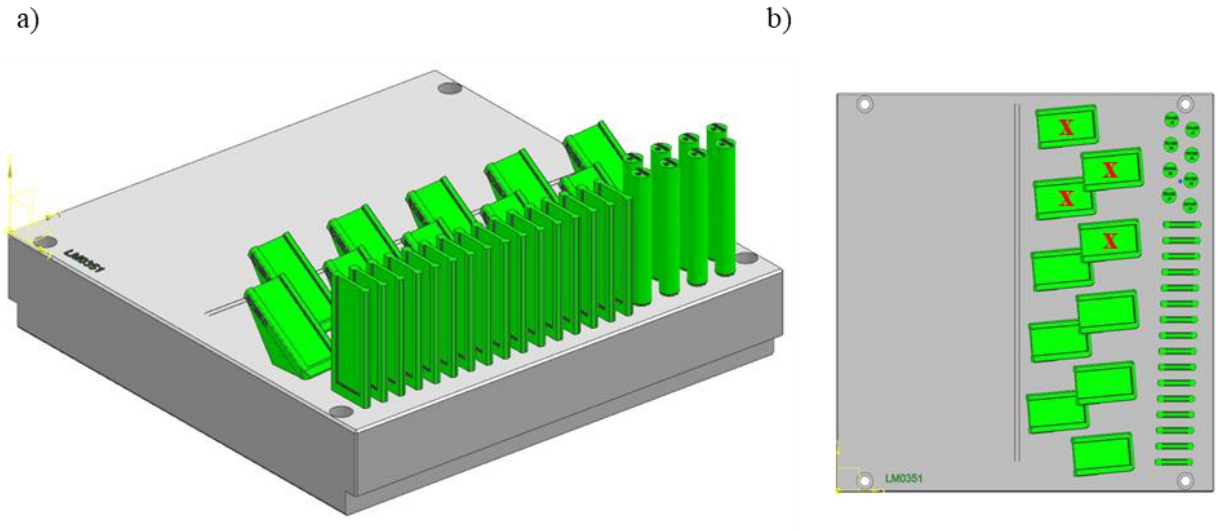

Figure 3.16. CAD schematics of thin plate architectures fabricated a) trimetric view b) top plane view with discontinued variants marked (provided by Rolls-Royce plc.).

Table 3.12. Parameter set summary with regards to equivalent energy density.

Parameter Set	E*	Number of Builds
1	Medium	2
2	High	4
3	Low	4
IN718 'Baseline'	Undisclosed.	3
CM247LC 'Baseline'	Undisclosed.	3

Once received, the thin plate architectures were removed from the build plate and two Ø9.5mm discs were extracted from each plate as represented in Figure 3.17 using EDM. Both specimens for each variant were prepared using the metallurgical procedures for SP disc preparation as outlined in Section 3.22, where they were ground from a thickness of 2.4mm to 0.5mm ± 0.005mm in accordance with the tolerances dictated by ASTM E3205-20 [131]. The top discs sectioned from each variant were subject to SPC testing, the procedures of which were detailed in Section 3.27 and the testing conditions employed shown in Table 3.13. The bottom discs were subject to high temperature SPT testing, the procedures for which are described in Section 3.28 and the testing conditions applied showcased in Table 3.14.

Post-test completion, the fractured specimens were cleaned using an ultrasonic bath and imaged using SEM for fractography analysis. Following fractography, they were mounted upside down with the circumferentially clamped region of material exposed for hot mounting. These samples were mounted in a conductive phenolic mounting resin and subject to the metallographic grinding, polishing and etching procedures designated to IN718 indicated in Section 3.21. They were subsequently characterised using electron microscopy, EDS and EBSD.

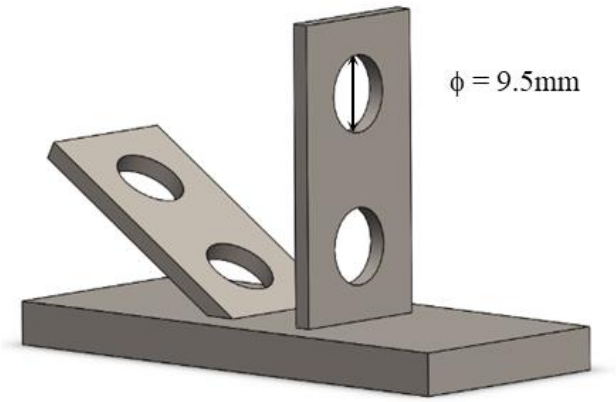

Figure 3.17. Sampling of SP specimens from LPBF IN718 thin plate architectures.

Table 3.13. Testing conditions employed during SPC testing of LPBF IN718 variants.

Specimen ID	Temperature (°C)	Load (N)	Comments
30°, Parameter Set 1, Build 1	650	500	Void Test
30°, Parameter Set 1, Build 2	650	500	Void Test
30°, Parameter Set 1, Build 3	650	500	None.
30°, Parameter Set 3, Build 1	650	500	None.
30°, Parameter Set 3, Build 2	650	500	None.
30°, Parameter Set 3, Build 3	650	500	None.
90°, Parameter Set 1, Build 1	650	500	None.
90°, Parameter Set 1, Build 2	650	500	None.
90°, Parameter Set 2, Build 1	650	500	None.
90°, Parameter Set 2, Build 2	650	500	None.
90°, Parameter Set 2, Build 3	650	500	None.
90°, Parameter Set 2, Build 4	650	500	None.
90°, Parameter Set 3, Build 1	650	500	None.
90°, Parameter Set 3, Build 2	650	500	None.
90°, Parameter Set 3, Build 3	650	500	None.
90°, Parameter Set 3, Build 4	650	500	None.
90°, IN718 Baseline, Build 1	650	500	None.
90°, IN718 Baseline, Build 2	650	500	None.
90°, IN718 Baseline, Build 3	650	500	None.
90°, CM247LC Baseline, Build 1	650	500	None.
90°, CM247LC Baseline, Build 2	650	500	None.
90°, CM247LC Baseline, Build 3	650	500	None.

Table 3.14. Testing conditions employed during SPT testing of LPBF IN718 variants.

Specimen ID	Temperature (°C)	Displacement Rate ($mm.min^{-1}$)	Comments
30°, Parameter Set 1, Build 1	650	0.5	None.
30°, Parameter Set 1, Build 2	650	0.5	None.
30°, Parameter Set 1, Build 3	650	0.5	None.
30°, Parameter Set 3, Build 1	650	0.5	None.
30°, Parameter Set 3, Build 2	650	0.5	None.
30°, Parameter Set 3, Build 3	650	0.5	None.
90°, Parameter Set 1, Build 1	650	0.5	None.
90°, Parameter Set 1, Build 2	650	0.5	Void Test.
90°, Parameter Set 2, Build 1	650	0.5	None.
90°, Parameter Set 2, Build 2	650	0.5	None.
90°, Parameter Set 2, Build 3	650	0.5	None.
90°, Parameter Set 2, Build 4	650	0.5	None.
90°, Parameter Set 3, Build 1	650	0.5	None.
90°, Parameter Set 3, Build 2	650	0.5	None.
90°, Parameter Set 3, Build 3	650	0.5	None.
90°, Parameter Set 3, Build 4	650	0.5	None.
90°, IN718 Baseline, Build 1	650	0.5	None.
90°, IN718 Baseline, Build 2	650	0.5	Void Test.
90°, IN718 Baseline, Build 3	650	0.5	Void Test.
90°, CM247LC Baseline, Build 1	650	0.5	None.
90°, CM247LC Baseline, Build 2	650	0.5	None.
90°, CM247LC Baseline, Build 3	650	0.5	None.

3.6 Melt Track and Defect Analysis in IN718

In this work package, a build comprising of 24 LPBF variants of CM247LC were fabricated in the form of cubes with an upside pyramid support structure as shown in the CAD schematics presented in Figure 3.18. These variants comprised of the same changes in linearly normalised beam speed, power and energy density employed in Section 3.4, with an overall summary shown in Table 3.15. These cubes were removed from the build plate using a hammer and chisel at the base of the support plate and sectioned in the same manner as depicted in Figure 3.11, where one cut was made perpendicular to the pyramid support structure for defect analysis and the other perpendicular to the scanning lines for melt track profiling. These cuts were made using the Struers Secotom-10 precision cutter with an Aluminum Oxide cutting wheel.

Table 3.15. Linearly normalised parameter sets employed within this DOE.

Sample ID	Speed	Hatch Spacing	Power	E*
1	0.51	2	1	0.98
2	0.51	2	1	0.98
3	0.40	2	1	1.25
4	0.40	2	1	1.25
5	0.31	2	1	1.61
6	0.31	2	1	1.61
7	0.65	2	2	1.54
8	0.65	2	2	1.54
9	0.51	2	2	1.96
10	0.51	2	2	1.96
11	0.41	2	2	2.44
12	0.41	2	2	2.44
13	0.83	2	3	1.81
14	0.83	2	3	1.81
15	0.65	2	3	2.31
16	0.65	2	3	2.31
17	0.52	2	3	2.88
18	0.52	2	3	2.88
19	1.00	2	4	2.00
20	1.00	2	4	2.00
21	0.81	2	4	2.47
22	0.81	2	4	2.47
23	0.63	2	4	3.17
24	0.63	2	4	3.17

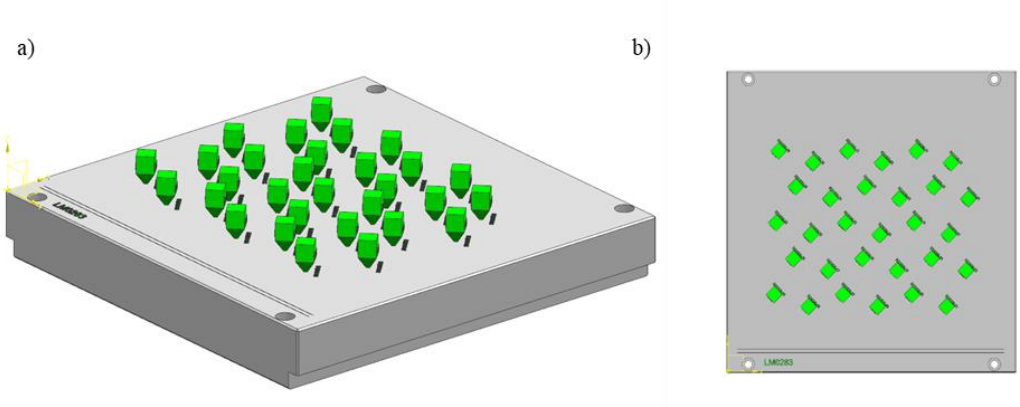

Figure 3.18. CAD schematics of cubes fabricated a) trimetric view and b) top plane view (provided by Rolls-Royce plc.).

The two sectioned regions of material were hot mounted using a conductive phenolic resin and ran through the series of metallurgical grinding and polishing procedures for IN718 outlined in Section 3.21. It is important to note that the cut intended for defect analysis was subjected to a repolish post chemical etching using step 4 as mentioned previously. Stitched optical microscopy using the ZEISS Axio Observer was employed at 200x magnification for the same ImageJ analysis employed previously. An initial measurement was taken corresponding with the scale bar present in order to relate distance measurements to pixels. From there, an overlaid square was applied to the region of interest, removing the edges and boundaries of the sample. The image was converted to a 32-bit type image to heighten contrast and the disparities in material discontinues to bulk material, where the image was thresholded to approximate and represent the density related features presiding. Post thresholding, the analyse particle function was employed with a sizing limit of $2\mu m^2$ - ∞, with raw data once again being generated and split to distinguish between porosity and other defects. All defects with a circularity $\geq$ 0.5 was considered porosity and < 0.5 other defects. In IN718, the other defects apparent seemed to be predominantly in the form of lack of fusion related features and as such are often referred to as lack of fusion related defects. An example of the overall ImageJ analysis setup for the Zeiss Axio Observer stitched imaging is shown in Figure 3.19. Numerical criterion such as percentage area, feature count and average feature size were once again considered and correlated to parameter deposition within this DOE.

For the second cuts, a collection of images was taken across the top layer of each variant. These images were analysed using ImageJ, where scaling was once again set to correlate distance measurements to pixel count. Manual melt track measurements were taken for both height and width across the collection of images with the same methodology previously utilised in section 3.4 as illustrated in Figure 3.20. Melt track height measurements were taken from the minimum point within the melt pool to the surface of the material, whereas half width measurements were taken perpendicularly from a vertical line corresponding with the minimum point of the material to where the

melt pool's circumference intersects the materials surface. These values were doubled to correspond to track width on the assumption that the melt pool's profiles were uniform. For all variants within this work package, a minimum of 50 melt track measurements were taken, which were subsequently correlated against the parameter selection employed within this DOE.

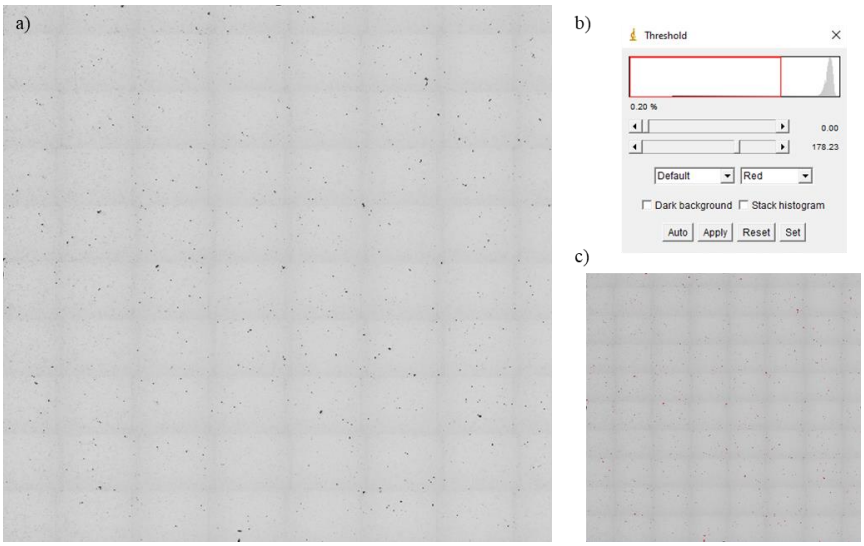

Figure 3.19. ImageJ data analysis example a) Zeiss Axio Observer stitched optical micrograph of a LPBF IN718 variant, b) thresholding setup and c) resulting thresholding contrast.

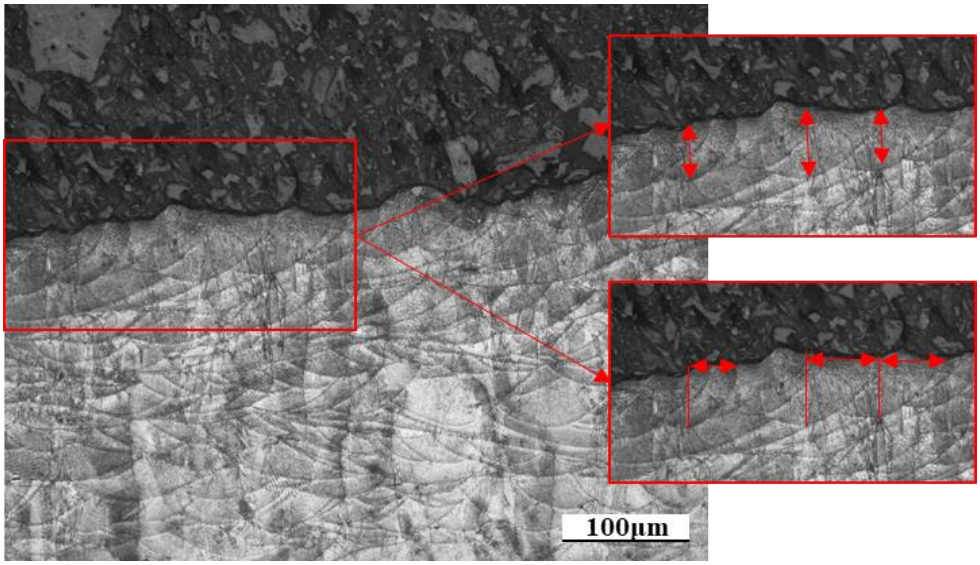

Figure 3.20. Methodology applied for measuring melt track height and width on a LPBF IN718 variant.

The following chapters will present the experimental findings and detailed results for each respective work package outlined in this chapter.

Chapter 4 – Small Scale Testing & Microstructural Characterisation of CM247LC

4.1 The Influence of Build Orientation on Small Punch Creep Performance

A series of SP creep results were amassed across multiple LPBF CM247LC variants with differing build orientations and parameter sets. The initial outlook was to ascertain the impact that build orientation exhibited on the material's resistance to high temperature mechanical deformation mechanisms such as creep. As illustrated in Figure 4.1 and Table 4.1, it was apparent that build orientation plays a significant role on creep deformation, with the 30° build orientation variants experiencing rupture considerably sooner (1.8 - 3.3 hours) than that of the 90° build orientations (21.5 - 59.2 hours). The explanatory reasons for these differences in behaviour become evident when examining the microstructure as shown in Figure 4.2, where the intrinsic epitaxial nature of ALM as previously discussed in Section 2.3.4 is further highlighted. Given the sectioning methodology, 30° build orientations consist of an equiaxed microstructure contrasting that of the columnar grain structure observed in 90° build orientations. Grain size measurements were conducted using EBSD grain mapping as displayed in Table 4.2, where both the average grain sizes and number of grains analysed highlight the fine to coarse grained extremities for each of the two orientations. As such, 30° build orientations inherently exhibit a higher volume fraction of grain boundaries and given creep deformation is a grain boundary initiated and dominated mechanism, is subject to substantially higher minimum displacement rates (0.135 – 0.214mm.hr^{-1}) than that of the 90° builds (0.019 – 0.045mm.hr^{-1}).

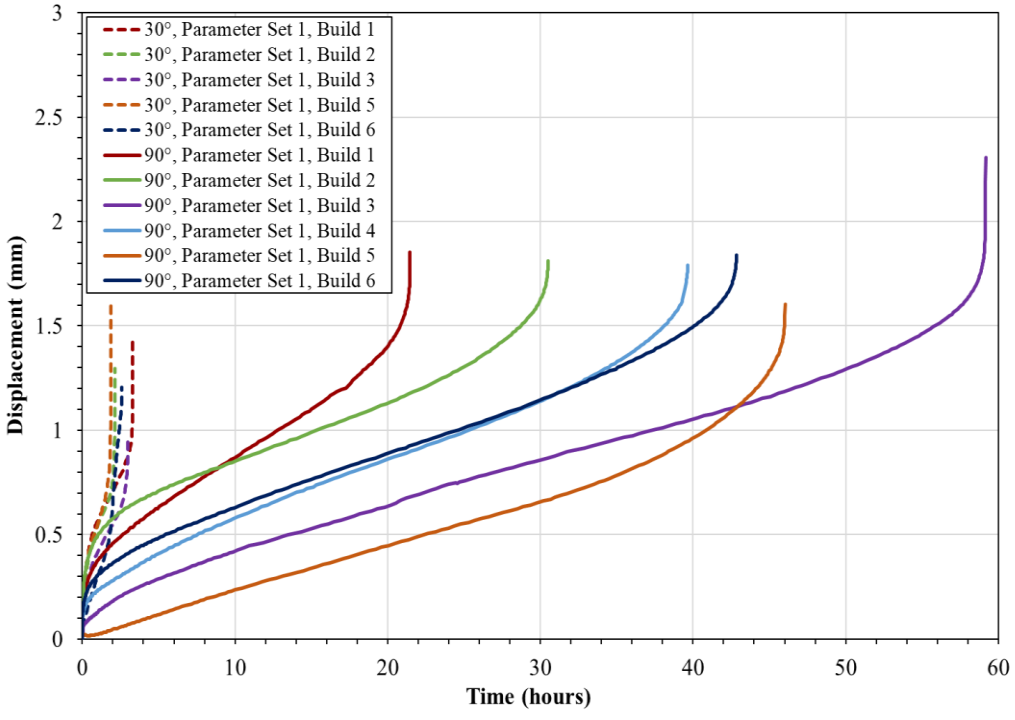

Figure 4.1. SPC results of 30° and 90° LPBF builds for Parameter Set 1 at 950°C, 150N load.

Table 4.1. Time to Rupture and Minimum Displacement Rate data for SPC tests conducted on 30° and 90° LPBF builds for Parameter Set 1.

Sample	Time to Rupture [Hours]	MDR [mm.hr^{-1}]
90°, Parameter Set 1, Build 1	21.5	0.045
90°, Parameter Set 1, Build 2	30.5	0.027
90°, Parameter Set 1, Build 3	59.2	0.019
90°, Parameter Set 1, Build 4	39.7	0.026
90°, Parameter Set 1, Build 5	46.0	0.020
90°, Parameter Set 1, Build 6	42.8	0.024
30°, Parameter Set 1, Build 1	3.3	0.135
30°, Parameter Set 1, Build 2	2.2	0.169
30°, Parameter Set 1, Build 3	3.0	0.128
30°, Parameter Set 1, Build 4	-	-
30°, Parameter Set 1, Build 5	1.8	0.199
30°, Parameter Set 1, Build 6	2.6	0.214

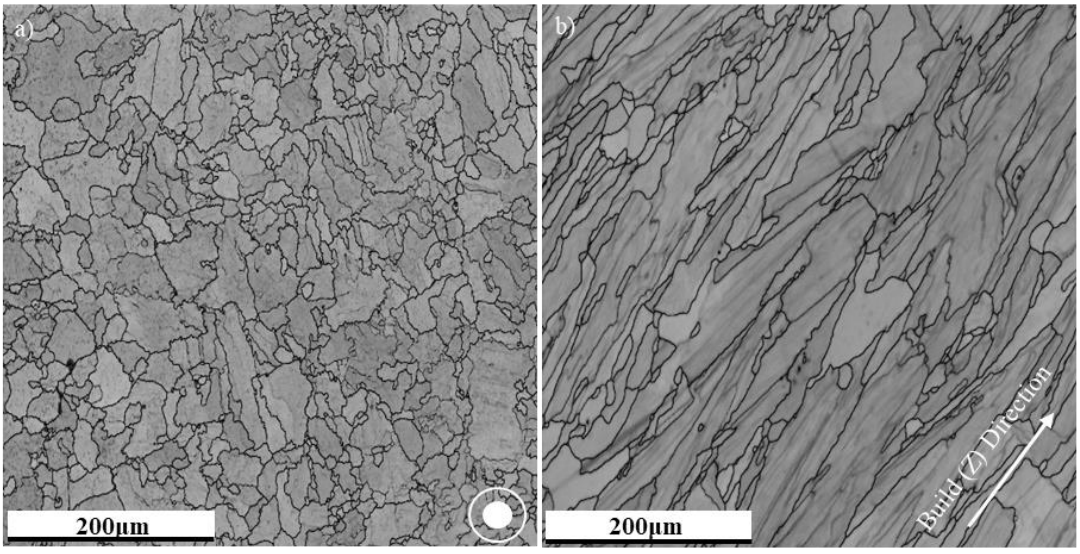

Figure 4.2. EBSD grain mapping using the elliptical fit method for a) 30°, Parameter Set 1, Build 1 and b) 90°, Parameter Set 1, Build 1.

Table 4.2. Grain size measurements calculated from EBSD grain mapping of CM247LC variants.

Sample	Average Grain Area (μm^2)	Average Grain Aspect Ratio	Average Grain Diameter (μm)	Grain Count
30^o, Parameter Set 1, Build 1	313.09	1.90	10.31	615
90^o, Parameter Set 1, Build 1	660.36	3.08	14.64	290

Despite the 30^o build orientations performing extensively worse than the 90^o build orientations, there appears to be a degree of variability for the 90^o variants across builds 1-6. From a general microstructural perspective, the epitaxial grain growth mechanisms previously mentioned are consistently observed regardless of the build iteration as exemplified below in Figure 4.3. One explanation for this degree of variation is their inherent failure mechanisms. Given the evident equiaxed grain structures observed in the 30^o build orientations, their geometric nature gives rise to 'triple point' or 'wedge' cracking as shown in Figure 4.4. These 'triple point' cracks are located at intergranular locations and can coalesce with similar intergranular cavities and features to act as a dominant catastrophic failure mechanism and thus explaining the consistency of poor performances with the little variability aforementioned. The 90^o builds comparatively display grain boundary cohesion with little presence of material density related issues as illustrated in Figure 4.5 and as such the existence of catastrophic failure mechanisms is considerably less frequent. Consequently, the degree of variation in lifetimes witnessed in these 90^o build orientations is likely to be attributed to the discrete localised testing nature of SP, where phenomena such as elastic heterogeneity arises. Given the small volume of material subjected to testing within SP, a localised region of material is subjected to testing and therefore may not give an accurate representation of the variant's bulk properties.

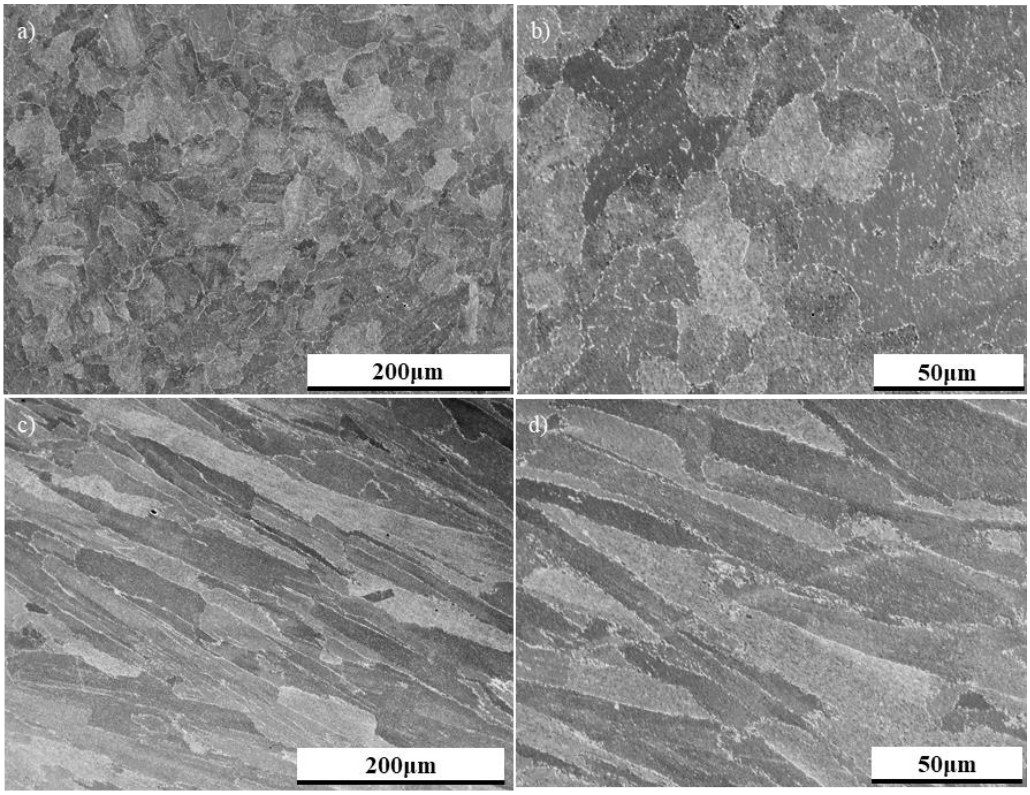

Figure 4.3. 30°, Parameter Set 1, Build 6's general microstructural observations displayed at a) low magnification b) higher magnification and 90°, Parameter Set 1, Build 6's general microstructural observations observed at c) low magnification d) higher magnification.

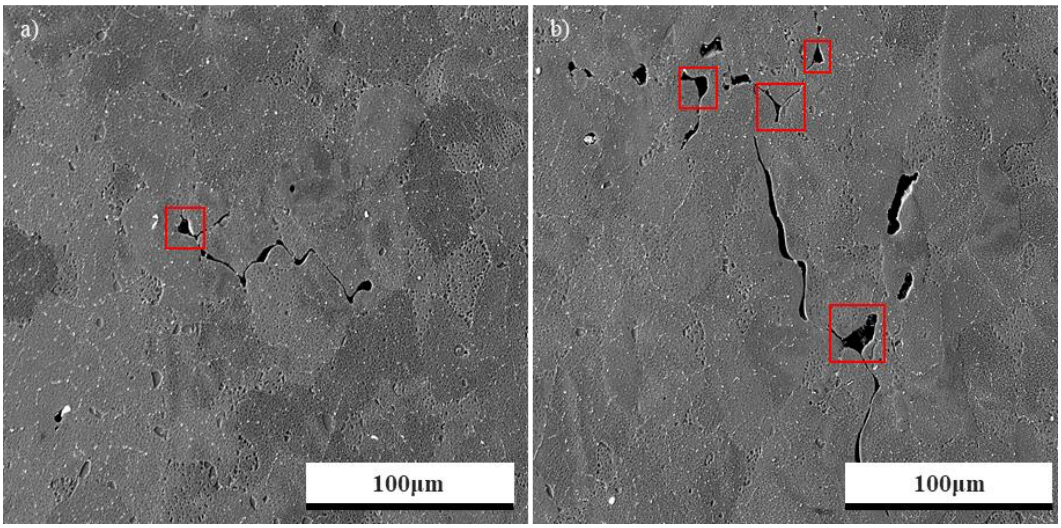

Figure 4.4. Triple point cracking and propagation within various 30° builds.

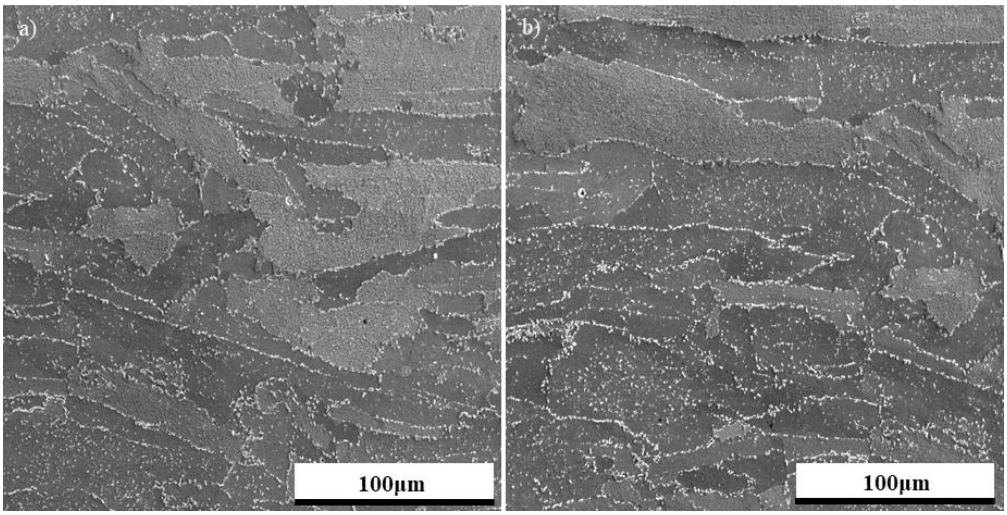

Figure 4.5. Grain boundary cohesion and material density witnessed in 90° builds.

In addition to the microstructural characterisation work carried out, fractographic analysis was conducted on all builds in order to help gauge an understanding as to the associated failure mechanisms discussed. It can be seen in Figures 4.6a & d, that the 30° build orientations rupture in a considerably more brittle manner to that of the 90° build orientations as seen with the emergence of 'starfish' radial cracking, where primary cracks emanate from the centre of the disc. This reflects the lack of ductility in the material, as the maximum principal stress remains in the central location of the disc, directly beneath the point at which the indenter is imparted. In a more ductile material, this stress would dissipate from this region according to the membrane stretching theory first proposed by Chakrabarty [150] and relates to the Von-Mises stress as failure, which would initiate from a location around the periphery of the punch head. Figures 4.6b & e highlight the prominence of intergranular cracking in relation to the directionality of grain growth within the disc, where it is self-evident that columnar grains align perpendicularly to the disc's surface in the 30° orientation and parallel to the disc's surface in the 90° orientation. Figures 4.6c & f further emphasise the intergranular manner of failure and showcases the existence of dimpled fracture surfaces, indicating that the fracture mechanisms observed are related to high temperature creep damage. The prevalence of features such as embrittled failures, intergranular cracking and dimpling is consistently seen regardless of the build iteration as shown in Figures 4.7 & 4.8. It can also be observed that in the instances of 30° orientations, the severity of embrittlement can in some cases lead to the fracture of deformed ligaments within the imaging process as shown in Figures 4.7a, b & d, giving a further insight into the materials lack of ductility. The only inconsistency noticed across the build iterations can be seen in Figure 4.8g, where the fracture surface appears to be covered with unusual features, as will be discussed later.

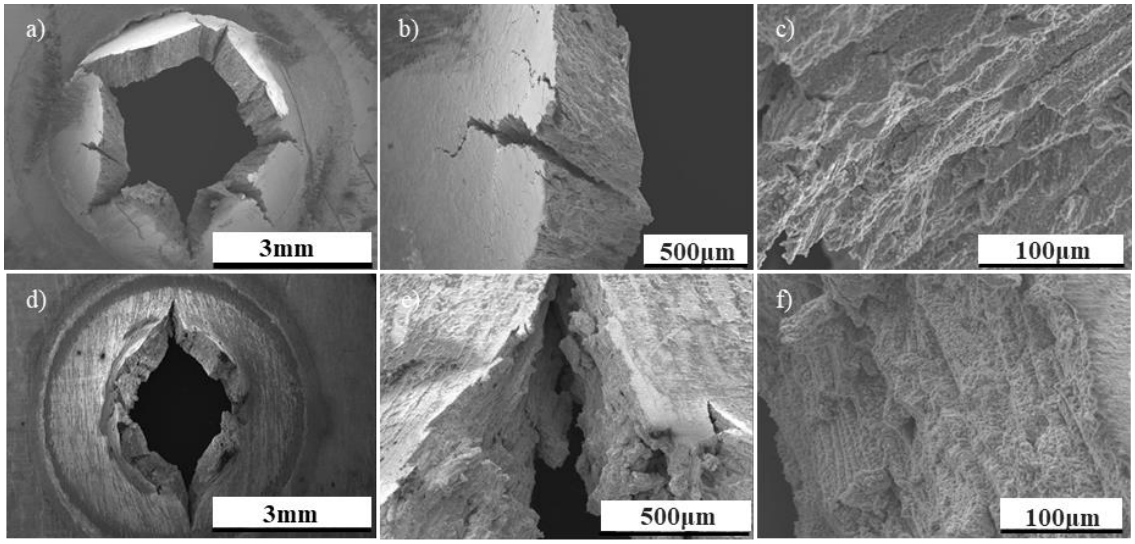

Figure 4.6. Low, medium and high magnification fractography for a) b) c) 30°, Parameter Set 1, Build 1 and d) e) f) 90°, Parameter Set 1, Build 1.

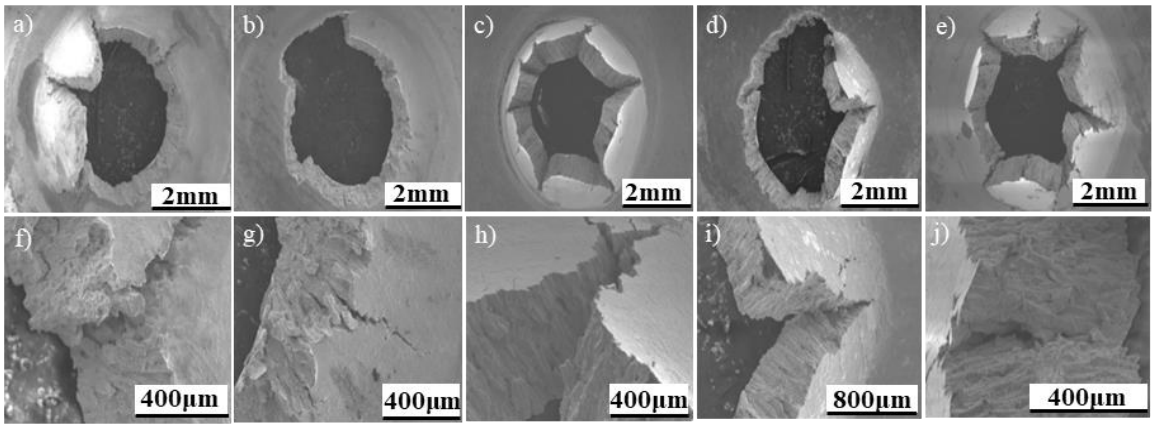

Figure 4.7. 30º, Parameter Set 1, a) f) Build 2, b) g) Build 3, c) h) Build 4, d) i) Build 5 and e) j) Build 6.

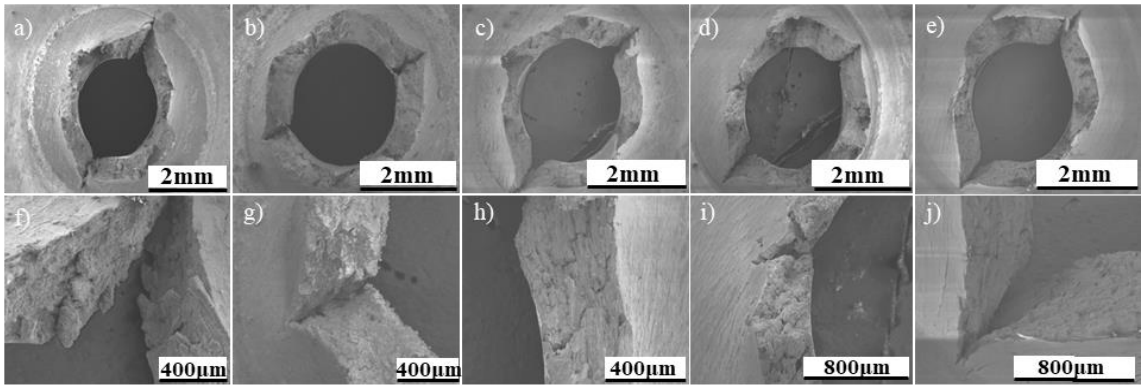

Figure 4.8. 90º, Parameter Set 1, a) f) Build 2, b) g) Build 3, c) h) Build 4, d) i) Build 5 and e) j) Build 6.

As discussed, the 90° builds display a greater range of performance in comparison to the 30° builds and considering elastic heterogeneity was proposed as the primary attributing mechanism, a furthered microstructural understanding is required. Figure 4.9 compares and contrasts both the fractographic and microstructural features observed in 90°, parameter set 1, build 1 and build 3; i.e. the worst and best performing samples. The dissimilar fracture surfaces can be seen in Figures 4.9a and e, where there appears to be the presence of nickel oxides within build 3. This is unveiled in greater detail in Figure 4.10, where its blocky structure can be observed, and its chemical composition validated through EDS analysis as shown in Figure 4.11. This is likely to be consequent to the premature loss of argon during the post-test cool down period discussed in Section 3.3, where the initiation of an oxidation type mechanisms has occurred. Nevertheless, when further evaluated at lower magnifications, there does not seem to be any drastic or noticeable microstructural changes as depicted in Figures 4.9b & d. However, higher magnification imaging does appear to reveal some subtle intrinsic microstructural details such as the existence of grain boundary cavitation in build 1 as shown in Figure 4.9c, which can only further exacerbate the disparities in mechanical performance. The cause of this grain boundary cavitation will be discussed later in greater detail. Figure 4.9g does show the existence of gas entrapped porosity in build 3, however given it is situated within a conglomerate of gamma prime, it is unlikely to impact creep resistance.

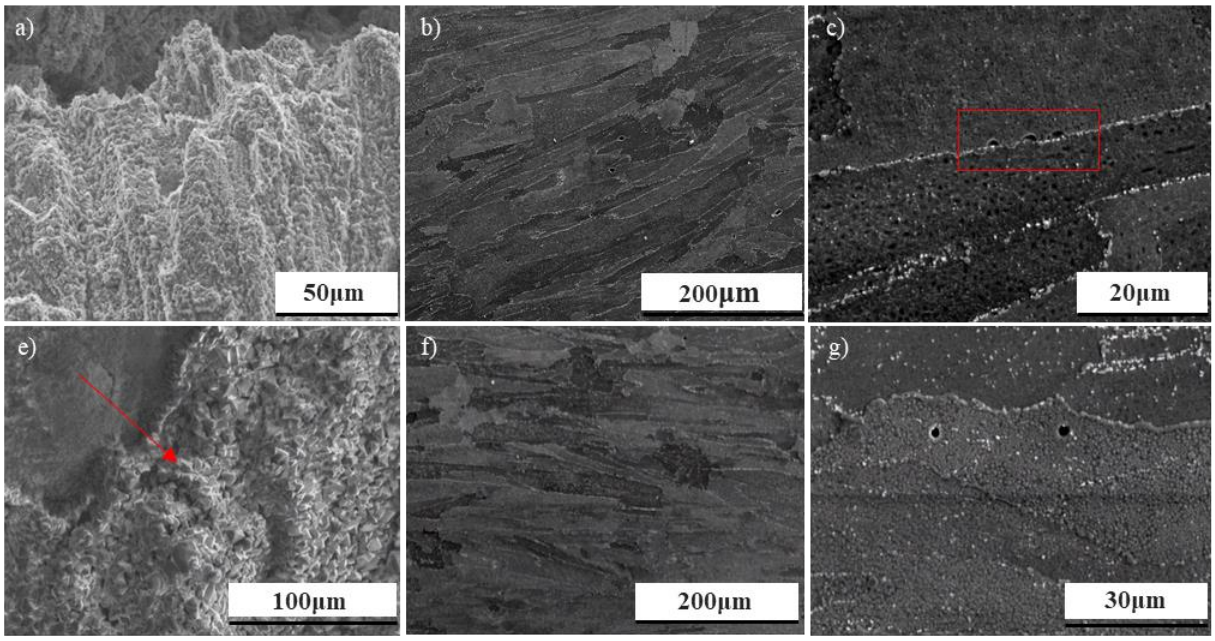

Figure 4.9. Fractographic and microstructural examinations of 90°, Parameter Set 1, Build 1 a) fracture surface b) low magnification microstructure c) higher magnification microstructure and Build 3 e) fracture surface f) low magnification microstructure g) higher magnification microstructure.

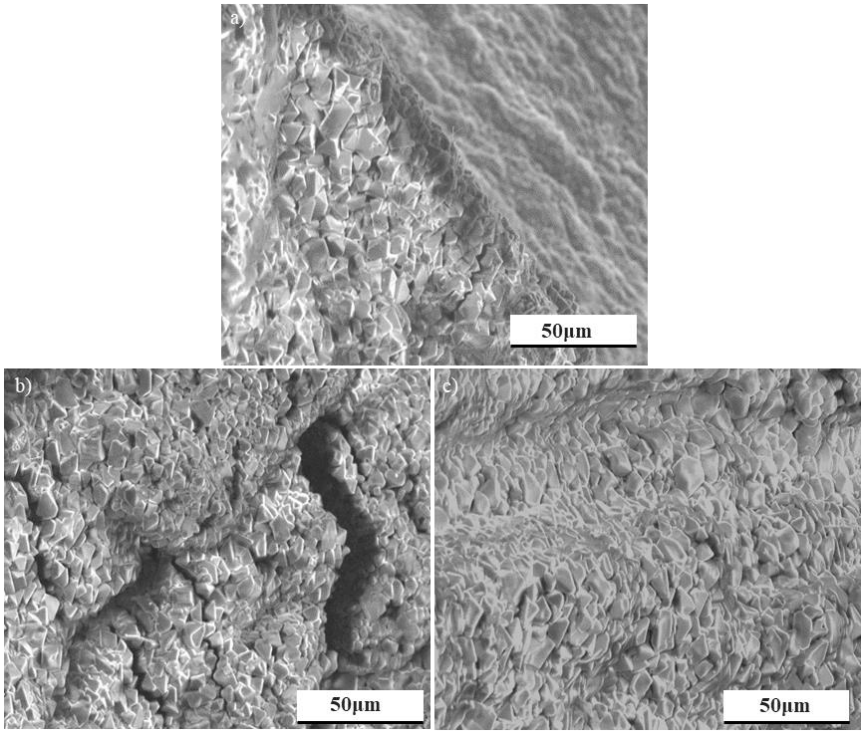

Figure 4.10. Nickel oxides exhibited on 90°, parameter set 1, build 3s fracture surface.

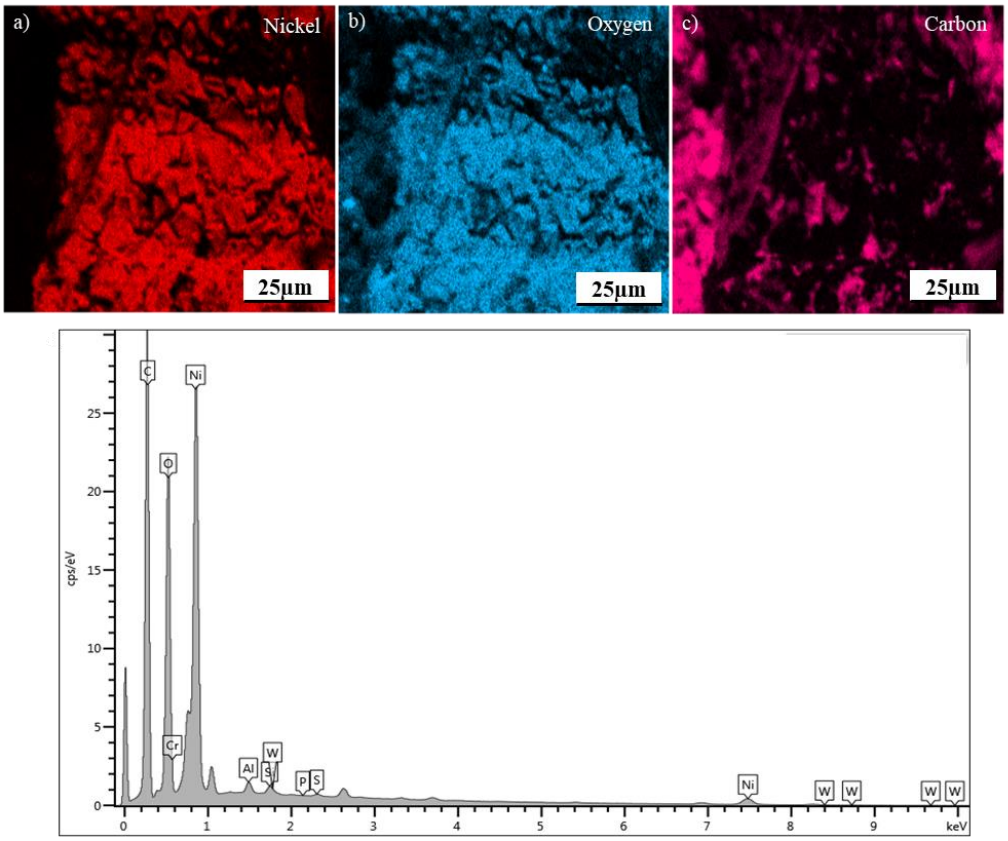

Figure 4.11. EDS analysis of the fracture surface of 90°, Parameter Set 1, Build 3 a) nickel, b) oxygen, c) carbon and d) EDS spectrum map.

In addition to general microscopy, EBSD analysis was also conducted on both build 1 and 3 as an alternate avenue in order to ascertain if there were any other underlying microstructural mechanisms that could not be revealed using standard microscopy techniques. Figures 4.12a & d showcase IPF Z maps with respect to arbitrary referencing points, giving an indication as to the macro textural behaviour within the material. It can be seen in both build 1 and 3 that there does not appear to be any discernible differences in textural development, where both microstructures appear to display a relatively uniform isotropic texture, with indications as to the initiation of texture being formed, as will be discussed later, comparative to alternate energy variants. Given the insignificant discrepancies between the two variants, it is reasonable to disregard its influence on the disparity in performance observed. Furthermore, localised average misorientation (LAM) mapping is represented in Figures 4.12b & e, where consistent characteristics are once again observed, particularly with respect to the presence of strain which appears to subside within grains in a linear fashion. There does appear to be a minor existence of strain accumulation along grain boundaries in build 3, for reasons which will also be explored with respect to changes in energy deposition. Figures 4.12c & d present recrystallisation fraction (RF) mapping, which to no surprise highlights similar behaviour with regards to the presence of substructure comparative to recrystallised material. This is to be expected given the existential relationship between recrystallisation and cooling rates, which are known to be significantly influenced by energy deposition [80] [170] and in this case, consistent given the same energy density being deployed.

Schmid factor mapping was utilised as shown in Figure 4.13a & c, displaying the preferentiality of grains to the available slip systems in polycrystalline nickel-based superalloys ⟨110⟩ {111}. There appeared to be the coexistence of soft and hard grains in both variants, the majority of which neared a Schmid factor of 0.4, which is highly likely to slip under loading conditions and be accommodating to deformation mechanisms. Grain boundary angle (GBA) mapping is presented in Figures 4.13b & d, highlighting the consistently heightened existence of high angle grain boundaries (HAGB), which once more coincides with the lack of textural development shown previous. The overall mechanisms discussed will be examined further relative to changes in parameter deposition in the next section, providing context as to their influence on mechanical performance. These observations however highlight extremely similar characteristics that were observed between build 1 and build 3, subsequent to the similar processing conditions being employed. This provides further credence that the disparity in mechanical performance was driven by the presence of defects, elastic heterogeneity and natural statistical variation rather than significant microstructural changes.

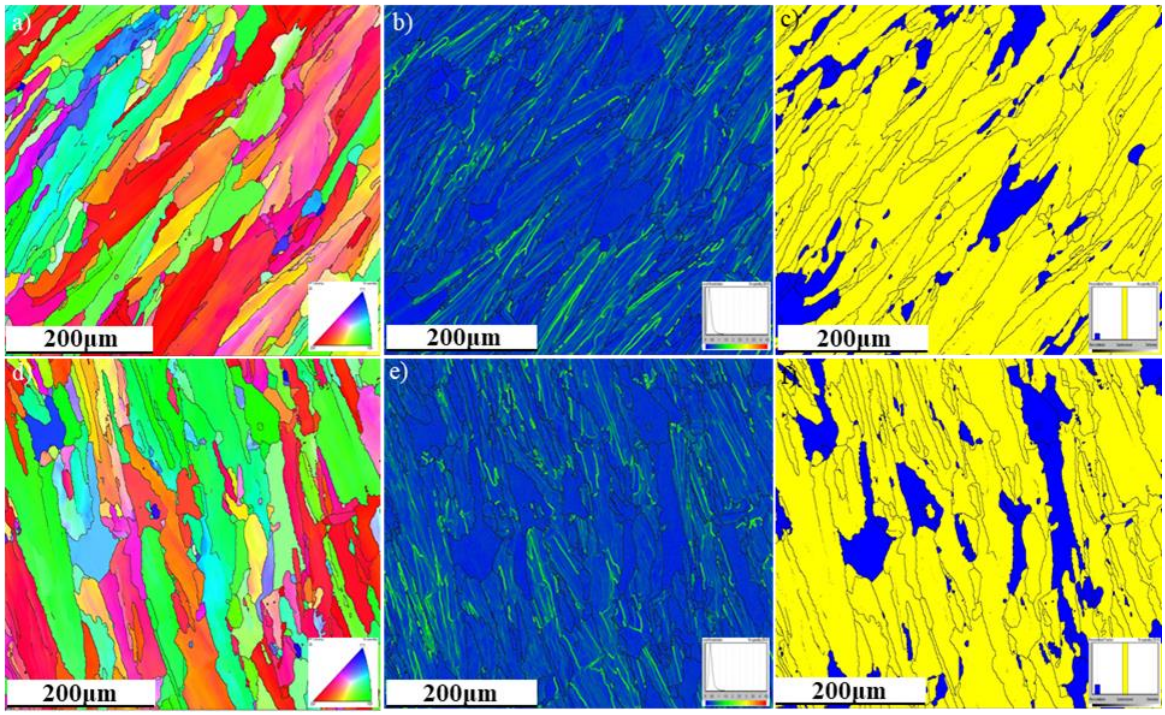

Figure 4.12. 90°, Parameter Set 1, Build 1 a) IPF Z b) LAM c) RF mapping and 90°, Parameter Set 1, Build 3 d) IPF Z e) LAM f) RF mapping.

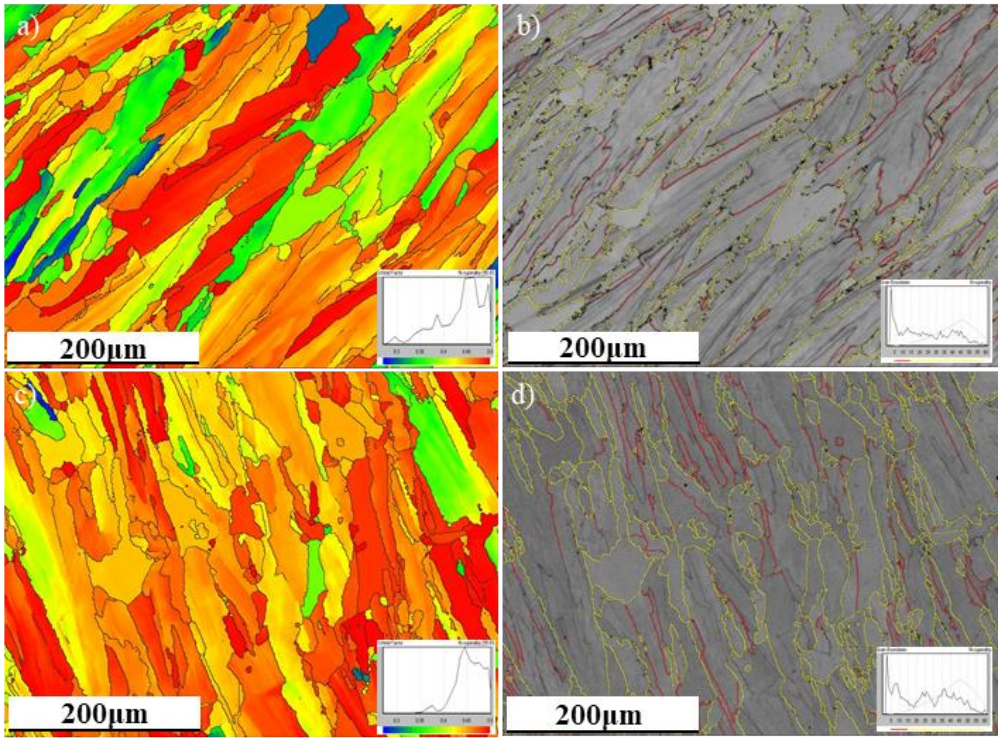

Figure 4.13. 90°, Parameter Set 1, Build 1 a) Schmid Factor b) GBA mapping and 90°, Parameter Set 1, Build 3 c) Schmid Factor d) GBA mapping.

A Monkman-Grant relationship was employed as shown in Figure 4.14, comparing time to rupture to the relative minimum displacement rate across all of the LPBF CM247LC variants tested. This included variations in both parameter set and post processing treatments, which will be discussed later in greater depth. It is evident that build orientation acts as the overriding dominant process variable despite the changes in parameter set and post processing route undertaken, given its substantial implications on the grain structure and morphology present. Despite this, a further understanding of alternate process variables is required in order to further refine and optimise the process within preferential build orientations.

The following section, however, will look at the influence of process parameter sets from within the normalised process window discussed in Section 3.3, which primarily focuses on changes incorporated with regards to energy density and hatch spacing. Considering that SP discs have a thickness of 500µm ± 0.005µm, the influence of epitaxial grain growth in 30° build orientations is somewhat restricted and as such there is an emphasis on the microstructural evaluation of 90° build orientations given their larger discrepancy in performances.

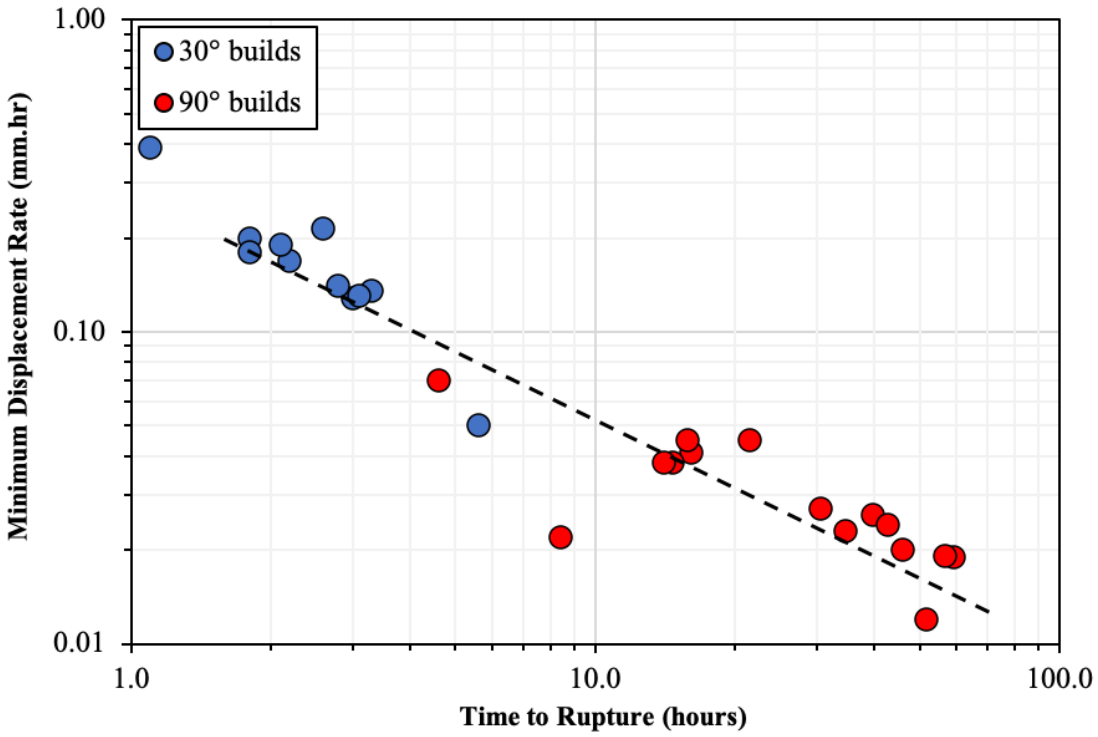

Figure 4.14. Monkman-Grant Relationships for all LPBF CM247LC builds SPC tested at 950°C, 150N.

4.2 The Influence of Parameter Selection on Small Punch Creep Performance

SPC tests were conducted on LPBF variants of differing parameter sets from different locations within the normalised process window, with variations in normalised energy density and normalised hatch spacing being considered. These results are displayed in Figure 4.15 and Table 4.3, where regardless of the parameter sets employed, the consistently poor performance for 30º build orientations (1.1 – 2.8 hours) continued to transpire given the dominant mechanisms previously reviewed. The same cannot be said for the 90º build orientations, where despite the similar range of performances (16.1 – 56.9 hours) in comparison to the previously discussed build iterations of parameter set 1 (21.5 - 59.2 hours), there appeared to be drastically different microstructural mechanisms that emerged consequent to these parameter-based changes; most of which appeared to manifest themselves predominately in the form of defects. A general microstructural overview of this is represented in Figure 4.16, where microstructures consequent to their parameter sets are displayed in relation to their position within the normalised process map.

It appeared that there was a direct correlation between energy input and resistance to creep deformation, with the lowest energy parameter set displaying the greatest resistance to creep deformation (56.9 hours) and the highest energy parameter set showcasing the worst (16.1 hours). This can be attributed to the microstructural phenomena observed, where parameter set 3 (low E*) appeared to achieve a highly dense material with no noticeable existence of defects or material abnormalities as shown in Figure 4.16d. As energy increases towards the mid-range (parameter set 1), the emergence of grain boundary cavitation occurs as highlighted in Figure 4.16c, which can act as a stress raiser or crack initiation point and thus marked a decreased time to rupture (30.5 hours). As energy continued to increase towards the higher end of the process window as represented in parameter set 2, the tendency for intergranular cracking arises as shown in Figure 4.16b. These features were frequently observed with further cases being displayed in Figure 4.17. This is likely to be as of consequence to both cavitation coalescence and residual stressing mechanisms, where higher energies are likely to give rise to larger divergences in thermal expansion coefficients as will be interpreted through alternative techniques. The heightened prominence of cracking appears to be consistent with the literature previously discussed in Section 2.3.2 from Carter et al [91] [106]. Furthermore, Figures 4.16a & e display the general microstructural observations for both low and high normalised hatch spacing for equivalent energy densities in respect to parameter set 1. It can be seen in Figure 4.15 that both extremities (parameter sets 4 & 5) exceed the performance of their mid-tier counterpart, with no drastic density related features being apparent and a generally good grain boundary cohesion being observed. This is further highlighted as shown in Figure 4.18. It should be noted that for these extremities, that parameter set 4 displayed a greater performance at 51.6 hours comparative to parameter set 5 at 34.7 hours, for reasons which are likely down to statistical variance rather than microstructural phenomena.

Nevertheless, a furthered understanding through the incorporation of in-depth material characterisation methods such as EBSD analysis was required, as it could ascertain underpinning microstructural mechanisms not visible with traditional microscopy techniques.

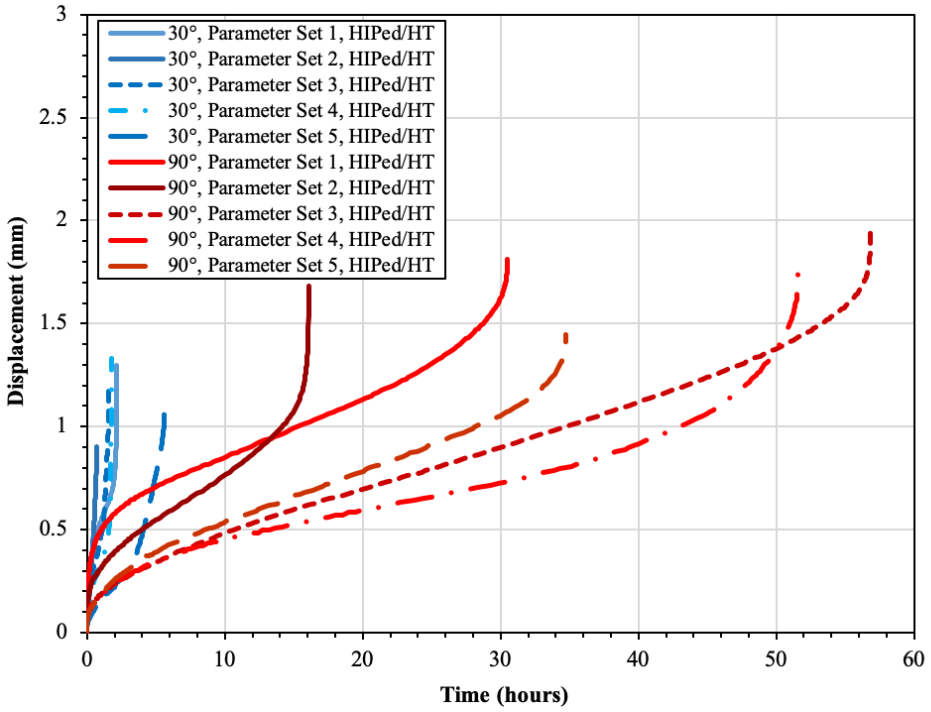

Figure 4.15. SPC tests at 950°C, 150N load for parameter variants across both 30° and 90° CM247LC LPBF builds.

Table 4.3. Time to Rupture and Minimum Displacement Rate data for 30° and 90° LPBF CM47LC variants with differing process parameter sets from within the normalised process window.

Sample	Time to Rupture [Hours]	Minimum Displacement Rate [mm.hr^{-1}]
30°, Parameter Set 1, HIPed/HT	2.2	0.169
30°, Parameter Set 2, HIPed/HT	1.1	0.39
30°, Parameter Set 3, HIPed/HT	2.8	0.14
30°, Parameter Set 4, HIPed/HT	1.8	0.18
30°, Parameter Set 5, HIPed/HT	5.6	0.05
90°, Parameter Set 1, HIPed/HT	30.5	0.027
90°, Parameter Set 2, HIPed/HT	16.1	0.041
90°, Parameter Set 3, HIPed/HT	56.9	0.019
90°, Parameter Set 4, HIPed/HT	51.6	0.012
90°, Parameter Set 5, HIPed/HT	34.7	0.023

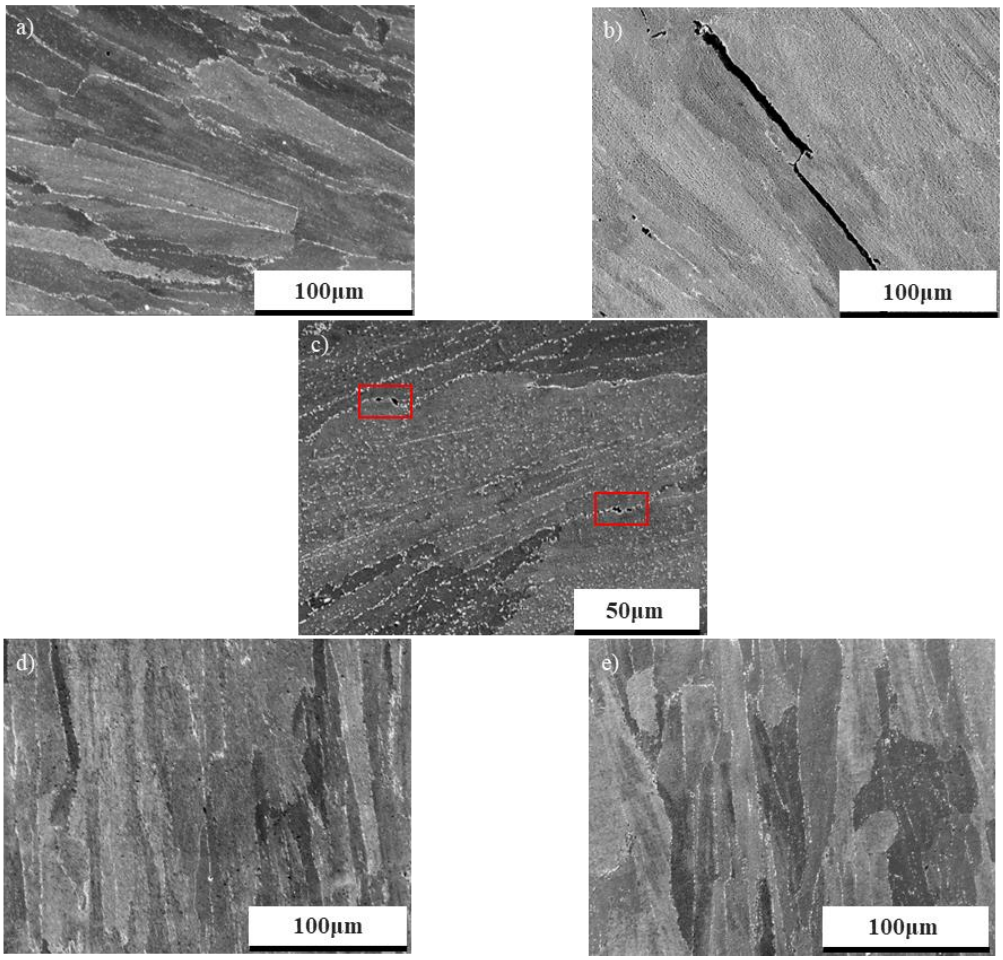

Figure 4.16. Microstructural observations of parameter sets in relation to their position within the normalised process window, a) Parameter Set 5, b) Parameter Set 2, c) Parameter Set 1, d) Parameter Set 3 and e) Parameter Set 4.

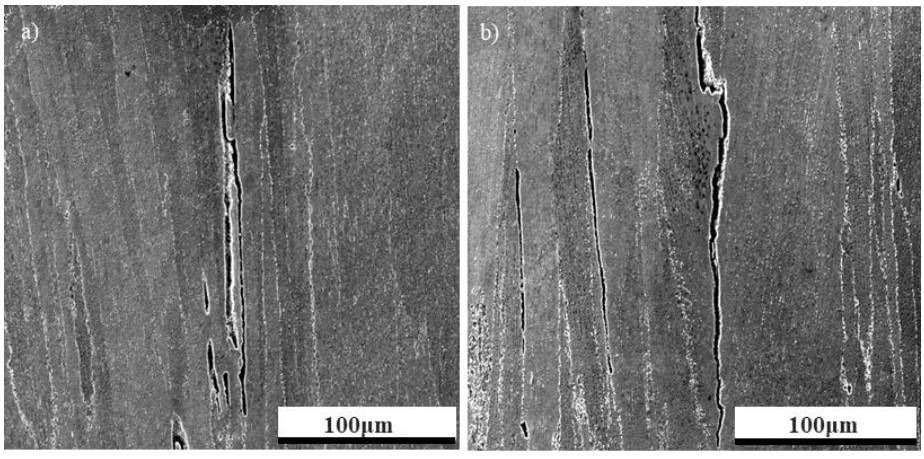

Figure 4.17. Intergranular cracking consequent to cavitation coalescence observed in 90°, Parameter Set 2, Build 1.

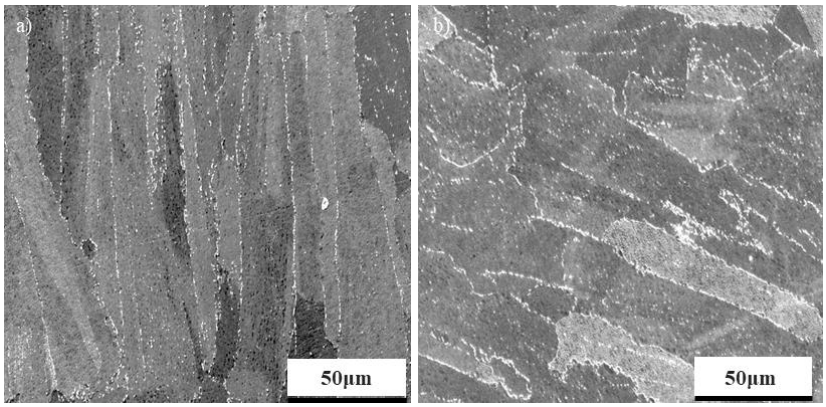

Figure 4.18. Grain boundary cohesion and lack of density related features witnessed in 90°, Parameter Sets a) 4 b) 5.

Table 4.4. EBSD grain size measurements conducted across each CM247LC LPBF 90° parameter set.

Sample	Average Grain Area (µm²)	Average Grain Aspect Ratio	Average Grain Diameter (µm)	Grain Count
90°, Parameter Set 1, HIPed/HT	660.36	3.08	14.64	290
90°, Parameter Set 2, HIPed/HT	796.67	2.94	9.11	243
90°, Parameter Set 3, HIPed/HT	538.23	2.56	8.93	351
90°, Parameter Set 4, HIPed/HT	813.55	2.91	17.42	241
90°, Parameter Set 5, HIPed/HT	835.59	2.51	19.87	236

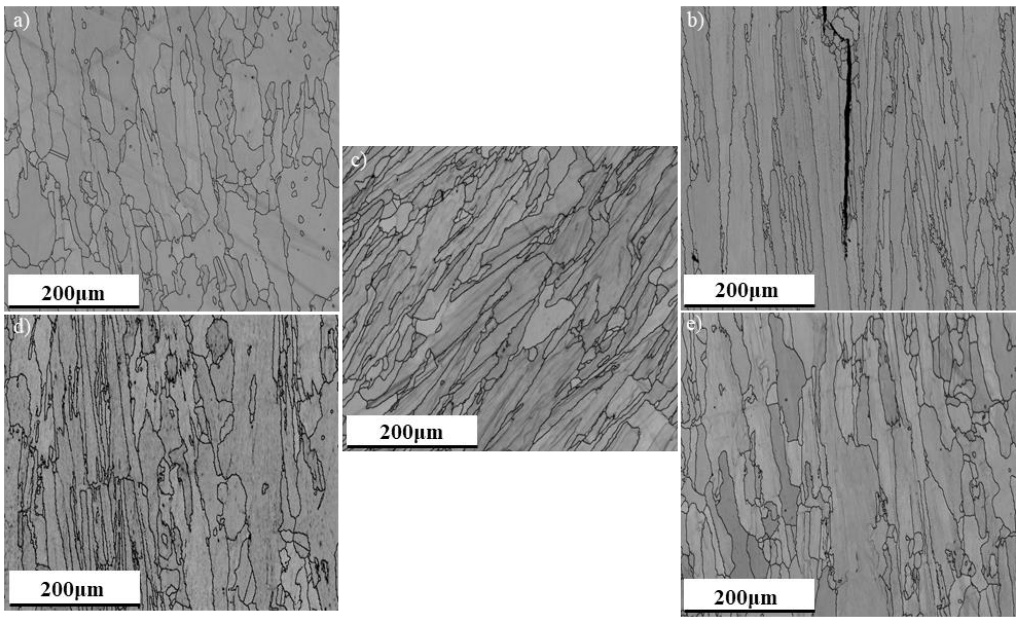

Figure 4.19. EBSD grain mapping of parameter sets in relation to their position within the normalised process window, a) Parameter Set 5, b) Parameter Set 2, c) Parameter Set 1, d) Parameter Set 3 and e) Parameter Set 4.

As mentioned, EBSD analysis was used to further the understanding of parameter set influence on both grain characteristics and their underpinning microstructural mechanisms. Grain size calculations were approximated as shown in Table 4.4 with respect to the grain contrast band maps showcased in Figure 4.19, where discrete changes in grain morphology and sizing can be observed. When considering energy density's influence, there appears to be a general coarsening behaviour observed with increasing energy input, where low energy variants display an average grain size of 538.23μm^2, medium energy variants 660.36μm^2, and high energy variants 796.67μm^2. These grain sizes inherently influence grain count given the respective area considered remains consistent, and are innately tied to the implications of energy density on cooling rate where higher energies are subsequently expected to lead to larger melt pool volumes which will intrinsically cool slower. Although the grain sizes displayed appear to contrast the creep performances displayed within this DOE despite the mechanisms discussed, it is important to note the propensity for defect formation associated with these parameter inputs which appear to dominate failure mechanisms. Bearing this in mind, the utilisation of a variety of mapping techniques in order to ascertain the underpinning mechanisms which promote cavitation formation and coalescence was considered.

Figure 4.20 showcases a variety of mapping techniques employed on both extremities of the process window with regards to energy density. Figures 4.20a & d highlight the evolution of texture consequent to increasing energy input, where a fairly uniform texture was observed in the low energy variant and textural development preferential to (101) was displayed in the high energy variant, which is most likely attributed to the extended cooling rate subsequent to higher energy inputs, thus aiding time dependent processes. Figures 4.20b & e showcase LAM maps of both variants, where a significant contrast in behaviour is apparent. Given the heightened existence of residual stressing present in additive processes consequent to the rapid onset of cooling as discussed in Section 2.3.5, strain accumulation is expected to be highly present in both variants. However, there appears to be a change in behaviour with regards to the locational presence of this strain accumulation, where it appears to primarily subside within grains in lower energy variants and is predominately situated along grain boundaries in high energy variants. This is most likely consequent to the contrasting behaviour in the cooling mechanics that melt pools of different sizes display, where smaller melt pools are more likely to cool not only faster but in a more uniform manner. In contrast, larger melt pools will innately cool slower, but given the heightened presence of melt pool circumferences being exposed to cooler regions of bulk material, will lead to greater non-uniformities in cooling rates. These discrepancies in cooling rates can give rise to mismatches in thermal expansion coefficients and thus amplify tensile loading which would principally manifest itself in the form of strain accumulation along grain boundaries, which in CM247LC's case appears to promote the onset of the existence of grain boundary cavitation and solidification cracking. Figures 4.20c & f showcase recrystallisation fraction mapping, where there doesn't appear to be a significant change in the volume fraction of recrystallised material evident, but

the recrystallised material existent in the higher energy variant appears to conform and elongate with the material consequent to the directional heat flow.

Furthermore, Figures 4.21a & c showcase Schmid factor maps highlighting the preference of grains to available slip systems in polycrystalline nickel-based superalloys ⟨110⟩ {111}, where the grains present in the higher energy variant seemingly showcase a slightly lower preference to slip, albeit still relatively favourable. This appears to coincide with the textural development observed in higher energy variants as previously discussed. What's more, Figures 4.21b & d illustrate the presence of grain boundary angles, where there appears to be a relatively uniform mixture of low and high angle grain boundaries. Although it would be expected that textural development would coincide with the presence of low angle grain boundaries (LAGB), it is important to consider two factors which may misrepresent this information. The first is that the fine region of material examined may not entirely represent the bulk material and the second being that it is difficult to ascertain the disparity in cooling rates given the ambiguity surrounding these parameter sets.

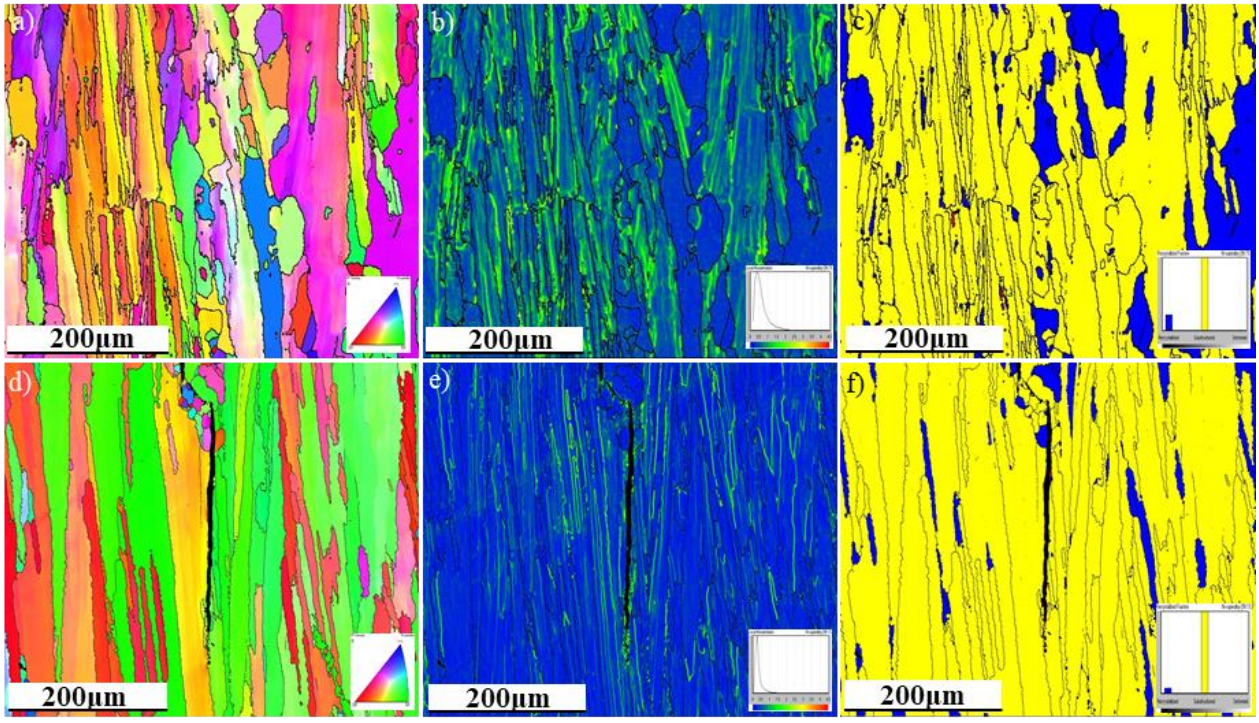

Figure 4.20. 90°, Parameter Set 3, Build 1 a) IPF Z, b) LAM c) RF mapping and 90°, Parameter Set 2, Build 1 d) IPF Z, e) LAM and f) RF mapping.

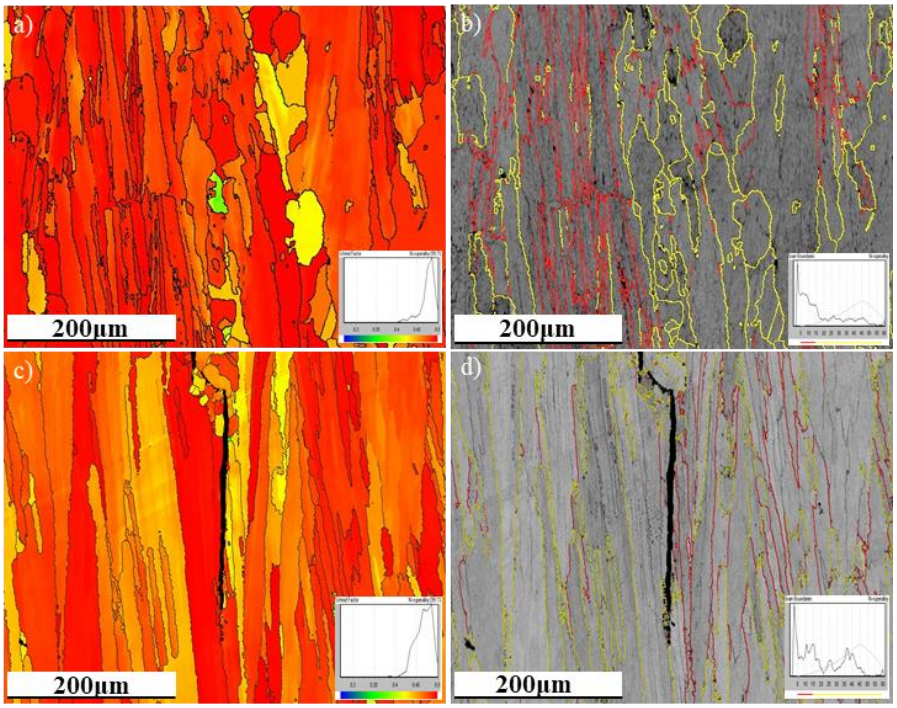

Figure 4.21. 90°, Parameter Set 3, Build 1 a) Schmid Factor b) GBA and 90°, Parameter Set 2, Build 1 c) Schmid Factor d) GBA mapping.

In addition to energy deposition, the influence of normalised hatch spacing in relation to equivalent energy density was analysed. There appears to be no significant change in textural evolution, strain accumulation, grains preferential to slip or grain boundary angles in relation to observations explored in parameter set 1. There was however a drastic change to recrystallisation volume fraction as shown in Figure 4.22, where both variants appeared to display larger regions of recrystalllised material which appeared to be relatively coarse. When comparatively relating this to the grain sizing calculations shown in Table 4.4, it becomes evident that coarsening behaviour is existential given the relatively large average grain sizes showcased, 813.55µm^2 and 835.59µm^2 respectively. When considering this in collaboration with the strong grain boundary cohesions previously observed, it becomes highly plausible that remelting processes are occurring subsequent to these changes in hatch spacing.

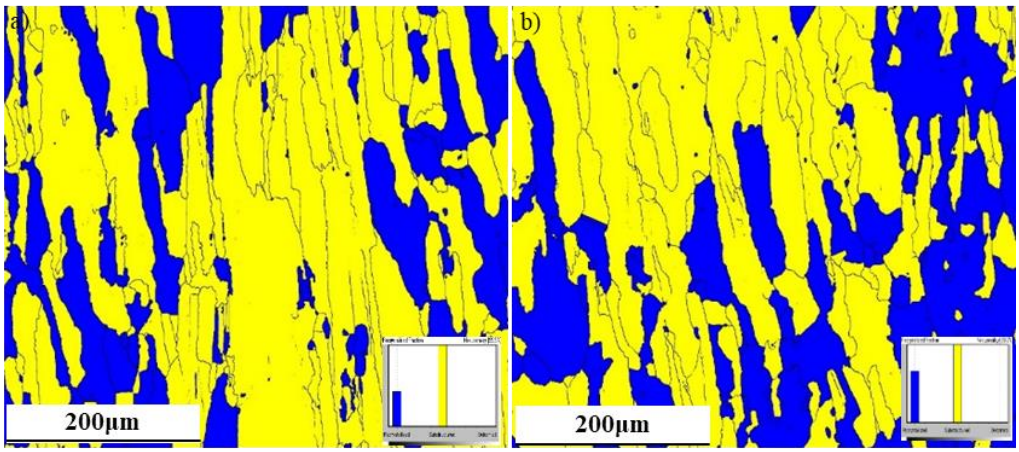

Figure 4.22. RF mapping of a) 90°, Parameter Set 4, Build 1 and b) 90°, Parameter Set 5, Build 1.

In addition to microstructural examination, fractographic analysis was conducted across all parameter sets for both 30° and 90° builds as shown in Figures 4.23 and 4.24. The severely embrittled failures previously witnessed in Section 4.1 for 30° build orientations continue to transpire regardless of the parameter set employed, where 'star-fish' radial primary cracking, propagating from the centre of the disc, is consistently displayed as seen in Figures 4.23a-d. It is worth noting that the loss of material mentioned previously can continue to occur during the imaging process given the materials highly embrittled nature post testing. The lack of diversity in the morphologies of the fracture surfaces is to be expected given that these specimens failed in considerably similar time frames (1.1 – 5.6 hours) and were dominated by the anisotropic characteristics discussed such as triple point cracking. Nevertheless, the fracture surfaces shown in Figures 4.23e-h continue to showcase the epitaxial grain structures associated with ALM alongside intergranular cracking with similar features to uniaxial testing methods such as dimpling being beheld in Figure 4.25.

Moreover, Figures 4.24a-d present low magnification imaging of the ruptured specimens for 90° build orientation across all parameter sets. Although it is evident that the associated failures still occur in a brittle fashion, the level of embrittlement displayed continues to not be as substantial as that of the 30° builds respectively, with the initiation of unidirectional failures being somewhat evident. Figures 4.24e-h further highlight the presence of elongated grain structure and intergranular cracking and what's more the eminence of secondary cracking around the periphery of the punch head. Moreover, given the mechanisms discussed, the incorporation of differing parameter sets does not appear to give rise to any substantial variation in the fractures displayed. Given this and the consistent presence of features such as facets and dimples observed at higher magnifications as shown in Figure 4.25, it becomes evident that there is not a change in failure mechanism rather just the time to rupture.

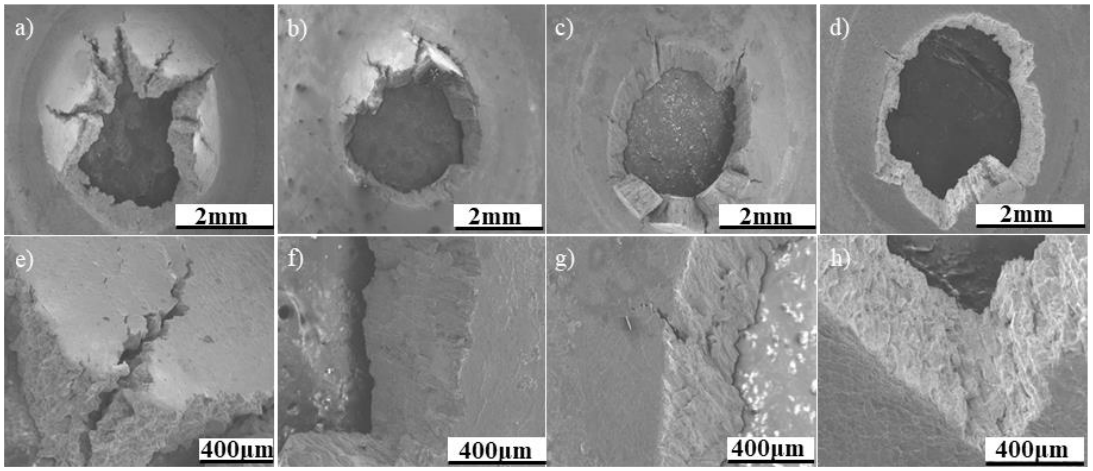

Figure 4.23. 30º builds with variations in Parameter Sets. a) e) 2, b) f) 3, c) g) 4 and d) h) 5 fractography.

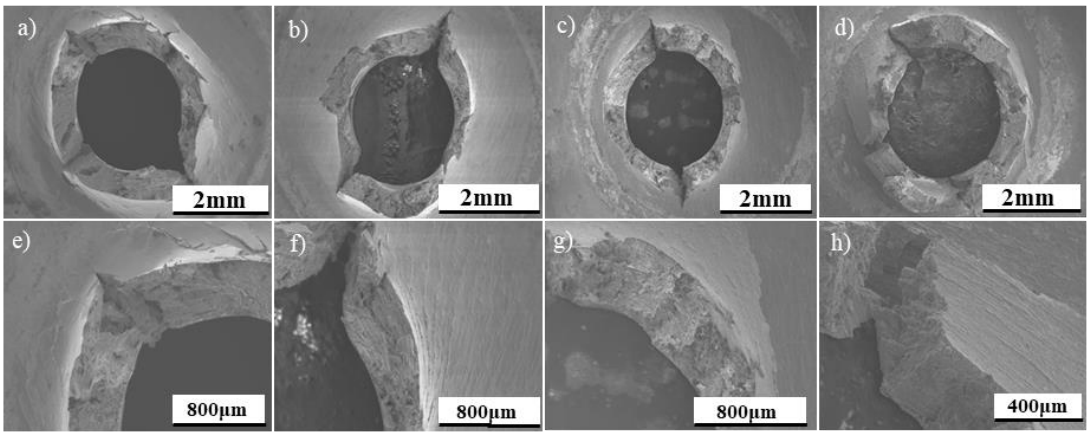

Figure 4.24. 90º builds with variations in Parameter Sets. a) e) 2, b) f) 3, c) g) 4 and d) h) 5 fractography.

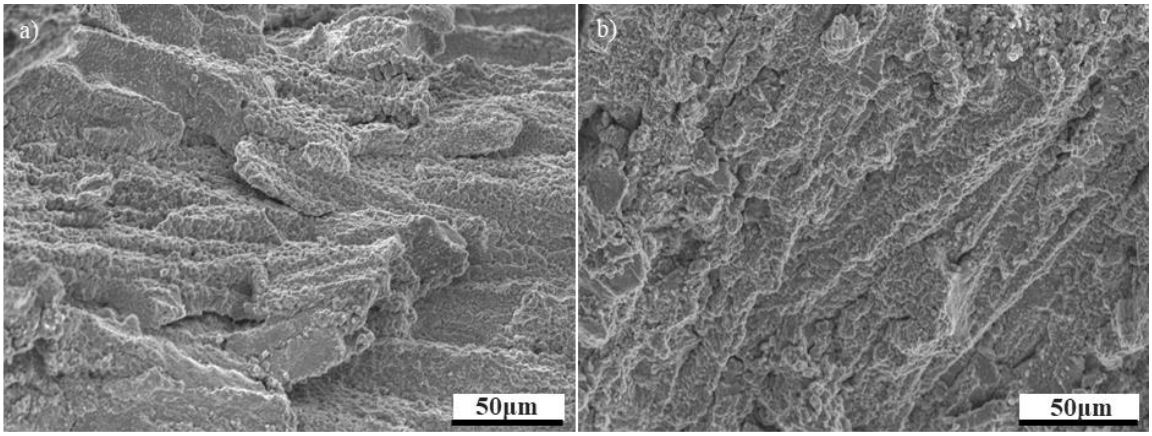

Figure 4.25. High magnification imaging of 30º, Parameter Set 3, build 1.

4.3 Summary

Overall, build orientation was shown to be the dominant influencer of mechanical properties given the characteristics of epitaxial grain growth evident in additive processes and its implications on grain sizing, morphology and subsequently the number of catastrophic features such as triple point cracking. Considering this, process parameter selection appeared to bear little significance within 30^{o} orientations given the dominating mechanisms presiding, but showed reasonable importance in the 90° orientations, particularly with regards to grain sizing, textural evolution and the propensity for defect formation consequent to melt pool mechanics. Given the existential relationship between energy deposition and melt pools discussed, a further understanding is required and as such, the need for a quantitative assessment as to the influence of process parameters on melt track sizing takes precedent, with considerations as to the presence of defects being taken into account. The following section will look to employ a robust statistical analysis on a collection of LPBF variants of differing normalised beam speeds, powers and energy densities, ascertaining individual and combined parameter influence on melt track height, width and LPBF CM247LC's predisposition for defects, specifically microcracking and porosity.

Chapter 5 – A Quantitative Approach to Melt Track & Defect Analysis in CM247LC

5.1 Melt Track Assessment of CM247LC Parameter Variants

An assortment of 50-70 manual melt tracks measurements were taken across 24 LPBF CM247LC variants, with measurements recorded for both height and width to identify the influence of differing normalised beam speeds, powers and energy densities on melt pool geometry and furthermore, the propensity for defect formation. It is self-evident in Figure 5.1 that there is a clear correlation displayed between melt pool size and normalised beam speed, where higher speeds lead to finer track sizing, with track width displaying a greater sensitivity than that of track height irrespective of the power settings employed. This somewhat validates the use of energy density as a metric and can be further observed in the relationships shown in Figure 5.2, where it is generally witnessed that there is a directly inverse relationship between track size and increasing normalised beam power, with higher powers leading to a generally coarsened track size. However, it can be seen that when higher speeds and powers are utilised in conjunction, this relationship can cease to exist suggesting that there is a level of variance and scatter for data sets of certain parameters, the extent of which fails to be fully represented.

The relationships discussed and revealed through this methodology can be given further credibility too through the microscopy presented in Figure 5.3, where (a, c & e) showcase the refinement of track sizes with increasing beam speed and conversely, (b, d and f) highlight the coarsening of track sizes consequent to increasing power input. Both of these trends further support and provide credence to the general use of energy density. Considering the aforementioned relationships observed, Figure 5.4 presents the comparative relationship between normalised energy density and track size across all 24 LPBF CM247LC variants. Despite there being a clear existential relationship between normalised energy density and track sizing, the degree of scatter present particularly with regards to melt track height can highlight the challenges associated with the characterisation of additive material, where energy density may not entirely capture melt pool physics in all instances. This highlights the need for further understanding, particularly with regards to the influence of process parameters on the consistency of the process.

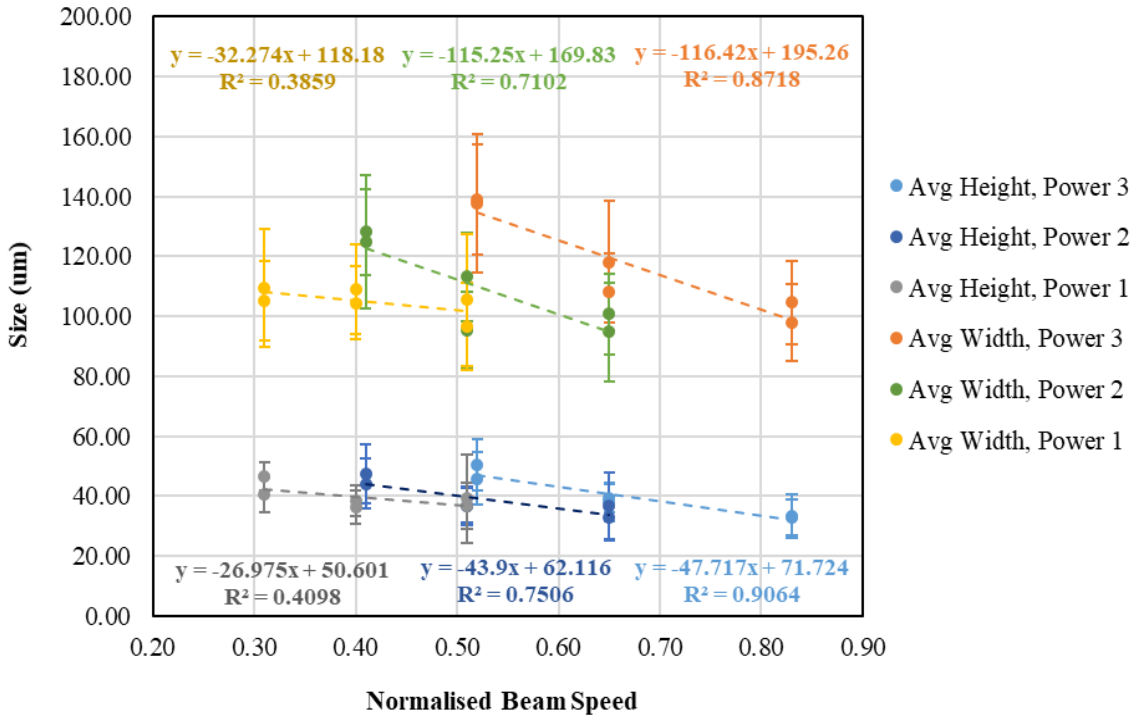

Figure 5.1. Influence of normalised beam speed on melt track height and width over a range of employed power settings for LPBF CM247LC.

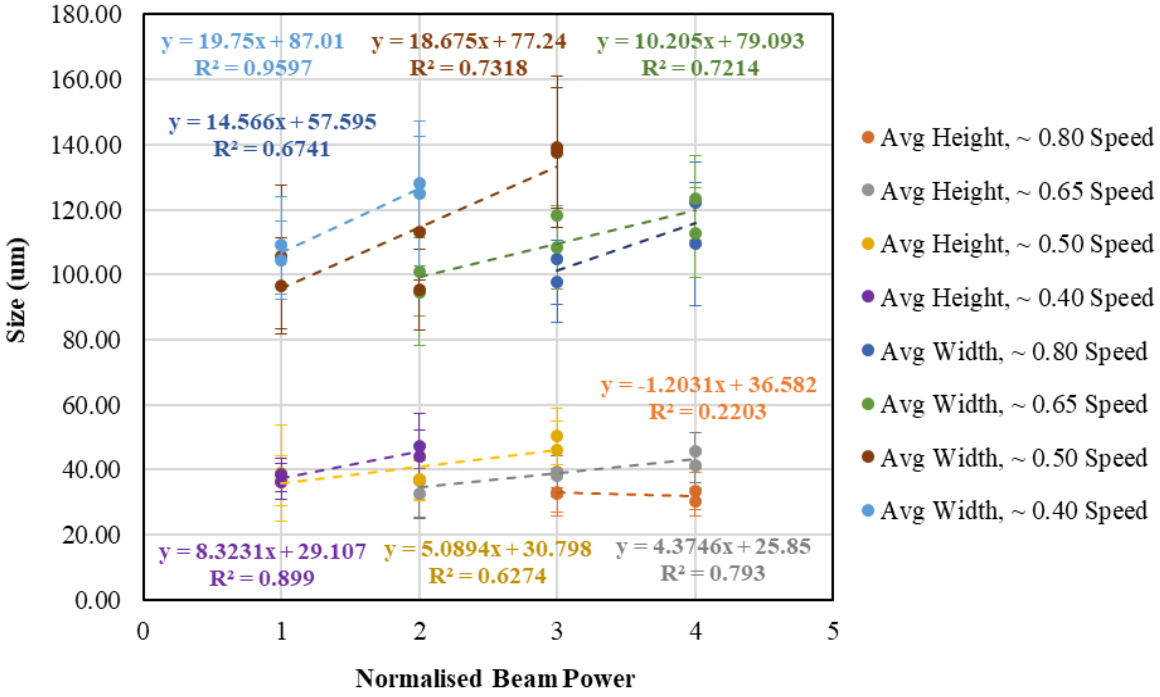

Figure 5.2. Influence of normalised beam power on melt track height and width over a range of employed speed settings for LPBF CM247LC.

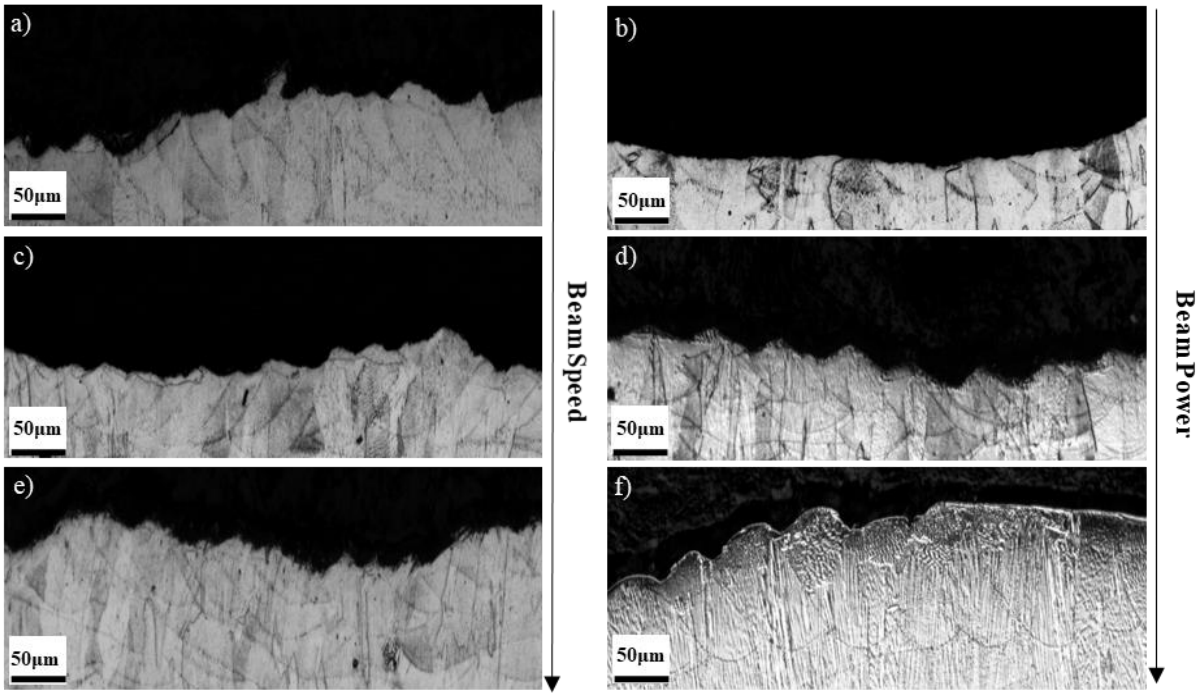

Figure 5.3. Microscopy of melt track profiles for a) c) e) increasing normalised beam speed and b) d) f) increasing normalised beam power.

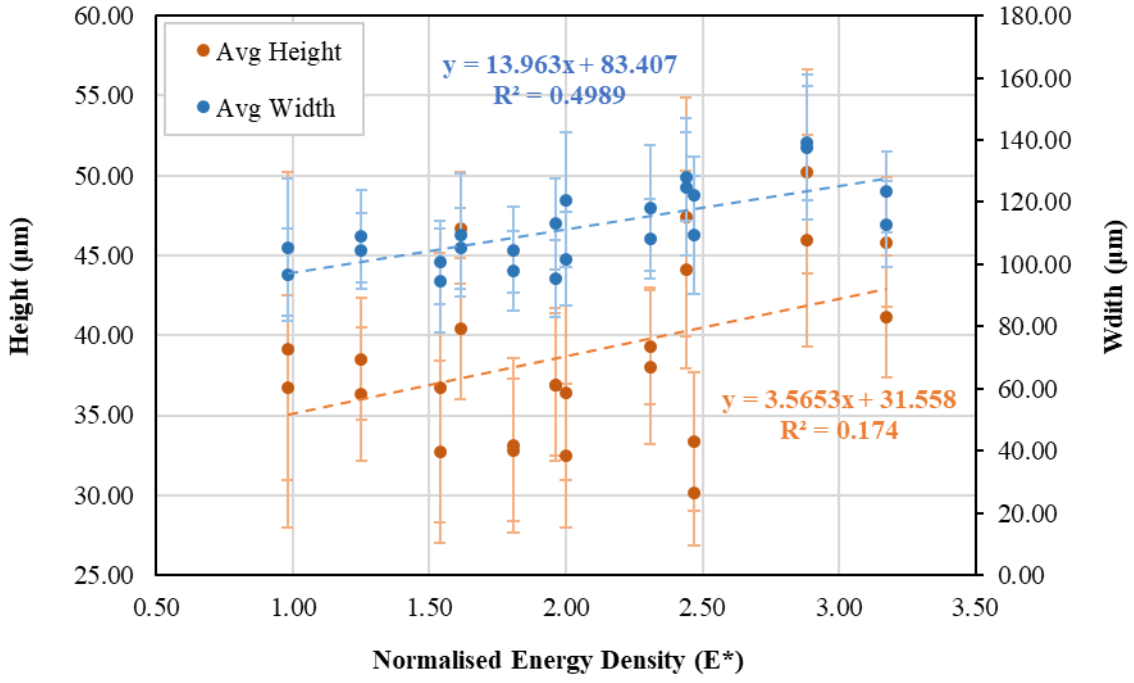

Figure 5.4. Influence of normalised energy density on melt track height and width across all LPBF variants within this CM247LC DOE.

5.2 Defect Analysis of CM247LC Parameter Variants in the As-Built Condition

In addition to melt track size, defect analysis was conducted over all CM247LC LPBF variants in order to gauge an understanding as to how process parameters influence the formation of porosity and other defects. As mentioned in Section 3.4, the other defects present appear to manifest themselves predominantly in the form of microcracking and will therefore often be referred to as such. The contrasting relationship between porosity and microcracking can be observed over a range of both speed and power settings as shown in Figures 5.5 & 5.7, coinciding to literature that suggests different mechanisms are present as discussed in Section 2.3.5. It can be seen in Figure 5.5, that as normalised beam speed increases, microcracking decreases irrespective of the power settings incorporated. It is hypothesised that this occurs consequent to the inherently lower energy inputs associated with higher beam speeds and thus a more uniform cooling rate is concurrent, minimising the generation of tensile loads and thus solidification cracking. The relationships portrayed using this methodology can be further validated with the use of high magnification stitched optical microscopy as shown in Figure 5.6, where the general observations of increased cracking at lower speeds can be seen, particularly in Figure 5.6a comparative to c. The same correlations cannot be observed entirely for that of porosity, where high speeds and powers appear to give rise to an increase in porosity, which is most likely linked to melt pool turbulence. This contradicts lower speed and power inputs in conjunction, where there is a noted decrease which is most likely attributed to low levels of spatter or gas entrapment. These relationships seem to emphasise that there does not appear to be a strong link between parameter selection and porosity within this DOE, but it is unclear as to whether this is because not all the processing information has been made available. As such, this will be subject to further investigation through alternative means

Considering the inverse relationship noted between speed and power as described previously, Figure 5.7 showcases similar characteristics. It can be seen that an increase in normalised beam power gives rise to microcracking irrespective of the beam speed settings incorporated, and it is again proposed that this is consequent to the inherently higher energy inputs and thus the development of steeper disparities in cooling rates across the melt pool. As discussed in Section 2.3.5, the ramifications of rapid cooling rates can give rise to heightened residual stressing which can typically manifest itself in the form of tensile loading if mismatches in contraction rate are apparent. This generation in tensile loading would aid the promotion of solidification cracking. The relationship between normalised beam power and microcracking is further substantiated in Figure 5.8, where high magnification stitched microscopy further illustrates the existence of microcracking in higher power samples as seen in Figure 5.8c, giving credence to the analytical methodology employed. As previously eluded too, there continues to be no direct link between parameter selection and porosity within this DOE. Finally, bearing in mind the relationships discussed, a comparison was drawn relating normalised energy density to the presence of

microcracking and porosity as shown in Figure 5.9. The existing trends give further standing to the behaviours deliberated, where there appears to be a direct relationship between increased normalised energy density and microcracking consequent to the mechanisms previously argued, once again supporting previously published literature [91] [106] [171]. These characteristics are given further credence in Figure 5.10, where a high volume of microcracking is exhibited in Figure 5.10c. It again seems evident that there appears to be a non-uniform relationship between process parameters and porosity within this DOE, with a significant degree of scatter being observed suggesting alternative variables act as the primary influencer. As such, alternative criteria will be considered.

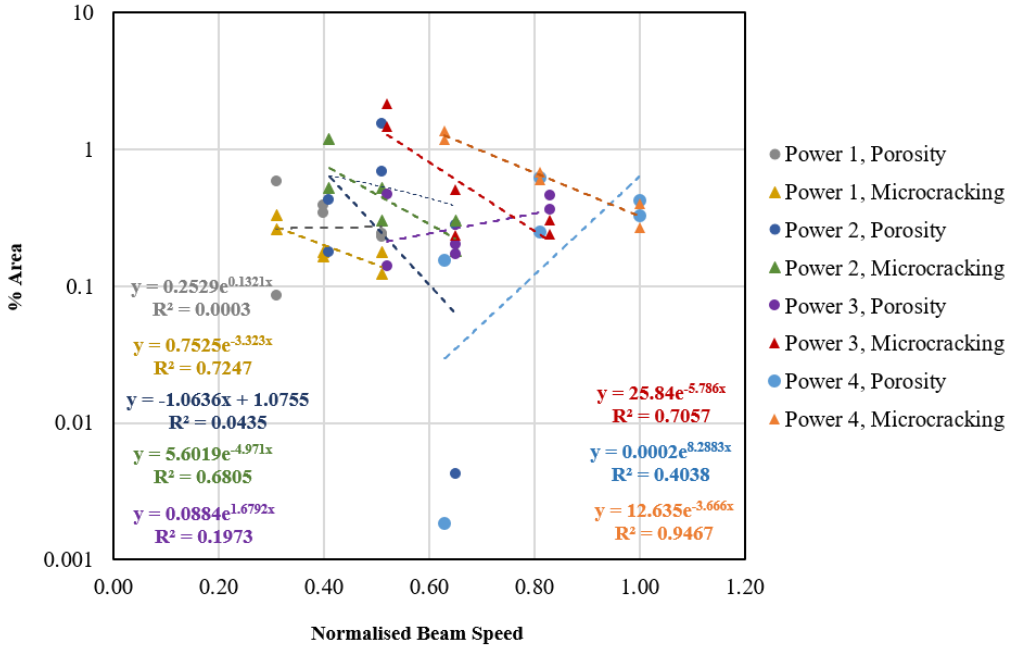

Figure 5.5. Influence of normalised beam speed on the % area of porosity and other defects in LPBF CM247LC variants.

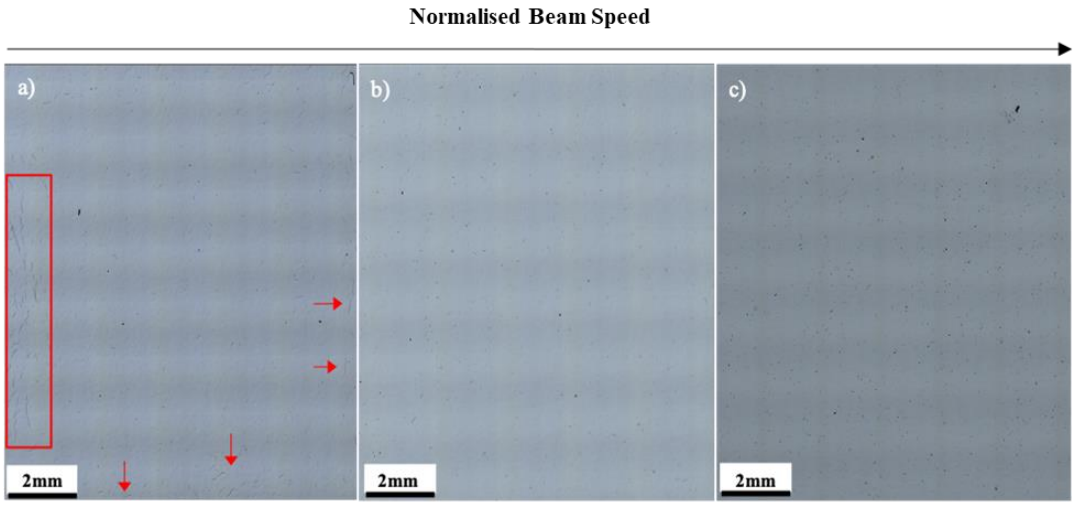

Figure 5.6. Stitched high magnification optical microscopy of LPBF CM247LC samples of increasing normalised beam speed (left to right) with the same power input.

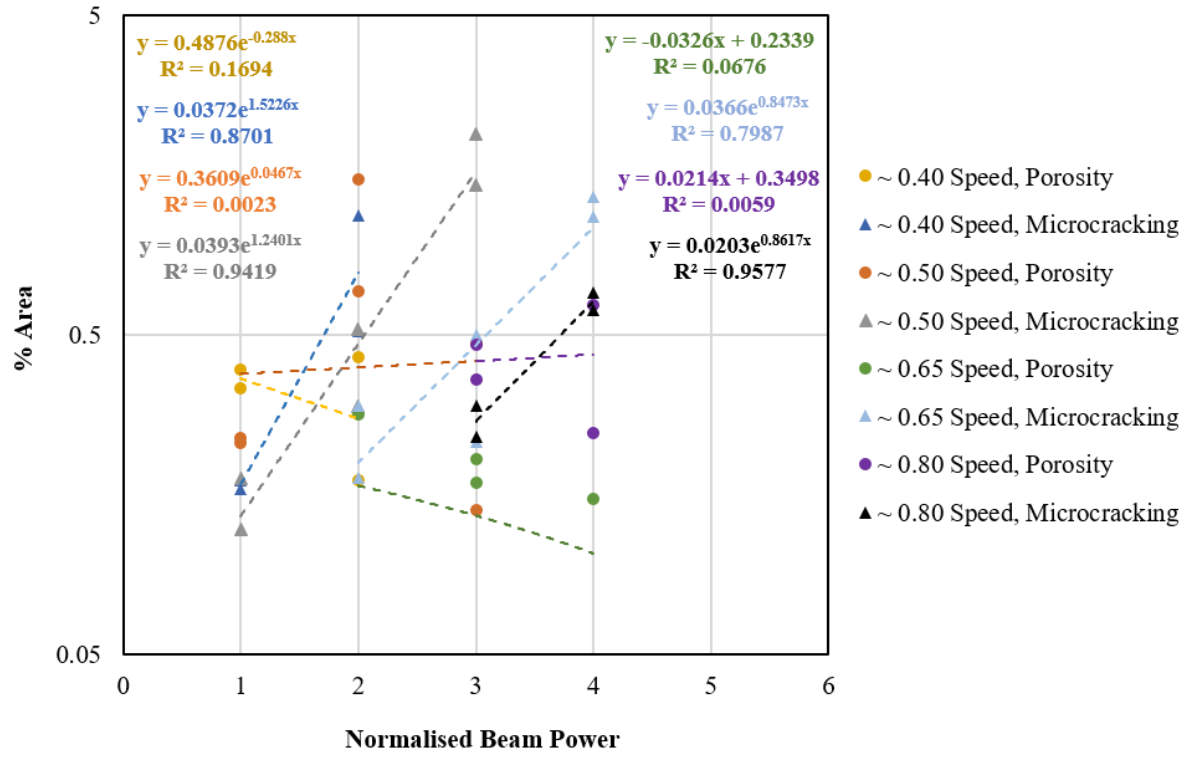

Figure 5.7. Influence of normalised beam power on the % area of porosity and other defects in LPBF CM247LC variants.

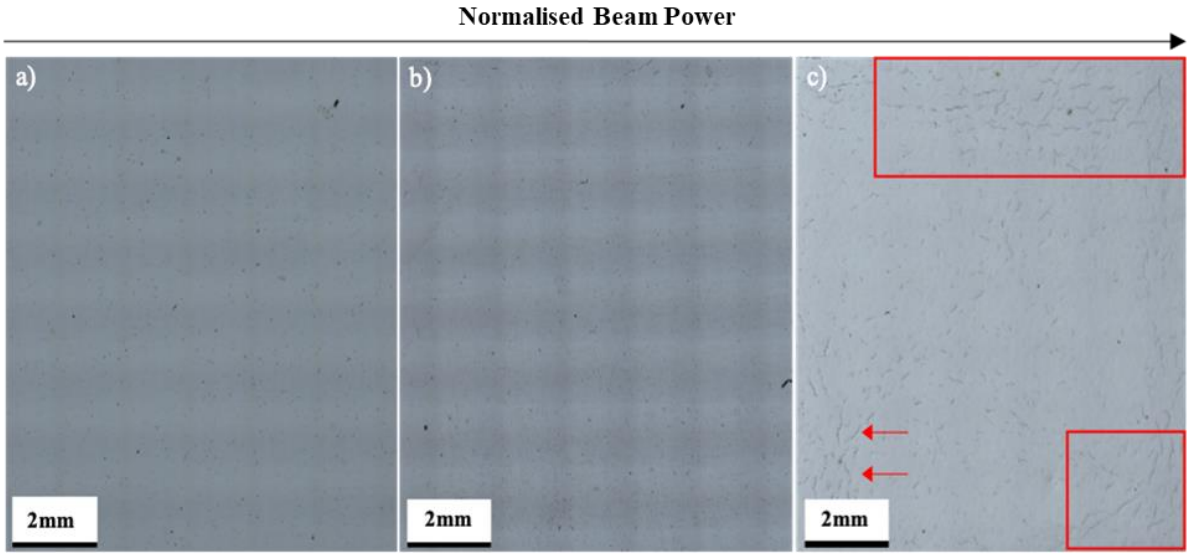

Figure 5.8. Stitched high magnification optical microscopy of LPBF CM247LC samples of increasing normalised beam power (left to right) with the same speed input.

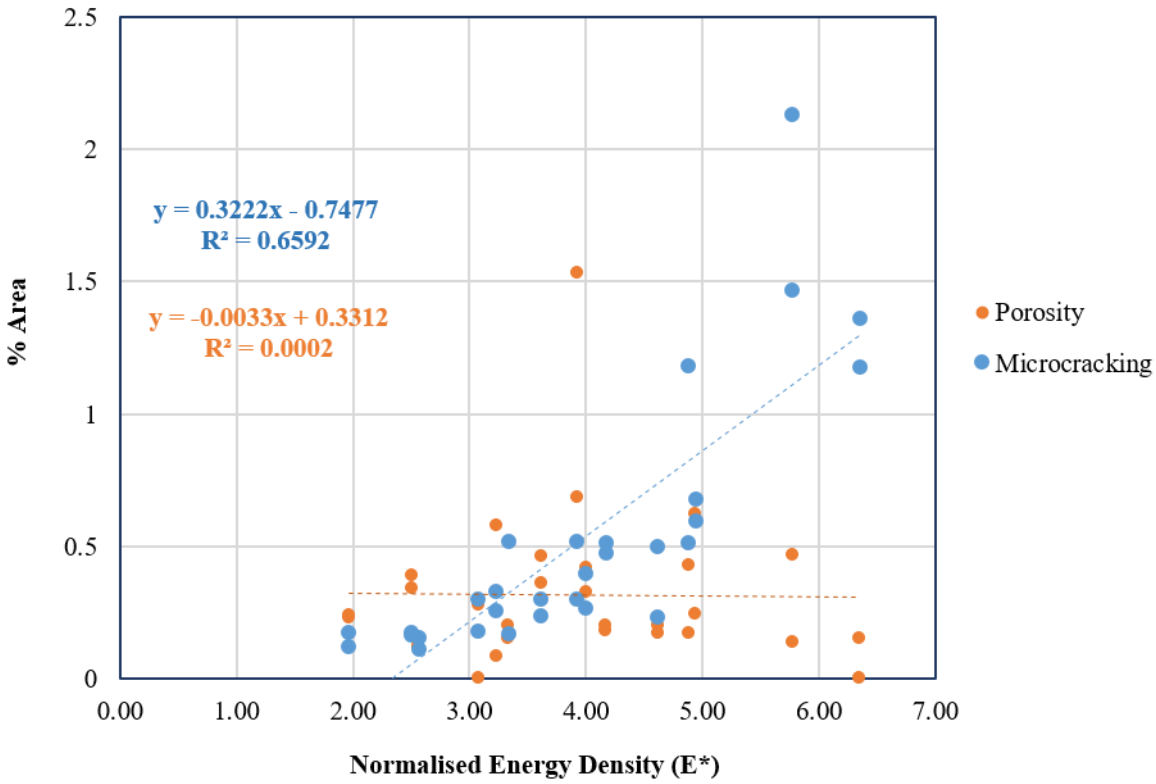

Figure 5.9. Influence of normalised energy density on the % area of porosity and other defects in LPBF CM247LC variants.

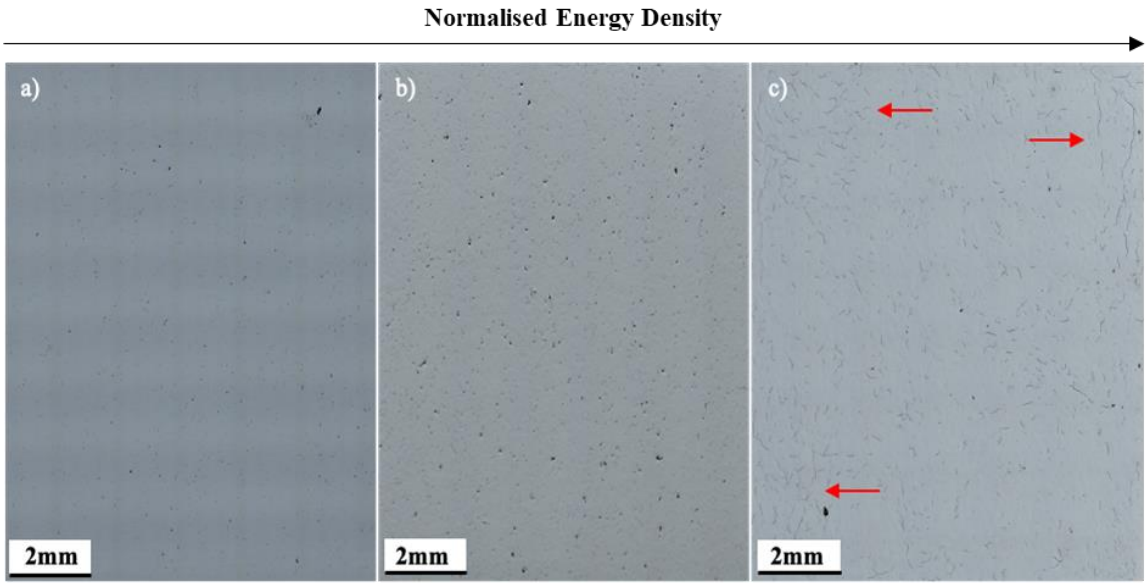

Figure 5.10. Stitched high magnification optical microscopy of LPBF CM247LC samples of increasing normalised energy density (left to right).

One potential criticism for the figures discussed is whether or not the use of area percentage as a metric is entirely representative to the underlying mechanisms at hand. This could act as an explanatory factor in regard to the porosity measurements discussed, where low frequencies of large pores and high volumes of small pores would in theory give the same area percentage, despite there being the probable existence of differing mechanisms at play. As such, the use of alternative criteria such as feature count and average feature size has been explored, in order to provide further insight as to the relationships observed. It can be seen in Figure 5.11 that the general observations witnessed previously continue to ensue, where lower occurrences of microcracking arise as normalised beam speed increases. This additionally appears to be the case for porosity, but it is unclear at this point whether this is down to data scatter as the relationships observed appear to stagnate at higher power settings. Figure 5.12 once again showcases the inverse relationship between beam speed and power as discussed, where there appears to be a clear discernible trend for microcracking where normalised beam power increases, but a level of ambiguity continues to surround porosity. Finally, a comparison was drawn between feature count and normalised energy density as displayed in Figure 5.13. It continues to be evident that there is a direct relationship between increasing normalised energy density and microcracking for reasons already discussed, where it is reasonable to assume that the area percentage rises previously explored are consequent to the more frequent presence of microcracking shown. There again continues to appear to be no notable relationship between energy input and porosity, where a large degree of scatter is observed, once more suggesting that alternative variables act as the driving influencer.

In addition to feature count, the influence of process parameters on the average size of said features was considered. It is shown in Figure 5.14 that the relationships discussed regarding microcracking once more become occurrent, where increases in normalised beam speed lead to a significant reduction in the average size of microcracking present. Considering that these results coincide with the previous metrics utilised, it is reasonable to conclude that an increase in normalised beam speed does lead to a reduction in the size, frequency and consequently the area percentage of microcracking within this DOE. Although it may appear that the average size of porosity is influenced by normalised beam speed, it is important to note that the existing disparities for porosity are substantially less than that of microcracking given the logarithmic scale. Figure 5.15 showcases the relationship between normalised beam power and the average size of features present, which once again coincides with the metrics previously discussed with a marked increase in microcracking. These relationships give strong viability to the notion that increasing beam power gives rise to the presence of larger and more frequent microcracking for reasons explored previously, both of which inherently contribute to the larger area percentages previously observed. There does appear to be a distant relationship between process parameters and the average size of porosity once again. Considering the relationships discussed for normalised beam speed and power and their innate ties to energy density, a

look at the role normalised energy density plays on the average size of such features across all LPBF variants was examined as shown in Figure 5.16. There appears to be a significant relationship between increasing normalised energy density and the broadening of microcracking. When considering this in conjunction with the behaviours associated with changes in normalised beam speed and power, it becomes well established that increasing normalised energy density leads to the inclusion of larger and more frequent microcracking and thus the larger area percentage originally showcased. The relationship to porosity continues to be unclear in which a large amount of scatter is once again observed in the mid region. When contemplating this in conjunction with the feature count and the obscurity of area percentage, there appears to be a reasonable indication that other variables act as the dominant influencer within this DOE.

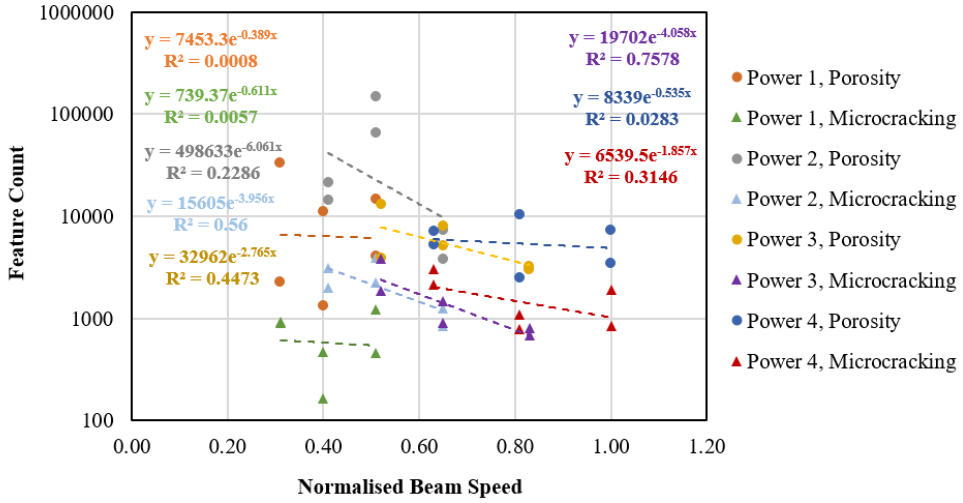

Figure 5.11. Influence of normalised beam speed on the count of porosity and other defects in the LPBF CM247LC variants within this DOE.

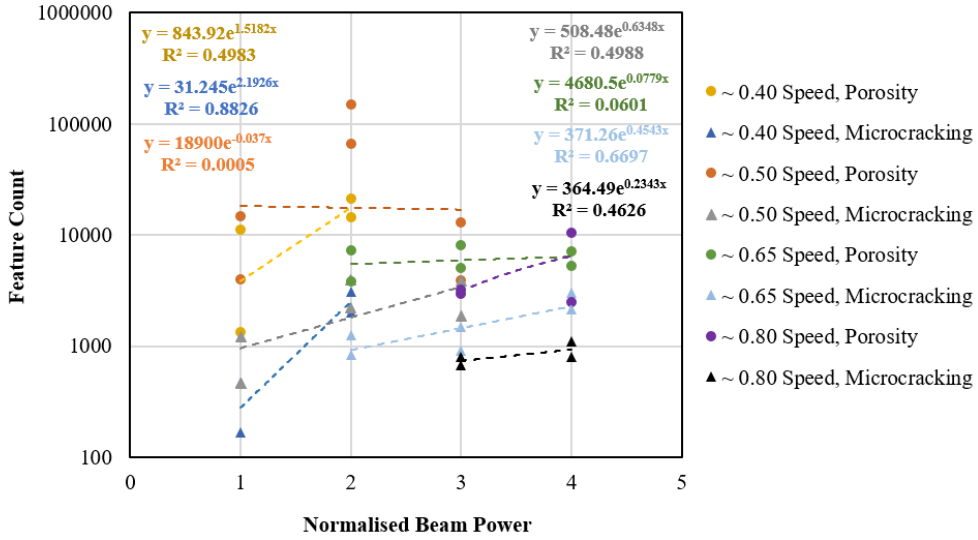

Figure 5.12. Influence of normalised beam power on the count of porosity and other defects in the LPBF CM247LC variants within this DOE.

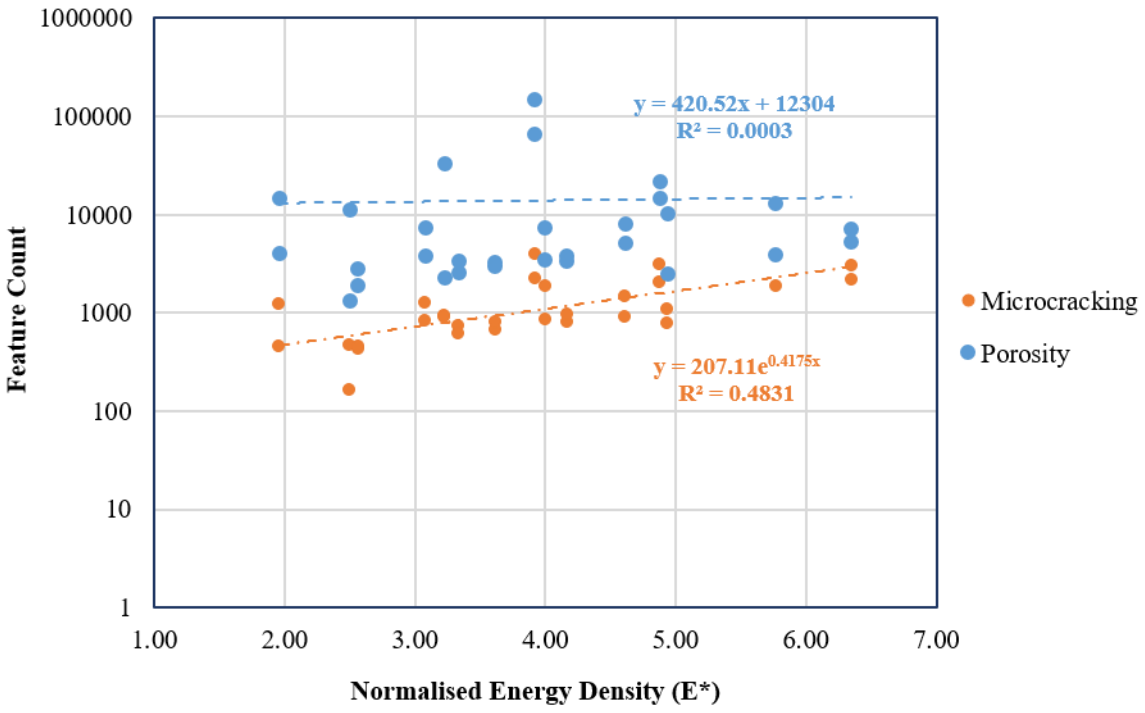

Figure 5.13. Influence of normalised energy density on the count of porosity and other defects in the LPBF CM247LC variants within this DOE.

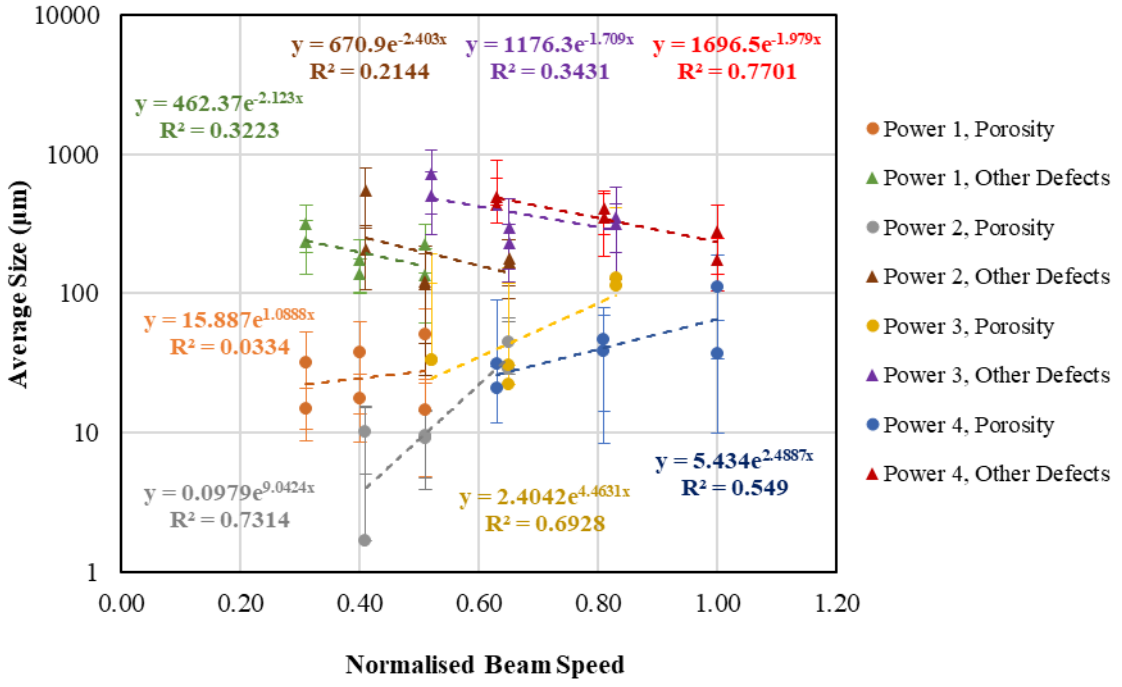

Figure 5.14. Influence of normalised beam speed on the average size of porosity and other defect features in the LPBF CM247LC variants within this DOE.

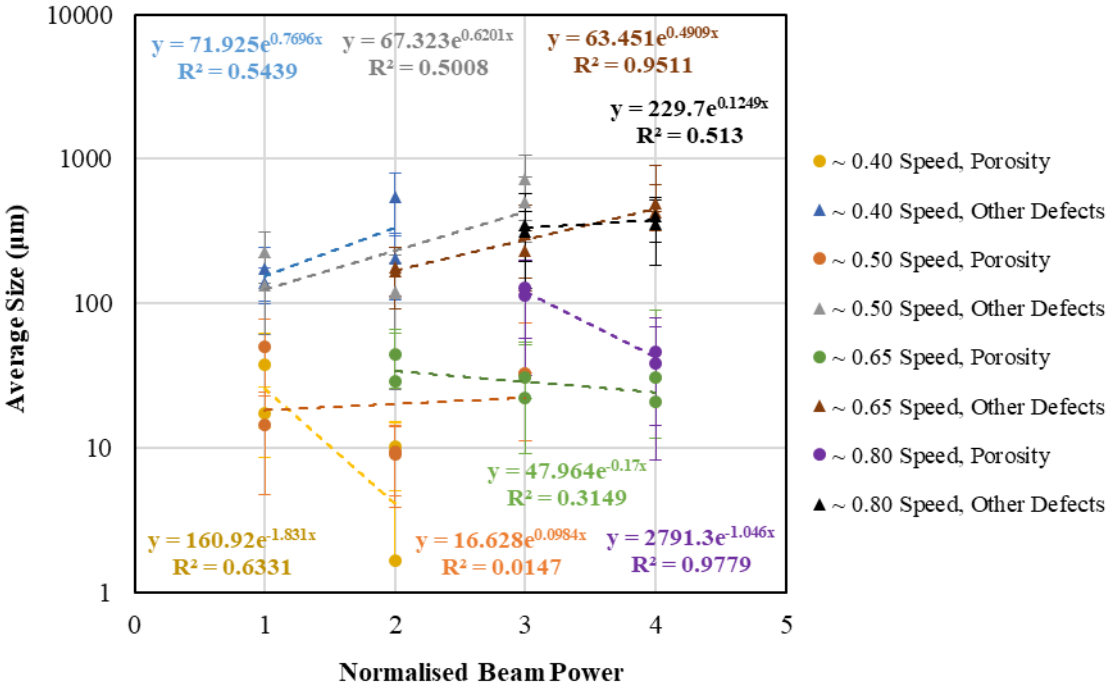

Figure 5.15. Influence of normalised beam power on the average size of porosity and other defect features in the LPBF CM247LC variants within this DOE.

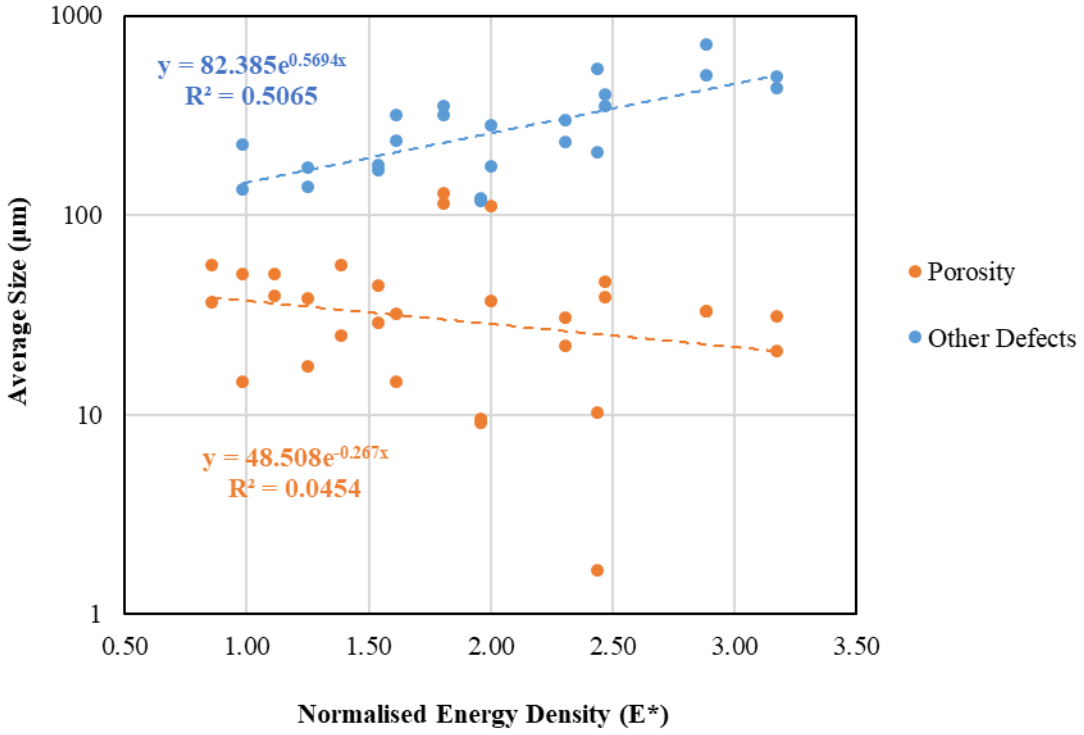

Figure 5.16. Influence of normalised energy density on the average size of porosity and other defect features in the LPBF CM247LC variants within this DOE.

5.3 The Apparent Macrocracking in HIPed Rod Parameter Variants

In addition to defect analysis, a HIPing procedure was conducted on back to back parameter sets in rod form, where in some instances macrocracking was observed. Measurements for both crack depth and width were taken across all 24 CM247LC LPBF variants with the procedures outlined in Section 3.4, where results were correlated to process parameters, to be discussed later. Figure 5.17 showcases that there appears to be an increase in the severity of tearing post HIP as normalised beam speed increases and this is further illustrated in Figure 5.18. When compared to the equivalent parameter sets in the as built state, the variants which displayed the most severe microcracking surprisingly appear to consolidate well and not tear post HIPing. This phenomenon further exists for normalised beam power as shown in Figure 5.19, where an increase in normalised beam power leads to little or no macrocracking, with lower ends of power displaying high degrees of tearing as visually highlighted in Figure 5.20. These behaviours continue to coincide with the observations previously discussed for the as-built counterparts, where high normalised beam power would give rise to high degrees of microcracking as discussed, once more highlighting this inverse relationship that is apparent.

When comparing the influence of normalised energy density on macrocracking post HIPing across all 24 CM247LC LPBF variants as shown in Figure 5.21, it is evident that increasing energy input leads to greater material consolidation post HIPing. It is clear that a directly inverse relationship exists between microcracking and tearing post HIPing, where material that displays prominent microcracking in the as built condition appears to show little to no macrocracking following post processing. As discussed earlier, the microcracking induced in the as-built variants is consequent to high energy density inputs. This subsequently leads to the heightened presence of larger melt pools which are innately more suspect to larger discrepancies in contraction rates which in turn generate both tensile loading and residual stressing. Given the relationship between microcracking and tearing previously showcased with changes in normalised beam speed, power and energy density, it is hypothesised that the microcracking observed in the as-built state inherently acts as a mechanism for stress relief. Considering this, the relief of stress would give a reasonable indication and insight as to why material that displays little to no microcracking in the as-built condition appears to tear within the HIPing process and material that displays large degrees of microcracking appears to consolidate fairly successfully. Furthermore, it is also worth noting that the direction of tearing and splitting witnessed within these rods coincides and aligns with the epitaxial grain growth directions present within ALM processes, suggesting that the phenomenon is both microstructurally driven and intergranular.

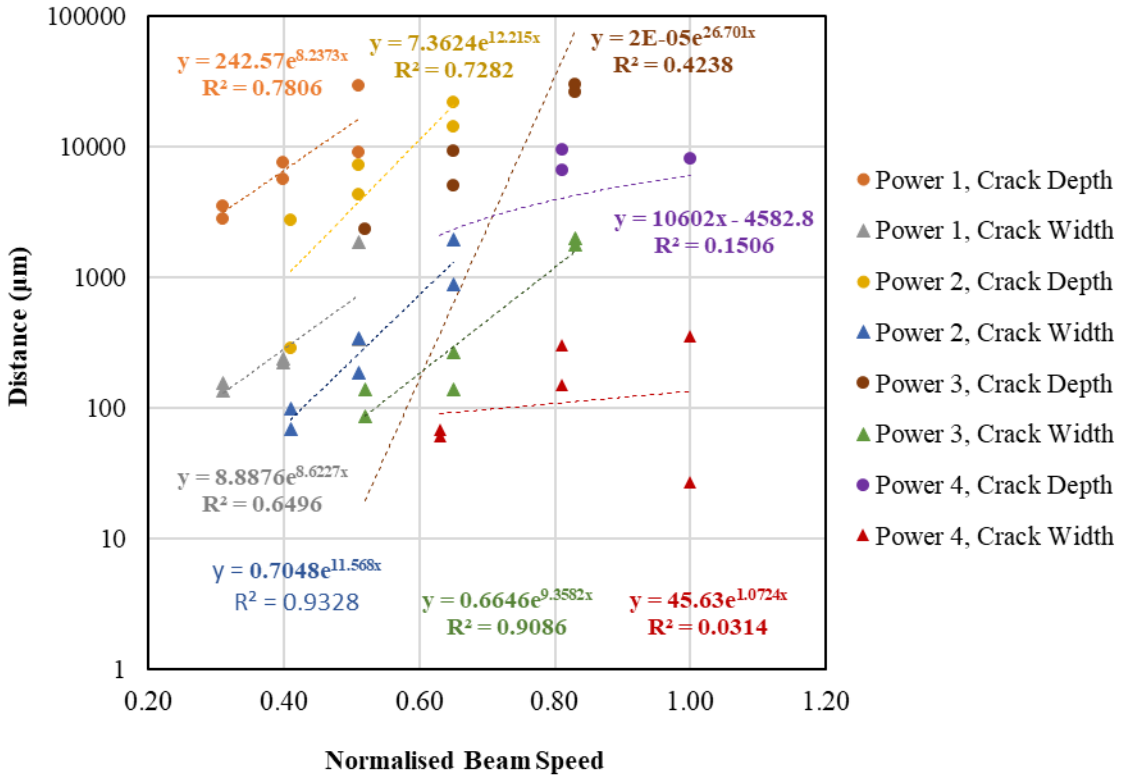

Figure 5.17. Influence of normalised beam speed on cracking measurements displayed post HIPing in the LPBF CM247LC rods.

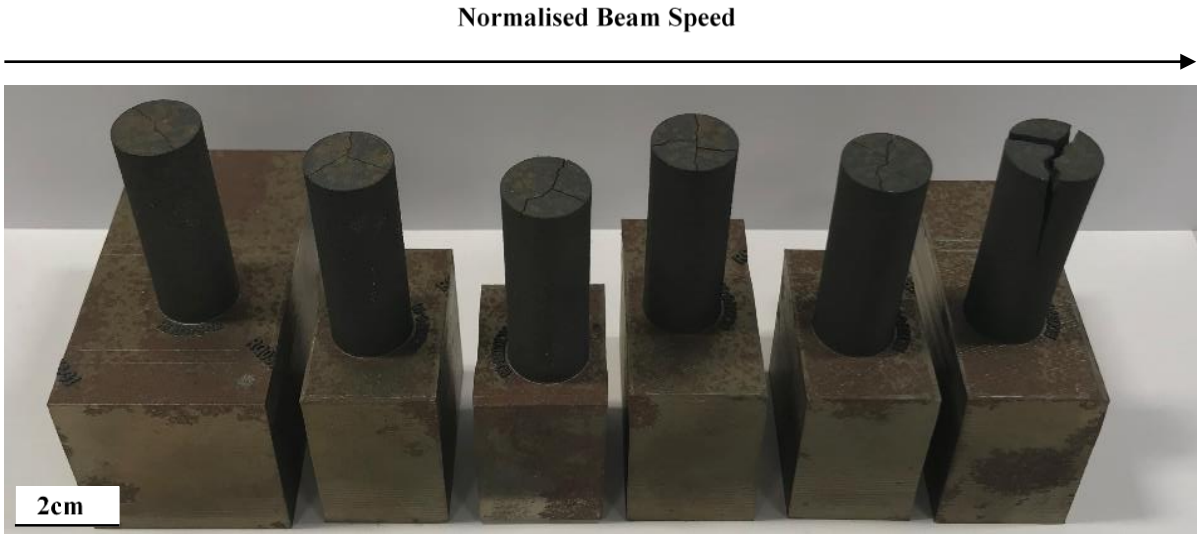

Figure 5.18. Cracking observations in LPBF CM247LC rods post HIPing from left to right in order of increasing normalised beam speed.

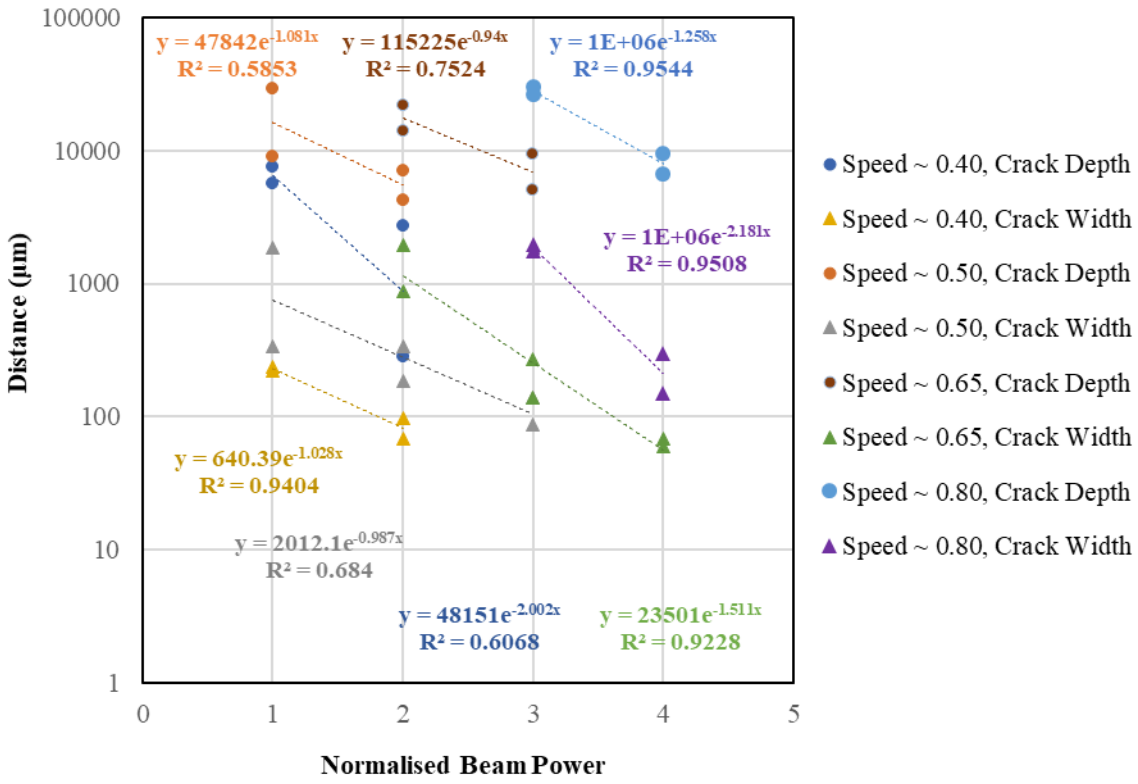

Figure 5.19. Influence of normalised beam power on cracking measurements displayed post HIPing in the LPBF CM247LC rods.

Figure 5.20. Cracking observations in LPBF CM247LC rods post HIPing from left to right in order of increasing normalised beam power.

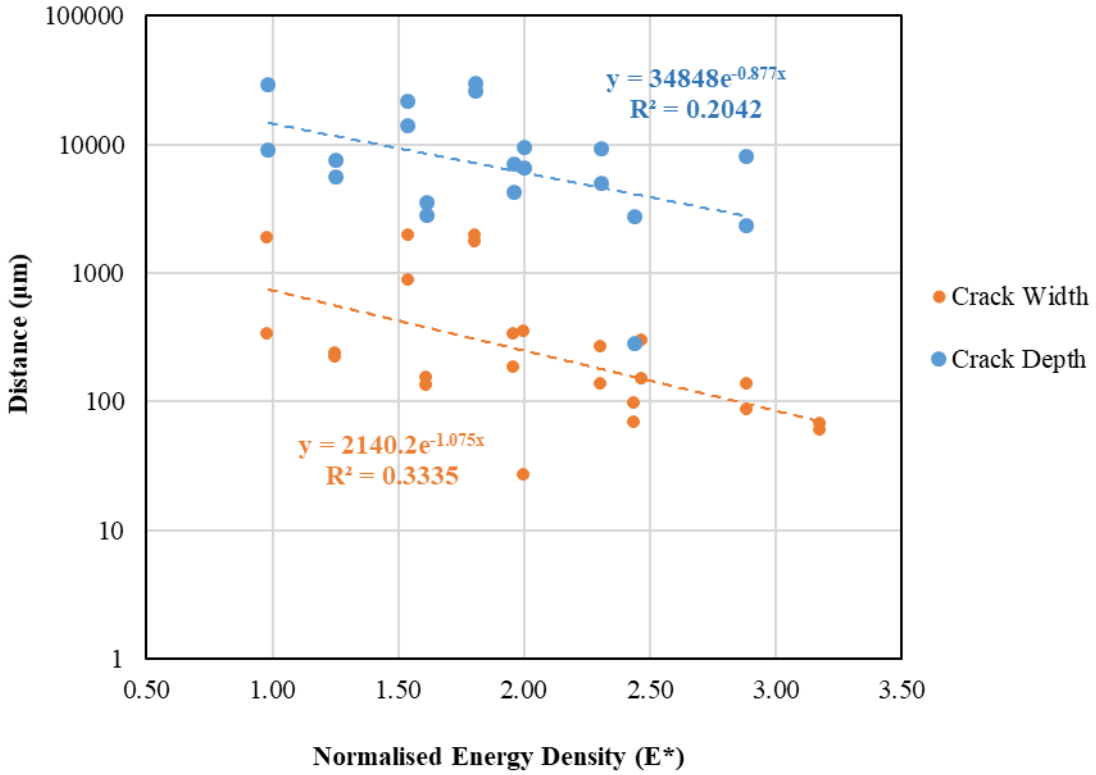

Figure 5.21. Influence of normalised energy density on cracking measurements displayed post HIPing in the LPBF CM247LC rods.

5.4 Process Variance in Paired Parameters

Within this DOE, there appears to be a relatively consistent and strong correlation between process parameters and material behaviour as to be expected. However, it is noticed in two instances that paired samples (1 & 2, 7 & 8) with the same parameter sets employed, display vastly different cracking behaviour as indicated in Table 5.1. Upon initial observations of the average melt track sizes of these samples, there appears to be a comparatively consistent outcome showcased with regards to parameter selection. For samples 1 and 2, track heights and widths of a similar range are observed (36.72 – 39.11µm, 96.93 – 105.47µm) and alike behaviour is displayed for samples 7 and 8 (32.75 - 36.75µm, 94.74 – 100.72µm). Despite this however, further statistical examination of the measurements conducted reveal underlying implications which can give insight as to these differences in behaviour. It can be seen in the box plot depicted in Figure 5.22a that irrespective of sample 1 and 2's similar average track sizes, there is evidently a large degree of variation in the measurements in sample 1 which coincides with the increased severity of macrocracking post HIP, as shown in Table 5.1 (1866.80µm average width, 29289.18µm depth). This can be further illustrated in the histograms presented in Figures 5.22b-e, where extremely different distribution profiles between samples 1 and 2 are depicted. Furthermore, similar behaviour is again observed between samples 7 and 8 as indicted in Figure 5.23a, where large degrees of data scatter are displayed, which again further corresponds to the increased

severity in macrocracking depicted in Table 5.1 (1950.63μm average width, 21864.39μm depth). The changes in distribution profiles are again highlighted with the histograms shown in Figure 5.23b-e. Considering that the large degree of data scatter seemingly appears to coincide with this tearing behaviour, it is reasonable to suggest that the consistency of the process for sample 1 and 8 is somewhat tarnished. Given this, an understanding as to the driver for this variation in track sizing is required.

One consideration within the LPBF manufacturing process which has yet to be explored is the effect that build architecture and more specifically location bears on the samples manufactured. High degrees of melt track size variation give a general indication that the presence of changes in cooling rates is apparent and considering that a consistent standard stripe hatching strategy with a 67° orientation was employed as outlined in Section 3.1.1, a further understanding is required as to why this occurs. Across all 24 samples within this DOE, a variance value for both melt track height and width was calculated from standard deviations and visually represented in a contour plot respective to its position on the build plate as illustrated in Figure 5.24. In these contour plots it becomes apparent that large degrees of melt track variation tend to arise towards the back right of the build plate, in close proximity to the wipers original position and the introduction of argon gas flow. Although it is difficult to provide any definitive determination given that not all processing information has been made available, it is hypothesised that there is a degree of gas trappage that occurs consequent to a variety of mechanisms, one of which includes powder-wiper interaction. As powder is pushed onto the bed, powder particles of a larger size are likely to congregate together which provides a poorer overall packing density with voids presiding between them. This lack of powder coverage upon melting, can contribute to the formation of porosity. It is also worth noting that the variance observed appears to be more evident for melt track width comparative to height, suggesting that the phenomenon that occurs is more prominent above the melt pool surface, further coinciding with the notion of argon trappage given argon's heavier density comparative to air.

Table 5.1. Data summary of paired parameters that displayed differing behaviour.

Sample	**Parameter Selection**			**Melt Tracks**		**HIPed Macrocracking**	
	v	h*	q	Avg Height (μm)	Avg Width (μm)	Avg Width (μm)	Depth (μm)
1	0.51	2	1	36.72	105.47	1866.90	29289.18
2	0.51	2	1	39.11	96.63	334.37	9002.85
7	0.65	2	2	36.75	94.74	880.95	14121.15

8	0.65	2	2	32.75	100.72	1950.63	21864.39

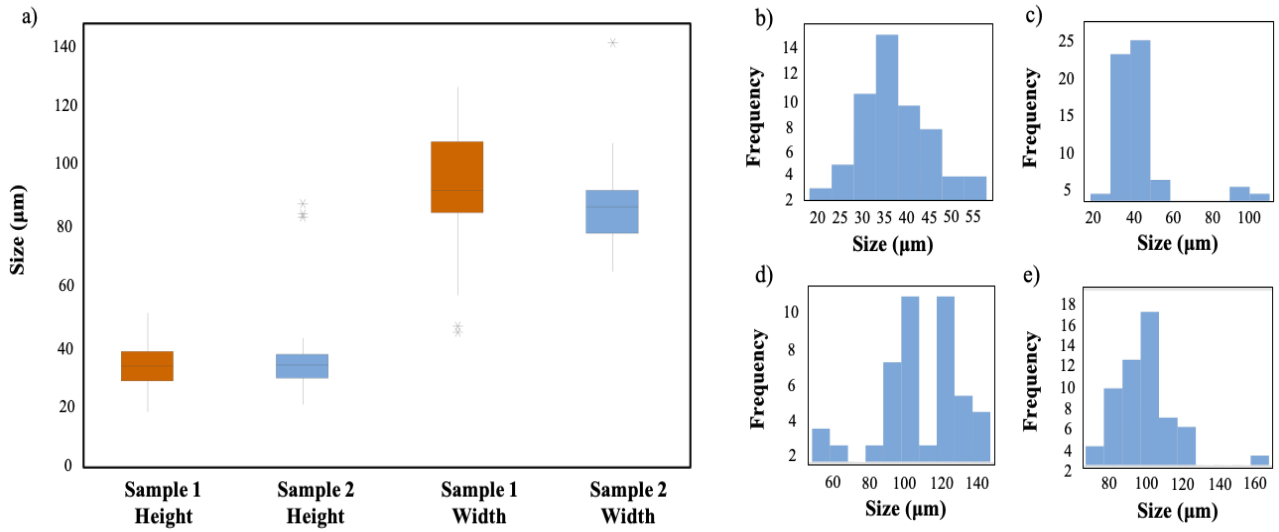

Figure 5.22. Melt track height and width variance for LPBF CM247LC samples 1 and 2 a) box plot b) sample 1 track height, c) sample 2 track height, d) sample 1 track width and e) sample 2 track width.

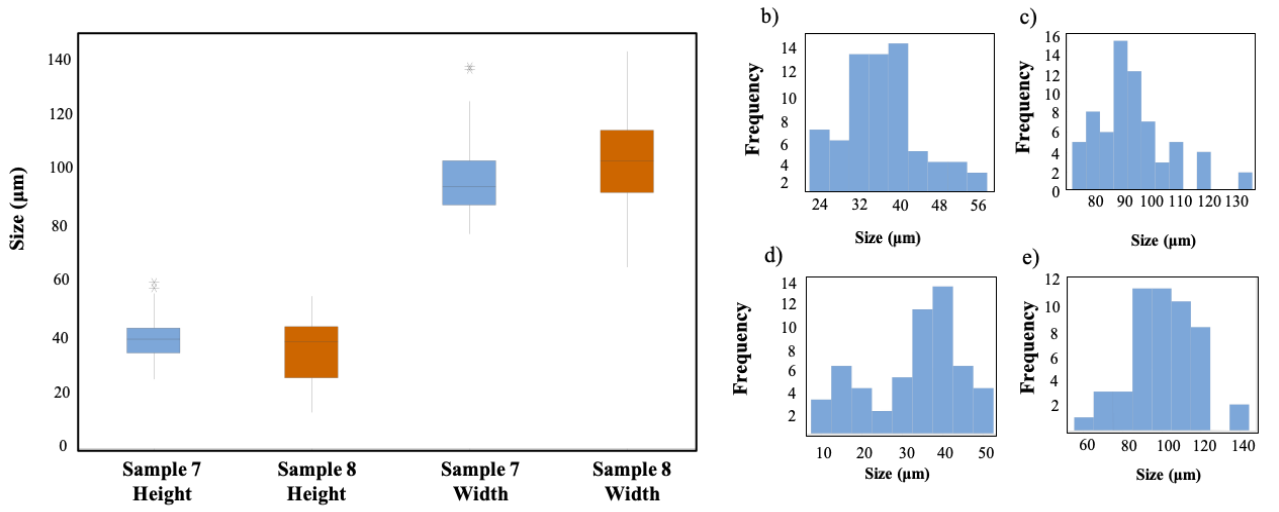

Figure 5.23. Melt track height and width variance for LPBF CM247LC samples 7 and 8 a) box plot b) sample 7 track height, c) sample 8 track height, d) sample 7 track width and e) sample 8 track width.

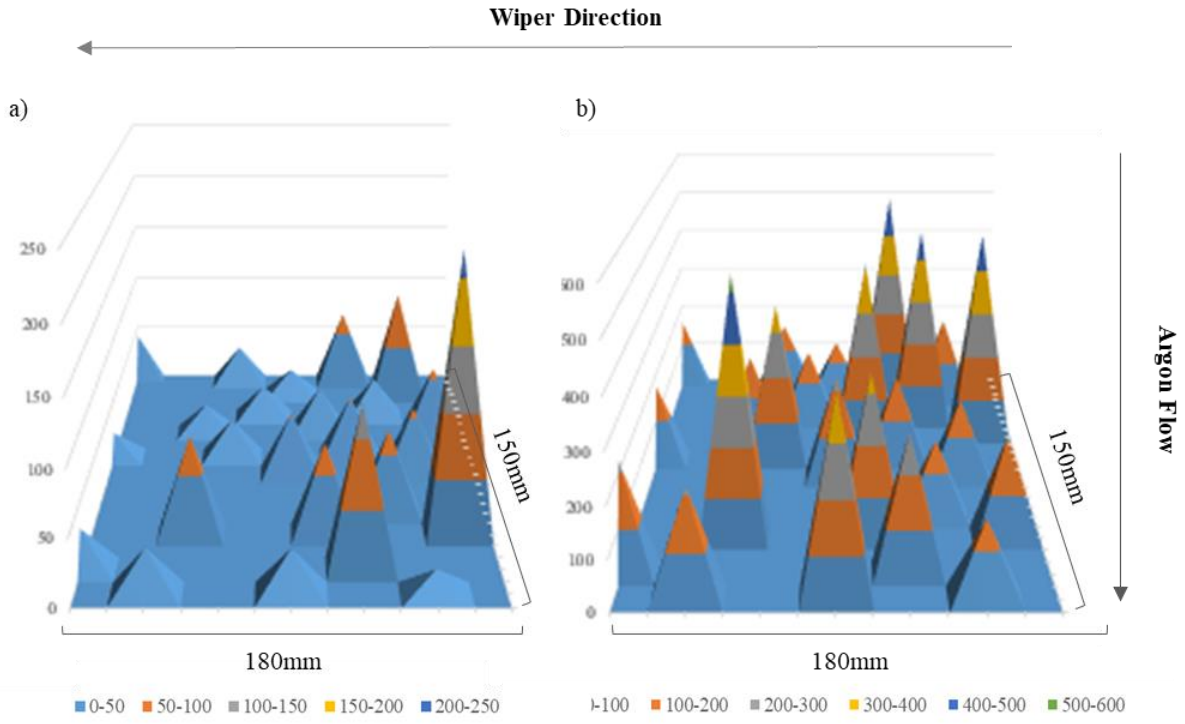

Figure 5.24. Melt track variance mapping in relation to build position for a) melt track height and b) melt track width for CM247LC LPBF builds.

5.5 Room Temperature Small Punch Tensile Testing of HIPed Rods

As mentioned, SPT testing was conducted on a selection of the HIPed rods both at room temperature (RT) and 950°C, in order to ascertain mechanical properties from small volumes of material and thus be used as a ranking tool for rapid validation. It is evident from the testing results displayed both in Figure 5.25 and Table 5.2 that parameter sets which inherently contribute to higher energy densities tend to display a greater tensile strength, in the form of maximum force (F_{Max}) as a trade-off for ductility (or disc deflection, d) at RT. This is illustrated with SPT1 (low E*, F_{Max} = 932.02N, d at F_{Max} = 0.96mm), SPT19 (medium E*, F_{Max} = 1210.61N, d at F_{Max} = 0.67mm) and SPT23 (high E*, F_{Max} = 1220.10N, d at F_{Max} = 0.60mm). This relationship can generally be further observed across the board for all individual parameter contributions, with increases in normalised beam speed continuing to display the inverse relationship previously explored with SPT 5 (low speed, F_{Max} = 1227.95N), SPT 3 (medium speed, F_{Max} = 1206.58N) and SPT 1 (high speed, F_{Max} = 932.02N) and increasing normalised beam power as represented in SPT1 (low power, F_{Max} = 932.02N) and SPT9 (medium power, F_{Max} = 1122.58N). There does appear to be one clear contradiction to the trend as observed in SPT18 (high power, F_{Max} = 589.34N), which performs considerable poorer than its surrounding LPBF variants, suggesting that is an anomaly for reasons which will be discussed later.

Microstructural evaluations were conducted on the low, medium and high energy variants tested above, where fairly minute changes were noticeable as shown in Figure 5.26. Although the mechanical trends shown would traditionally contrast Hall-Petch theory [165] and the results to be expected given the implications of energy density on grain sizing previously explored in Section 4.2, it is important to note that the sectioning methodology employed as outlined in Section 3.4 has changed with respect to the plane of view and thus a fine-grained equiaxed microstructure is subject to testing. When considering the directional heat flow apparent in additive processes, it is reasonable to assume that parameter based influence would have a lessened impact on grain size with respect to this plane. As such, alternate considerations need to be made. One observation which could innately explain the mechanical performances displayed is the change in nature of carbides as seen in Figure 5.26, where carbides appear to be more pronounced in the lower energy variants as seen in Figure 5.26a. As mentioned, additive processes and particularly lower energy depositions are suspect to more rapid solidification and as such the influence of time dependent processes such as diffusion are diminished. As energy increases, the inherent larger melt pools consequent will be subject to slower solidification rates and as such time dependent processes will be supported and in this instance it would appear as though the carbide sizing has been reduced. The influence of grain boundary precipitates and particularly carbides has been the subject of numerous investigations, where it is generally accepted that they act as obstacles for dislocation movement and thus benefit tensile performance. As such, coarsened carbides would be less favourable for pinning dislocation movement, which is why lower F_{Max} values are witnessed. Given the strengthening effect of impeded dislocation movements and precipitation strengthening, a natural drop in ductility follows suit.

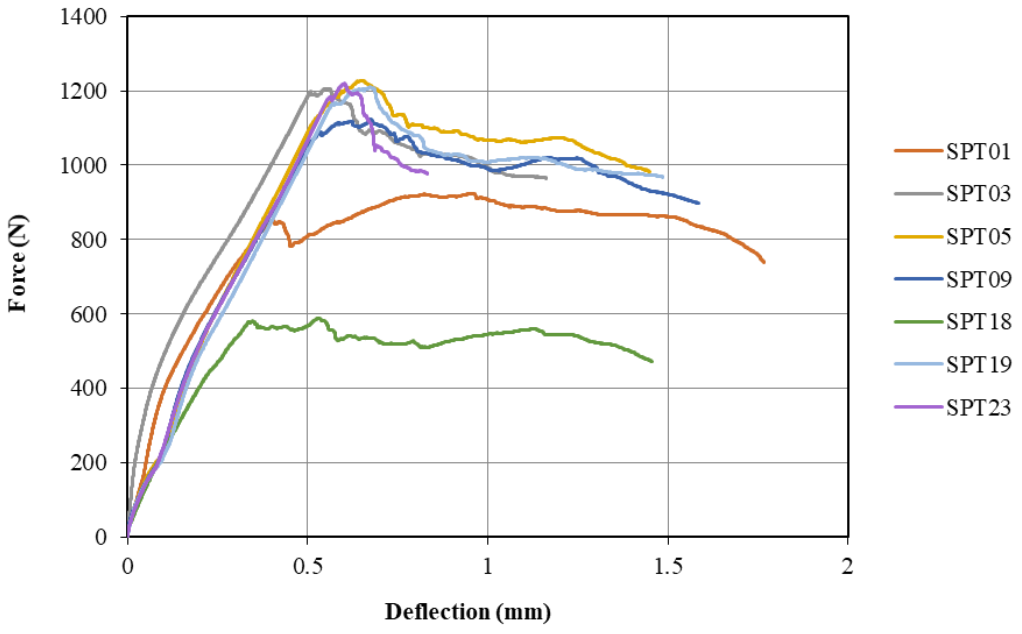

Figure 5.25. SPT testing of HIPed CM247LC LPBF variants at room temperature under a displacement rate of 0.5mm/min.

Table 5.2. Test data from SPT testing of HIPed LPBF variants at room temperature.

Sample	F_{Max} (N)	d at F_{Max} (mm)	dL at F_{Max} (mm)	F_{Break} (N)	d at break (mm)	dL at break (mm)
SPT1	923.02	0.96	1.01	738.51	1.77	1.80
SPT3	1206.58	0.56	0.81	965.30	1.16	1.27
SPT5	1227.95	0.65	1.04	982.34	1.45	1.60
SPT9	1122.58	0.68	0.89	898.06	1.59	1.58
SPT18	589.34	0.53	0.58	471.46	1.46	1.26
SPT19	1210.61	0.67	0.94	968.48	1.49	1.47
SPT23	1220.10	0.60	0.88	975.87	0.83	1.11

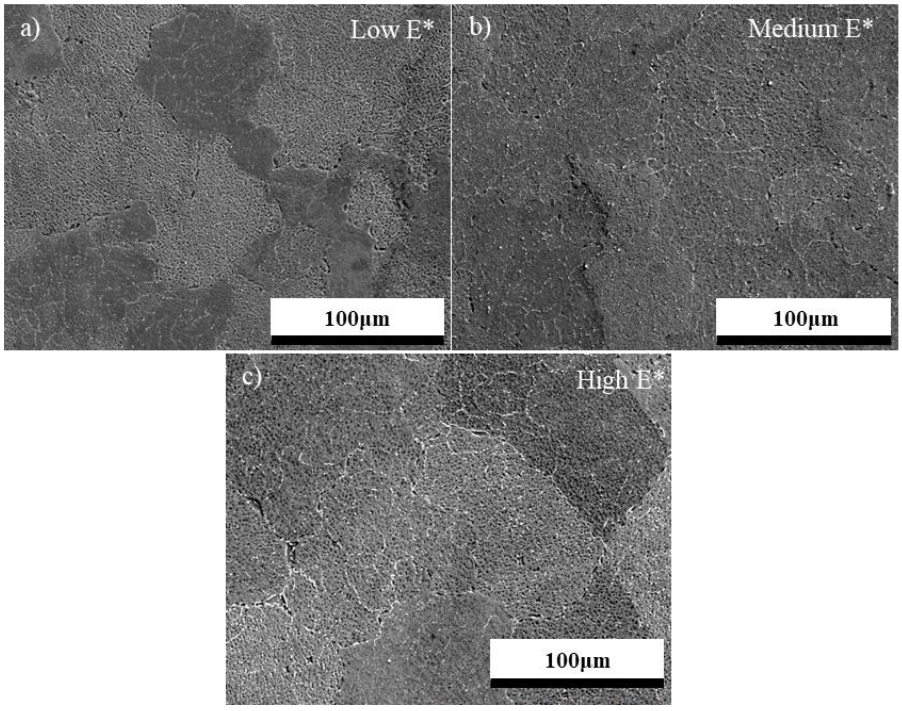

Figure 5.26. Microstructures of SPT tests conducted at RT for a) SPT1 (low energy), b) SPT19 (medium energy) and c) SPT 23 (high energy) CM247LC LPBF variants.

The relationships discussed are further examined and can be visually represented and validated in the form of low magnification fractography as shown in Figures 5.27a-e, where fractures are displayed in relation to their parameter input. Although all the fractures seen are inherently brittle given the highly strengthened nature of the alloy, it is apparent that the higher energy sample displayed in

Figure 5.27b is significantly less so with a 'moon and crescent' fracture appearance, showcasing less evident primary cracking comparative to the low energy variant seen in Figure 5.27e. This is consequent to the test determination criteria employed which is a 20% drop off in F_{Max}, with the high energy deposition variant showcasing a relatively poor damage tolerance behaviour given its loss in ductility comparative to the lower energy variant and therefore less displacement ensued. This relationship is contrasted for the lower energy variant which as mentioned, showcased respectively greater ductility behaviour and as such exhibited greater damage tolerance post rupture, leading to higher displacements being recorded before test finish. The mid-range variants for both speed and power as shown in Figures 5.27c & f appear to illustrate the transition from radial to 'moon and crescent' type cracking, where primary cracking disseminating outwards continues to ensure. The only stark contrast to the relationships discussed can be seen in the form of SPT 18 as displayed in Figure 5.27g, where given the marked decrease in F_{Max}, it is highly likely that this result is consequent to elastic heterogeneity as a result of the discrete localised region of material being subject to testing. If you consider the force decrease in relation to the damage tolerance behaviour, it is likely that this volume of material's F_{Max} performance was driven by the presence of a catastrophic defect, hindering the materials ability to withstand force, but post rupture displayed excellent damage tolerance driven by the microstructural features discussed such as grain size and carbide precipitation.

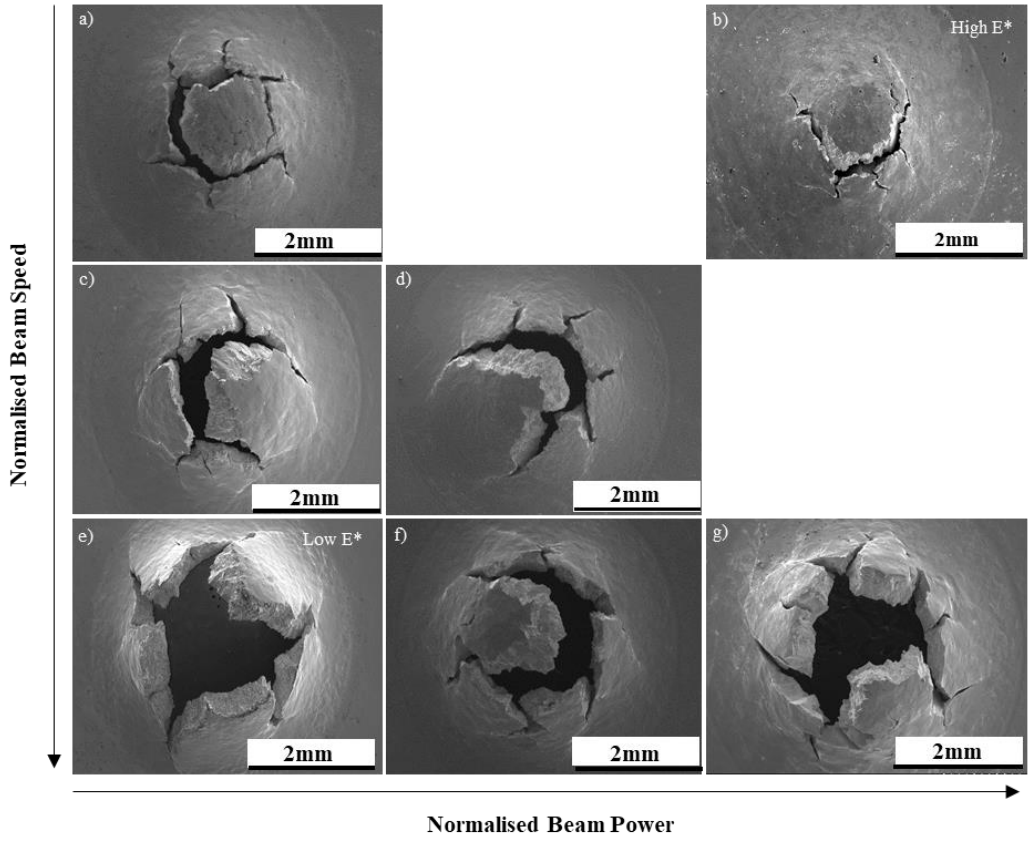

Figure 5.27. SPT fracture morphologies of tests conducted at RT positionally related to their parameter contribution a) SPT5 b) SPT23 c) SPT3 d) SPT19 e) SPT1 f) SPT9 and g) SPT18.

5.6 High Temperature Small Punch Tensile Testing of HIPed Rods

High temperature SPT tests were conducted on the same back-to-back LPBF variants previously tested at RT, as shown in Figure 5.28. It is worth noting that the comparison of process parameters in this instance becomes somewhat challenging given the premature failure of SPD01 as depicted in Figure 5.29, which occurred during the circumferential clamping process. Despite this, it is worth considering that this premature failure gives insight as to the structural integrity of the sample consequent to parameter selection and furthermore, suggests that its tensile performance would be considerably poor. Nevertheless, the existence of a notable decrease in tensile performance across the results is witnessed with F_{Max} values substantially dropping from a range of 589.34-1227.95N shown previously in Table 5.2 to 342.06–433.80N as represented in Table 5.3, corresponding with the uniaxial tensile performances at elevated temperatures referred to in Section 2.2.3.1. In addition to this, there is a substantial drop in displacement values displayed at a 20% drop off for F_{Max} post rupture, from 0.83-1.77mm to 0.52-0.72mm as shown in Tables 5.2 and 5.3, indicating that the material exhibits a substantial ductility drop at higher temperatures and thus the material's ability to withstand damage tolerance is lessened, corresponding with the relationships shown by Kim et al [51].

Given the premature failure of SPD01 and the relationships observed in Figure 5.28 and Table 5.3, similar trends to those discussed at RT partly continue to ensue. This particularly appears to be the case with regard to low energy variants performing the worst; however, it is worth noting that this relationship seems to break down as energy density increases. It can be seen that the mid-range samples for both beam power and energy density appear to display the greatest tensile strength at high temperature, SPD9 (medium power, F_{Max} = 391.53N) and SPD19 (medium energy, F_{Max} = 433.80N). This contradicts the relationships observed between process parameters and tensile performance at RT and is likely to be as of consequence to two phenomena which will be considered. The first contemplation is that the difficulties of interpreting small punch data for highly brittle materials is well documented as discussed in Section 2.4.3, and given the ductility drop observed at elevated temperatures, the data is subject to more variance given the existence of highly brittle failures which are characteristically rapid and catastrophic. As such, the existence of data crossover is of reasonable probability. The second consideration is the discrete sampling size associated with small punch which has been explored previously, where given the localised regions of microstructure subject to scrutiny, the pickup of abnormal microstructural features bears greater impact on mechanical performance and is not entirely representative of bulk properties.

The relationships and in particular the ductility drops discussed can be witnessed further during post rupture fractography across Figure 5.30, where the prominence of 'star-fish' type cracking across all samples is evident. As mentioned previously, 'star-fish' characteristics gives the indication that

stresses are at a maximum and initiate from the centre of the disc and thus radially propagates outwards, giving the implication that highly brittle failures have taken place with little to no membrane stretching. It can be seen that both the highest E* and the contributing parameter extremities (low speed, high power) samples display the least severe cracking, albeit still with brittle characteristics, supporting that of the tensile results. Microstructural analysis once again picked up the refinement of carbides with higher energy input as showcased in Figures 5.31a & b, which is to be expected considering the samples tested at both RT and 950ºC were sectioned from the same rods. Given the thin nature of the samples, minute variations in microstructural features is to be expected.

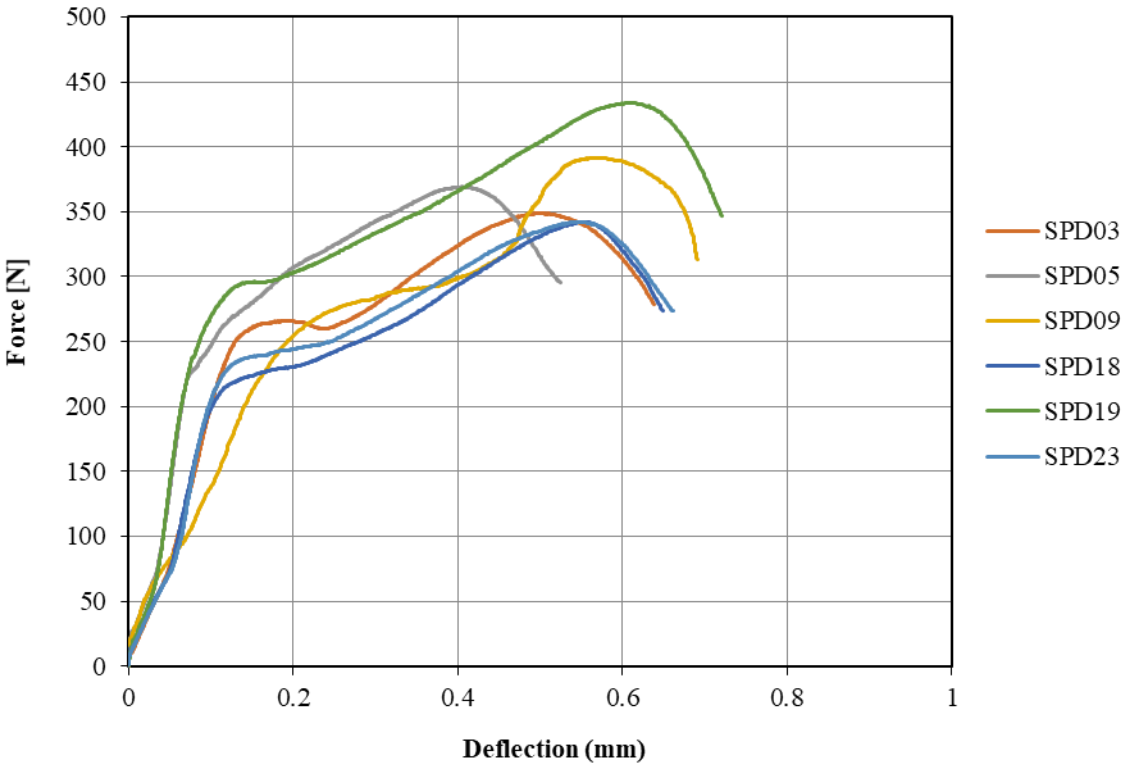

Figure 5.28. SPT testing of HIPed CM247LC LPBF variants at 950°C under a displacement rate of 0.5mm/min.

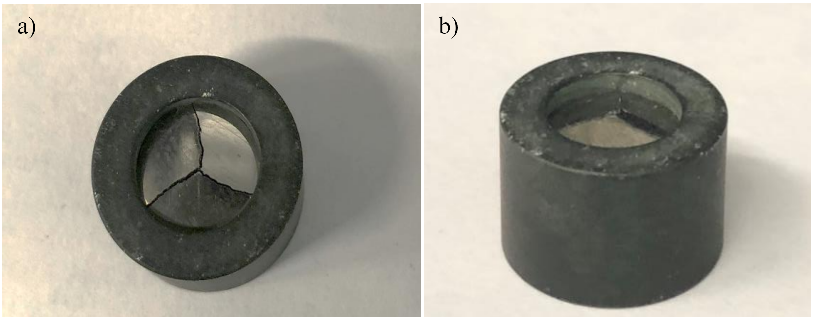

Figure 5.29. SPD1 sample cracking during circumferential clamping prior to testing.

Table 5.3. Test data from SPT testing of HIPed CM247LC LPBF variants at 950°C.

Sample	$F_{Max\ (N)}$	d at F_{Max} (mm)	dL at F_{Max} (mm)	F_{Break} (N)	d @ break (mm)	dL at break (mm)
SPD1	-	-	-	-	-	-
SPD3	348.72	0.50	0.82	278.98	0.64	0.94
SPD5	369.18	0.41	0.62	295.34	0.52	0.73
SPD9	391.53	0.57	0.72	313.07	0.69	0.81
SPD18	342.06	0.55	0.65	273.65	0.65	0.73
SPD19	433.80	0.61	0.70	346.97	0.72	0.77
SPD23	342.19	0.54	0.61	273.68	0.66	0.69

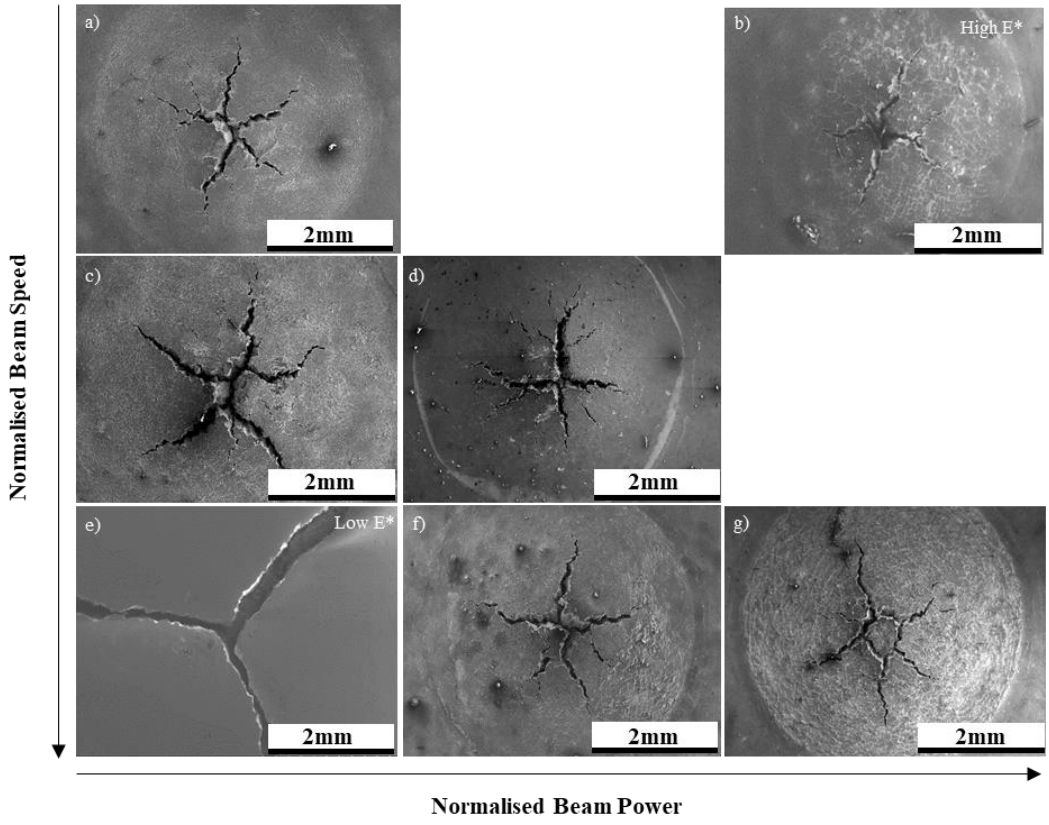

Figure 5.30. SPT fractography of CM247LC LPBF tests conducted at 950°C positionally related to their parameter contribution a) SPD5 b) SPD23 c) SPD3 d) SPD19 e) SPD1 f) SPD9 and g) SPD18.

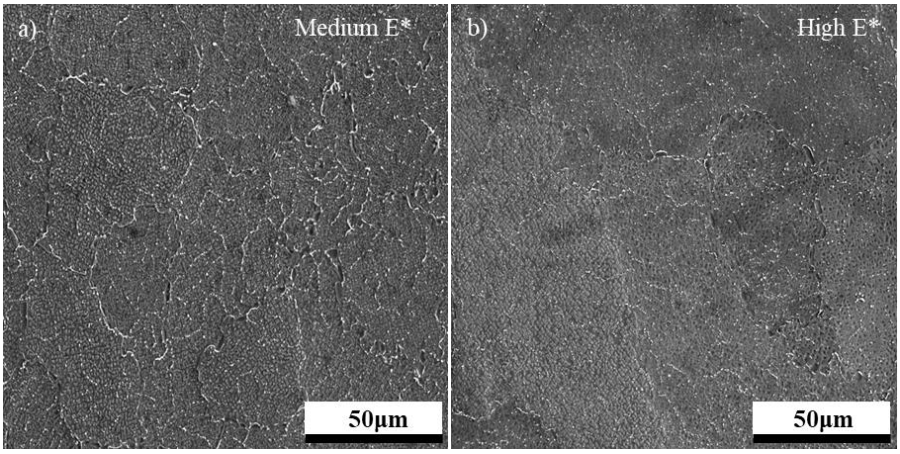

Figure 5.31. Microstructures of a) SPD19 (medium energy) and b) SPD23 (high energy) variants conducted at 950°C.

5.7 Small Punch Creep Testing of HIPed Rods

In addition to both RT and high temperature SPT tests conducted on these variants, SPC testing was employed to drive a further understanding as to the material's resistance to high temperature mechanical deformation within this DOE. Figure 5.32 displays the creep performance of these variants where it becomes apparent that SPC1 was once again subject to premature failure given the substantially lower total displacement and lack of primary region, indicating that the material ruptured prior to the traditional yielding region. It is likely that this rupture occurred either during the circumferential clamping process or subsequent to thermal expansion upon test setup. Considering this, both the time to rupture and minimum displacement rates shown in Table 5.4 for SPC1 can be disregarded. Figure 5.32 and Table 5.4 highlights the limited differentiation between process variants with regards to both time to rupture (2.48 - 7.9 hours) and minimum displacement rate (0.02452 - 0.07874mm.hr^{-}). Considering the heavy influence of anisotropic characteristics highlighted previously in Sections 2.3.4 & 2.4.5 and the apparent fine-grain equiaxed microstructures evident, these diminutive differentiations further highlight the limitations of using SPC for specific orientations in highly anisotropic materials, where in this instance, performances are more likely to be influenced by statistical variance consequent to the catastrophic failure mechanisms discussed rather than parameter-based phenomena. The minute variations discussed are further illustrated with low magnification fractography as shown in Figure 5.33, where highly brittle fractures that displayed substantial primary cracking emanating from the centre of the disc as previously discussed are consistently observed (disregarding Figure 5.33e). In addition to this, the existence of secondary cracking around the periphery of the punch tip can be seen, further highlighting both the severity and consistency of embrittlement. When considering this in relation to the microstructural imaging shown in Figures 5.34a-d, there appears to be the existence of consistent microstructural features irrespective of the changes in parameter selection, where fine-grain equiaxed microstructures with no distinguishable changes in grain sizing are present.

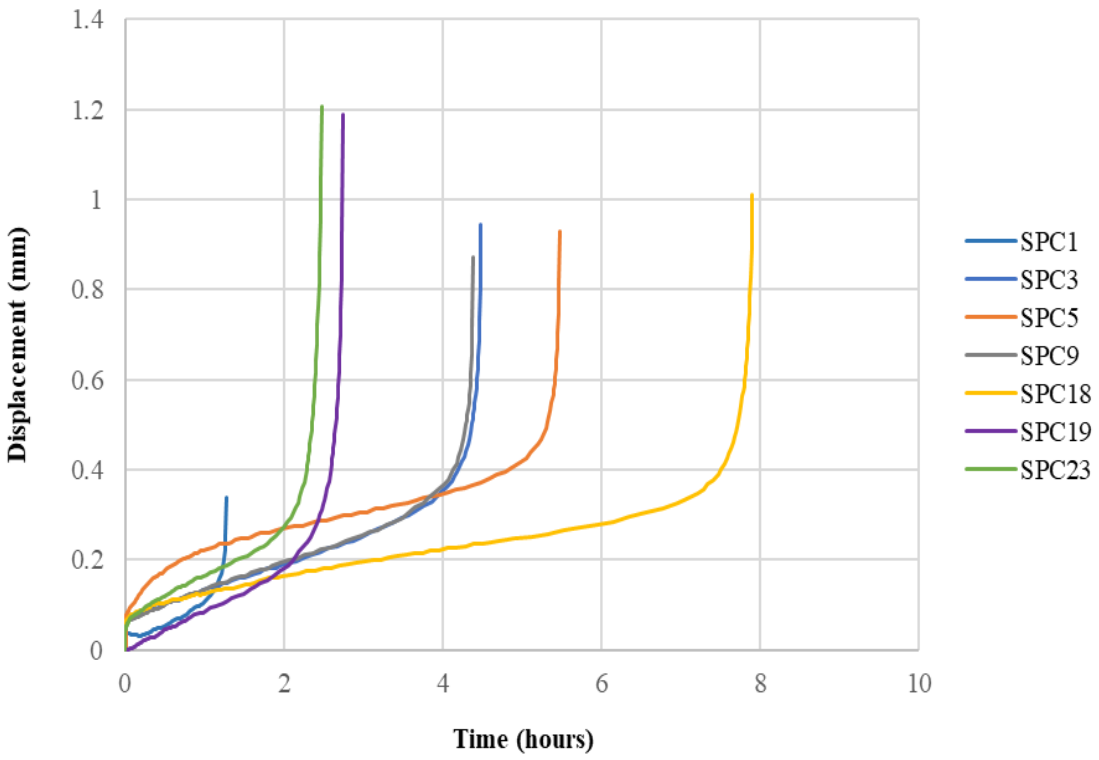

Figure 5.32. SPC testing of HIPed LPBF variants at 950°C, 150N load.

Table 5.4. Time to Rupture and Minimum Displacement Rate data for SPC variants tested at 950°C, 150N load.

Sample	Time to Rupture [Hours]	Minimum Displacement Rate [mm.hr^{-1}]
SPC1	1.28	0.01299
SPC3	4.48	0.05361
SPC5	5.48	0.03546
SPC9	4.38	0.05596
SPC18	7.90	0.02452
SPC19	2.75	0.07874
SPC23	2.48	0.07845

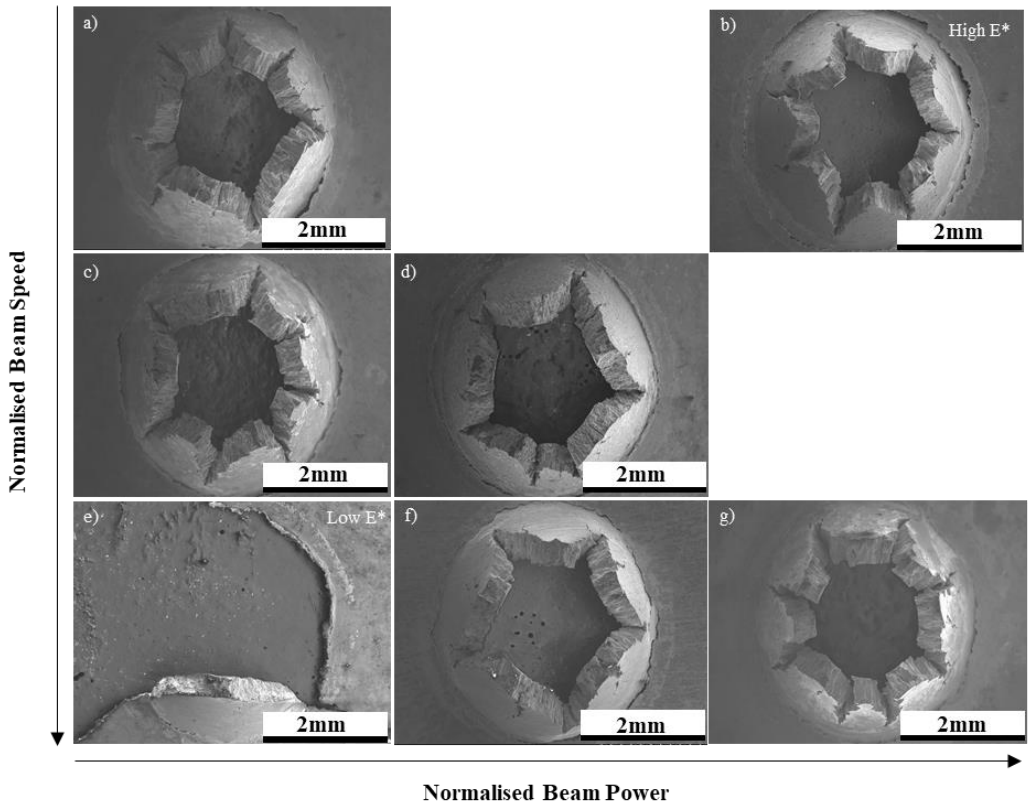

Figure 5.33. Fractography of SPC tests conducted at 950°C positionally related to their parameter contribution a) SPC5 b) SPC23 c) SPC3 d) SPC19 e) SPC1 f) SPC9 and g) SPC18.

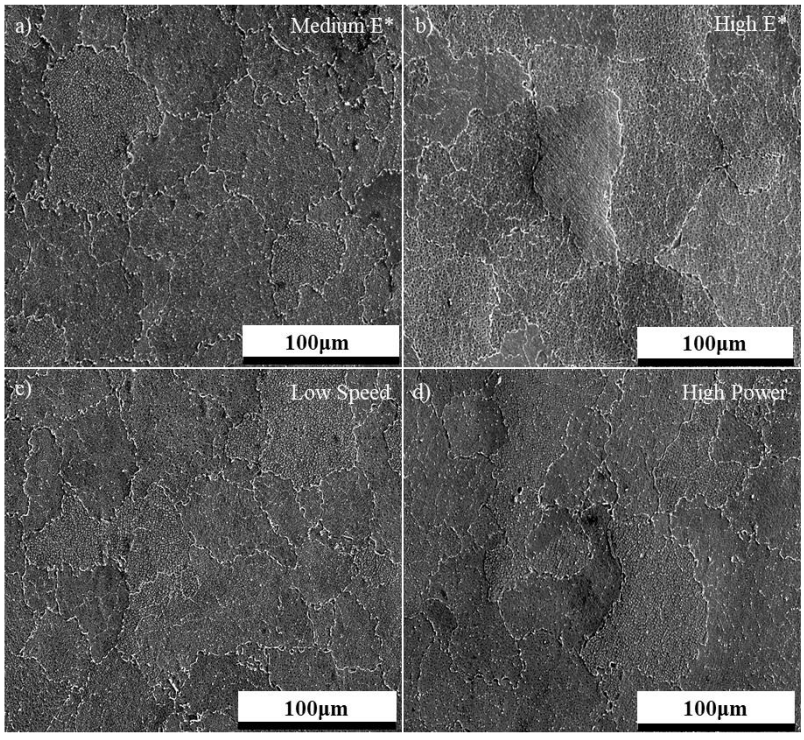

Figure 5.34. Microstructures of a) SPC19 (medium energy), b) SPC23 (high energy), c) SPC5 (low speed) and d) SPC18 (high power) creep variants conducted at 950°C, 150N load.

5.8 Summary

Overall, a robust analytical methodology was employed using manual melt track measurements alongside the image thresholding of high resolution stitched optical microscopy on an array of CM247LC LPBF variants which included changes in normalised beam speed, power and energy density. It became apparent that direct increases in normalised energy density or any subsidiary parameters inherently increased both melt track height and width. In addition to this, the propensity of CM247LC to cracking mechanisms was apparent and coincided with increases in normalised energy density, giving credence to both literature and the work showcased in Chapter 4. There was seemingly no clear existential relationship between parameter selection and porosity. The following section will look to assess whether the anisotropic behaviour explored continues to ensue in the highly weldable alloy IN718. In addition to this, variations in parameter selection will be evaluated in order to ascertain the impact of energy deposition and to establish if cracking mechanisms are solely consequential to parameter deposition or whether alloy chemistry plays a significant contributing role.

Chapter 6 – Small Scale Testing & Microstructural Characterisation of IN718

6.1 The Influence of Build Orientation on Small Punch Creep Performance

A sequence of SP creep results were collected across multiple LPBF IN718 variants, with the key distinguishing variables in this instance being build orientation and parameter selection. The initial premise of this work package was to once again evaluate the role that build orientation plays on resistance to creep deformation as shown in Figure 6.1 and Table 6.1. It is evident that build orientation contributes substantially to creep performance, where 30° builds display a time to rupture range of 1.2 – 5.6 hours in comparison to 90° builds (3.1 – 1101.5 hours). Although there does appear to be relatively miniscule crossover, it is worth noting that this only appears to be the case for parameter sets 3, (4.1 – 5.6 hours for 30° builds and 3.1 – 12.2 hours for 90° builds), which will be discussed later. Nevertheless, the relationship between 30° and 90° orientations is consistently observed across the results, with the large discrepancies of performances for 90° orientations correlating directly to parameter selection, as will be examined later.

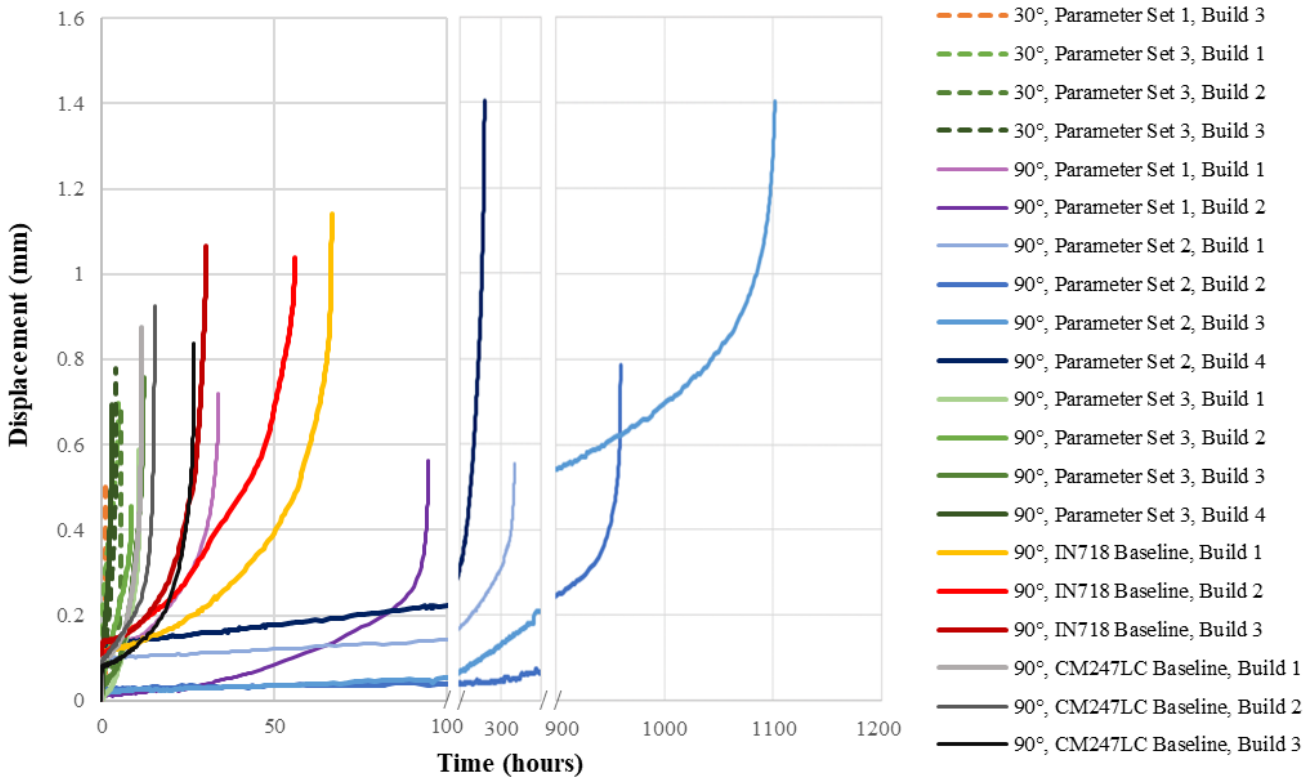

Figure 6.1. SPC results for IN718 LPBF variants at 650°C, 500N load.

Table 6.1. Time to Rupture and Minimum Displacement Rate data from all IN718 LPBF variants tested within this DOE, conducted at 650°C, 500N load.

Sample	Time to Rupture [Hours]	Minimum Displacement Rate [mm.hr^{-1}]
30°, Parameter Set 1, Build 3	1.2	0.02658
30°, Parameter Set 3, Build 1	4.9	0.07369
30°, Parameter Set 3, Build 2	5.6	0.00676
30°, Parameter Set 3, Build 3	4.1	0.08124
90°, Parameter Set 1, Build 1	33.9	0.00129
90°, Parameter Set 1, Build 2	94.6	0.00005
90°, Parameter Set 2, Build 1	351.5	0.00007
90°, Parameter Set 2, Build 2	959.7	0.00031
90°, Parameter Set 2, Build 3	1101.5	0.00011
90°, Parameter Set 2, Build 4	240.5	0.00058
90°, Parameter Set 3, Build 1	10.9	0.00918
90°, Parameter Set 3, Build 2	8.8	0.03309
90°, Parameter Set 3, Build 3	12.2	0.00535
90°, Parameter Set 3, Build 4	3.1	0.09784
90°, IN718 Baseline, Build 1	66.7	0.00044
90°, IN718 Baseline, Build 2	56.0	0.00461
90°, IN718 Baseline, Build 3	30.3	0.00021
90°, CM247LC Baseline, Build 1	11.8	0.00052
90°, CM247LC Baseline, Build 2	15.4	0.00486
90°, CM247LC Baseline, Build 3	26.8	0.00098

The changes in mechanical performance seen between 30° and 90° builds can be fundamentally explained through the microstructural examination displayed in Figure 6.2, where once more the prevalence of anisotropic microstructures consequent to the directional heat flow within the ALM process is evident. Figure 6.2a highlights the existence of an equiaxed microstructure, whilst Figure

6.2b showcases the presence of a columnar grain structure, both of which are numerically quantified in Table 6.2 through EBSD grain mapping. The grain size calculations shown in Table 6.2 approximated through the elliptical fit method indicates the occurrence of fine grains (average area 229.75μm^2) which inherently lead to a higher grain count (1337) within the captured area in the 30^o orientations; contradicting that of the 90^o orientation, which consists of coarsened grains (average area 701.02μm^2) and thus an innately lower grain count (439). As discussed previously in Chapter 4, creep deformation is a grain boundary initiated and dominated mechanism and given the heightened presence of grain boundaries apparent in 30^o orientations, a substantial rise in minimum displacement rate is to be expected (0.00676 – 0.08124mm.hr^{-1}). Conversely, the reduction in grain boundary volume fraction observed in the 90^o orientations innately rationalises the lower displacement rates witnessed (0.00005 – 0.09784mm.hr^{-1}).

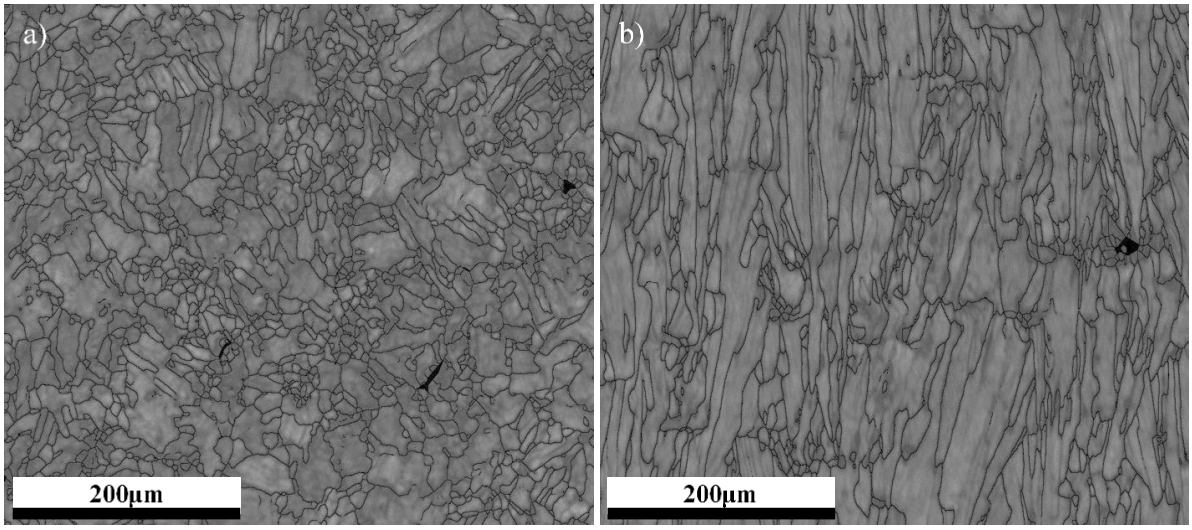

Figure 6.2. Grain boundary contrast maps of a) 30^o, Parameter Set 1, Build 3 and b) 90^o, Parameter Set 1, Build 1 at 200x magnification.

Table 6.2. Grain size measurements calculated from EBSD grain boundary contrast maps of IN718 variants.

Sample	Average Grain Area (μm^2)	Average Grain Aspect Ratio	Average Grain Diameter (μm)	Grain Count
30^o, Parameter Set 1, Build 3	229.75	1.98	11.45	1337
90^o, Parameter Set 1, Build 1	701.02	3.48	10.88	439

In addition to grain size analysis, general microstructural overviews were captured through the SEM as shown in Figure 6.3, where the changes in grain morphology, shape and size (fine grain equiaxed to coarsened columnar), can once again be observed. It can also be seen that a reasonable material density is achieved with no clear existence of cracking being observed and furthermore, the presence of unknown spherical deposits on grain boundaries appear prominent irrespective of orientation, as will be discussed later. Fractographic analysis was conducted as shown in Figure 6.4 to further understand the associated failure mechanisms, where Figures 6.4a & b emphasise the difference in embrittlement for each variant. Figure 6.4a displays the 'star-fish' cracking discussed in previous chapters, where stress appears to originate from the centre of disc and travel radially outwards, indicating a highly brittle failure as to be expected. Figure 6.4b showcases the existence of unidirectional features indicating a transition to ductile failure. However, there still appear to be signs of stress originating from the centre of the disc, which is likely down to the testing conditions selected nearing the material's capability. Nevertheless, a greater ductility than the 30^{o} orientation is underlined, albeit in still a relatively brittle fashion. Figures 6.4c & d highlight the directionality of grains respective to the material's surface, where grains are observed to be perpendicular to the materials surface in the instance of 30^{o} orientations and parallel for 90^{o} orientations. Additionally, the sharp features observed highlight intergranular failure, which is consistent with that of creep deformation, further validating the similarity of mechanisms observed between uniaxial and SP creep.

Finally, a Monkman-Grant Relationship was plotted as shown in Figure 6.5, comparing time to rupture to the minimum displacement rates seen across all variants within this DOE, including changes in parameter sets which have yet to be discussed in detail. It can be seen that build orientations and their subsequent anisotropic behaviour act as the dominant prevailing mechanism influencing creep performance, for reasons which have been explored. There does appear to be diminutive crossover within specific parameter sets as briefly mentioned, giving rise to the need for a further understanding as to the influence that parameter selection and specifically beam settings play on microstructural features and thus performance. The following section will give an overview as to this influence, with low, medium and high energy density variants being considered.

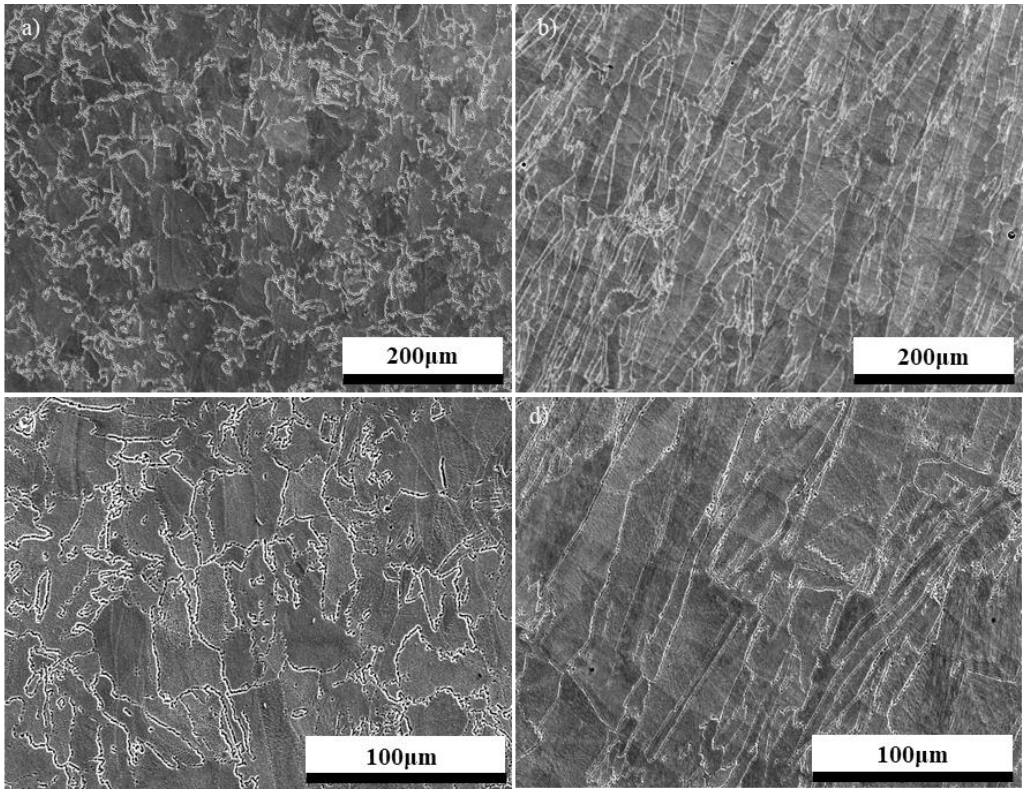

Figure 6.3. 30º, Parameter Set 1, Build 3's general microstructural observations displayed at a) low magnification c) higher magnification and 90º, Parameter Set 1, Build 1's general microstructural observations observed at b) low magnification d) higher magnification.

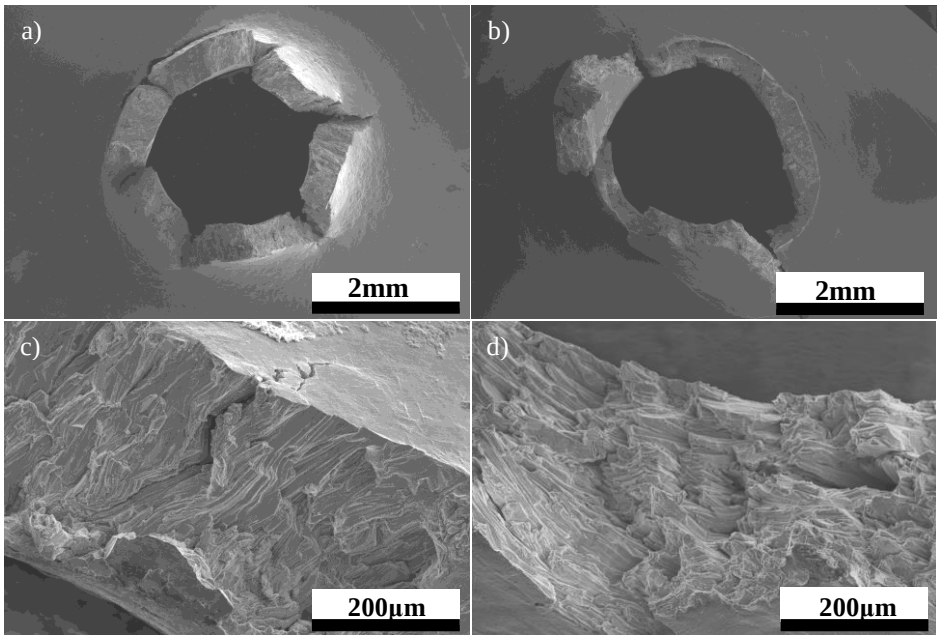

Figure 6.4. Fractographic imaging of 30º Parameter Set 1, Build 3 at a) low magnification, c) high magnification and 90º, Parameter Set 1, Build 1 at b) low magnification, d) high magnification.

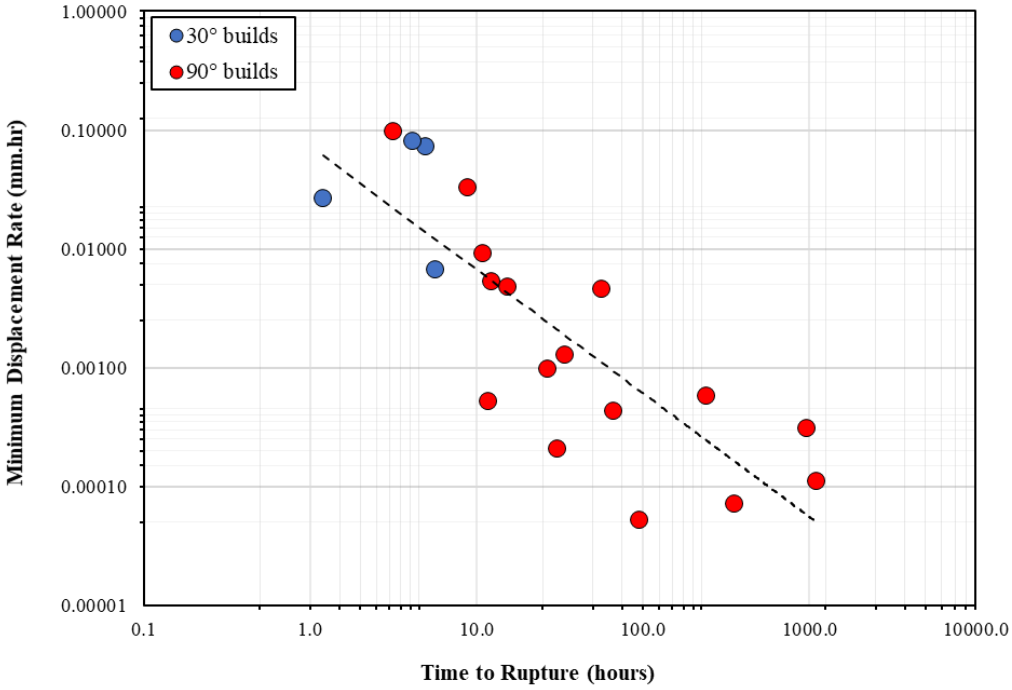

Figure 6.5. Monkman-Grant Relationships for all SPC results on IN718 LPBF builds at 650°C, 500N.

6.2 The Influence of Parameter Selection on Small Punch Creep

SPC tests were employed on a series of LPBF IN718 samples within this DOE with variations in parameter selection. Figure 6.1 and Table 6.1 showcases the influence of parameter selection on creep performance, where minute and inconsiderable changes in performance are observed for 30° orientations, irrespective of energy input (1.2 - 5.6 hours). This is further highlighted in the microstructural analysis presented in Figures 6.6, where subtle changes in relation to each other which bear no significance are observed. One observable feature however which will be discussed later in further depth is the existence of an unknown spheroidal precipitate, suspected to be delta phasing, which appears to predominantly reside along grain boundaries in this instance. As discussed in Section 2.2.3.2, IN718 is primarily strengthened by gamma double prime which is a metastable phase which is suspect to transformation into undesirable delta phasing at temperatures above 650°C. This phase transformation typically coincides with the loss of material strength consequent to gamma double prime formers being leached within the phase transformation process. EDS analysis was employed in order to confirm this phase change as shown in Figure 6.7, but it was unclear as to whether this was the case. One thing that was apparent however was evidence of niobium depletion around these precipitates as shown in Figure 6.7b, indicating leaching mechanisms consistent with the phase transformation discussed. This will be explored later as it seems to be concurrent with changes in energy density.

Fractographic analysis was conducted as shown in Figure 6.8 in order to ascertain the impact of process parameters within 30° orientations, which was seemingly insignificant given the dominant anisotropic characteristics discussed. There appeared to be substantial evidence of primary cracking emanating from the centre of the disc in all samples, once more highlighting extremely brittle failures. Considering the lack of variation witnessed and the underlying epitaxial grain growth mechanisms which are intrinsically restricted in 30° build orientations, this work will place a major emphasis on 90° orientations, given the exacerbated differentiation in performance between variants (3.1 – 1101.5 hours).

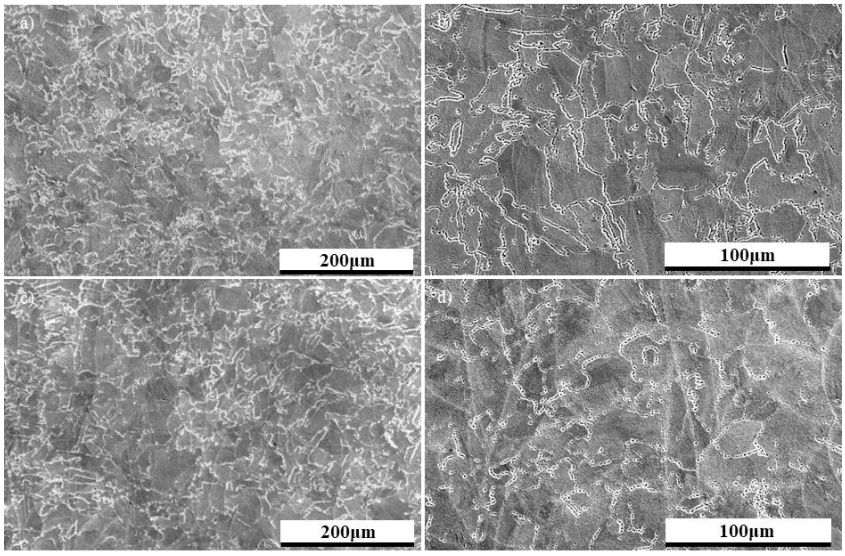

Figure 6.6. Microstructural imaging of 30° variants, a) b) Parameter Set 3, c) d) Parameter Set 1.

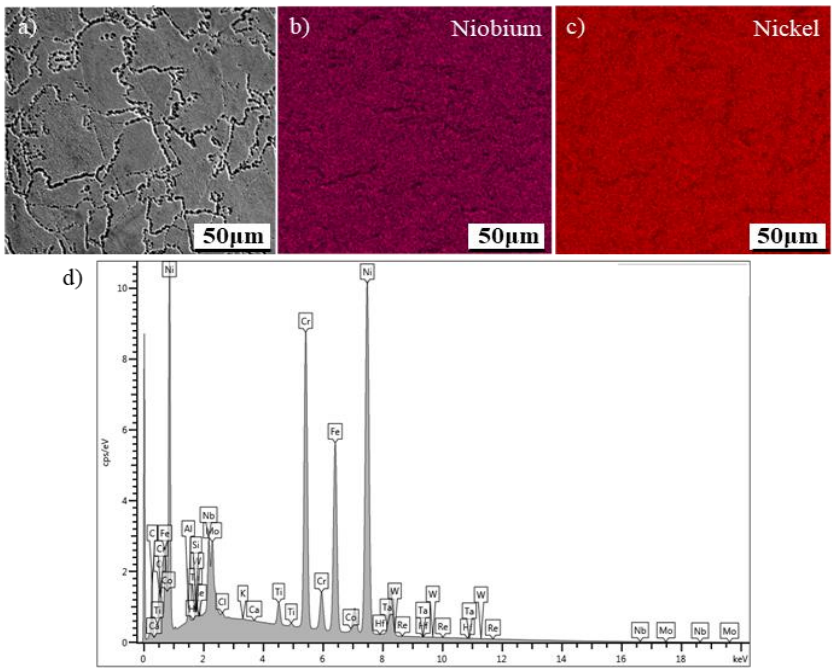

Figure 6.7. EDS analysis of spheroidal precipitates apparent in the 30°, Parameter Set 3, Build 1 sample a) SEM imaging b) Niobium c) Nickel and d) EDS spectrum.

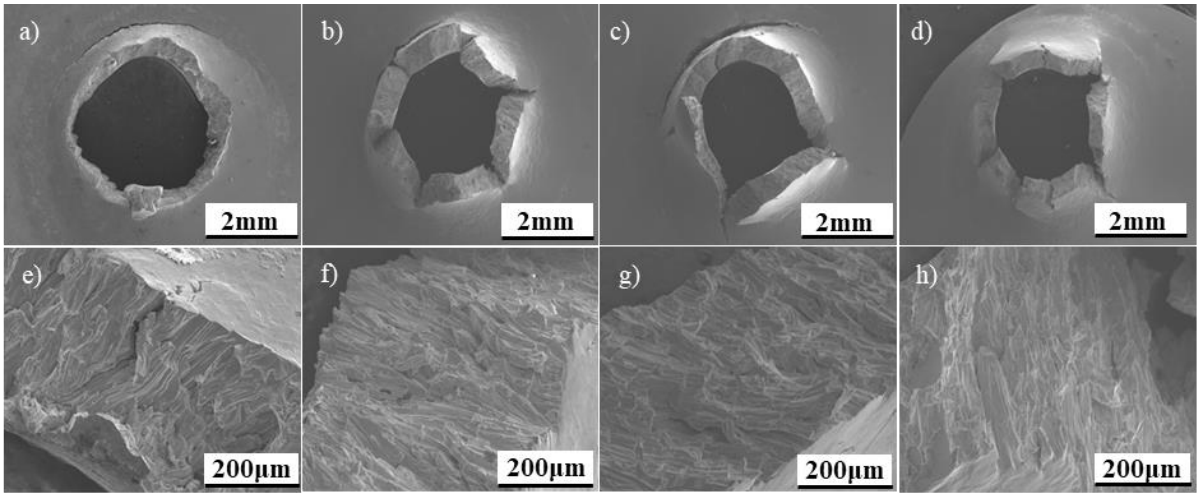

Figure 6.8. Fractographic imaging of IN718 LPBF 30° variants, Parameter Set 3 a) e) Build 1 b) f) Build 2 c) g) Build 3 and Parameter Set 1 d) h) Build 3.

For 90° orientations, it can be seen in Figure 6.1 and Table 6.1 that there appears to be a major discrepancy in performance between parameter sets, with low energy variants performing significantly poorer (3.1 – 12.2 hours), in respect to medium and high energy variants. These performances can be rationalised through both the EBSD in Figures 6.9 & 6.10, alongside microstructural analysis presented in Figure 6.11, where considerable detrimental features are commonly observed across 2 separate builds.

From a generic microstructural outlook, grain size approximations were calculated through EBSD analysis as shown in Table 6.3, giving a general indication as to the grain sizing and morphologies present in these low energy builds comparative to medium and high energy variants. It can be witnessed that these lower energy builds tend to exhibit a considerably smaller average grain size (374.74µm^2 and 517.322µm^2) and subsequently higher grain count, respective to the alternate energy variants present, which is likely to be as of consequence to the more rapid cooling rates associated with lower energy inputs. It is worth noting that although there appears to be no significant influence on average grain aspect ratios and diameters, however averages may not fully encapsulate the grain growth mechanisms consequent to this energy input as will be discussed later. The ramifications of finer grain sizes are similar to that previously explored, where creep is ultimately a grain boundary dominated mechanism and the presence of finer grains will innately lead to the heightened volume fraction of grain boundaries, giving rise to the accelerated minimum displacement rates observed (0.00918mm.hr^{-1} – 0.09784mm.hr^{-1}).

Considering the influence of cooling rates on grain size, EBSD mapping techniques were utilised in order to further understand the ramifications of these cooling rates on the underlying

microstructural mechanisms not detectable through standard electron imaging. IPF Z mapping was deployed as illustrated in Figure 6.9a, highlighting a fairly uniform texture with respect to the referencing directions employed, which consequently would support grain boundary movement as no textural or effective structural unit (ESU) mechanisms are apparent. In addition, grain size distribution mapping as displayed in Figure 6.9b highlights the presence of a bimodal grain structure, where localised regions of fine grain material are apparent. These pockets of material seemingly coincide with that of recrystallised material shown in Figure 6.9c, where there appears to be the initiation of the recrystallisation process, which looks to be stifled by the shortened freezing ranges consequent to the ALM process. This would be especially apparent in lower energy inputs, where smaller melt pools are likely to cool at a higher rate when in contact with previously deposited layers or surrounding solidified material. Given the relationship between grain size and creep rates discussed, these regions of fine grains are probable to further accelerate creep deformation by acting as initiation sites.

Figure 6.10a showcases Schmid factor mapping which illustrates how prone each grain is to crystallographic slip with respect to the available slip systems prominent in polycrystalline nickel-based superalloys ⟨110⟩ {111}, where it would seem apparent there are many grains favourable to slip deformation. Figure 6.10b represents localised average misorientation mapping, revealing high degrees of misorientation in abundance throughout the microstructure, indicating a presence of 'strain' within the microstructure which is likely to be consequent to the residual stressing mechanisms prevalent within additive processes. Finally, Figure 6.10c displays GBA mapping which reveals the degree of misorientation between adjacent grains, where HAGBs (>15^{o}) are frequently observed and are noted to be highly detrimental to creep performance within literature [9] [172]. These HAGB's coincide with the textural mapping previously examined and considering their high degree of misorientation, the pinning effects of grain boundary precipitates are substantially lessened and therefore accommodate processes such as grain boundary sliding.

Furthermore, general microstructural observations as shown in Figure 6.11 pick up the heightened presence of what appears to be delta phasing, which is predominantly situated on grain boundaries. As mentioned in Section 2.2.3.2, delta phasing is an undesired orthorhombic phase which is subsequent to overaging and the metastable transformation of gamma double prime at temperatures greater than 650^{o}C. Considering this phase's incoherency with the gamma matrix and its likelihood to form at the expense of gamma double prime, this could prove to be a contributing factor to the variant's substantially poor performance. Although EDS analysis was inconclusive to confirm the presence of this phasing, the existence of niobium depletion was apparent as shown in Figure 6.7, consistent with that of delta formation and it's leaching of strengthening alloying additions. Although the temperature fields and kinetics of delta phase formation is highly disputed in literature [42] [173], these globules appear to be relatively similar to observed cases and furthermore, are well documented to be preferential

to high angle grain boundaries [174]. While it remains unclear, it is reasonable to assume that it is fairly plausible that this could be delta phasing given the niobium depletion witnessed and its consistency with literature and if so, would inherently contribute to the variant's loss in high temperature performance.

Finally, Figure 6.11 appears to highlight the existence of lack of fusion welds throughout the microstructure, which as explored in Section 2.3.5, is subsequent to the energy input not being sufficient enough to fully melt and consolidate the material. This mechanism is given further credence too and substantiated in Figure 6.12, where un-melted powder particles are frequently observed and embedded within the microstructure. The highly detrimental features discussed appear to manifest themselves in the fractography shown in Figure 6.13, where the uniform texture explored corresponds with the existence of primary cracking which radially travels outwards in a highly brittle fashion.

Table 6.3. Grain size measurements calculated from EBSD grain maps of IN718 LPBF variants.

Sample	**Average Grain Area (μm^2)**	**Average Grain Aspect Ratio**	**Average Grain Diameter (μm)**	**Grain Count**
90^o, Parameter Set 1, Build 1	701.02	3.48	10.88	439
90^o, Parameter Set 1, Build 2	1148.2	4.03	18.49	172
90^o, Parameter Set 2, Build 2	1288.6	2.87	16.10	242
90^o, Parameter Set 2, Build 3	1286.06	3.02	10.09	228
90^o, Parameter Set 3, Build 2	517.322	3.20	15.73	379
90^o, Parameter Set 3, Build 3	374.74	2.84	11.84	527

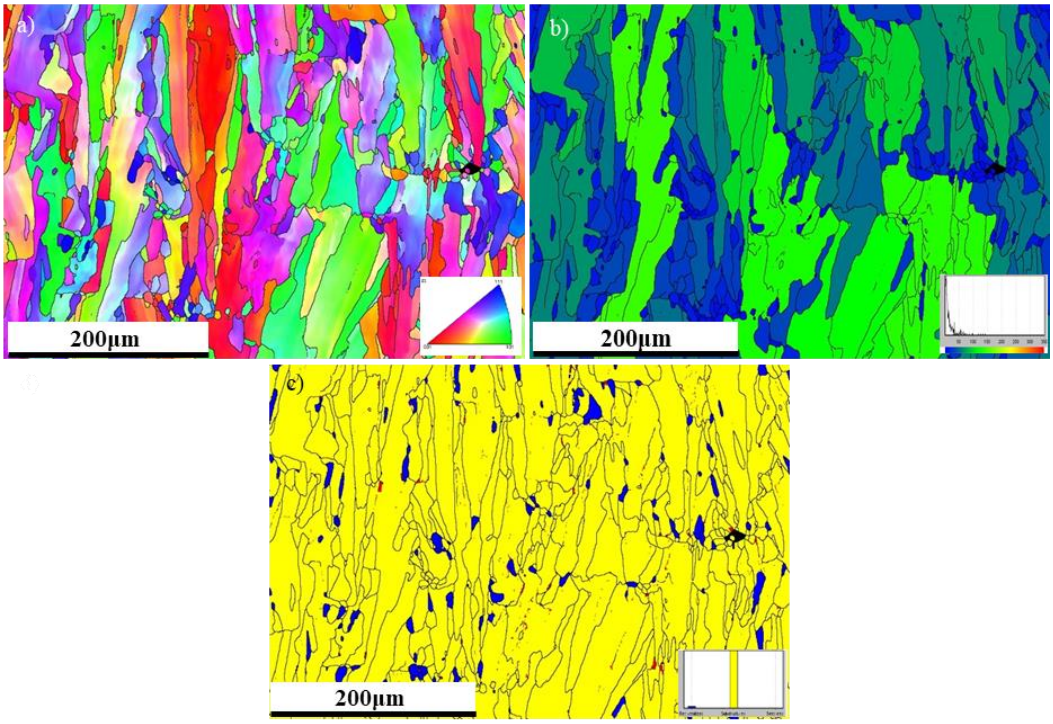

Figure 6.9. EBSD analysis of 90°, Parameter Set 3 variant a) IPF Z, b) Grain Size Distribution and c) RF mapping.

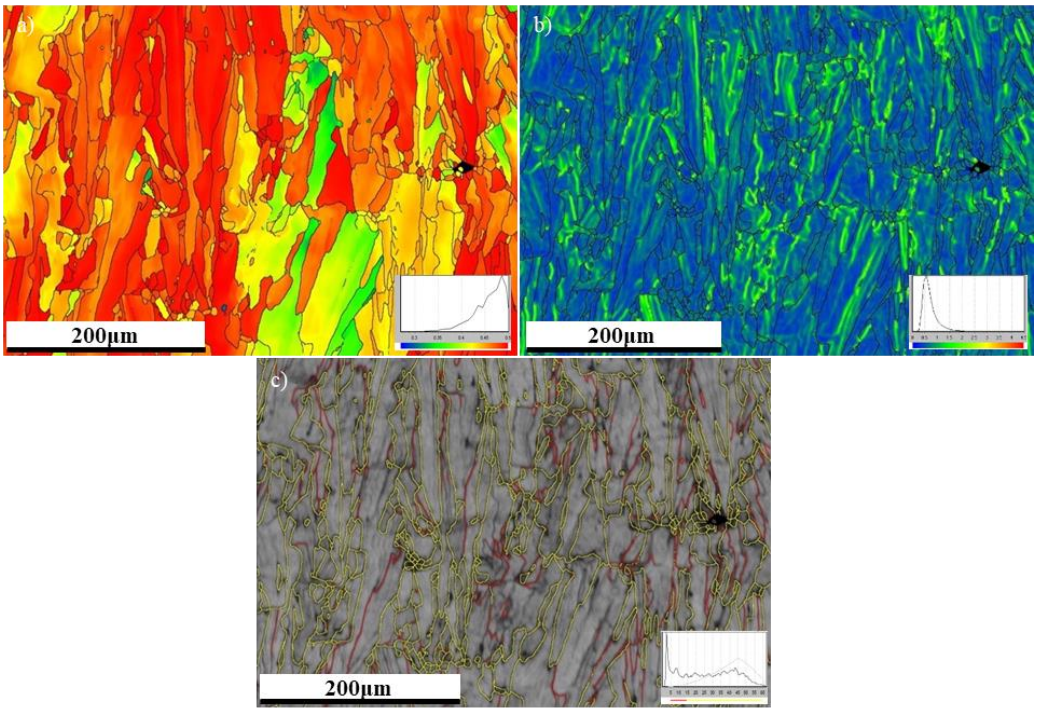

Figure 6.10. EBSD analysis of 90°, Parameter Set 3 variant a) Schmidt Factor, b) LAM c) GBA mapping.

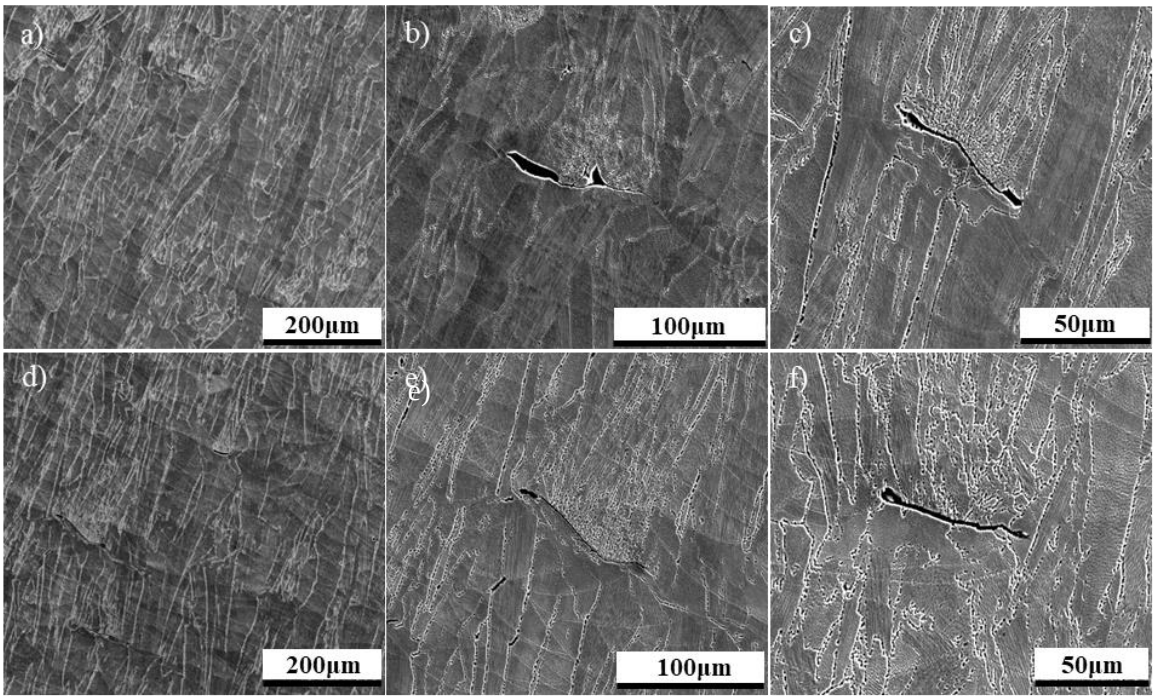

Figure 6.11. 90º, Parameter Set 3, Build 2 at a) low magnification b) medium magnification c) high magnification and Build 3 at d) low magnification e) medium magnification and f) high magnification.

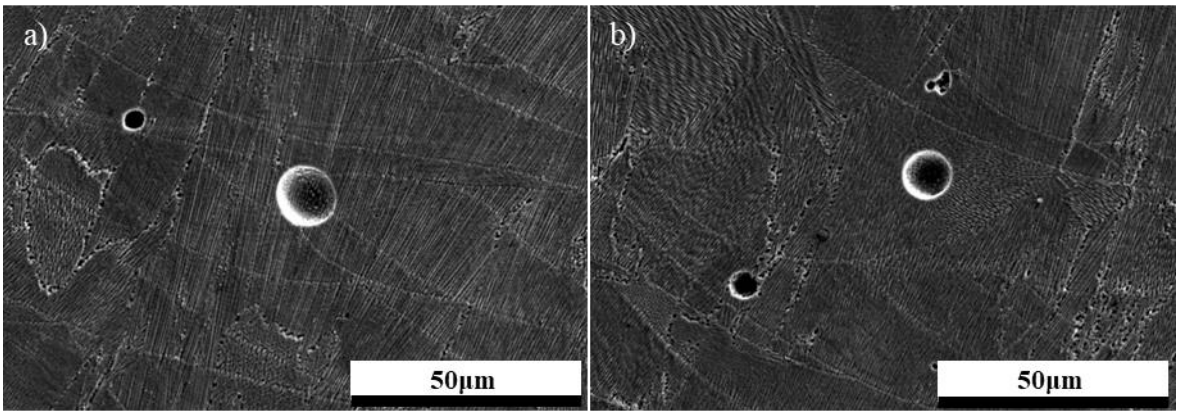

Figure 6.12. Un-melted powder particles observed in low energy IN718 LPBF variant.

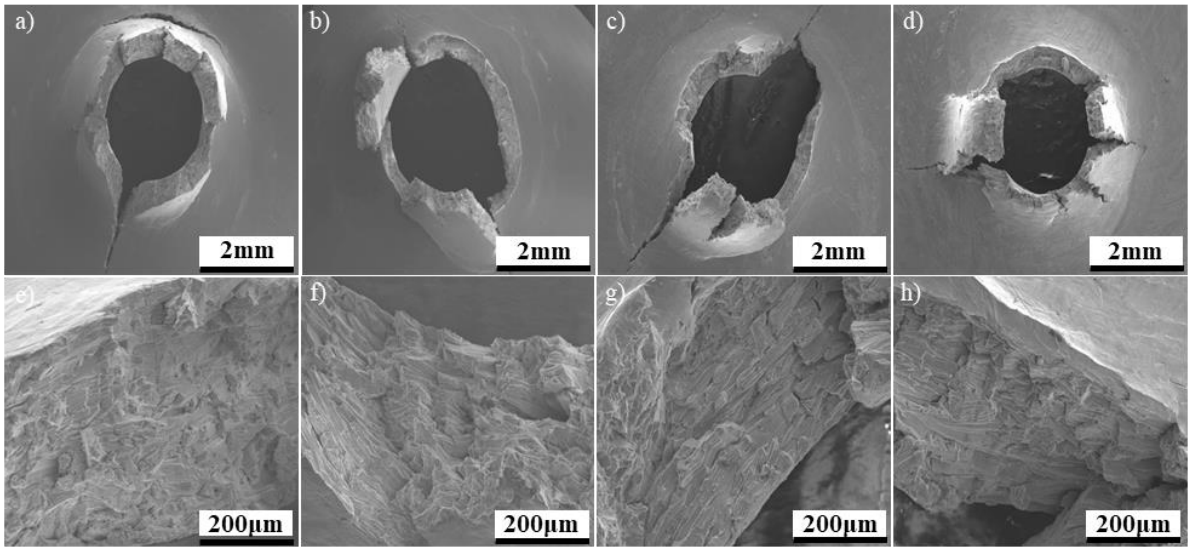

Figure 6.13. Fractography of 90°, Parameter Set 3 a) e) Build 1 b) f) Build 2 c) g) Build 3 d) h) Build 4.

Multiple medium energy density variants were tested as shown in Figure 6.1 and Table 6.1, where a marked increase in creep resistance was observed as energy input was increased (33.9 and 94.6 hours), in comparison to that of their lower energy counterparts previously discussed. Naturally, considering that creep is a statistical and time dependent phenomenon, greater high temperature mechanical performance will lead to a larger degree of disparity in the times to rupture as seen. Nevertheless, these performances can be intrinsically rationalised through a combination of general microstructural analysis and EBSD, where a reduction in the aforementioned detrimental features was observed.

Analysis of both grain size and morphology as represented in Table 6.3 indicates the presence of what is seemingly grain coarsening, where larger average grain sizes are observed (701.02 & 1148.2µm^2) in combination with a relatively lower grain count (172 & 439) across the area captured. Although there is minute crossover in regards to grain count, it is important to note the dynamic changes of grain size distribution which will be addressed. On a similar note, the average grain aspect ratio appears to increase (3.48 & 4.03) suggesting the elongation of grains, which will also be explored. The coarsening behaviour observed can be innately explained by the change of cooling dynamics consequent to increasing energy input, where it is likely that a larger energy density will lead to a larger melt pool which would be subject to a generally slower cooling rate, the extent of which cannot be quantified due to the ambiguity surrounding normalised process parameters. Nonetheless, coarsened grain structures will coincide with a lower volume fraction of grain boundaries and thus decelerate creep deformation and lessen the minimum displacement rates observed, which appears to be the case here (0.00005mm.hr^{-1} & 0.00129mm.hr^{-1}).

Additionally, EBSD mapping was exploited in order to access any underlying changes in microstructural mechanisms that have evolved comparative to the lower energy counterparts previously explored. IPF Z mapping as depicted in Figure 6.14a gives an indication as to the development of texture, specifically favourable to the ⟨001⟩ reference point, giving rise to a macro-textural effect which could benefit creep performance by acting as an effective structural unit (ESU). Furthermore, grain size distribution maps are shown in Figure 6.14b highlighting the existence of grain coarsening and the inhibition of highly bimodal grain structures, where what was previously fine grain structures appear to coarsen and elongate. This once again seemingly coincides with the recrystallisation mapping represented in Figure 6.14c, where elongated grains which are shown to recrystallise give credence to the inherently slower cooling rates attributed to increasing energy input.

Schmid factor mapping was employed as shown in Figure 6.15a to encapsulate the propensity and likelihood for grains to slip with respect to polycrystalline nickel-based superalloys available slip systems ⟨110⟩ {111}. Although the occurrence of relatively soft grains with Schmid factors in the realm of 0.4 - 0.5 is prominent, it is important to note the reduction of favourability for these grains in comparison to the lower energy variants previously discussed. LAM mapping was conducted as illustrated in Figure 6.15b, which continues to show the existence of highly 'strained' regions of material, which is to be expected given the residual stressing typically present in ALM materials. There does however appear to be a general increase in misorientation which is likely to be as of consequence of the influence of increasing energy inputs on melt pool dynamics. Although larger melt pools will innately cool slower, it will also be subject to greater disparities in cooling rates as larger melt pool circumferences will be in contact with previously deposited layers or substrates. This non-uniformity in cooling could give rise to differing thermal expansion coefficients which would likely lead to the generation of tensile loading. Finally, GBA mapping was employed as shown in Figure 6.15c, where the evolution of texture previously discussed appears to manifest itself in the formation of low angle grain boundaries (LAGB) ($<5^{o}$). Low angle grain boundaries are considerably more favourable for creep deformation as they accentuate grain boundary pinning affects and are therefore less preferential to grain boundary movement.

In addition to EBSD analysis, general microstructural observations as shown in Figure 6.16 emphasise a reasonable reduction in the volume fractions of the same precipitates witnessed in low energy variants. Although there was a level of uncertainty surrounding these precipitates, given the partial niobium depletion in surrounding regions previously showcased in Figure 6.7 alongside their similarity to delta phasing observed in literature [41] [42], it was hypothesised with reasonable plausibility that these precipitates were consequent to the metastable transformation of gamma double prime to thermodynamically stable delta phasing. It would appear in this instance, that not only has there been a reduction in volume fraction, but these precipitates seem to be more finely dispersed and

not coalesced. Furthermore, these precipitates appear to not only situate along grain boundaries, but to subside within grains. Considering this and the inherently brittle nature of TCP phasing, the reduction of their prominence on grain boundaries are likely to benefit resistance to grain boundary slippage. Finally, the microstructures appear to display a high density with strong material consolidation, where no instances of lack of fusion welds or un-melted powder particles were observed, which would no doubt bear significant influence on mechanical performance.

In view of the reduction in detrimental features alongside the development of material texture, it would appear that these mechanisms present themselves in the fractography displayed in Figure 6.17. Comparative to the low energy variants which were considerably radial, the failures observed appear to transition to and near towards unidirectional behaviour, consistent with that of the texture formation and consequently, these failures are showcased to be distinctively less brittle. Despite this, higher magnification fractography illustrates the same failure mechanisms to those previous with the presence of intergranular features, indicating that it is only the failure rate which is distinctly influenced.

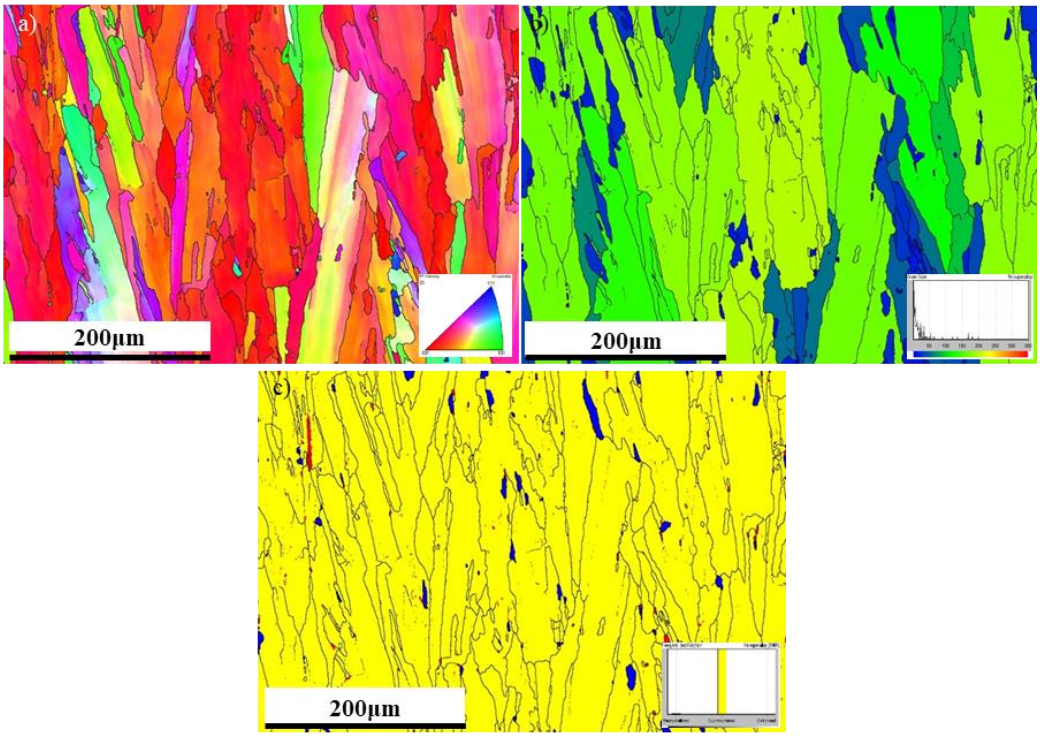

Figure 6.14. EBSD analysis of 90°, Parameter Set 1 variant a) IPF Z, b) Grain Size Distribution and c) RF mapping.

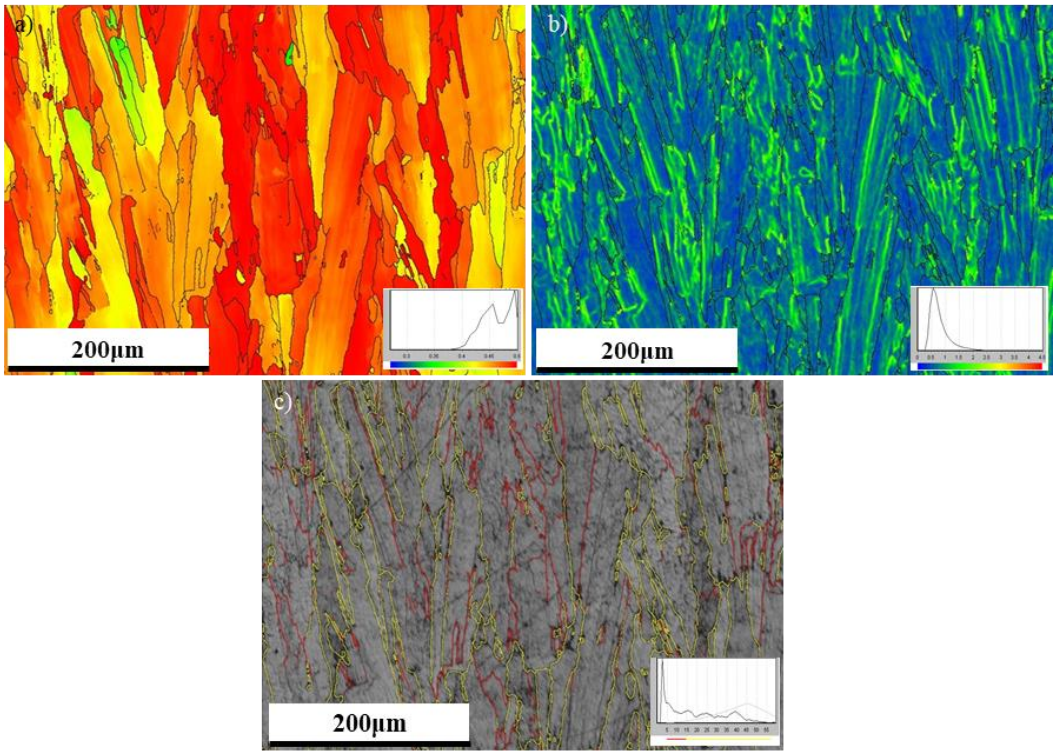

Figure 6.15. EBSD analysis of 90°, Parameter Set 1 variant a) Schmidt Factor, b) LAM and c) GBA mapping.

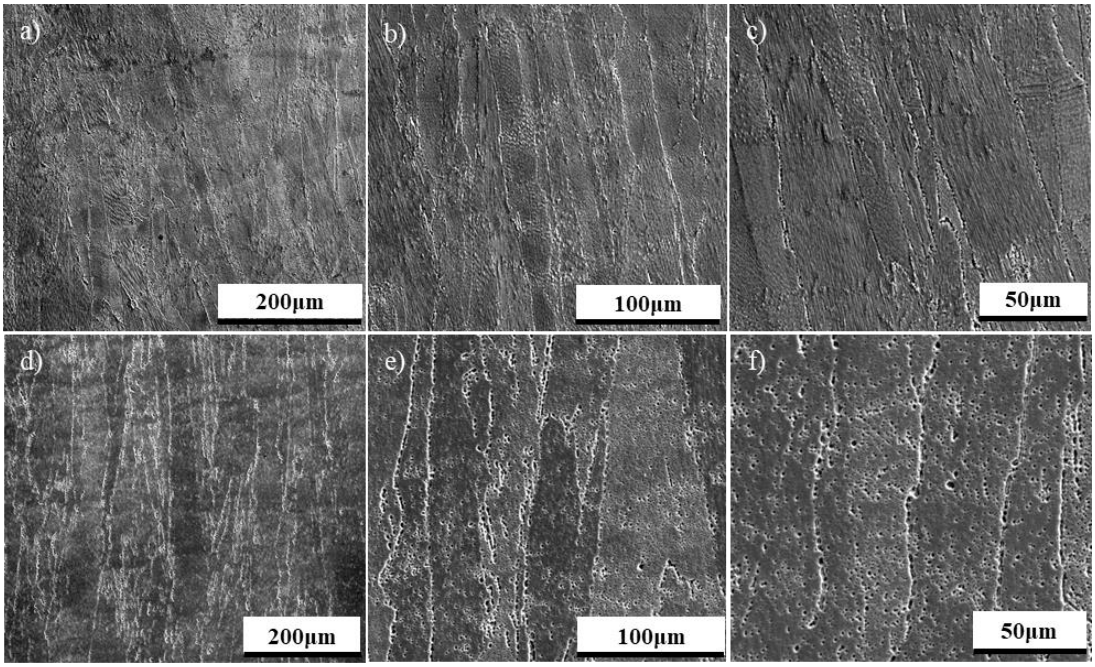

Figure 6.16. 90º, Parameter Set 1, Build 2 at a) low magnification b) medium magnification c) high magnification and Build 3 at d) low magnification e) medium magnification and f) high magnification.

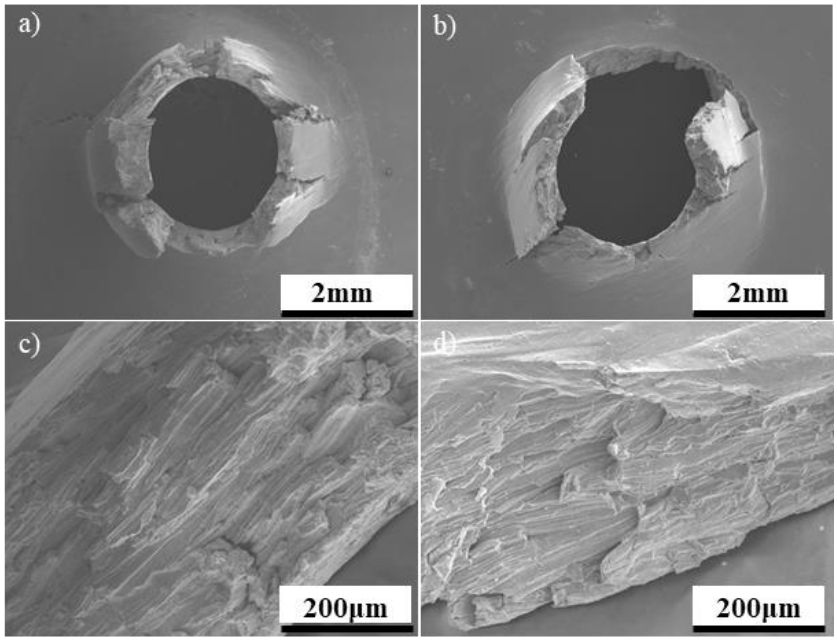

Figure 6.17. Fractography of 90°, Parameter Set 1 a) c) Build 1 b) d) Build 2.

Finally, the high energy variants tested and displayed in Figure 6.1 and Table 6.1 perform substantially greater than that of both their medium and low energy counterparts, with a time to rupture range of 240.5 – 1101.5 hours being demonstrated. Once again, given the significant increase in specimen lifetime, it is self-indicative that larger ranges in performance are observed for reasons which have been discussed. All the same, microstructural examination methodologies were adopted to further understand the principal mechanisms that underpin these high temperature performances.

Grain approximation techniques were employed in order to gauge an understanding as to the influence that energy input has on both grain size and morphology, with Table 6.3 indicating once again that further grain coarsening is apparent with respect to higher energies (1288.6µm^2 & 1286.06µm^2), for reasons which have been deliberated. Accordingly, a reduction in grain count is observed (242 & 228) across the sampled area and the average aspect ratio of grains appears to drop relative to the medium energy variants previously discussed (2.87 & 3.02), of which will be examined and explored later. Despite this, considering the obvious coarsening behaviour apparent, it is self-evident that highly coarsened grains will once again lead to a significant reduction in the volume fraction of grain boundaries and given the explored relationship with respect to creep deformation, lead to a reduction in displacement rate. This was observed as shown in Table 6.1 (0.00007mm.hr^{-1} – 0.00058mm.hr^{-1}). When considering all three energy variants, it becomes eminent that there is a clear noted relationship between average grain size and high temperature performance and it is therefore hypothesised that this acts as the predominant mechanism of performance within this alloy, coinciding with literature previously discussed [125].

Further EBSD techniques such as mapping variations were used as shown in Figures 6.18 & 6.19 in order to further the understanding of this variant and the evolving mechanisms with respect to low and medium energy inputs. Figure 6.18a depicts IPF Z mapping which once again highlights the heightened presence of texture which concurs with the textural development previously witnessed in the medium energy samples. Figure 6.18b illustrates grain size distribution mapping which indicates the clear existence of coarsened grains. However, it is worth noting the difficulty of ascertaining grain size distributions of highly coarsened material considering the sampling size of the region examined, which is why grains of a particular sizing seemingly appear to dominate the distribution. Nonetheless, the continuance of correspondence with the recrystallisation mapping indicated in Figure 6.18c continues to transpire, where recrystallised material further elongates and somewhat coarsens, providing further credence to the slower cooling rates discussed.

Schmid factor mapping as shown in Figure 6.19a highlights a reasonable reduction in the grains preferential to the slip systems available in nickel-based superalloys ⟨110⟩ {111}, where relatively soft grains consistently nearing 0.45 are occurring. Despite the soft nature of these grains, it marks an adequate reduction when compared to the bimodal distribution apparent in medium energy variants, where systems that prominently near both 0.45 & 0.5 are detected. The minimisation of grains that near 0.5 would realistically impact grain boundary sliding and thus delay processes such as creep deformation and high temperature performance. LAM mapping displayed in Figure 6.19b highlights the evolution of strain within the material, where localised hot spots of misorientation situated along grain boundaries is clear. As previously discussed, the existence of strain within the material is most likely a by-product of the residual stressing apparent in ALM processes. Considering the higher energy inputs and subsequently inherent larger melt pools, the non-uniformity of cooling is amplified given the greater volume of liquid exposed to cooler substrates/solidified material. As such, this magnified presence of disparities in cooling rate would enlarge the differentiations in thermal expansion coefficients and thus generate tensile loading, which would likely manifest themselves along grain boundaries. Given the inherent ductility of IN718, these localised regions of high misorientation and strain do not express themselves in the form of solidification cracking. GBA mapping as shown in Figure 6.19c highlights the further development of LAGBs, consistent with both the textural observations previously discussed and the slower cooling rates hypothesised. As mentioned, LAGBs are preferable with regards to creep deformation as they reinforce textural behaviour and the likelihood of adjacent grains acting as an ESU.

Moreover, observational microscopy as represented in Figure 6.20 highlights a significant reduction in what was hypothesised to be delta phasing, where the distribution of this precipitate appears to not only conglomerate along grain boundaries but subside within the matrix itself. Although it is unclear as to whether this is delta phasing, given the ambiguity of its kinetics as highlighted previously,

delta phase precipitation along grain boundaries has been shown to restrict and inhibit grain growth [175]. This could characteristically contribute to the finer grain structures observed within low energy variants, where these features are highly prominent along grain boundaries and conversely, play a minimal role in the coarsened grain structures present in the high energy variant, where their presence is more uniformly dispersed. This could provide further weight to the hypothesis that they are in fact delta phase. Considering the evolution of mechanisms explored with regards to increasing energy input, Figure 6.21 highlights their impact on fracture behaviour, where the transition from radial to unidirectional primary cracking is continuing to ensue and is heightened. It is important to note the lack of fracturing deformed ligaments witnessed in these high energy variants comparative to the medium energy variants previously shown, demonstrating improved ductility. Finally, Figures 6.21e-h highlight the similarity in the fracture surfaces, where intergranular failures are once more prevalent indicating the same failure mechanism to that of low and medium energy variants, with the key distinguishing differential being failure rate.

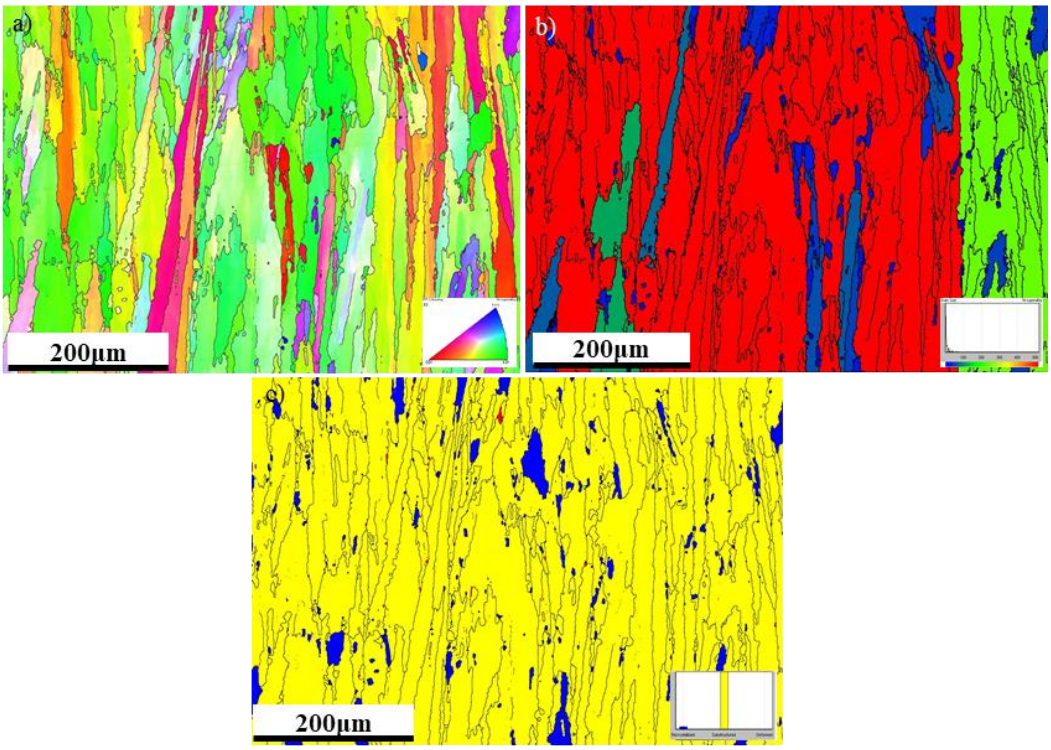

Figure 6.18. EBSD analysis of 90°, Parameter Set 2 variant a) IPF Z, b) Grain Size Distribution and c) RF mapping.

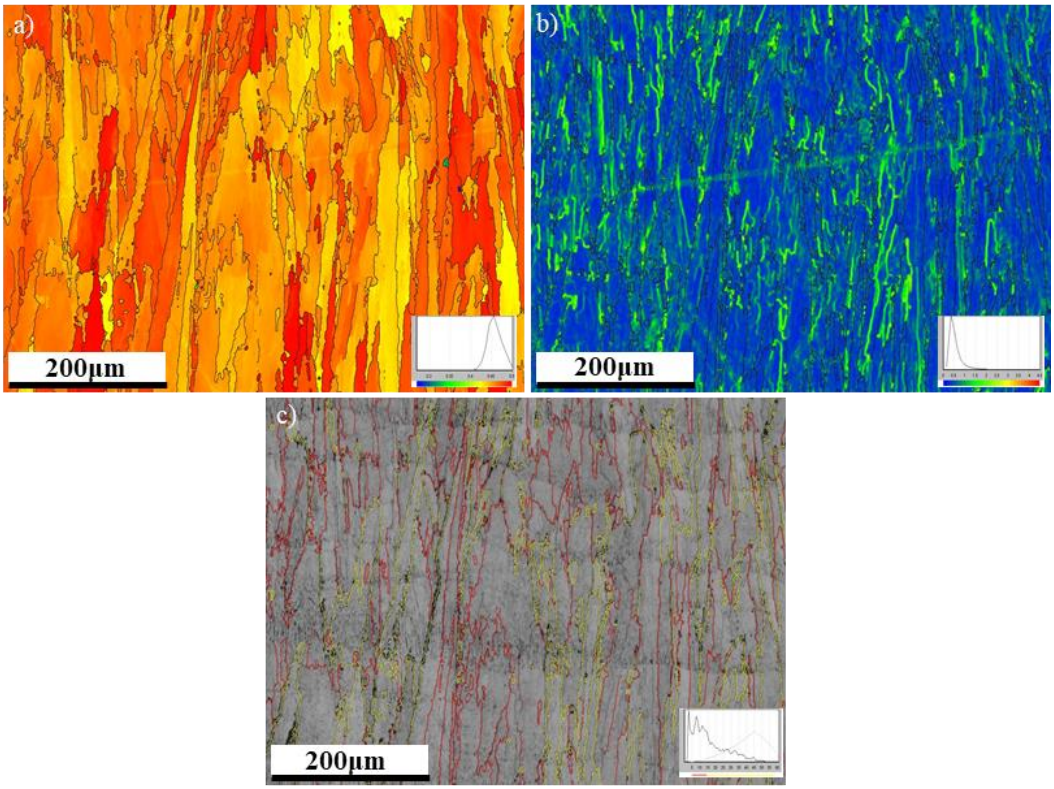

Figure 6.19. EBSD analysis of 90°, Parameter Set 2 variant a) Schmidt Factor, b) Localised Average Misorientation and c) GBA mapping.

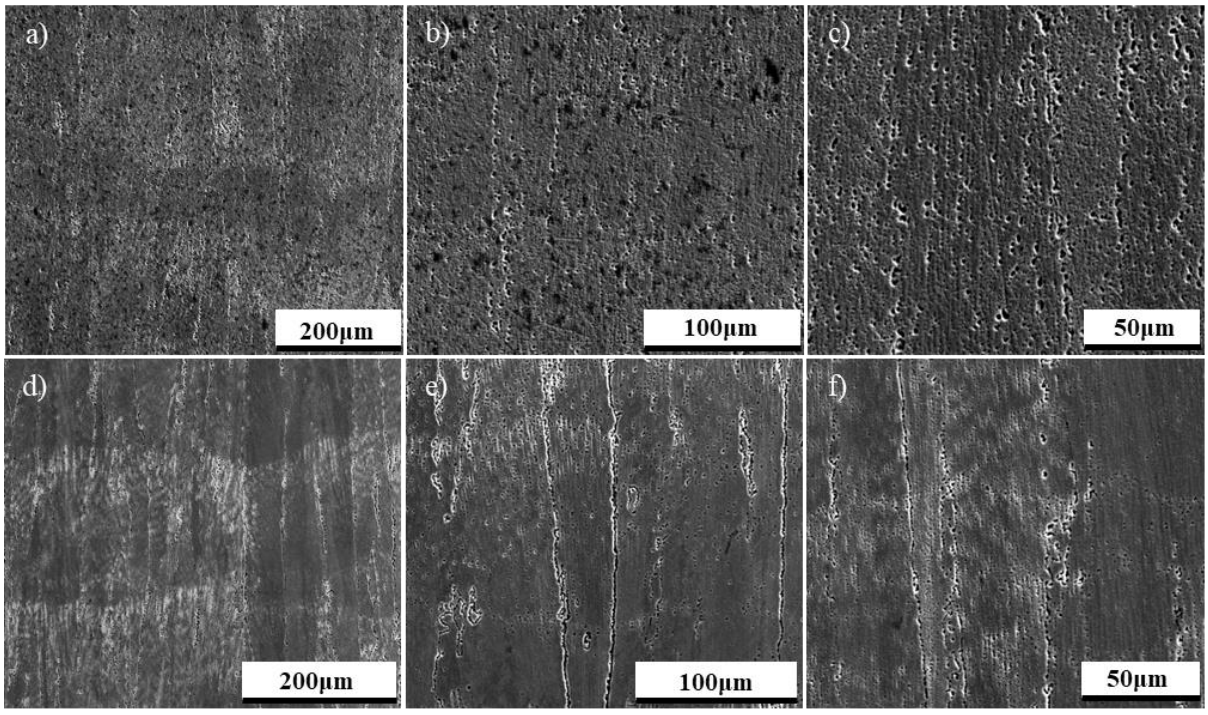

Figure 6.20. 90º, Parameter Set 2, Build 2 at a) low magnification b) medium magnification c) high magnification and Build 3 at d) low magnification e) medium magnification and f) high magnification.

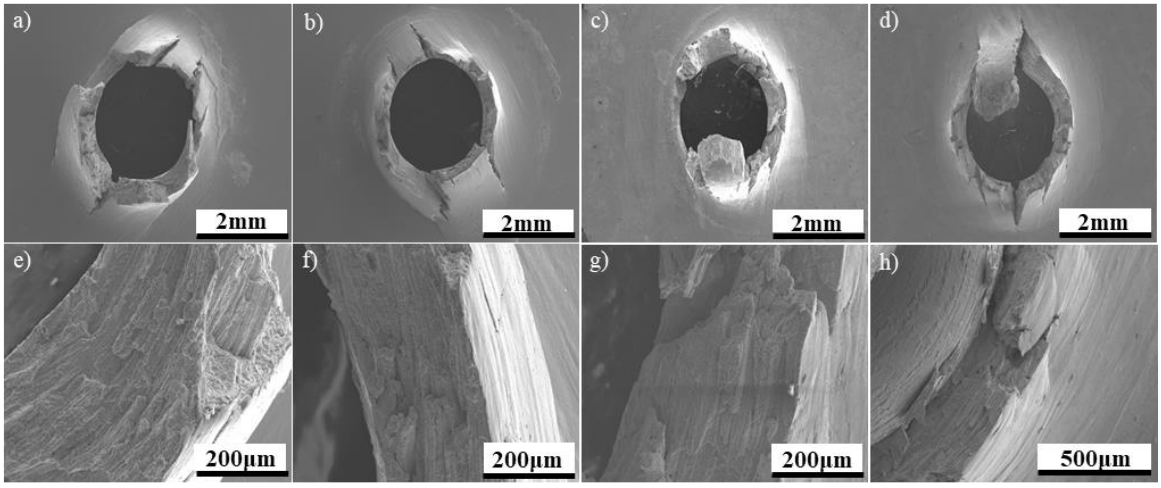

Figure 6.21. Fractographic imaging of 90°, Parameter Set 2, variants a) e) Build 1 b) f) Build 2 c) g) Build 3 d) h) Build 4.

6.3 The 'Baseline' Variants Small Punch Creep Performance

In addition to the low, medium and high energy variants discussed, undisclosed parameter sets were fabricated using both Rolls-Royce plc.'s 'baseline' IN718 and CM247LC's LPBF parameter settings. Although it may be difficult to comment on these parameter settings given the ambiguity surrounding this information, it may be feasible to approximate these parameter conditions and compare them contextually given the mechanical performance of these variants in combination with the observations and microstructural mechanisms previously explored. As such, grain size calculations, EBSD analysis, general microstructural observations and fractographic analysis were conducted.

It can be seen in Figure 6.1 and Table 6.1 that the CM247LC 'baseline' variants failed reasonably sooner (11.8 – 26.8 hours) than that of the IN718 'baseline' variants (30.3 – 66.7 hours). When considering grain sizing and morphology approximations taken from build 1 of each parameter input as shown in Table 6.4, there doesn't appear to be any significant discrepancy in grain size (501.3µm^2 and 511.1µm^2), grain count (614 & 600) for the comparative sampled regions or grain aspect ratios (3.37 & 3.46). Although a more significant separation would be expected that, it is likely that both elastic heterogeneity alongside statistical variation plays a sizeable role in this crossover. Considering this, further evaluation is needed and employed in the form of microstructural observations as shown in Figure 6.22, where material density issues such as void formation is witnessed in the CM247LC LPBF 'baseline' parameter set. The arising of this phenomenon gives a noteworthy indication that the energy input is not sufficient enough to fully consolidate this material, suggesting that the energy input nears the low energy variant previously discussed. The IN718 LPBF 'baseline' parameter set to the contrary displays no noticeable density issues and considering this in combination

with its greater performance and coarser grain structure, albeit miniscule, is likely to have been subject to greater energy input. As deliberated previously, these presence of density issues and in particular void features can accelerate creep deformation and act as initiation sites as supported in Table 6.1.

EBSD mapping was incorporated to assess underlying mechanisms, where Figure 6.23 compares and contrasts the evolution of texture, grain size distribution and recrystallisation of the two materials. It can be seen in Figure 6.23a that the development of texture is seemingly initiating in the IN718 'baseline' material, suggesting once more that this alloy is subject to slower cooling rates consequent to higher energy inputs. This appears to be contradicted in the CM274LC baseline variant as shown in Figure 6.23d which displays a highly uniform texture. Grain size distribution mapping in conjunction with recrystallisation mapping further support this notion of increased energy input, where coarsened and elongated grains with some prevalence of recrystallisation, similar to what was observed in the medium energy variants is present in Figures 6.23b & c. This once again is contrasted in Figures 6.23e & f, where a highly bimodal grain structure is evident, suggesting the existence of more significantly rapid cooling that can manifest itself in the form of deformed structure.

Schmid factor mapping coincides with these energy approximations as shown in Figure 6.24a & d, where a reduction in grains preferential to nickel's slip systems is detected in IN718's 'baseline' variant, ~ 0.45 relative to CM247LC's 'baseline' variant which displays a bimodal distribution preferential to both 0.45 & 0.5. This is once again consistent with the low to medium energy observations interpreted previously. LAM mappings showcased in Figures 6.24b & e depict the existence of high misorientation, indicating strain, which as explored is consequent to the heightened residual stressing present in additive processes. However, IN718's 'baseline' variant is showcasing the initial stages of strain localisation which appear to run parallel to the columnar grain structure apparent in the material. Finally, when considering GBA mapping as shown in Figures 6.24c & f, CM247LC's 'baseline' variant appears to display a higher prominence of LAGBs, comparative to IN718's 'baseline' variant which appears to show a gradual increase in HAGBs.

Fractographic analysis shown in Figures 6.25 and 6.26 highlight the implications of the underlying mechanisms on the overall rupture of these failures, where despite the discussed distinguishment in energy deposition, the materials' inherent brittle natures are commonly observed. Unidirectional failures seem to be readily apparent in the IN718 'baseline' builds whereas CM247LC's 'baseline' builds are seemingly at a transitionary standpoint between radial and unidirectional cracking. When bearing in mind CM247LC's propensity to crack with excess energy disposition as highlighted both in the literature discussed in Section 2.3.3 and the results explored in Section 4.2, and the apparent mechanisms discussed above, it is reasonable to hypothesise that the 'baseline' parameter set nears the low energy variants previously examined. To the contrary, considering IN718's well acknowledged

ductility and weldability in combination with the evidence discussed, it's fairly plausible that the energy deposition is in the mid region between the low and medium energy variants previously analysed.

Table 6.4. Grain size calculations for LPBF IN718 and CM247LC 'baseline' parameter sets.

Sample	Average Grain Area (μm^2)	Average Grain Aspect Ratio	Average Grain Diameter (μm)	Grain Count
90^o, IN718 Baseline, Build 1	511.1	3.46	11.10	600
90^o, CM247LC Baseline, Build 1	501.3	3.37	14.05	614

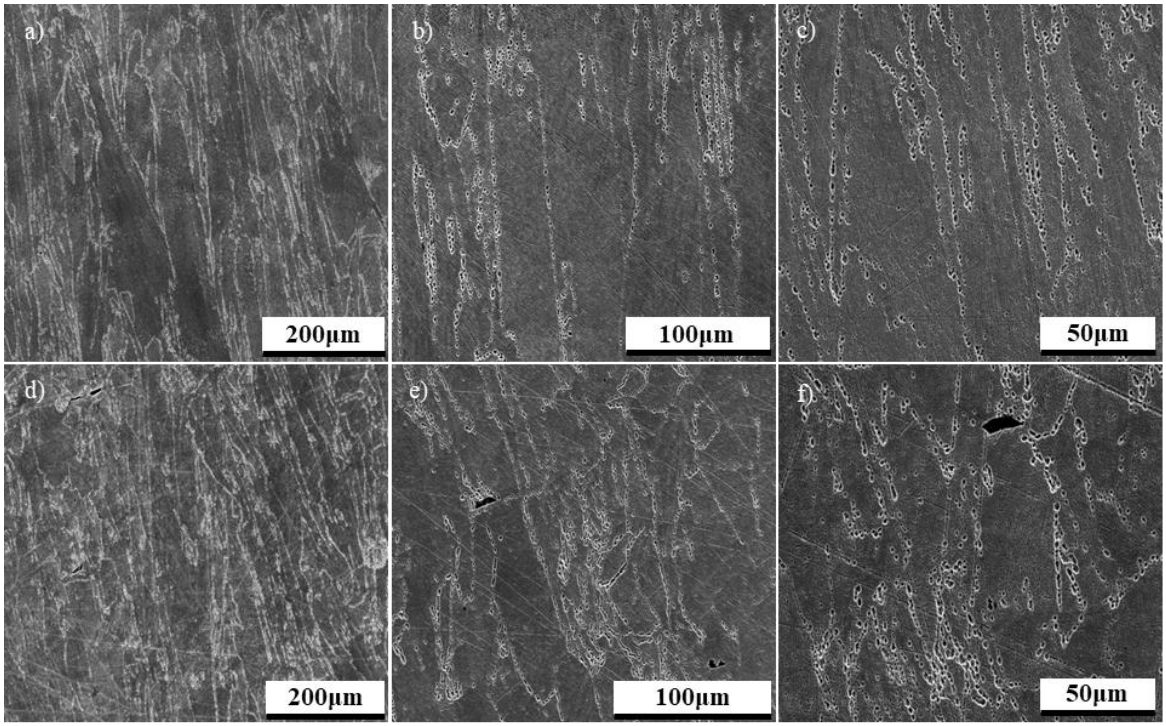

Figure 6.22. Low, medium and high microstructural imaging of a) b) c) LPBF IN718 'Baseline' d) e) f) LPBF CM247LC 'Baseline' variants.

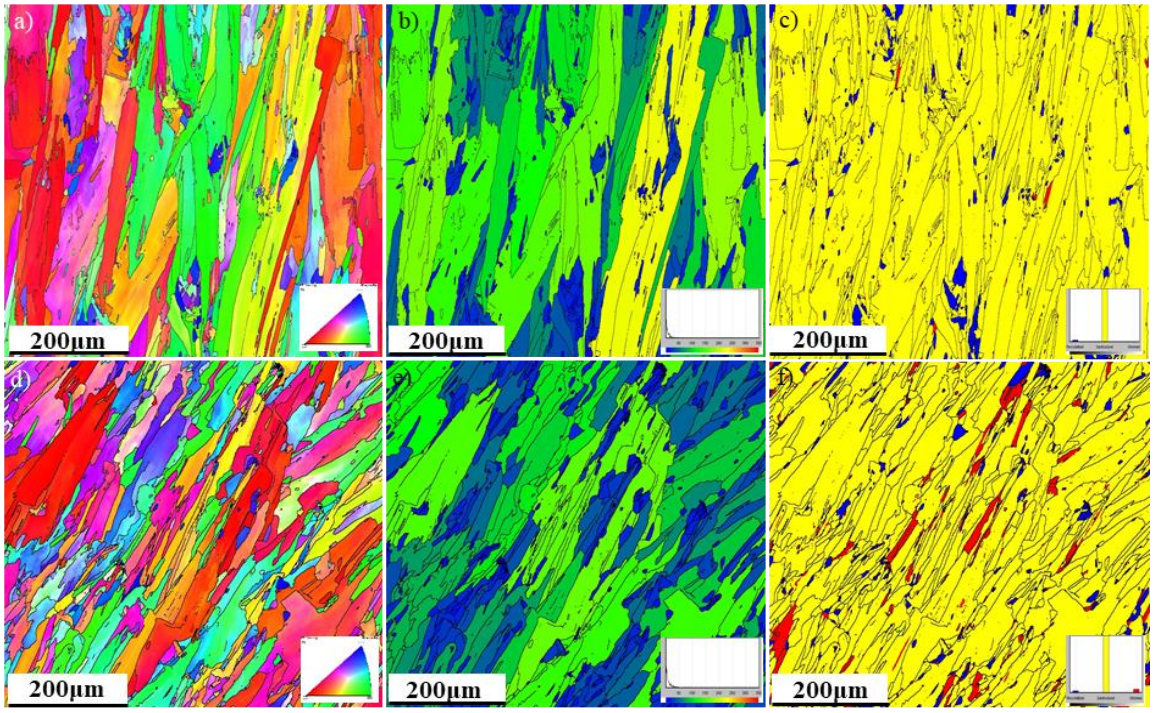

Figure 6.23. IN718 LPBF 'Baseline' Parameter Set a) IPF Z b) Grain Size Distribution c) RF mapping and CM247LC LPBF 'Baseline' Parameter Set d) IPF Z e) Grain Size Distribution and f) RF mapping.

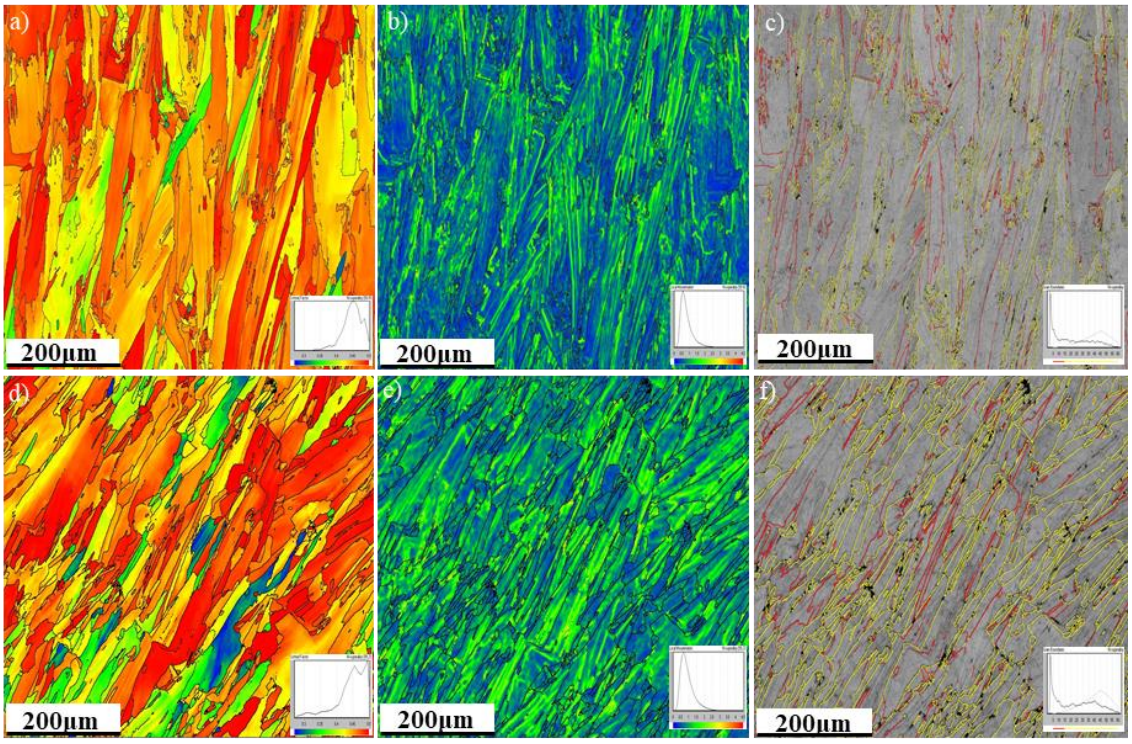

Figure 6.24. IN718 LPBF 'Baseline' Parameter Set a) Schmid factor b) LAM c) GBA mapping and CM247LC LPBF 'Baseline' Parameter Set d) Schmid factor e) LAM and f) GBA mapping.

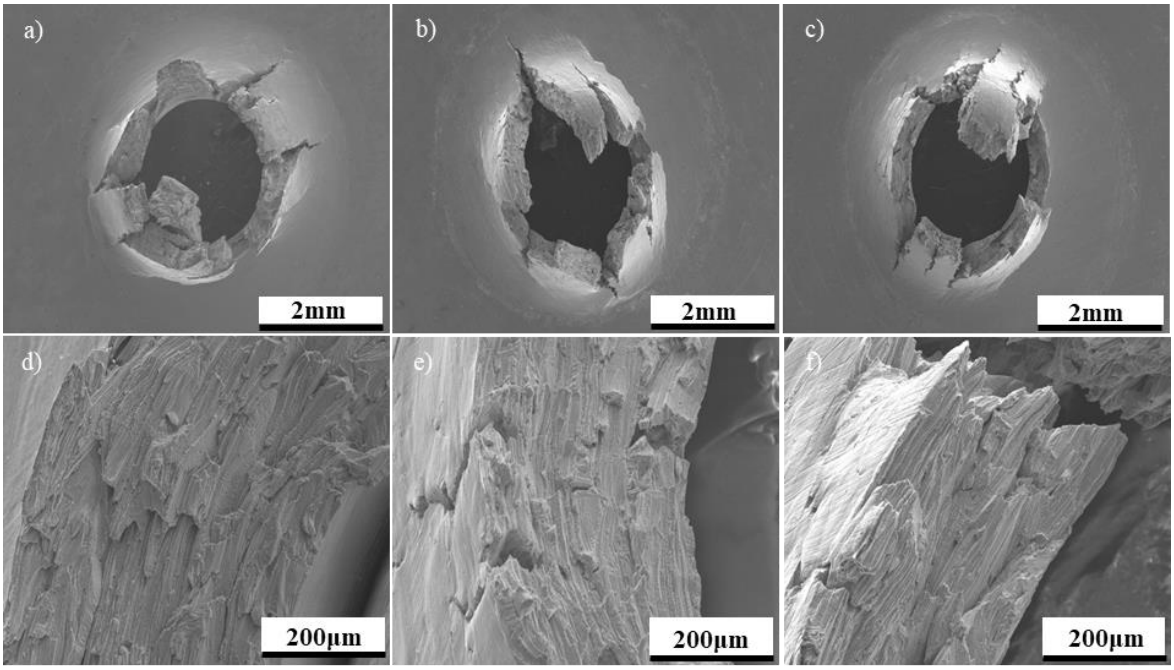

Figure 6.25. Fractographic imaging of LPBF ‘IN718 Baseline’ a) d) build 1, b) e) build 2, c) f) build 3.

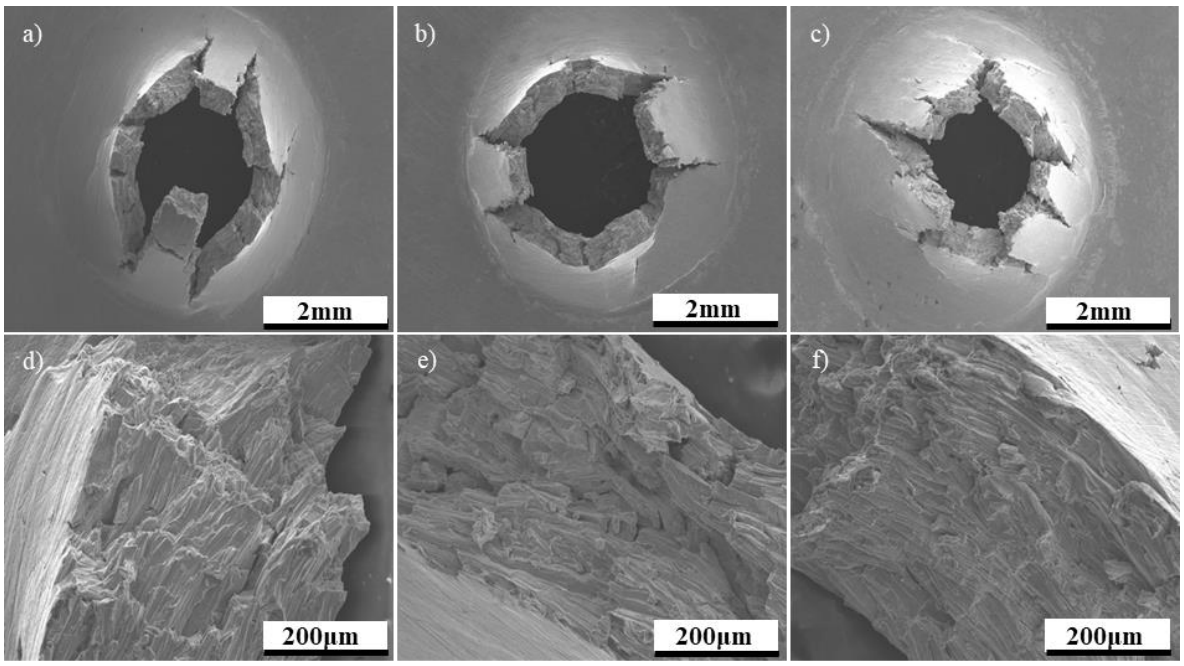

Figure 6.26. Fractographic imaging of LPBF ‘CM247LC Baseline’ a) d) build 1, b) e) build 2, c) f) build 3.

6.4 The Small Punch Tensile Performance of the 90º Parameter Variants

In addition to SPC testing, back to back LPBF variants were subjected to high temperature SPT testing at 650ºC, with a displacement rate of 0.5mm/min being employed. The influence of low, medium and high energy inputs was considered first as represented in Figure 6.27 and Table 6.5, where there appears to be a general relationship observed between energy input and high temperature tensile performance.

When considering F_{Max} as a criterion, there appears to be a relatively consistent relationship displayed with increasing energy input, where low energy samples displayed the poorest performance range (1206.26N – 1356.81N). When relating these performances to the microstructural examinations previously deliberated in Figure 6.11, it becomes apparent that lower energy inputs were subject to the influence of material consolidation and density issues, particularly lack of fusion welds and unfused powder particles. As such, it comes as no surprise that there was a considerable drop off in F_{Max} observed, as these sites can inherently weaken the material system when subject to tensile loading. Despite the presence of defects which will intrinsically inhibit the maximum force in which the system can withstand before rupture, it is worth noting the sizeable displacement at break values demonstrated (0.80 – 1.43mm) with respect to the displacements observed at F_{Max} (0.70 – 0.79mm), indicating a reasonable level of damage tolerance post rupture. This can innately be explained through the grain size measurements showcased in Table 6.3, where low energy variants were shown to display a substantially finer grain size. It is well acknowledged that tensile performance is directly related to grain size in accordance to Hall-Petch theory [165].

The microstructural examinations previously interpreted as shown in Figures 6.16 and 6.20 for medium and high energy builds appear to display little to no material consolidation issues, providing context as to the crossover in F_{Max} values, 1365.28N & 1437.65, in comparison to 1326.11N – 1849.11N. The higher F_{Max} values in respect to their lower energy counterparts can be exemplified by parameter set 2, build 3, the major outlier from a performance standpoint (1849.11N). When comparing the SPT performances of these samples to their back to back SPC variants they appear to generally corroborate, with parameter set 2, build 3 again displaying the most significant lifetime with a time to rupture of 1105.5 hours. These correlations indicate that these F_{Max} values are driven by the material's resistance to high temperature deformation mechanisms. Furthermore, it is worth noting that the damage tolerance and force drop off behaviour observed post rupture appears to behave in a relatively similar manner, which is most likely consequent to their coarsened grain structures as highlighted in Table 6.3. As previously discussed, grain size would bear significant implications on damage tolerance as coarsened grains would lead a to lower volume fraction of grain boundaries and inherently minimise obstacles for dislocation movement.

The mechanisms discussed can be further represented in the fractographic images shown in Figure 6.28 – 6.30, where the test determination criteria of a 20% drop off in F_{Max} takes precedent. Considering the high damage tolerance prevalent in low energy variants, considerably more displacement is required to lead to the adequate level of force drop-off for test completion. This is particularly illustrated in Figure 6.28, where more established primary cracking was witnessed. When taking into account the rapid drop off in force observed post rupture in the medium energy variants, very little displacement was accumulated and therefore the existence of primary cracking was miniscule in comparison as shown in Figure 6.29. It is worth noting however that despite this, the failure continues to behave in a brittle fashion given the temperature conditions nearing the materials' limitations. Finally, the fractography of the high energy samples displayed in Figure 6.30 once again show more significant cracking consequent to the high displacements attributed to the material's damage tolerance capabilities.

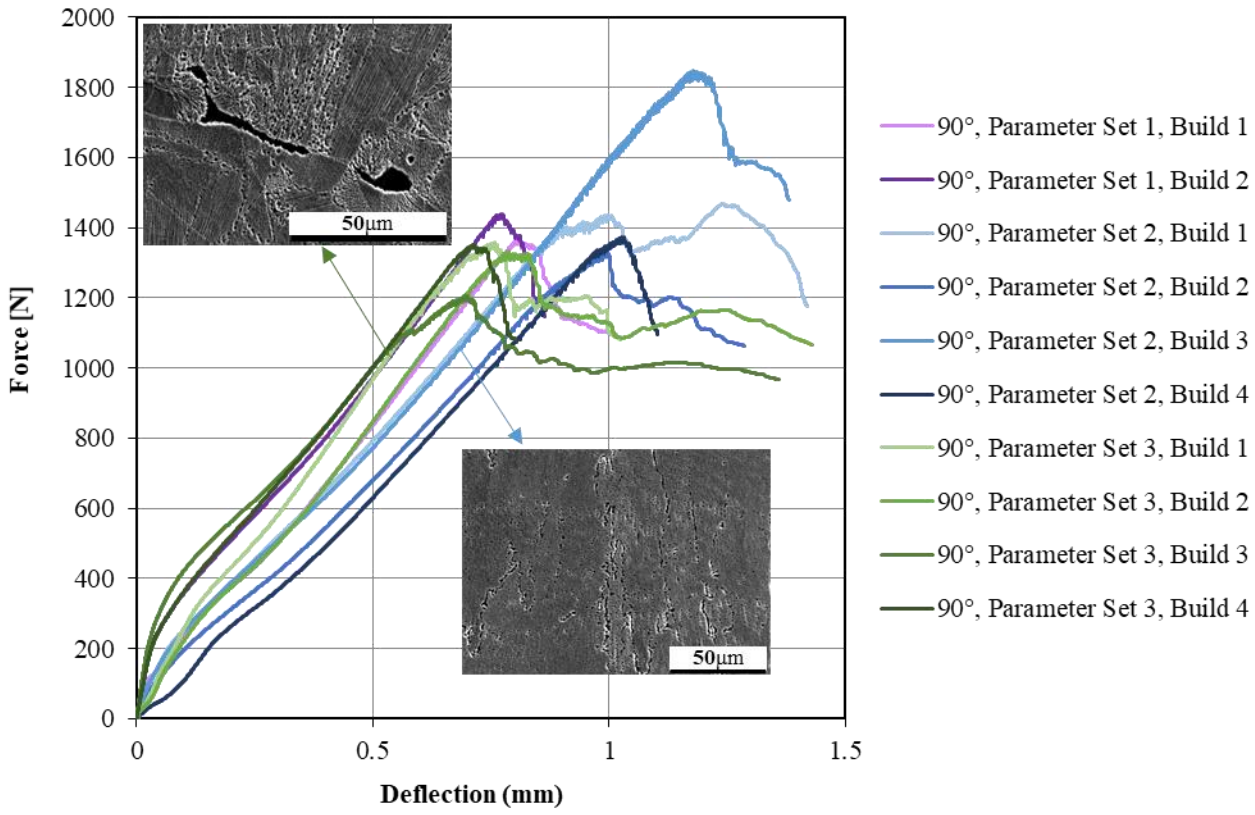

Figure 6.27. SPT testing of IN718 LPBF parameter variants at 650ºC, 0.5mm/min displacement rate.

Table 6.5. SPT test data from IN718 LPBF parameter variants tested at 650°C, 0.5mm/min.

Sample	$F_{Max\ (N)}$	d at F_{Max} (mm)	dL at F_{Max} (mm)	F_{Break} (N)	d @ break (mm)	dL at break (mm)
90°, Parameter Set 1, Build 1	1365.28	0.81	1.06	1092.60	1.01	1.23
90°, Parameter Set 1, Build 2	1437.65	0.77	1.14	1146.39	0.86	1.20
90°, Parameter Set 2, Build 1	1469.10	1.24	1.55	1175.14	1.42	1.70
90°, Parameter Set 2, Build 2	1326.11	0.99	1.35	1061.17	1.29	1.62
90°, Parameter Set 2, Build 3	1849.11	1.18	1.53	1479.24	1.38	1.72
90°, Parameter Set 2, Build 4	1371.65	1.03	1.38	1096.89	1.10	1.43
90°, Parameter Set 3, Build 1	1356.81	0.76	1.03	1082.00	1.02	1.25
90°, Parameter Set 3, Build 2	1331.04	0.79	1.03	1065.00	1.43	1.59
90°, Parameter Set 3, Build 3	1206.26	0.70	0.89	965.71	1.36	1.47
90°, Parameter Set 3, Build 4	1350.85	0.71	0.97	1080.96	0.80	1.03

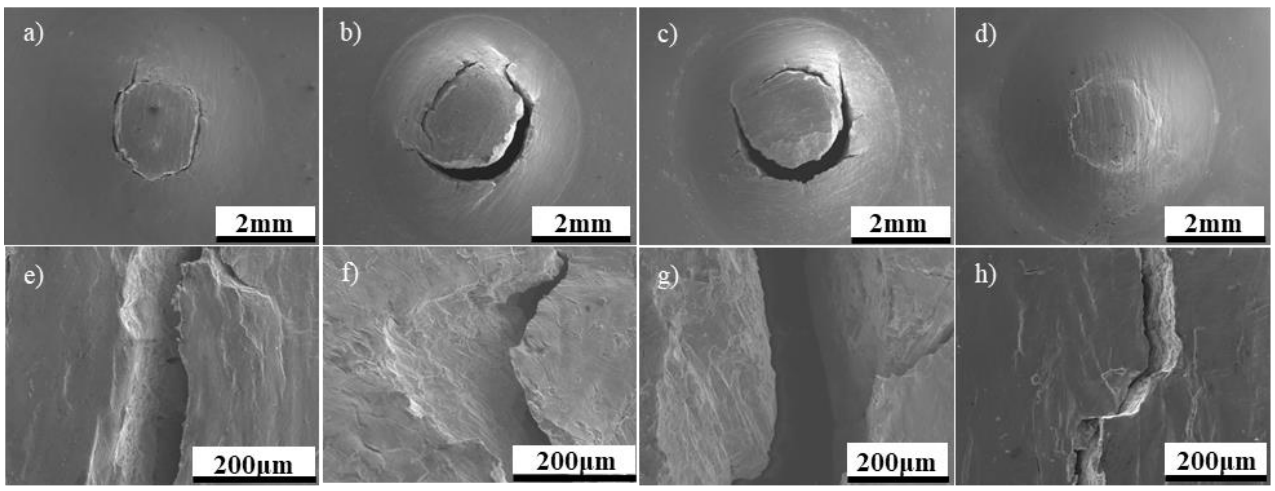

Figure 6.28. Fractographic images from SPT tests on 90°, Parameter Set 3 variants SPT a) e) Build 1, b) f) Build 2, c) g) Build 3, d) h) Build 4.

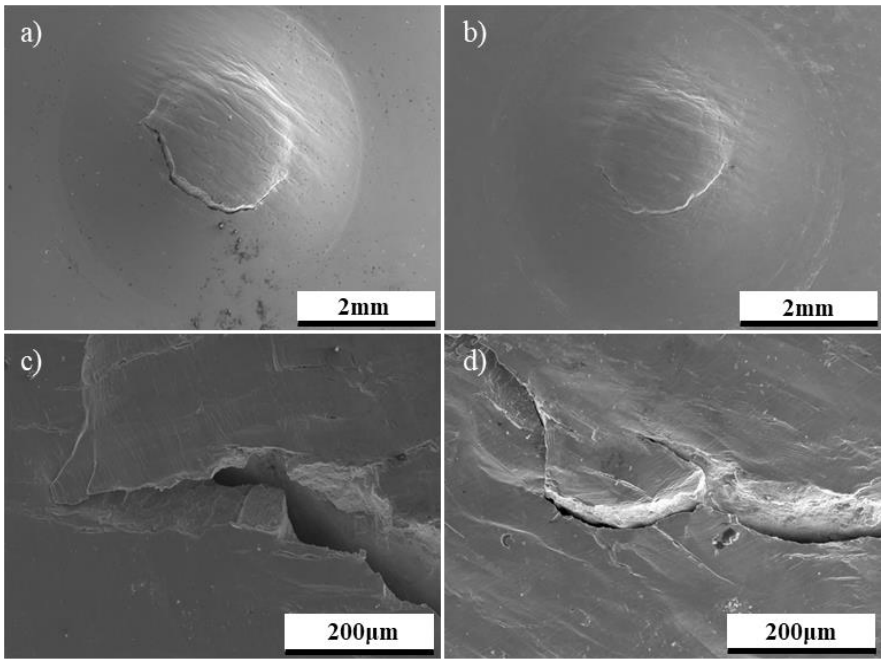

Figure 6.29. Fractographic images from SPT tests on 90°, Parameter Set 1 variants a) c) Build 1, b) d) Build 2.

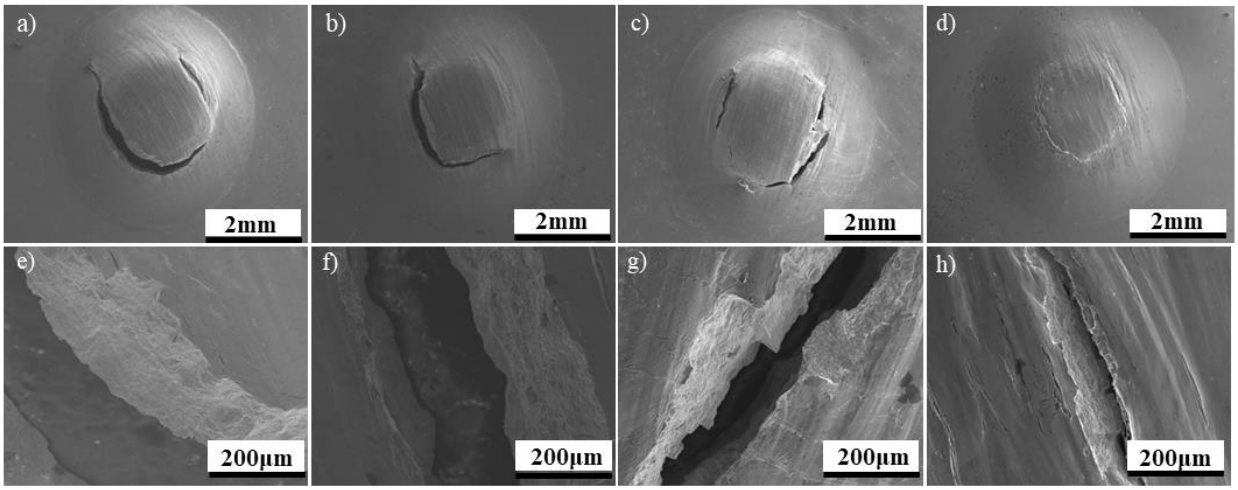

Figure 6.30. 90°. Fractographic images from SPT tests on Parameter Set 2 variants a) e) Build 1, b) f) Build 2, c) g) Build 3, d) h) Build 4.

6.5 The Small Punch Tensile Performance of 30º and 'Baseline' Variants

The influence of build orientation was also interpreted as shown in Figure 6.31 and Table 6.6, where 30º orientations displayed similar performances to that of their 90º energy counterparts, irrespective of the significant changes in grain structure presented previously. When considering F_{Max}, 30º orientations displayed a range in performance of 1293.76 – 1367.27N, nearing that of the 90º low and medium energy ranges explored beforehand. Despite fine equiaxed grains being favourable for tensile performance, these performances are most likely driven by the material density features commonly observed and shown in Figure 6.32, where lack of fusion welds and voidage is evident. As discussed, the presence of such features are likely to open and act as initiation sites for failure under tensile loading, thus inhibiting the force in which the material can withstand. This once again does not appear to influence the damage tolerance behaviour of the material however, where a reasonable display of damage tolerance is observed post rupture, 0.84 - 1.45mm displacement at test completion in comparison to 0.54 – 0.73mm displacement at F_{Max}. This indicates once again that fine grain size dictate this behaviour, where the amplified volume of grain boundaries can act as obstacles and impede dislocation movement.

As discussed previously, Rolls-Royce plc.'s undisclosed 'baseline' parameter sets were employed as part of the DOE, where creep performance alongside microstructural examination was utilised in order to approximate energy input. SPT testing was performed on these variants, with the one IN718 'baseline' build successfully tested displaying an F_{Max} value of 1391.03N, with a substantial displacement at F_{Max} value being observed (1.42mm). Given the relatively successful nature of material consolidation where no noticeable defects were apparent, alongside the favourable high temperature performance displayed in the creep variant, it is not surprising that this variant displays excellent high temperature ductility. Once rupture ensues however, it's damage tolerance capability is limited as shown by displacement values at test completion (1.57mm) which is likely to be consequent to its coarsened grain size, where the innate implications on grain boundary volume fraction leads to the lower existence of dislocation motion obstruction. The CM247LC 'baseline builds' appear to display a similar range in F_{Max} values (1285.12 – 1432.73N), which is contradictory to the grain sizing apparent but is expected given the continued existence of lack of fusion welds as shown in Figure 6.33. It's damage tolerance capabilities however appear to be lessened which is contrary to the mechanisms previously discussed. However, it is worth noting the test failure criterion employed (0.8 F_{Max}) and its implications on SPT results as highlighted in [176], could impact the perception of damage tolerance. Furthermore, there is also the element of elastic heterogeneity as previously discussed.

Fractographic analysis was conducted on these variants in order to further the understanding of these failures, where 30º build orientations displayed significantly more brittle ruptures with multiple

primary cracks emanating outwards as shown in Figure 6.34. The separation of the failure from the bulk material is also evident given the heightened displacements consequent to the relatively significant damage tolerances displayed. This separation behaviour is also exhibited in the IN718 'baseline' variant shown in Figure 6.35a, but as discussed, this variant's apparent high temperature ductility is not subject to radial cracking but rather unidirectional failure. Finally, the fractographic images of the CM247LC 'baseline' variants presented in Figure 6.35b-d showcase very little separation from the bulk material given the lower damage tolerance behaviour displayed, which consequently interrupts further displacement. However, the fractures appear to exhibit the mid-region between the 30° and IN718 variant with regards to ductility.

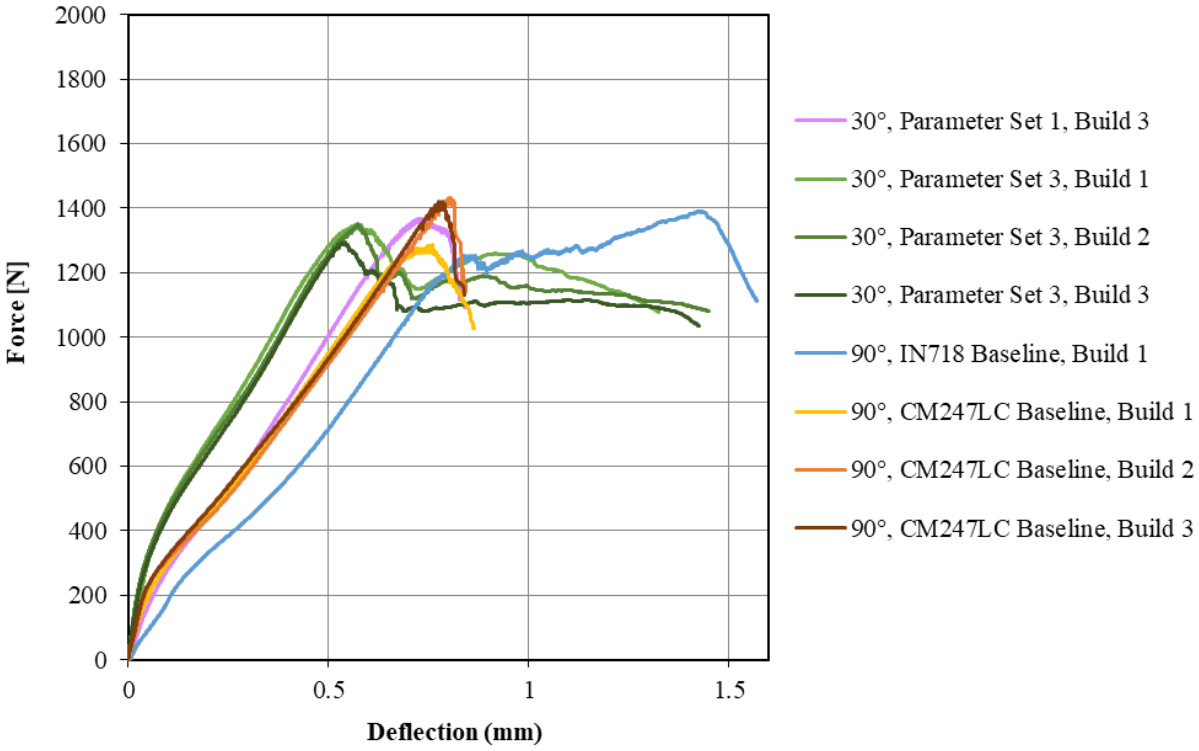

Figure 6.31. SPT results for IN718 LPBF 30° and 'Baseline' variants at 650°C, 0.5mm/min displacement rate

Table 6.6. SPT data for IN718 LPBF 30º and 'Baseline' variants tested at 650ºC, 0.5mm/min.

Sample	$F_{Max\ (N)}$	d at F_{Max} (mm)	dL at F_{Max} (mm)	F_{Break} (N)	d at break (mm)	dL at break (mm)
30º, Parameter Set 1, Build 3	1367.27	0.73	0.97	1094.17	0.84	1.06
30º, Parameter Set 3, Build 1	1347.72	0.57	0.90	1078.34	1.33	1.48
30º, Parameter Set 3, Build 2	1350.24	0.57	0.87	1080.52	1.45	1.45
30º, Parameter Set 3, Build 3	1293.76	0.54	0.84	1035.65	1.42	1.47
90º, IN718 Baseline, Build 1	1391.03	1.42	1.77	1112.79	1.57	1.88
90º, CM247LC Baseline, Build 1	1285.12	0.76	1.09	1028.05	0.86	1.18
90º, CM247LC Baseline, Build 2	1432.73	0.81	1.11	1141.96	0.84	1.13
90º, CM247LC Baseline, Build 3	1421.60	0.78	1.03	1131.09	0.84	1.06

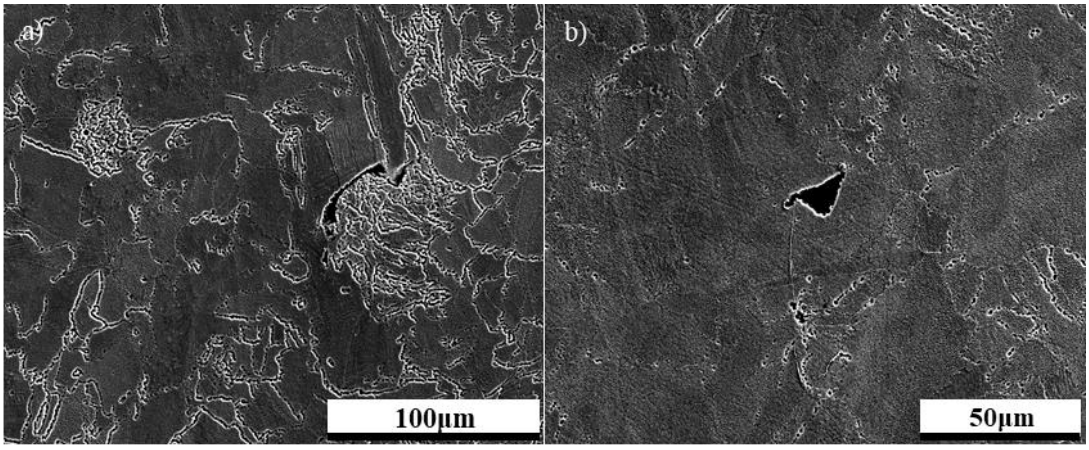

Figure 6.32. Microstructural observations of poor density in LPBF IN718 variants, 30º a) Parameter Set 3, Build 1 and b) Parameter Set 1, Build 3.

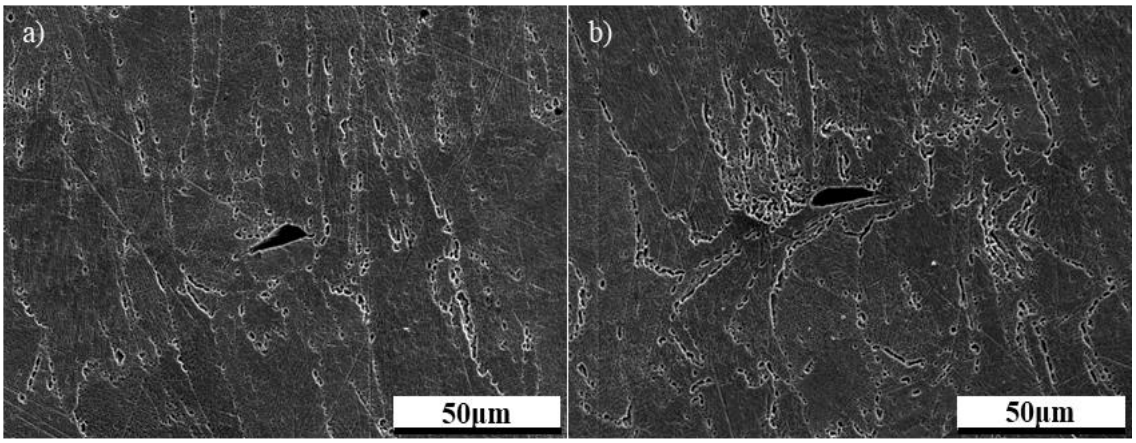

Figure 6.33. Lack of fusion voids witnessed in LPBF IN718 ‘CM247LC Baseline’, Build 2 variant.

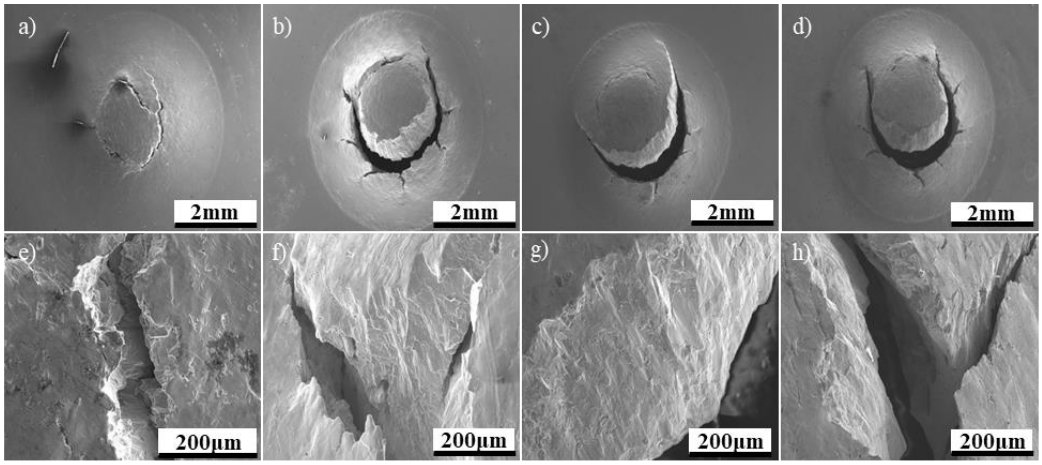

Figure 6.34. Fractographic images from SPT tests on 30^{o}, Parameter Set 1, a) e) Build 3 and 30^{o}, Parameter Set 3 b) f) Build 1, c) g) Build 2, d) h) Build 3.

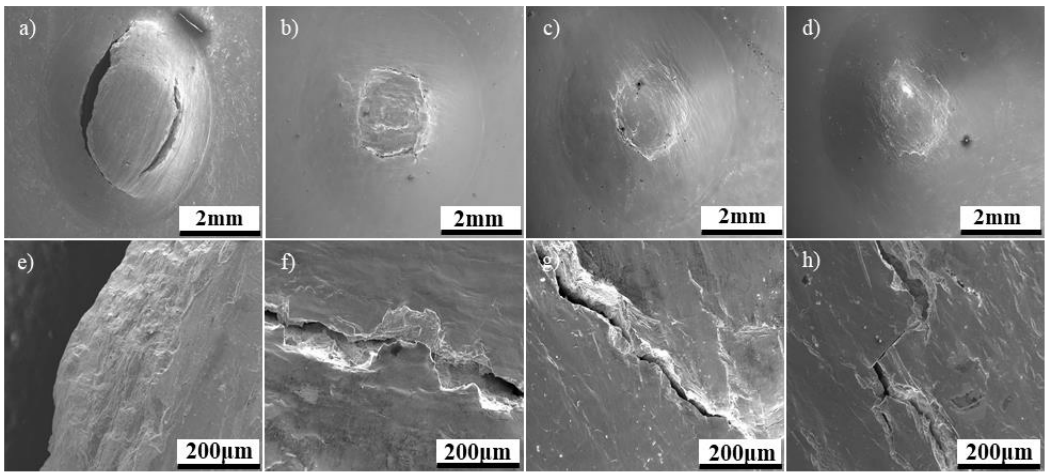

Figure 6.35. Fractographic images from SPT tests on IN718 LPBF ‘Baseline’ a) e) Build 1 and CM247LC LPBF ‘Baseline’ b) f) Build 1, c) g) Build 2 and d) h) Build 3.

6.6 Summary

Overall, both SPC and SPT experiments were performed on an array of LPBF IN718 variants, which incorporated changes in build orientation and parameter set. Build orientation was shown to be a primary driver in SPC performance given the implications of epitaxial grain growth apparent in ALM processes on grain sizing, morphology and grain boundary volume fraction. As such, parameter sets were shown to have little influence on creep performance within the 30° orientations given the overriding mechanisms inherent, but appeared to exhibit a significant influence on microstructural development and the discrepancy in SPC performances within the 90° orientations. Higher energy densities appeared to reduce the presence of significant density related features, coarsen grain sizing and aid textural development. Despite the finer grain sizing evident in low energy variants which would be expected to be favourable for impeding dislocation movement under tensile loading, the SPT performances and particularly the F_{Max} values displayed by the low energy variants were inhibited by the presence of density related features such as lack of fusion welds. The damage tolerance capabilities post rupture however did not appear to be significantly impacted.

Given the degraded mechanical properties observed consequent to the existence of lack of fusion related features, a furthered understanding as to the influence of parameter selection on the propensity for defect formation is required. The following chapter will employ the same robust statistical analysis implemented in Chapter 5 on a series of LPBF IN718 variants of differing normalised beam speeds, powers and energy densities in order to assess the impact on melt track sizing and defect formation.

Chapter 7 – A Quantitative Approach to Melt Track and Defect Analysis in IN718

7.1 Melt Track Assessment of IN718 Parameter Variants

A series of manual melt track measurements, (50-70 measurements for both height and width per sample) were taken across 24 IN718 LPBF variants with changes in normalised beam speed, power and energy density being considered. When considering the influence of individual process parameters, Figure 7.1 highlights the influence of normalised beam speed over a range of power settings, where it becomes evident that an increase in normalised beam speed leads to finer track sizing for both height and width. This is to be expected given the intrinsic relationship between beam speed and energy density, where faster laser movement would lead to an inherently lower uptake in energy and thus melt volume. When considering normalised beam power, it is apparent that an inverse relationship comparative to beam speed is displayed as shown in Figure 7.2, where an increase in beam power leads to a coarsened melt pool consequent to the increased energy uptake associated with this. These relationships can be innately displayed in Figure 7.3, where a clear existential relationship between normalised energy density and melt pool size for both height and width respectively is showcased, validating the use of energy density as a metric. However, there does seemingly appear to be the existence of data scatter and variance, which can be attributed to both the subjectivity of the melt track measurement system employed and the notion that energy density may not entirely encapsulate and represent melt pool physics. Despite this, the relationships discussed can be represented in Figure 7.4, giving credence to this methodology, where a gradual refinement of melt track size is observed with increasing beam speed (a, c & e) and coarsening behaviour witnessed for increasing beam power (b, d & f).

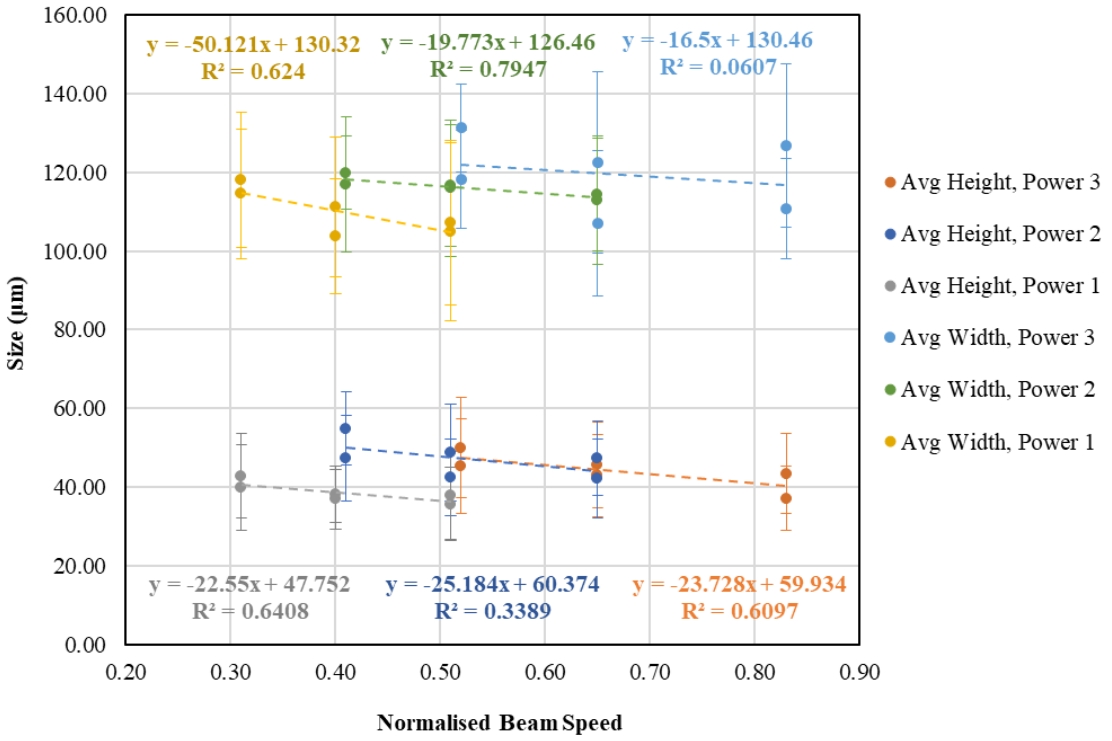

Figure 7.1. Influence of normalised beam speed on melt track height and width over a range of employed power settings for LPBF IN718.

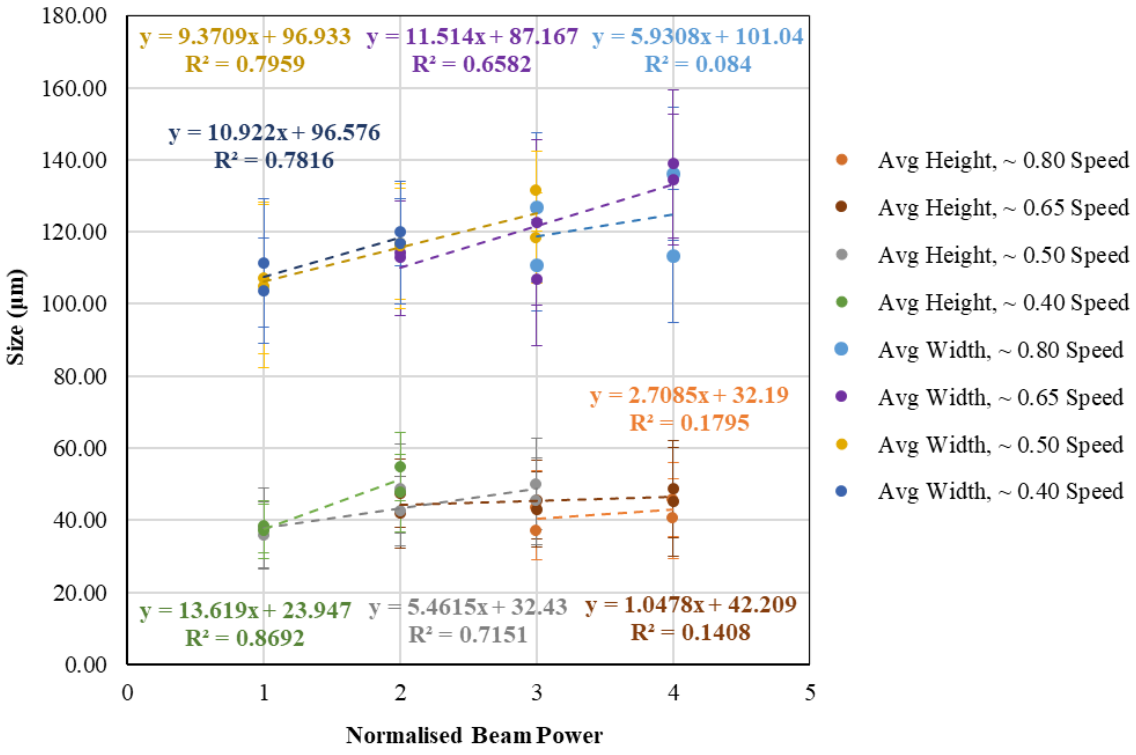

Figure 7.2. Influence of normalised beam power on melt track height and width over a range of employed speed settings for LPBF IN718.

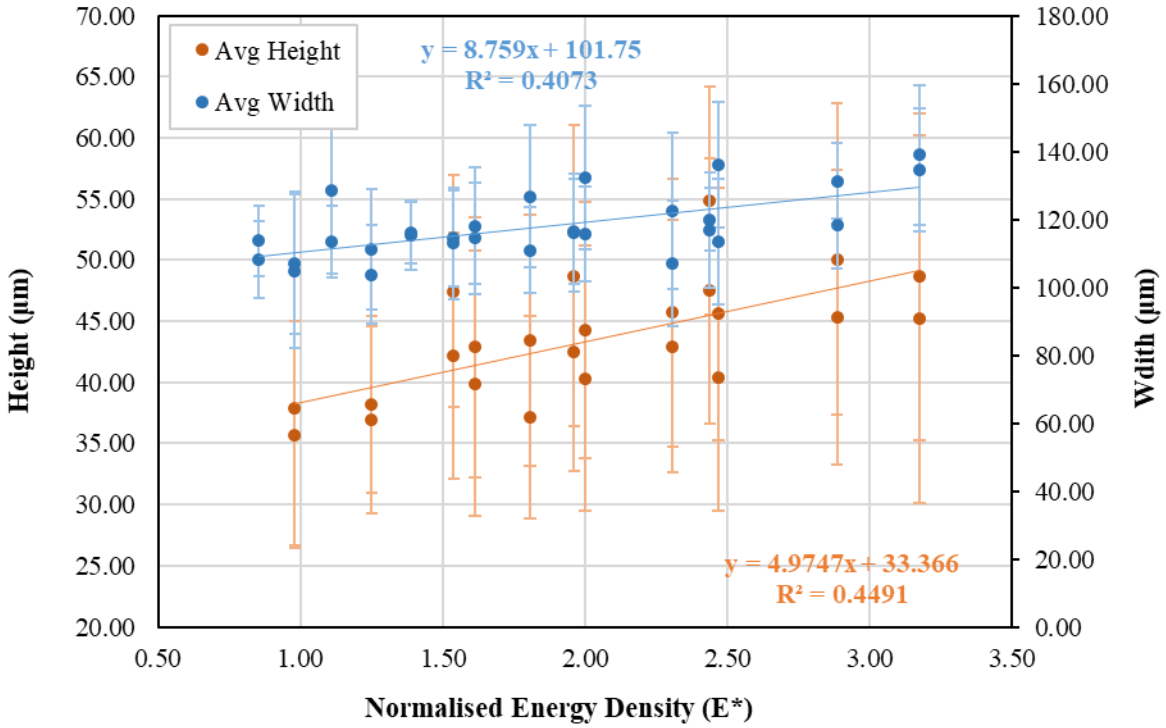

Figure 7.3. Influence of normalised energy density on melt track height and width across all LPBF variants within this IN718 DOE.

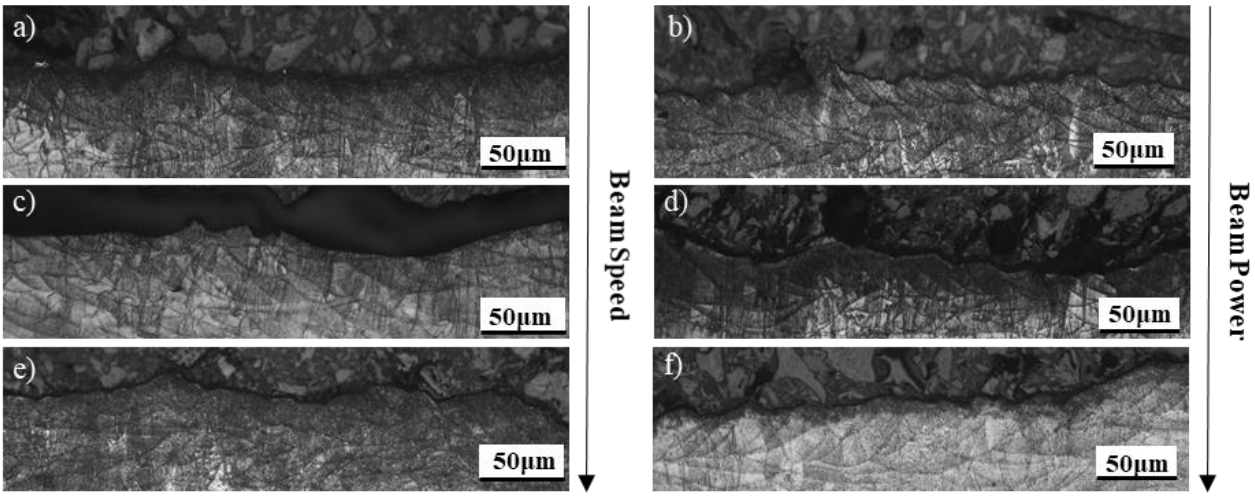

Figure 7.4. Microscopy of melt track profiles for a) c) e) increasing normalised beam speed and b) d) f) increasing normalised beam power.

7.2 Defect Analysis of IN718 Parameter Variants in the As-Built Condition

Defect analysis was conducted on all 24 LPBF variants in order to further the understanding of defect formation within IN718 consequent to varying process parameter selection. Considering that little to no solidification cracking was apparent in this alloy for reasons explored in Chapter 6, the only alternative density related issues other than porosity were associated to a lack of consolidation, i.e. the presence of lack of fusion welds or voidage. As such, these features are referred to as 'other defects'. The influence of normalised beam speed on the presence of both porosity and other defects over a range of power settings is presented in Figure 7.5, where there is a clear correlation with increasing any input in relation to the presence of these features. This is likely to be a consequence to the existential relationship between beam speed and energy density as previously discussed, where increasing beam velocity will inherently reduce energy absorbance and refine melt track sizing, leading to lessened material consolidation and re-melt. This is supported in the stitched optical imagery showcased in Figure 7.6, where the presence of porosity and other defects seemingly worsens with increasing beam speed under consistent power settings.

The mechanism discussed is further supported in Figure 7.7, where increasing normalised beam power leads to a reduction in the occurrence of porosity and other defects over a range of power settings. This once again coincides with the inverse behaviour noted between beam speed and beam power as previously eluded too, giving further credibility to the use of energy density as a metric. As explored, it is hypothesised that greater energy input and the larger associated melt tracks gives rise to greater material consolidation as a consequence to more adequate melting, thus decreasing the presence of density related phenomena. This relationship is supported through the use of stitched optical microscopy images as shown in Figure 7.8, where an increase in beam power gives a gradual rise to material density and minimises the presence of porosity and other defects. Seeing as the influence of individual parameter selection is intimately tied to its implications on energy density, a comparison was drawn across all 24 IN718 LPBF variants between normalised energy density and the prevalence of these features. This is represented in Figure 7.9, where despite there being one significantly outlying data point as will be discussed later, there is a significant correlation between increasing normalised energy density and relative component density, most likely being subsequent to the consolidation mechanisms discussed. It is important to note that naturally this relationship is non-linear, where the observed impact of increasing energy is substantially more discernible at lower energy inputs and gradually plateaus in effect as energy is increased towards the higher end. These relationships can be visually represented and observed once again with stitched optical microscopy as shown in Figure 7.10, where a gradual increase in energy density leads to greater material consolidation and the reduction in defects.

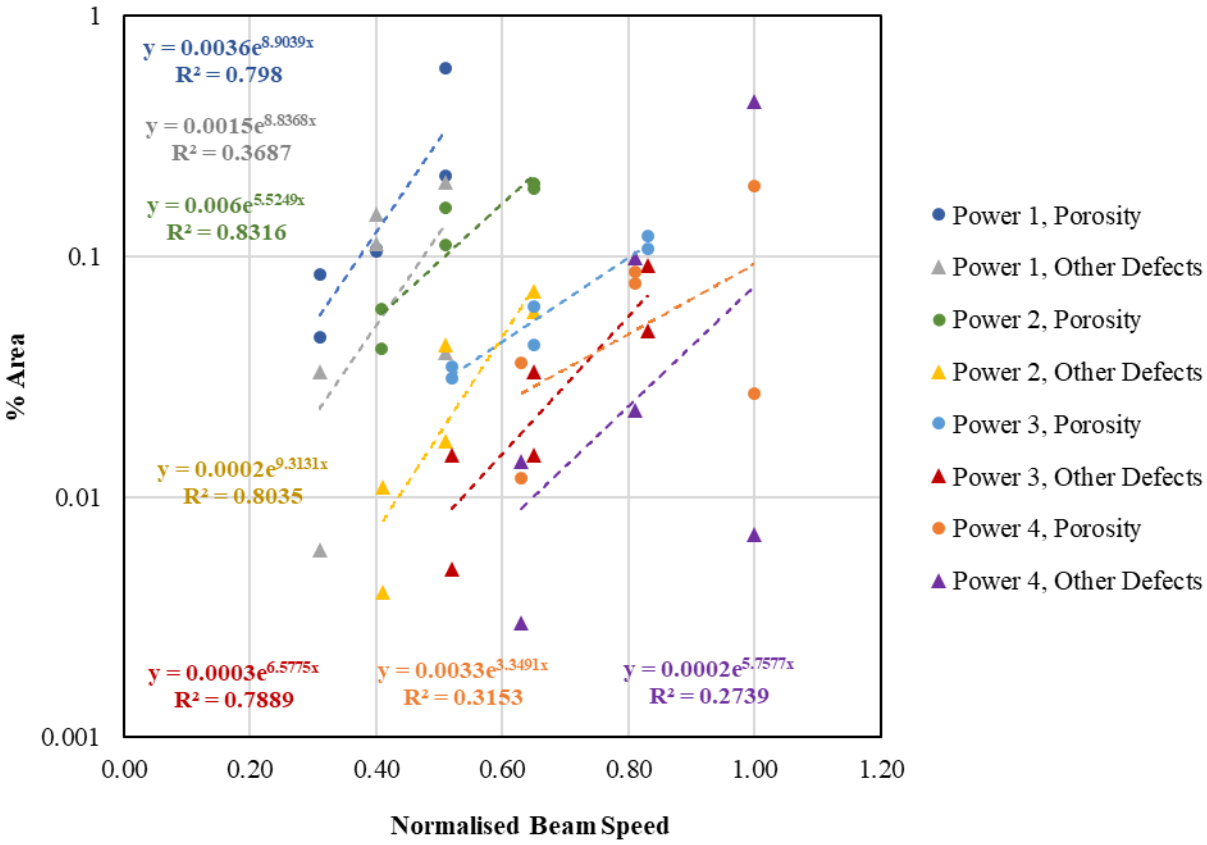

Figure 7.5. Influence of normalised beam speed on the % area of porosity and other defects over a range of power settings within this LPBF IN718 DOE.

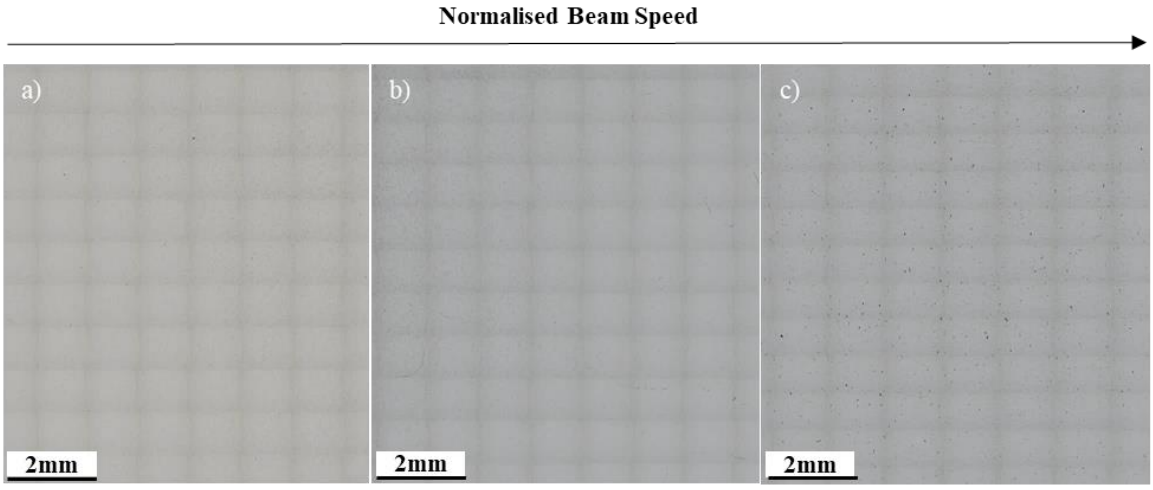

Figure 7.6. Stitched high magnification optical microscopy of LPBF IN718 samples of increasing normalised beam speed (left to right) with the same power input.

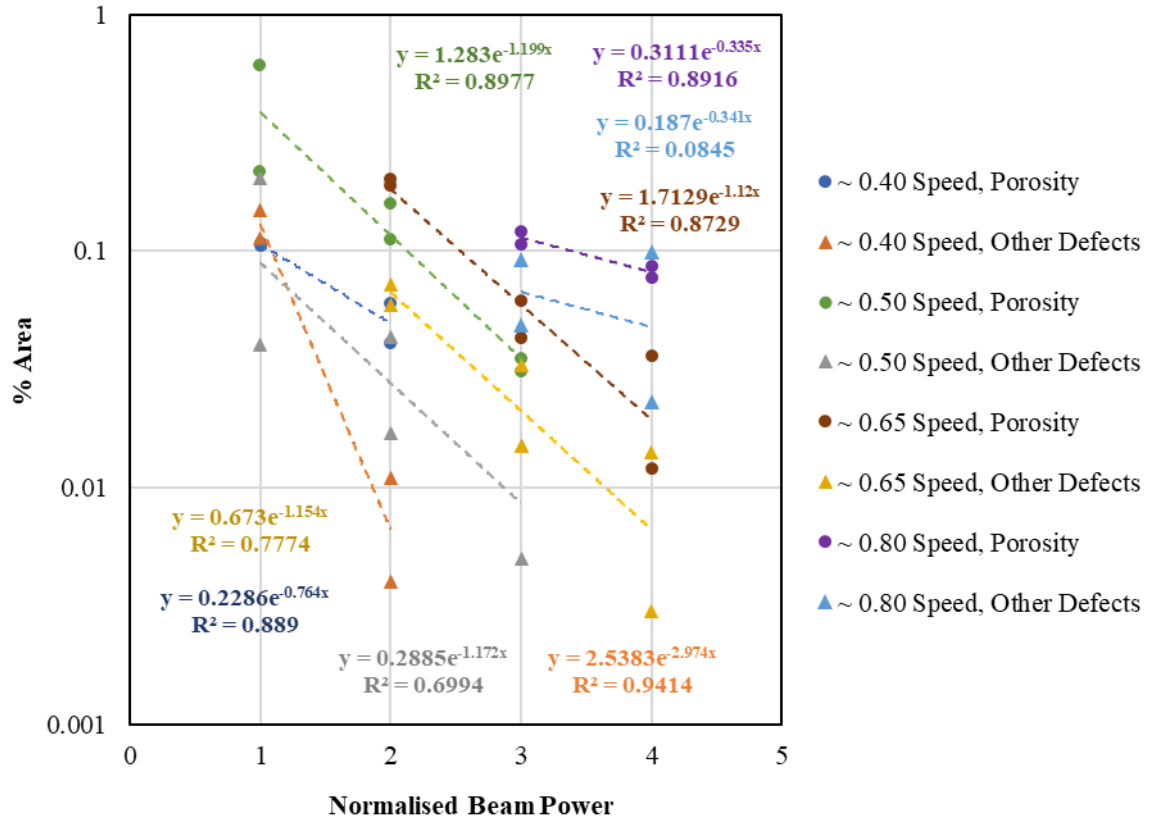

Figure 7.7. Influence of normalised beam power on the % area of porosity and other defects over a range of speed settings within this LPBF IN718 DOE.

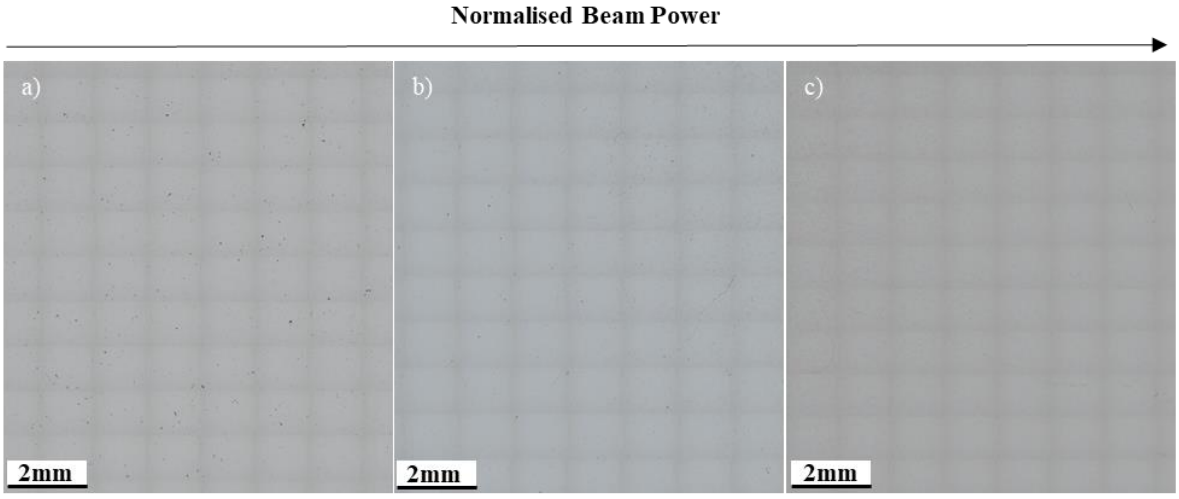

Figure 7.8. Stitched high magnification optical microscopy of IN718 samples of increasing normalised beam power (left to right) with the same speed input.

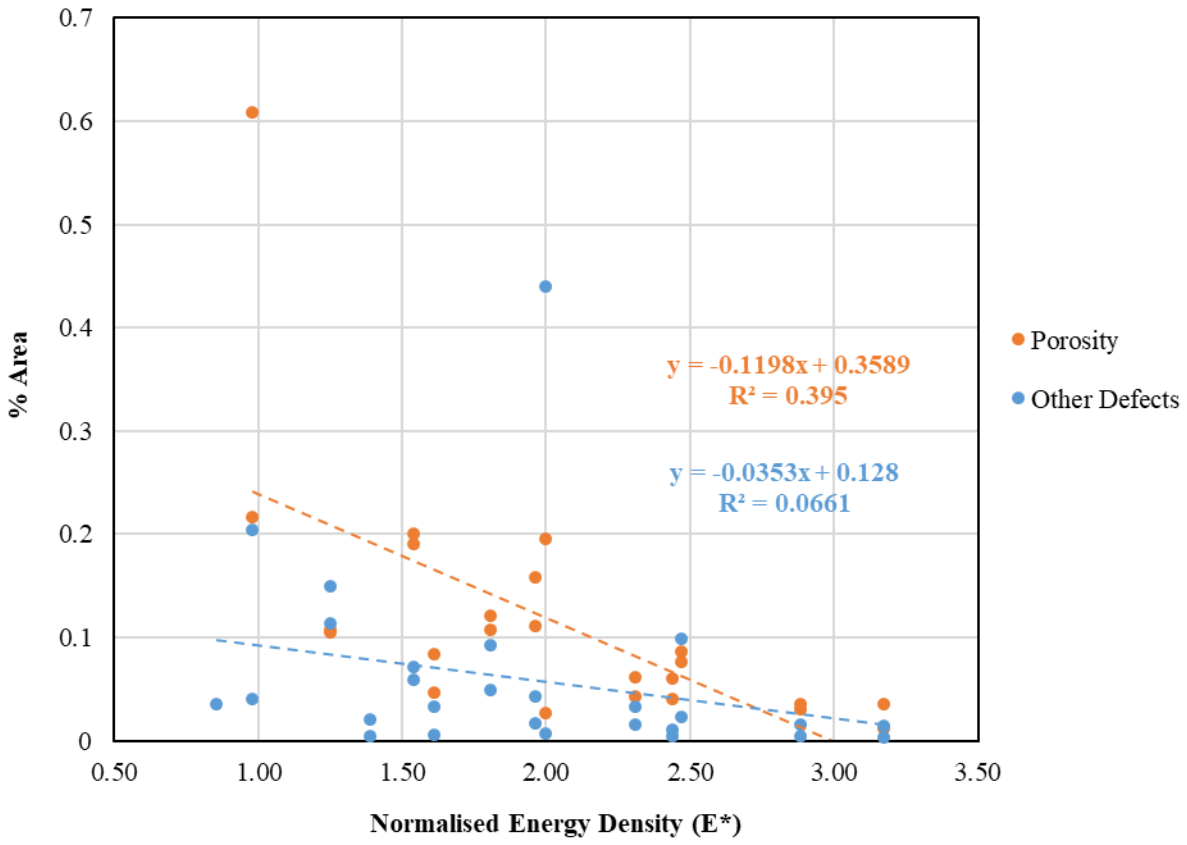

Figure 7.9. Influence of normalised energy density on the % area of porosity and other defects present within LPBF IN718 variants analysed in this DOE.

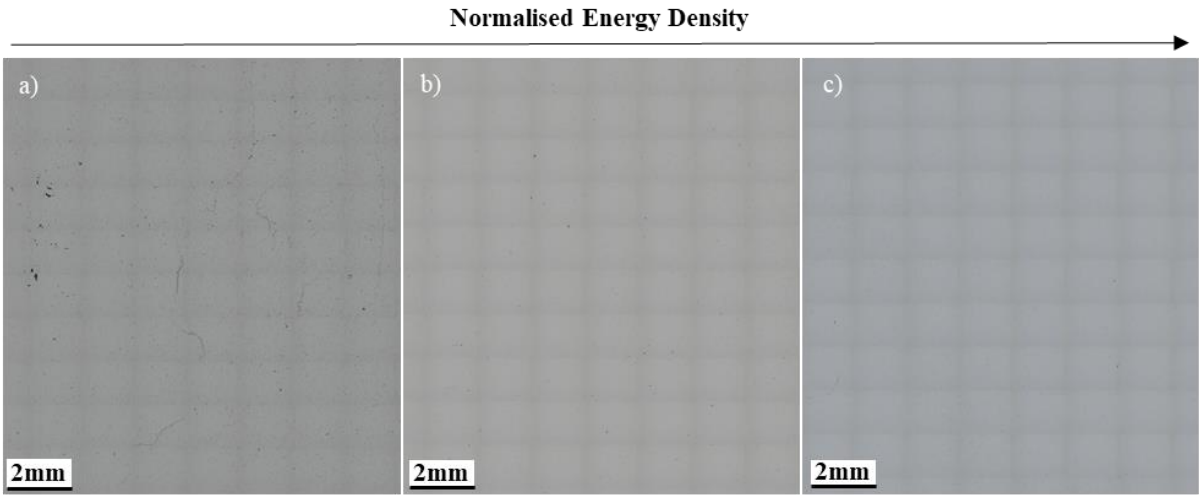

Figure 7.10. Stitched high magnification optical microscopy of LPBF IN718 samples of increasing normalised energy density (left to right).

Although there was a considerably strong agreement between parameter selection and the % area of material discontinuities, it is important to utilise alternative metrics in order to fully capture the influence that process sets have. As explored previously in Section 5.2, the amplified presence of smaller pores comparative to infrequent large pores could in theory provide a similar value and as such, different criteria should be evaluated to drive a further understanding. As such, the use of feature count and average feature size will once again be employed.

The relationship between normalised beam speed and the count of features such as porosity and other defects over a range of power settings can be perceived in Figure 7.11, where generally as beam speed increases, the incidence of porosity and other defects also increases in parallel. Considering that feature count is likely to innately contribute to % area, it is unsurprising that where once again the implications of beam speed on energy density and melt dynamics is palpable. There does appear to be one outlier in the form of power 1, other defects, but this seemingly coincides with the average size of these features as will be mentioned later. Nevertheless, a strong agreement which coincides with % area is observed. In addition, the influence of normalised beam power on the frequency of porosity and other defects over a range of speed settings is represented in Figure 7.12. It can be seen that as normalised beam power increases, there is a marked decrease in the frequency of porosity and other defects, further establishing its relationship to energy density, where higher beam power inherently leads to greater energy density and thus superior material consolidation dynamics. Once more, there is the presence of outliers which intrinsically impacts the trend observed for ~ 0.50 speed, other defects, but it is important to note that the data point which influences this is once again the same previously observed. As such, this data point will be subject to further scrutiny as will be explored later. When bearing in mind that the influence of individual process parameters is hypothesised to be ultimately dictated and driven by energy density, Figure 7.13 provides more merit. It can be seen that there once again is a clear existential relationship between normalised energy density and the presence of porosity and other defects, now understood not only to be in the form of % area but fundamentally feature count.

Furthermore, the influence of process parameters on the average sizes of both porosity and other defects present was evaluated, with Figure 7.14 showcasing the influence of normalised beam speed. There appears for the most part to be an apparent relationship between the average size of lack of fusion related defects and speed input, with higher speeds leading to the presence of larger features. This is likely to occur due to the increasing energy input's ability to overcome the minimum energy density threshold to achieve material consolidation. This relationship is not concurrent with what was noted to be seen in porosity, where increasing beam speed over a range of power settings appeared to have a negligible effect. It is highlighted in Section 2.3.5 that porosity is predominantly caused by gas entrapment which is consequential to the presence of hollow powder particles and parameter selection. However, the likelihood that parameter selection would lead to a substantial change in gas entrapment

which would adversely influence porosity size is unlikely and thus minute variations in porosity size are detected. It is worth noting that there appears to be the presence of data outliers in the form of power 1, other defects, which coincides with what was observed in the feature count relationships previously discussed. In this instance, there appears to be a notable rise in the average size of lack of fusion features which coincides with the marked reduction in feature count. This appears to be uncharacteristic with regards to its parameter set and paired variant which will be interpreted. Considering that the influence of beam speed is inherently tied to its implications on energy density, the influence of normalised beam power over a range of speed settings was also evaluated as shown in Figure 7.15. It can be seen once more that increasing normalised beam power seemingly reduces the average size of lack of fusion related defects but its influence on porosity was shown to have no major significance. These notions can be further represented in Figure 7.16, where the influence of normalised energy density on the average size of porosity and other defects was depicted. There results correspond with the relationships discussed, where higher energy inputs seemingly lead to a marked decrease in the presence of lack of fusion related defects, but porosity remains marginally unaffected.

Overall, increased energy density appears to significantly reduce the % area of porosity and other defects through the diminishing of the frequency in which these features occur. This is consequent to higher energies aiding material consolidation and possibly increasing the presence of remelting processes. From a size perspective, only lack of fusion related features appear to be influenced by energy input.

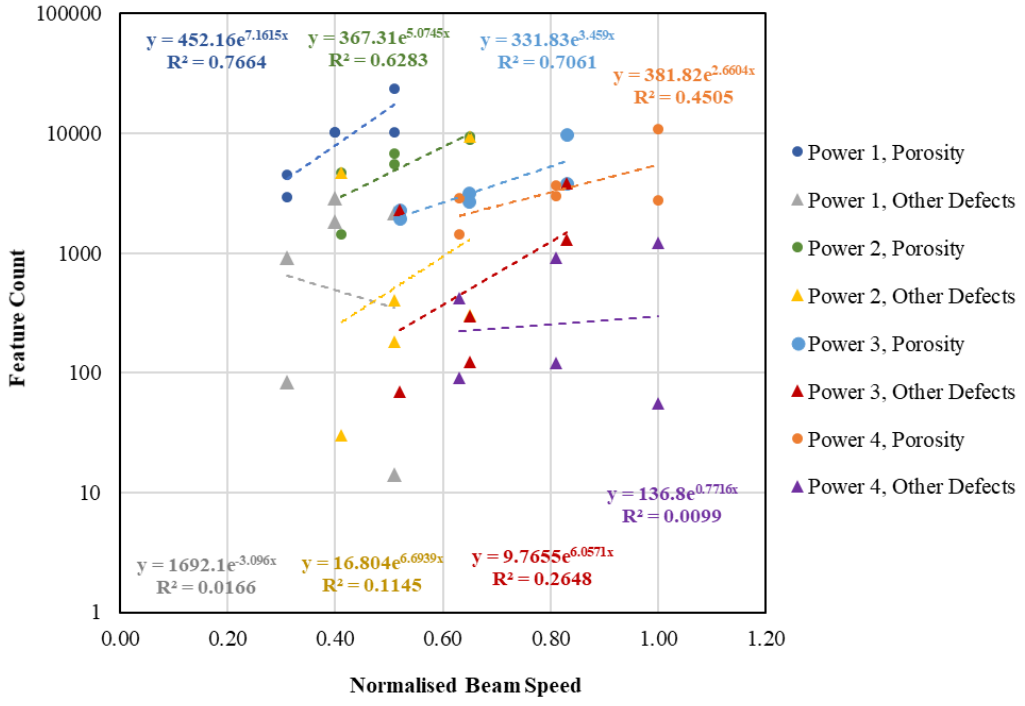

Figure 7.11. Influence of normalised beam speed on the count of porosity and other defects over a range of power settings employed within this LPBF IN718 DOE.

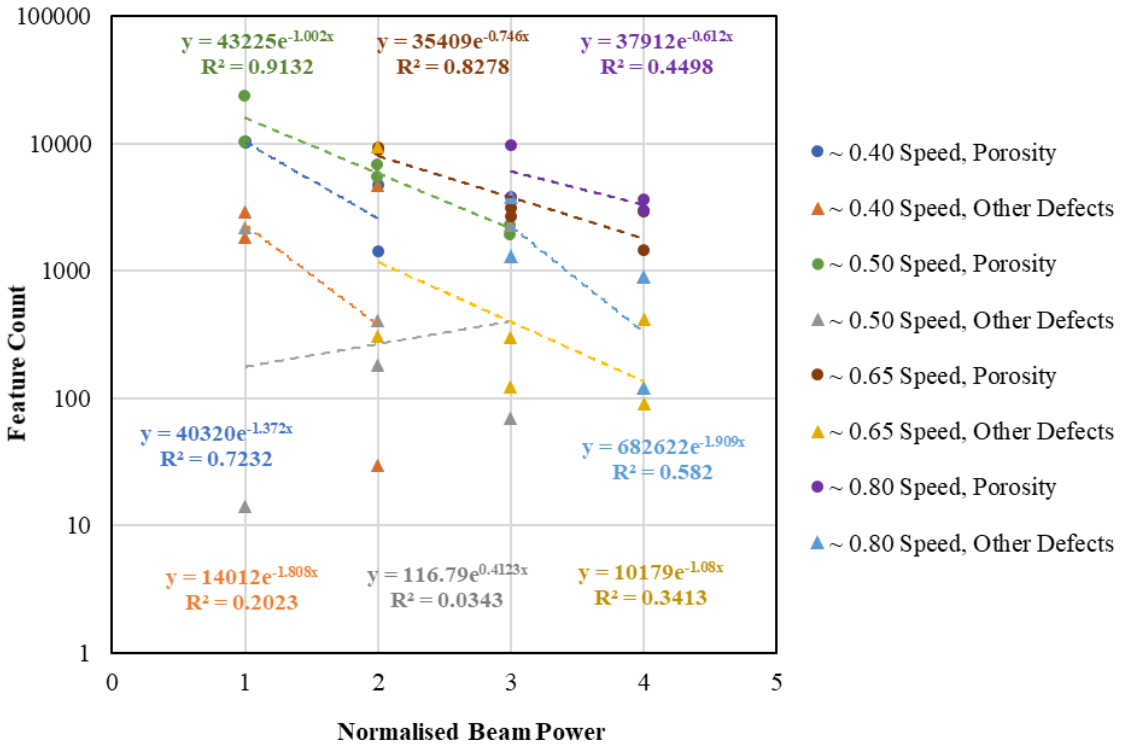

Figure 7.12. Influence of normalised beam power on the count of porosity and other defects over a range of speed settings employed within this LPBF IN718 DOE.

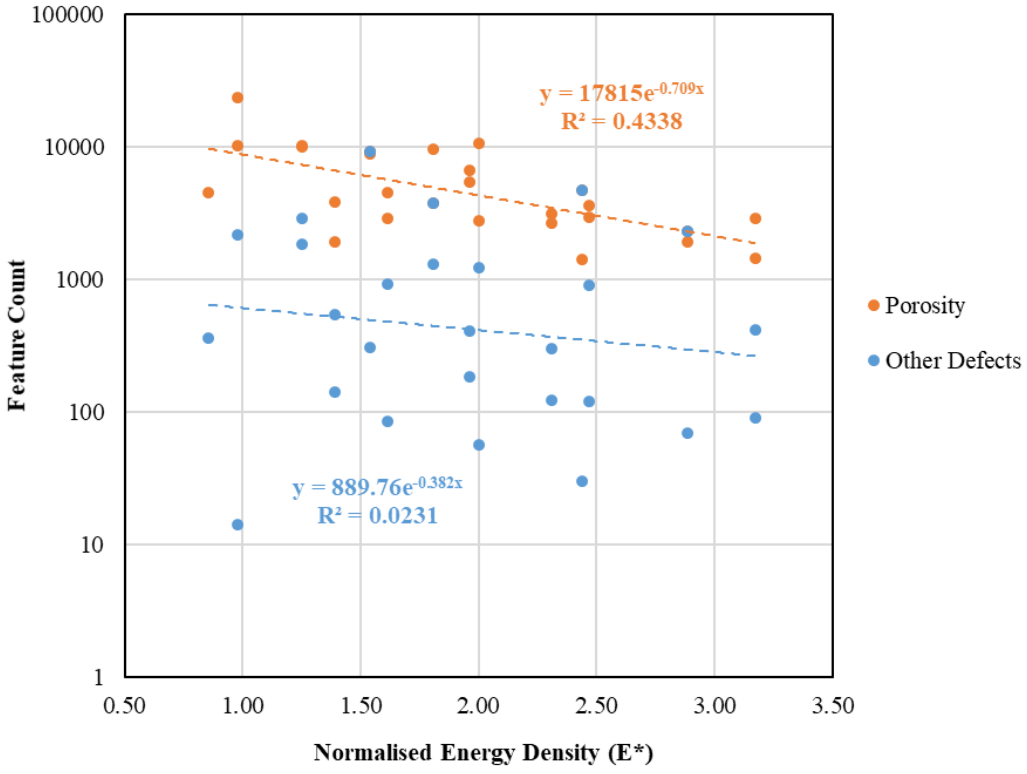

Figure 7.13. Influence of normalised energy density on the count of porosity and other defects present within LPBF IN718 variants analysed in this DOE.

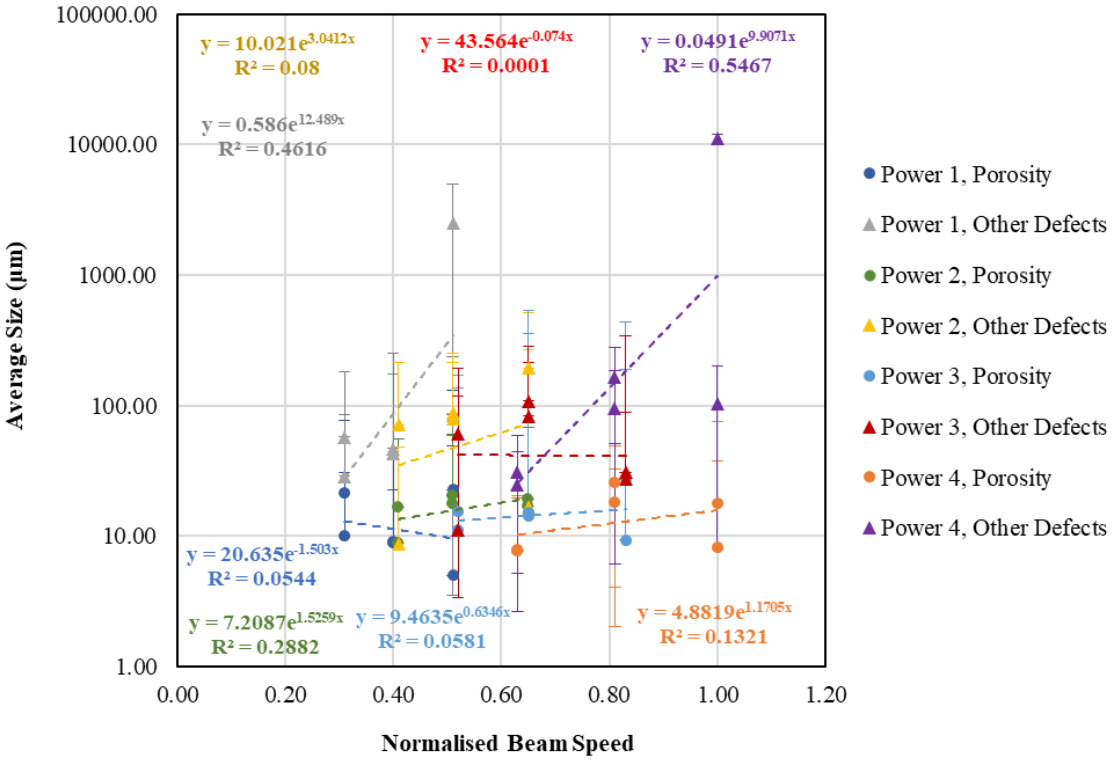

Figure 7.14. Influence of normalised beam speed on the average size of porosity and other defects over a range of power settings employed within this LPBF IN718 DOE.

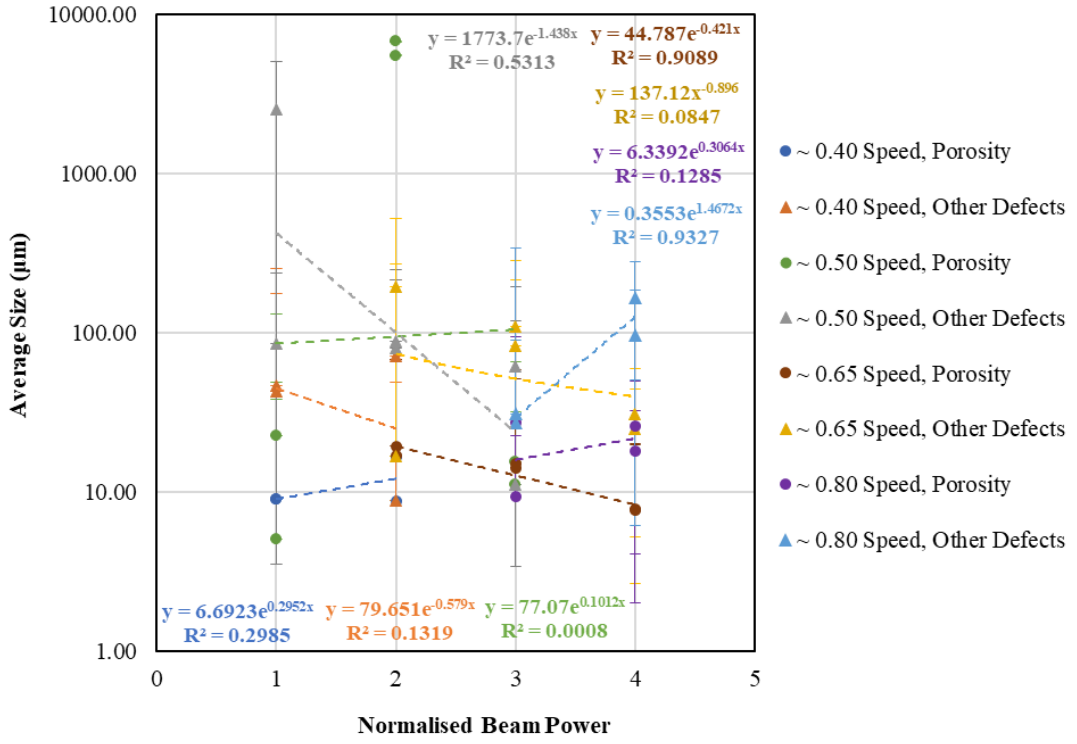

Figure 7.15. Influence of normalised beam power on the average size of porosity and other defects over a range of speed settings employed within this LPBF IN718 DOE.

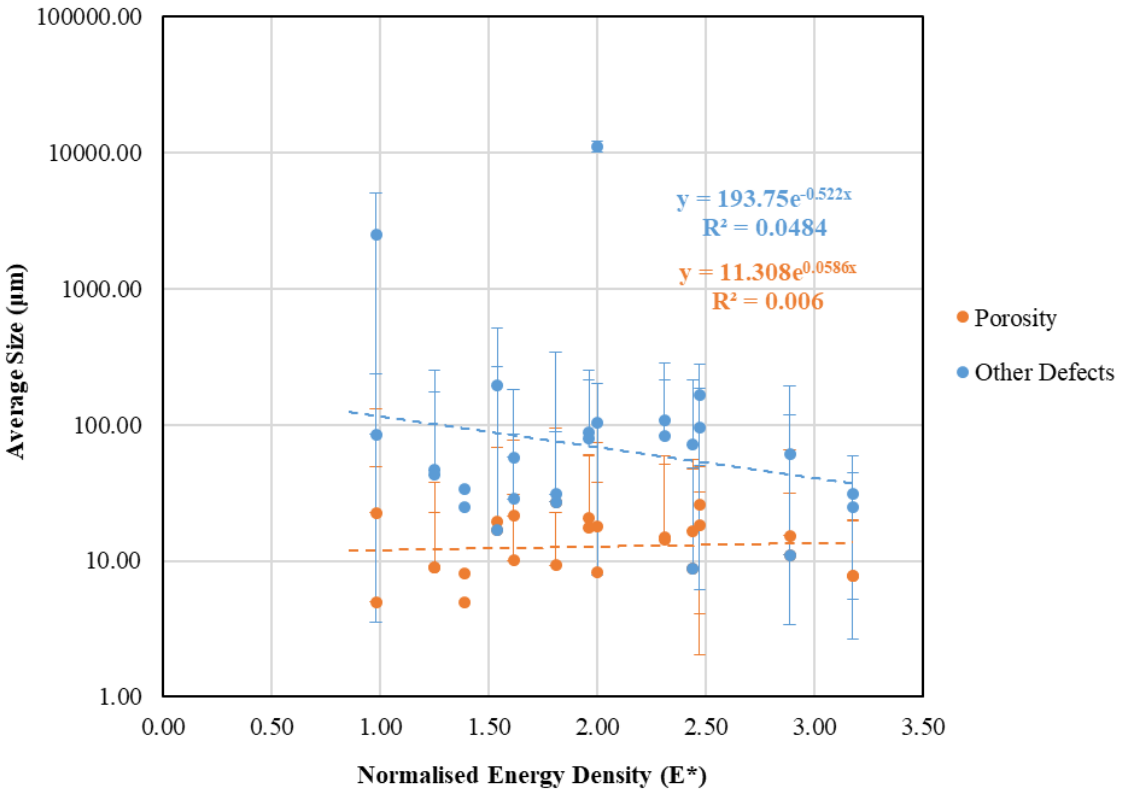

Figure 7.16. Influence of normalised energy density on the average size of porosity and other defects present within LPBF IN718 variants analysed in this DOE.

7.3 Process Variance in Paired Parameters

Although the LPBF IN718 builds within this DOE showcased a relatively strong consistency with regards to the relationship between parameter deposition and defect formation, there was the existence of significant variation observed within specific parameter pairings. These changes in behaviour predominantly manifested themselves in the form of lack of fusion related defects and were picked up as discussed previously, significantly reducing feature count and increasing average feature sizes, both of which deviated from the general trend of behaviour. The most noteworthy example of this can be highlighted in the stitched optical micrographs showcased below in Figure 7.17, where it I evident that sample 19 showcases the prevalence of lack of voidage consequent to poor material consolidation comparative to sample 20, despite the same energy input. This becomes of particular interest when considering that the parameter set deployed consisted of a relatively high energy density comparative to other variants within this DOE and therefore completely contrasts the trends and consolidation mechanisms discussed. Nevertheless, when considering these micrographs, it is evident that the prevalence of these features are a real phenomenon and not limitations of the analytical methodology and therefore further analysis is required in order to gauge an understanding as to why these features occur.

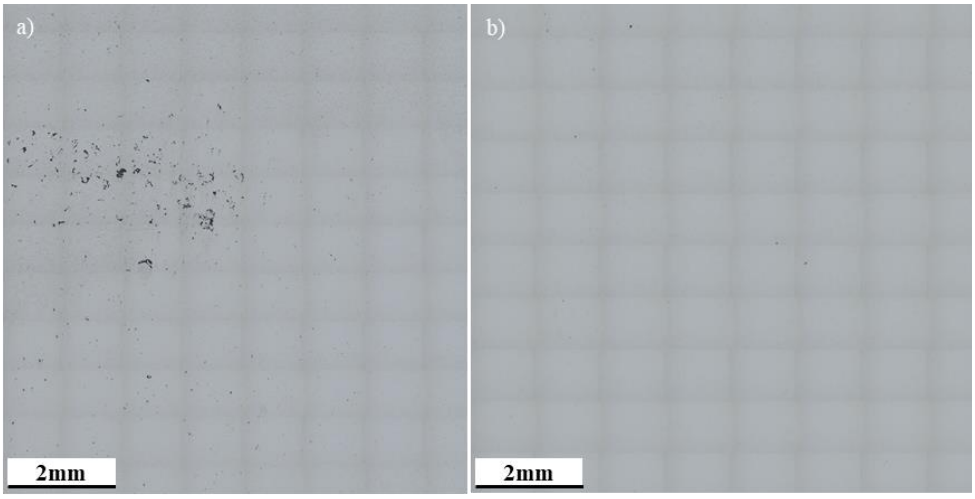

Figure 7.17. Stitched high magnification optical microscopy of paired parameter sets a) 19 and b) 20.

When bearing in mind that the presence of lack of fusion related defects are magnified in specific variants despite the same parameter sets being employed as shown in Table 7.1, alternate considerations need to be taken into account. When interpreting melt track sizing, samples 19 and 20 displayed a relatively similar track height but a reasonable change in track width, although nothing that appears to be significant. When considering these track sizes from a statistical standpoint however, irrespective of average track size, there appears to be a substantial discrepancy in track variance once again, particularly with regards to width and this is particularly evident in sample 19, coinciding with the lack of consolidation observed. All 24 melt track variances for both height and width with respect to their location on the build plate were represented in the form of a contour plot as shown in Figure 7.18, where there appears to be little to no correlation between track height variance with respect to geometric location. There does however once again appear to be a slight relationship observed for track width variance similar to what was observed in Section 5.4, where it was hypothesised previously that this occurred consequent to this location's proximity to the argon gas flow and the wiper starting point, potentially leading to gas trappage that could impact the consistency of the process. Whilst that may hold true for cracking related phenomena which is directly subsequent to non-uniformity in cooling rates and the generation of tensile loading through differing expansion coefficients, this is unlikely to be the case for lack of fusion related irregularities and as such differing criterion must be evaluated. When displaying the average size of lack of fusion related defects with regards to build plate location as shown in Figure 7.19, there is seemingly an external influence which appears to coincide with geometric location. It is apparent that larger average sizes for lack of fusion features are present when in closer proximity to the wipers initiation point, of which appears to plateau off the further the wiper travels. This effect also appears to be exacerbated towards the back of the build plate where argon gas flow is introduced to the system.

When taking into account the underlying mechanisms which underpin lack of material consolidation, although energy deposition is a primary factor, there also needs to be a consideration for powder rheology which could act as an explanatory factor. Although powder was not a significant area of research within this study, it is well acknowledged in literature [177] [178] that not all powder has uniform flowability and that finer particle sizes with a rounder morphology will flow and spread with greater ease. When bearing this in mind and considering that the presence of larger average lack of fusion features lowers with respect to an increased distance from the wiper's initiation point, it is reasonable to suggest that particles with poorer flowability will be more prominent in closer proximity to the wiper. As such, these powder particles could be more suspect to a range of features which are unfavourable to powder packing density such as high aspect ratio particles, the presence of surface satellites or a non-uniform powder size distribution of larger particles, which could innately support void regions that would not be filled during consolidation processes.

Table 7.1. Average melt track sizing and feature % area data from paired parameters that displayed substantial change in behaviour.

Sample	**Parameter Selection**			**Melt Tracks (μm)**				**Features (% Area)**	
	v	h*	q	Avg Height	σ^2	Avg Width	σ^2	Porosity	Other Defects
19	1.00	2	4	40.31	117.72	132.28	449.32	0.196	0.440
20	1.00	2	4	44.27	109.63	115.68	198.30	0.027	0.007

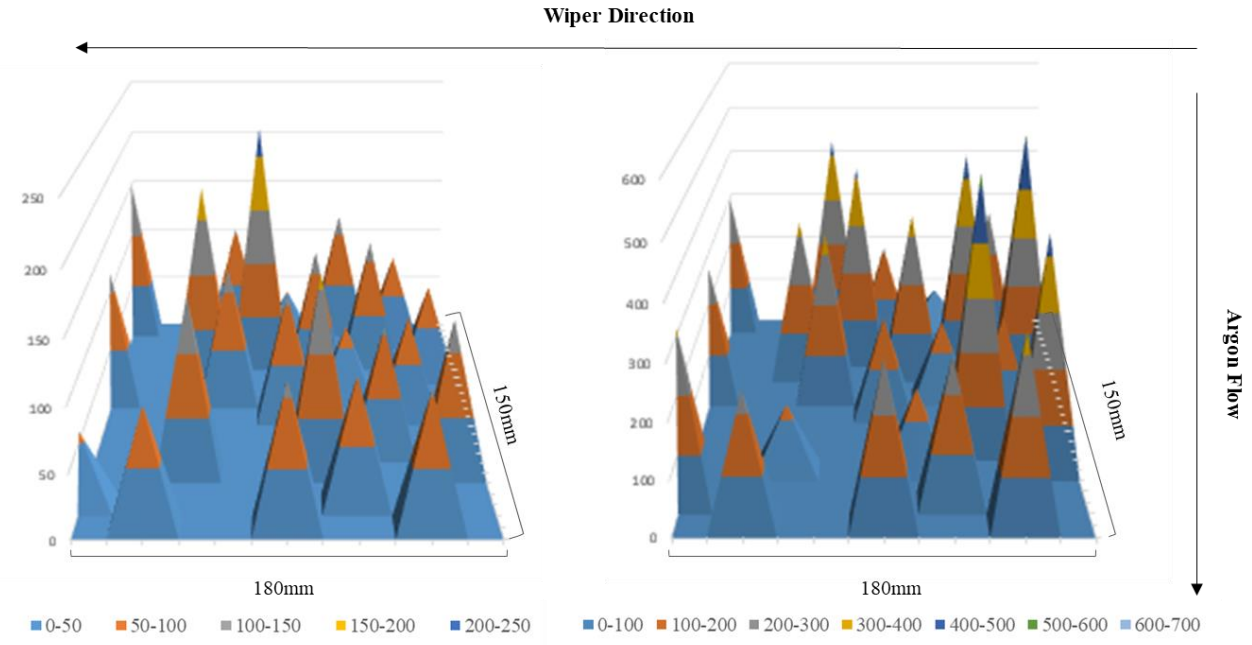

Figure 7.18. Melt track variance mapping in relation to build position for a) melt track height and b) melt track width for LPBF IN718 builds.

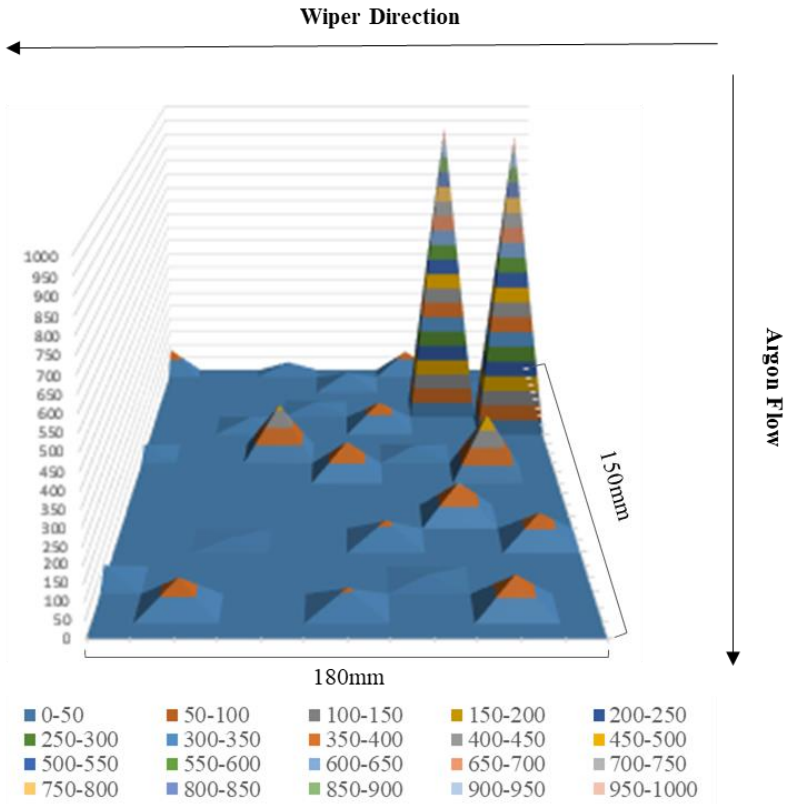

Figure 7.19. Melt track variance mapping in relation to build position for a) melt track height and b) melt track width for LPBF IN718 builds.

7.4 Summary

In summary, a collection of melt track measurements for both height and width was taken in accordance with optical microscopy on a range of LPBF IN718 variants comprising of changes in normalised beam speed, power and energy density. There appeared to be a significant correlation between increasing normalised energy density or contributory parameters and track coarsening given the increased energy uptake subsequent. In addition to this, a robust statistical approach for defect analysis was considered, where numerical criterion such as percentage area, feature count and average feature size was considered with respect to parameter selection. Lower energy densities appeared to showcase the heightened prominence of lack of fusion related defects and porosity, which was seemingly mitigated with increasing energy input within this DOE as consolidation mechanisms were supported.

Overall, a series of LPBF variants with differing process conditions for the contrasting nickel-based superalloys CM247LC and IN718 were subject to miniaturised mechanical testing methodologies alongside a variety of microstructural evaluation techniques. This included optical microscopy, electron microscopy, EDS and EBSD. In addition to these methodologies, an in-depth, robust analytical methodology was employed to access the influence of process parameters on both melt track sizing and the presence of a variety of defects, helping drive a further understanding as to the underlying mechanisms which underpin their formation. The following section will discuss the results shown with respect to the entire scope of the study, drawing comparisons and evaluating the similarity and contrasting behaviours observed between both CM247LC and IN718.

Chapter 8 – General Discussion

From the work carried out within this study, there appears to be the existence of both some significant similarities and differences observed between LPBF CM247LC and IN718's behaviour, irrespective of their alloying chemistry and the contrasting volume fraction of strengthening precipitates. The following section will look to compare and contrast these behaviours with regards to the entire scope of the study, taking into account the mechanical testing performed, the microstructural analysis of mechanisms that underpin their behaviour and a robust quantitative analysis, which evaluated both melt track formation and the propensity for defect formation consequent to parameter deposition.

8.1 Build Orientation

A series of LPBF variants for both CM247LC and IN718 were fabricated with changes in build orientation and parameter deposition. It was evident that both alloys were subject to highly anisotropic behaviour throughout this study given the directional heat flow and epitaxial grain growth mechanisms apparent in additive processes. The sectioning methodology conducted in collaboration with SPC testing highlighted significantly contrasting grain sizes and morphologies as shown in Figures 4.2 & 6.2, consequent to the two distinct build orientations, 30^{o} and 90^{o}. The grain structures observed in 30^{o} orientations consistently comprised of fine-grain equiaxed microstructures, contrasting that of 90^{o} orientations which exhibited coarsened columnar grain structures, both of which were verified through general microstructural observations alongside EBSD grain size calculations, as shown in Tables 4.2 & 6.2, which occurred independent of alloying chemistry. The grain structures seen displayed significant implications on the creep performance of both alloys, where the heightened volume fraction of grain boundaries apparent in the 30^{o} orientations rapidly accelerated minimum displacement rates and lower time to ruptures as depicted in Tables 4.1 & 6.1, consequent to creep deformation being grain boundary initiated and dominated.

Microstructural observations revealed the existence of triple-point or wedge cracking in CM247LC's 30^{o} orientations as illustrated in Figure 4.4, which was hypothesised to be consequent to heightened stresses at these triple-point regions and given their inherently large nature, more likely led to the onset of catastrophic failure. This appeared to manifest itself in the form of consistently short rupture lives within 30^{o} orientations, irrespective of parameter deposition within this DOE. There was no notable existence of triple point cracking in the IN718 30^{o} variants as showcased in Figure 6.3, which could suggest a greater tolerance to strain accumulation along grain boundaries but it was unclear as to whether this was the case as it could be consequent to the different testing conditions employed, despite the loading conditions on LPBF IN718 being significantly higher at 500N comparative to 150N for

CM247LC. Nevertheless, consistently poor performances of a similar range were once again observed, further supporting the notion that grain sizing and morphology generally dictates creep performance within these variants.

The observations discussed can be visually represented in the Monkman-Grant relationship shown in Figure 8.1, which comprises of merged data from Chapters 4 & 6 for all LPBF CM247LC and IN718 variants subjected to SPC testing within both respective DOEs. It is evident that 30° orientations are susceptible to substantially faster displacement rates than their 90° counterparts and this phenomenon occurs regardless of alloy chemistry, which subsequently correlates and leads to a marked decrease in creep performance. Although it can be misleading to draw direct comparisons between the trendlines' numerical notations given the individually distinct testing conditions utilised, there does appear to be a marked decrease in the minimum displacement rates observed within IN718s DOE which corresponds to their comparatively extended lifetimes.

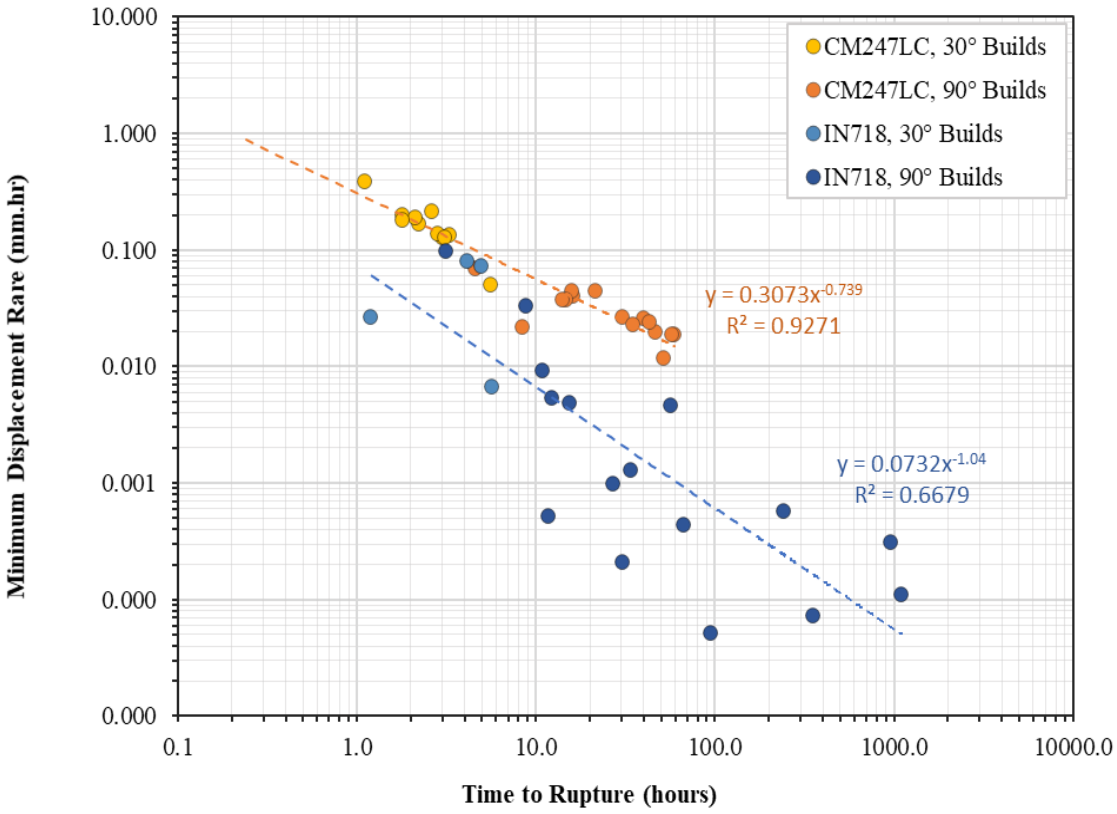

Figure 8.1. Monkman-Grant Relationship for LPBF IN718 (650°C, 500N) and CM247LC Builds (950°C, 150N) subjected to SPC testing.

8.2 Parameter Selection

Despite the existential similarity in behaviour between LPBF CM247LC and IN718 from an anisotropic standpoint, there appeared to be some noteworthy dissimilarities with regards to parameter selection and in particular energy deposition, regardless of the similar textural evolution and underpinning mechanisms being highlighted in EBSD analysis. A generic low, medium and high energy density was employed on both alloys, with CM247LC's DOE also including variations in normalised hatch spacing. Although there are some limitations to drawing direct comparisons given the ambiguity surrounding the process parameter sets, alongside the differentiations in testing conditions employed, general microstructural observations consequent to energy deposition and their impact on high temperature mechanical performance can be drawn.

It was shown within the CM247LC's variants that a general increase in energy density appeared to subsequently degrade creep performance, as shown in Table 4.1, through the development of defects, in particular intergranular cracking. Low energy variants appeared to be relatively dense with little presence of defects and no clear signs of grain boundary decohesion as depicted in Figure 4.16d, which was likely to be consequent to the material's consolidation threshold being reasonably surpassed. This variant showcased a heightened creep performance with respect to the medium and high energy variants, despite the existence of finer grain sizing and lack of textural development evident in Table 4.4, Figures 4.20a-c and 4.21a & b. Medium energy density variants showcased the initial signs of grain boundary cavitation as illustrated in Figure 4.16c, consequent to the higher non-uniformity in cooling rates likely to be apparent in larger melt pools, which would initiate tensile loading and strain accumulation along grain boundaries. This can be observed in Figure 4.12b & e. These variants displayed a marked decrease in creep performance and as such it would appear that these cavitations drove the mechanical performance of this material variant, irrespective of the initiation of textural development and coarsened grain sizes that were also apparent. High energy variants showcased the frequent presence of intergranular cracking, likely to be consequent to cavitation coalescence as a result of heightened strain accumulation along grain boundaries as shown in Figures 4.16b & 4.17, subsequent to the additional disparity in contraction rates. This led to a further decrease in creep lifetime regardless of the furthered textural development represented in Figure 4.20d-f and Figures 4.21c & d alongside coarsened grain sizing showcased in Table 4.4, once again indicating that the performance of this variant was dictated and dominated by the presence of defect features.

The trends discussed appeared to be in contrast to the IN718 variants, where an increase in energy density generally improved creep performance, as shown in Figure 6.1, subsequent to the reduction of defects in combination with textural development and coarsened grain sizing. Low energy variants appeared to be highly susceptible to density related issues, particularly in the form of the lack

of fusion welds and unfused powder particles revealed in Figures 6.11 & 6.12, suggesting that the energy deposition was not sufficient enough to entirely surpass the materials' consolidation threshold. The prominence of these features in combination with the finer grain sizing and lack of textural development showcased in Table 6.3 and Figures 6.9 & 6.10 led to a substantial reduction in performance comparative to its medium and high energy counterparts as highlighted in Table 6.1. Medium energy variants showcased the minimal presence of defects which inherently led to the materials' performance being microstructurally driven. Coarsened grain sizing, as highlighted in Table 6.3, alongside the development of material texture through the form of an increased presence in LAGBs, as shown in Figure 6.15, facilitated greater resistance to creep deformation as a result of larger regions of material behaving as an ESU. High energy densities once again showcased a minute presence in defects consequent to considerable material consolidation, allowing the variants' properties to be driven by microstructural phenomenon. The grain sizing calculations showcased in Table 6.3 revealed a considerably coarsened grain structure comparative to the low and medium energy counterparts previously examined, minimising the presence of grain boundaries subject to creep deformation. In addition to this, EBSD analysis showcased further textural development with an enlarged presence of LAGBs, as shown in Figure 6.19c, further aiding and amplifying the existence of an ESU. It was noticed once again that strain accumulation appeared to localise along grain boundaries in these variants as illustrated in Figure 6.19b, given the greater degree of non-uniformity and discrepancy in contraction rates, which is inherent in larger melt pools. However, this strain accumulation did not appear to heighten the presence of grain boundary decohesion or degrade mechanical properties, suggesting that the exceptional creep performances observed relative to the rest of the DOE were driven by a combination of textural development and coarsened grain sizing.

When considering the relationships discussed, it becomes apparent that the underlying microstructural mechanisms consequent to energy deposition, particularly grain coarsening and textural development are relatively consistent across both alloys. Despite this, there is a considerable change with regards to how this manifests itself, particularly with regards to the development of defects which appear to be innately tied to the alloy's individual chemistry. Given the highly strengthened nature of CM247LC and its prominent dislocation activity, heightened strain accumulation along grain boundaries appear to give rise to grain boundary decohesion subsequent the materials intrinsic ductility drop. IN718 on the other hand, appears to be highly tolerable to this strain accumulation along grain boundaries given its inherent ductility and weldability and as such, the manifestation of defects appears to be limited. This allows its subsequent creep performance to be driven by microstructural phenomenon such as texture and grain sizing rather than the presence of density related issues.

8.3 Melt Track Analysis

Given the existential relationships between energy deposition, melt pool characteristics and the propensity for defect formation as discussed, a quantitative understanding of the influence of process parameters on melt pool geometries is needed. As such, a numerical approach for quantifying melt track profiles was employed, where 50 to 70 manual measurements for both track height and width were collected on an assortment of LPBF variants, with changes in normalised beam speed, beam power and energy density across both CM247LC and IN718.

The influence of individual process parameter selection was firstly considered in the form of normalised beam speed, where increases in beam speed led to the refinement of track sizes for both height and width, irrespective of the alloy. This was to be expected given the well-established relationship between beam speed and energy density, where higher beam velocities would inherently reduce energy uptake, providing further credence to the use of energy density as a metric. These results were validated in Figures 5.3 & 7.4 and consistently showcased an inverse relationship with regards to an increase in normalised beam power, which generally resulted in track coarsening for both height and width, once more coinciding with energy density principles. Considering the concurrence of the experimental results shown and the use of energy density as a quantitative metric, the influence of normalised energy density was considered across all process variants for both alloys, where numerical data from Chapters 5 and 7 were amalgamated as shown in Figure 8.2. For the most part, there was a considerable agreement between normalised energy density and melt track profile, with higher energy inputs leading to a largening of track height and width, where track width appeared to display a greater sensitivity. There did seem to be some data variation, which was most prominent within the melt track heights observed in CM247LC, but this is to be expected given the subjective nature of the measurement system. Nevertheless, the largening of melt tracks consequent to increasing energy densities consistently seen in both CM247LC and IN718 corresponds with the physiothermal characteristics of the process, which inherently dictate the anisotropic microstructures and directional heat flow mechanisms previously examined.

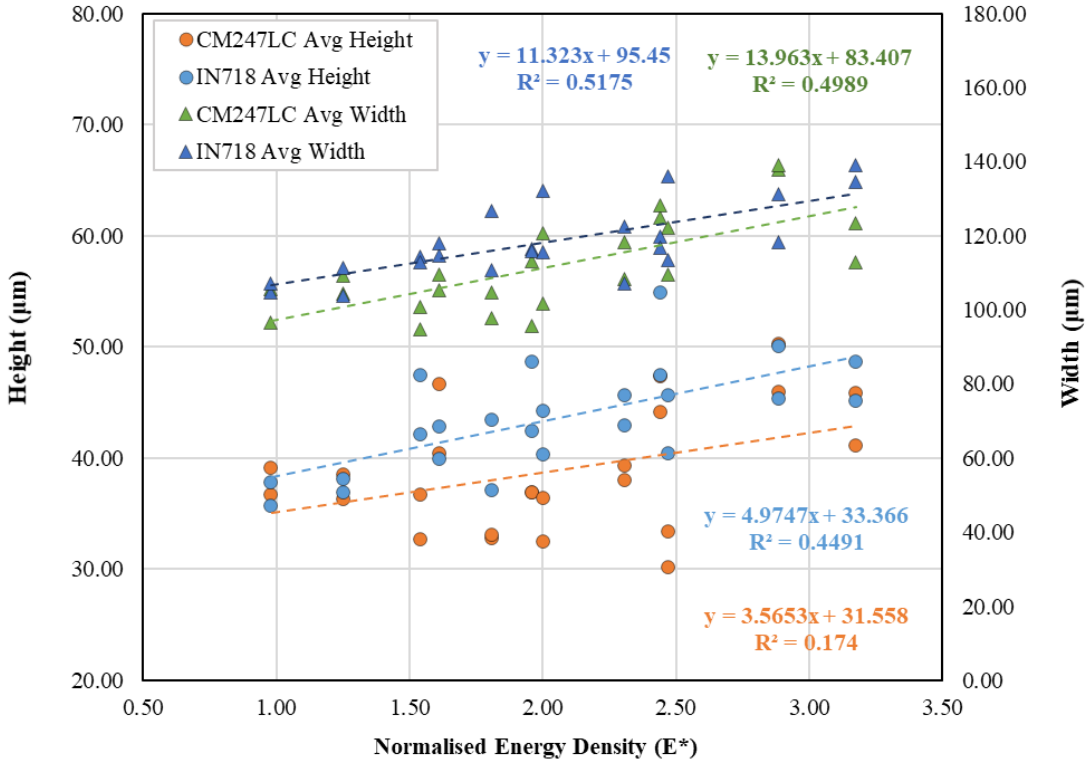

Figure 8.2. Influence of normalised energy density on the average melt track height and width apparent in the LPBF CM247LC and IN718 DOE.

8.4 Defect Analysis

Considering the dominant influence of defect population on the creep performances previously explored in Chapters 4 & 6, the need for the quantification of such features and each alloys' overall propensity for defect formation is seemingly evident. As such, stitched optical imaging at 200x magnification was collected across 24 LPBF variants in each alloy, with changes in normalised beam speed, power and fundamentally energy density being considered. These images were thresholded appropriately in order to encapsulate the presence of defects within this material, with the raw data generated being numerically distinguished with considerations to the microscopy collected in order to represent specific types of additive features present. This presence of features was correlated against the changing parameters using a series of numerical measures, with data sets from Chapters 5 & 7 being compounded.

The first quantitative metric considered was the influence that parameter selection had on the area percentage of features, as represented in Figure 8.3. Within CM247LC, increases in normalised energy density significantly contributed to the propensity of microcracking apparent, coinciding with the results shown in Chapter 4 and the considerable amounts of literature explored in Section 2.3.3. These findings were given further credence to when considered in respect to the optical images presented in Figures 5.6, 5.8 & 5.10, substantiating the analytical methodology employed. Given the

coherency of these results with the work outlined previously, it was hypothesised that this is once more consequent to the same mechanism previously explored, where the larger volumes of melt pool subsequent to higher energy inputs are more suspect to amplified discrepancies in solidification and contraction rates. These discrepancies heighten strain accumulation along grain boundaries which manifest itself in the form of grain boundary decohesion, cavitation coalescence and consequently intergranular cracking.

Within IN718, there appears to be no propensity for microcracking behaviour despite the same parameter sets being utilised, highlighting the contrasting behaviour observed between the two alloys with regards to energy conduction and tolerance. Furthermore, the lower end of energy densities employed within this DOE appear to give rise to the presence of lack of consolidation related defects in IN718, which were not present in CM247LC, once again highlighting the disparities in energy tolerance. As normalised energy density increased, the presence of these lack of consolidation related features appeared to be significantly reduced, suggesting that the energy densities employed within this DOE appeared to cross the material consolidation threshold range towards the higher end. These analytical findings were once again substantiated when considered in respect to the optical microscopy images represented in Figures 7.6, 7.8 & 7.10.

When considering the presence of porosity, the comparative relationships observed between CM247LC and IN718 once again showcased noteworthy dissimilarities. There appeared to be the presence of a non-linear relationship for porosity presiding within CM247LC, providing ambiguity with regards to the overall relationships apparent. This was not seemingly the case for IN718, where a clear existential relationship between normalised energy density and porosity was apparent, with higher energies leading to a marked reduction in the presence of porosity from an area percentage standpoint. This was presumed to be as of consequence to higher energy inputs aiding and accommodating consolidation mechanisms as previously explored. When taking into consideration the ambiguity in porosity measurements observed within CM247LC proportional to IN718, despite the same process variants being employed, it is important to note the divergence in alternative features such as microcracking and lack of fusion as explored. This gives the introspection that these alloys are subjected to different regions within their respective process window which may also intrinsically be of different sizes as shown in Section 2.3.3 and highlighted in Figure 2.18. When bearing this in mind, given the non-linear relationship between porosity accumulation and energy input as highlighted in literature [94] [171], the ambiguity in results may be consequent to the pickup of data oscillation and this is given further credence with the coefficient of determination value being substantially lower in CM247LC than in IN718. Nonetheless, alternative numerical metrics such as feature count and average feature size were used in order to further the understanding of defect formation.

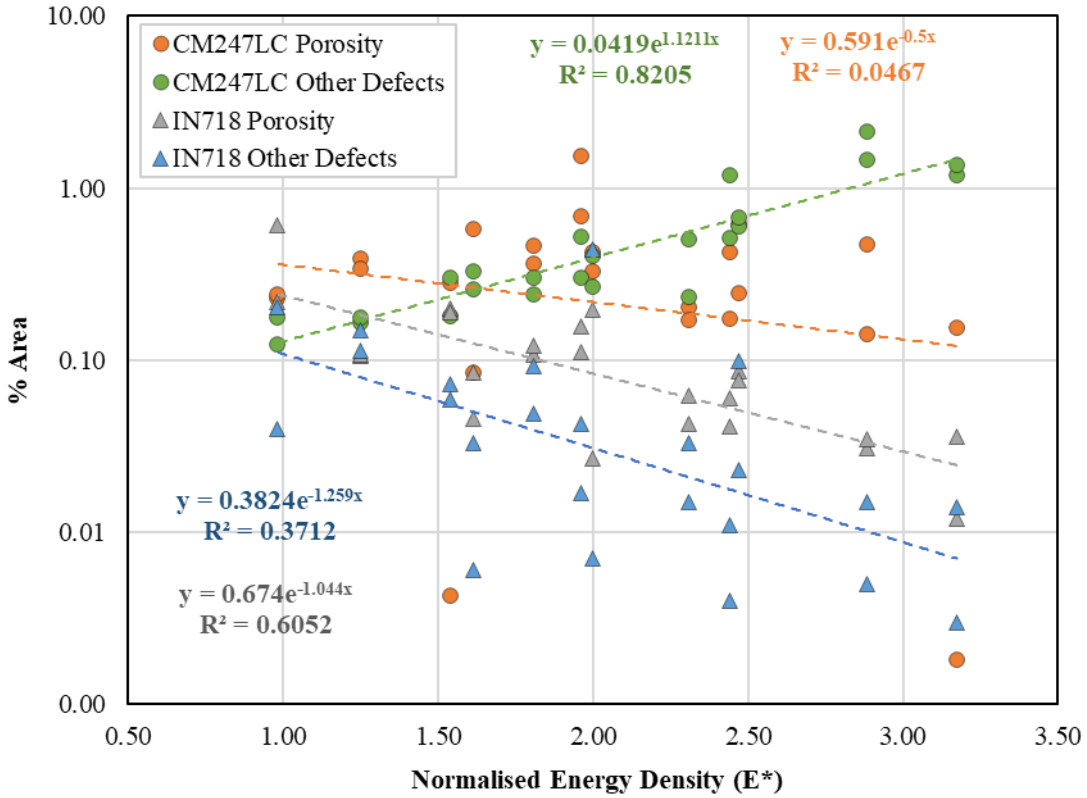

Figure 8.3. The influence of normalised energy density on the area percentage of defects present in all variants within the LPBF IN718 and CM247LC DOEs.

As mentioned, the use of alternative arithmetical criterion such as feature count and average feature size were used in an attempt to further encapsulate the population of defects within both CM247LC and IN718. The relationship between normalised energy density and the frequency of these features is presented in Figure 8.4, which comprises of collective data from Chapters 5 and 7. It becomes apparent that the general observations perceived with regards to area percentage for microcracking and lack of fusion related defects within CM247LC and IN718 continue to ensue for feature count. Higher energy densities seemingly led to the heightened frequencies of microcracking present in CM247LC and a reduction in the frequency of lack of fusion related defects in IN718, suggesting that there is an empirical relationship between area percentage and feature count that exists and acts as the primary underpinning mechanism. Furthermore, the average size of these features was also considered with collated data from Chapters 5 and 7 as represented in Figure 8.5, where the average size of these features appeared to considerably coincide with the trends observed with regards to the frequency of their occurrence. There was seemingly more scatter apparent with respect to the lack of fusion related defects, but this inversely corresponded with the scatter evident in feature count.

Despite the use of alternative numerical metrics, the ambiguity surrounding CM247LC's porosity analysis continued to transpire, where the relationships observed for both feature count and

average size appeared to once more concur with area percentage. When considering the contrasting behaviour with regards to microcracking or lack of fusion related defects, despite the same parameter settings being employed, it is apparent that this DOE is subjecting these two alloys to different regions of their retrospective process window, which will innately differ. Consequently, the indefinite relationship consistently observed across different quantitative criterion is likely consequent to the pickup of data oscillation as discussed, where localised regions within a sinusoidal relationship was subject to scrutiny as visually represented in Figure 8.6. This obscurity in porosity did not appear to be the case for IN718, where a strong agreement was established with regards to increasing normalised energy density and a decrease in the frequency in porosity observed, given that higher energies are more accommodating to material consolidation mechanisms as discussed. There appeared to be no significant influence on the average size of porosity which is to be expected given that the mechanism for porosity formation, gas entrapment, is unlikely to change consequent to energy deposition and as such the relative sizing of these features will be unaffected.

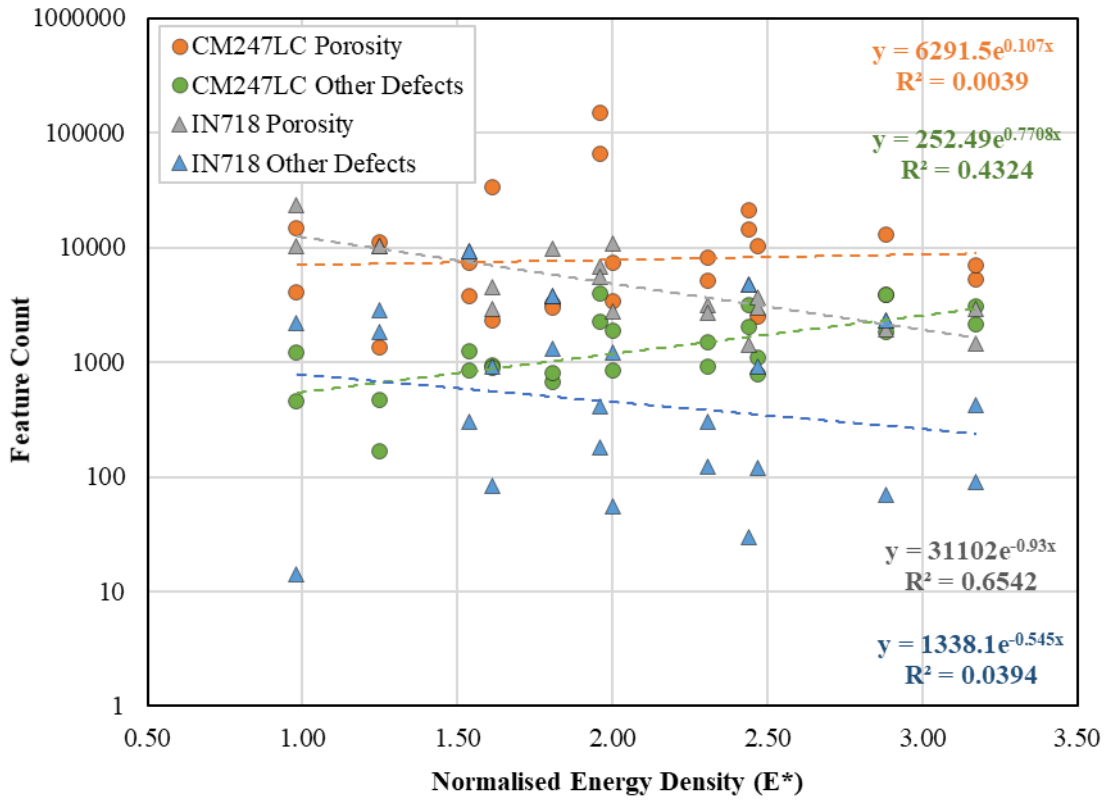

Figure 8.4. Influence of normalised energy density on the presence of defects in all variants within the LPBF CM247LC and IN718 and DOEs.

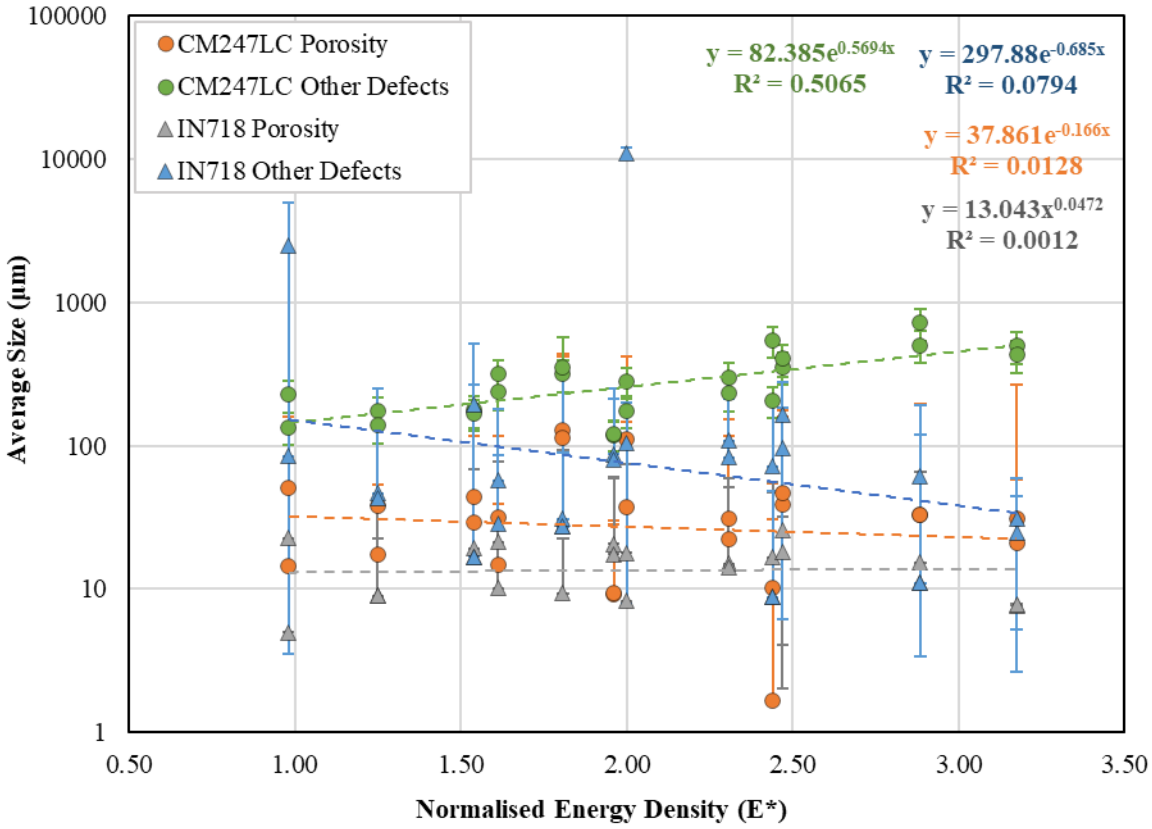

Figure 8.5. Influence of normalised energy density on the average size of features present in all variants within the LPBF IN718 and CM247LC DOEs.

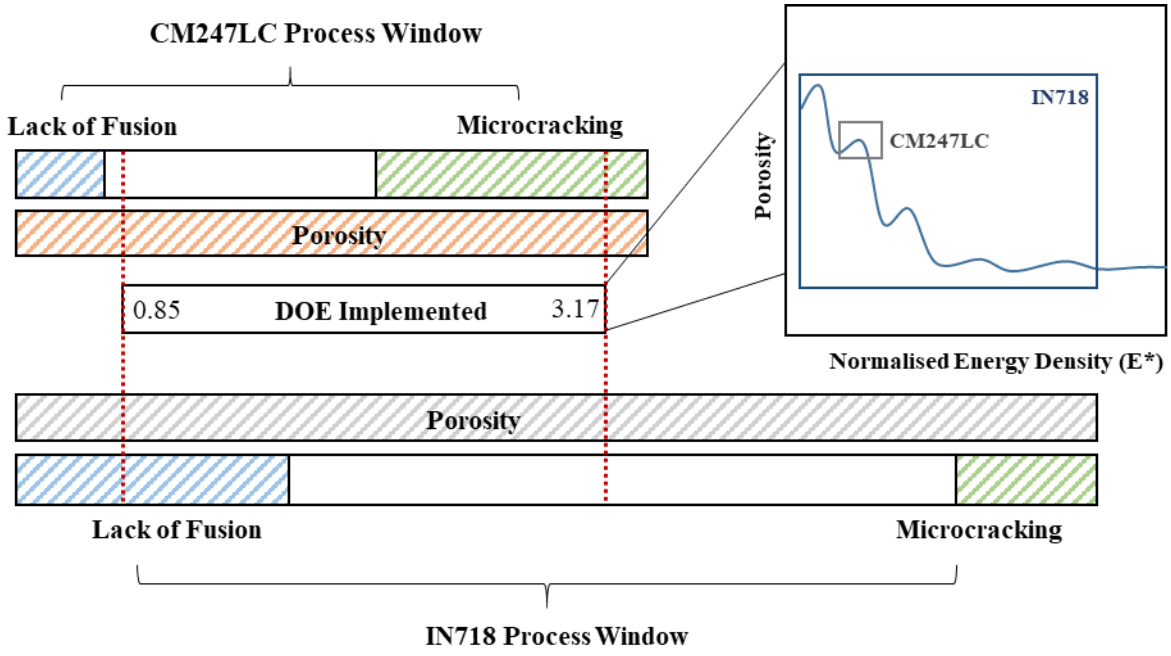

Figure 8.6. Visual representation of the porosity ambiguity hypothesis in LPBF CM247LC comparative to IN718, highlighting the dissimilarities in material thresholds to specific defects (not drawn to scale).

Chapter 9 – Conclusions and Recommendations for Future Work

Within this study, multiple investigative techniques were employed on a series of laser powder bed fused (LPBF) variants for the two contrasting nickel-based superalloys CM247LC and IN718. These techniques included the use of a miniaturised mechanical testing methodology, in-depth microstructural characterisation through electron microscopy, and a robust statistical approach for quantifying melt track profiles and defect propensity utilising optical microscopy. This chapter will briefly summarise the main findings presented and highlight some of the themes of research and areas of interest which could complement and add to the results presented.

9.1 Conclusions

Build orientation was shown to be the most significant influencer of small punch creep (SPC) performance in both LPBF CM247LC and IN718, where 30° orientations appeared to perform consistently poorer than that of 90° orientations, irrespective of parameter deposition. This was consequent to the evident existence of highly anisotropic microstructures subsequent to the epitaxial grain growth mechanisms apparent in additive processes, which was revealed and quantified through electron microscopy. 30^{o} builds consisted of a fine-grain, equiaxed microstructure comparative to the coarsened columnar grain morphology evident in 90^{o} orientations. As a result of this, the 30° orientation variants were subject to a higher volume fraction of grain boundaries, inherently accommodating creep deformation which innately accelerated the minimum displacement rates and time to ruptures observed.

Parameter selection was revealed to substantially impact the SPC performance of both alloys in different manners, despite relatively similar textural evolution being observed. In CM247LC, an increase in energy density appeared to degrade resistance to high temperature deformation mechanisms, through the form of grain boundary decohesion and cavitation coalescence, which innately promoted intergranular cracking. Regardless of the textural development apparent, the performances displayed were intrinsically dominated by the existent density related features, specifically solidification cracking. These features were consequent to the heightened strain accumulation evident along grain boundaries, given the magnified mismatch in contraction rates inherent to larger melt pools. These relationships were in contrast to IN718, where increasing energy density innately benefitted SPC performance by reducing the density related issues present in lower energy inputs, allowing SPC performance to be driven by the microstructural phenomenon existent. This included the grain coarsening subsequent to the extended cooling rates associated with increasing energy inputs, alongside textural development through the reduction of high angle grain boundaries (HAGBs), which aided the presence of an effective structural unit (ESU) and therefore benefitting SPC behaviour.

The influence of individual parameter selections such as normalised beam speed and beam power on melt track sizing appeared to be inversely related and reasonably concurrent with normalised energy density, providing further credence for its use as a metric for encapsulating melt pool profiles. As such, increases in normalised energy density were considered and appeared to showcase a strong correlation to the coarsening of track sizes with respect to track height and width, with width seemingly being more sensitive. This relationship appeared to consistently transpire in both CM247LC and IN718, irrespective of alloy chemistry.

Investigations into the propensity for defect formation in CM247LC and IN718 was conducted using several quantitative metrics including percentage area, feature count and average feature size, where there appeared to be a stark contrast in each alloys' behaviour. In CM247LC, there appeared to be a strong agreement between increasing normalised energy density and the alloy's predisposition to microcrack, where higher percentage areas were observed consequent to the heightened frequency and enlargement of these features. IN718 on the other hand did not appear to be suspect to microcracking but rather lack of fusion related defects, where lower energies led to the prominence of such features in a similar manner, with higher area percentages being witnessed consequent to the increased frequency and size of these features once again. Despite the same processing conditions being employed, the significant dissimilarities in defect formation highlights the disparity in each alloys' respective process windows, where the highly strengthened CM247LC appears to be more susceptible to solidification cracking and IN718 suspect to lack of consolidation issues, coinciding with the work outlined in previous chapters.

A contrast in the presence of porosity presiding within both alloys with respect to the same changes in normalised energy density was witnessed, where an ambiguous non-uniform trend was evident in CM247LC and a clear existential trend revealed in IN718. In CM247LC, the percentage area of porosity was seemingly amplified in the mid-range energy densities and this was further reiterated when considering both feature count and average feature size. IN718 on the other hand, displayed a significantly clear correlation with regards to a reduction in the percentage area of porosity, with respect to increasing normalised energy density. This appeared to coincide with a decline in the frequency of porosity present, but bared no significant influence on the sizing of porosity given there being no substantial change in mechanism. The overall relationship apparent in IN718 was hypothesised to be consequent to consolidation mechanisms being aided with increasing energy input. Given the innate discrepancies in each alloys' corresponding process window, it was hypothesised that the porosity relationship displayed in CM247LC was consequent to data oscillation, where an extremely localised region of porosities overall influence was subject to inspection.

9.2 Recommendations for Future Work

A vast amount of small punch (SP) testing, both creep and tensile, was completed on an array of LPBF variants for both a weldable and 'unweldable' nickel-based superalloy within this study. It may provide further insight if interrupted tests conducted at different stages of displacement were carried out, in order to supplement the understanding of deformation mechanics in these materials within these testing techniques. In addition to this, the utilisation of back-to-back traditional uniaxial testing methodologies could give greater confidence in the results, considering that SP testing was utilised within this work as an effective ranking methodology for rapid validation. The derivation of baseline tensile and creep properties for the cast and wrought forms of these alloys would also prove to be beneficial from a comparative standpoint. In order to further compliment the SP testing conducted, the defect analysis incorporated in Chapters 5 & 7 could be employed on SP specimens pre-testing, in order to quantify the density of the materials and correlate performance to the presence of specific types of defects.

The contrast in microstructural and mechanical behaviour between LPBF CM247LC and IN718 has been well explored in this study with a particular emphasis drawn to the localisation of strain accumulation evident, consequent to residual stressing. As such, the use of residual stress measurements in the form of hole drilling, X-ray diffraction or neutron diffraction would prove useful in quantifiably assessing the magnitude of residual stressing apparent. Moreover, the manifestation of residual stressing in the form of grain boundary decohesion in CM247LC comparative to IN718 was particularly emphasised in this study consequent to changes in the abundance of strengthening precipitates. As such, the utilisation of transmission electron microscopy could characterise these changes, particularly with regards to dislocation networks and how they impact grain boundary sliding.

The lack of processing information made available within this study significantly weakened the ability to correlate process parameters, microstructural features and mechanical properties, with the quality and controllability of the parameters selected alongside additional process information such as machine calibration, inter and intra-build porosity variation hindering the ability to interpret the results generated. An example of this can be seen with respect to the statistical explorations of melt pool dimensions discussed in Chapters 5 & 7, where poor correlations were observed between melt pool height and width. The variation of melt pool dimensions with respect to different volumetric energy density bands is well documented, with the relationship between beam power and melt pool depth being thought to be quadratic as an example. As such, the use of ambiguous normalised process parameter values provides a significant hindrance, as the discrepancies between 180-200W and 200-300W would be substantially influential on the results produced.

Although the statistical analysis employed on multi-pass welds within this work has provided some useful insight, it may have contributed to and exacerbated some of the variances observed. As such, it would prove valuable to adopt single track welds with the same assortment of process settings in order to compare, contrast and ascertain the statistical variation between these two procedures. As mentioned, the ambiguity of normalised process parameters provided clear limitations to the work carried out, particularly with regards to the statistical explorations discussed. It would be advantageous to have discernible values for hatch spacing in order to establish the link between melt track overlap and defect formation, with some literature suggesting higher levels of remelt leads to a reduction in defects at the expense of favourable process economics. On a similar note, it would also be beneficial to have palpable values for layer thickness, where the tolerance for melt pool penetration can be evaluated and correlated to defect formation.

Defect analysis was employed from a two dimensional perspective using micrographs in order to assess the frequency and existence of specific types of defects. It would prove useful to incorporate a three dimensional methodology such as X-ray diffraction and computed tomography, in order to further assess the presence of defects and how these develop from a multiaxial standpoint with respect to changes in parameter deposition. Furthermore, the use of the more well recognised Archimedes method for density measurements could have been conducted pre sectioning in order to provide additional analysis and validate the novel methodology employed. The utilisation of electro-etching in combination with particle analysis would also prove valuable in order to understand the influence that process settings on gamma prime size distributions, more specifically how the rapid freezing ranges associated with the process impose on the size and coherency of strengthening precipitates.

Throughout the scope of this study, logistical constraints have led to some inconsistencies with regards to the abundance of process variants fabricated and examined in each chapter. The expansion of these work packages to provide additional variants would prove useful from a comparative standpoint. These expansions would include a plethora of as-built and post processed variants for both materials, examples of which include the incorporation of parameter sets 4 and 5 within the IN718 DOE analysis alongside heat treated and hot isostatically pressed (HIP) forms of these variants. In addition, the fabrication of HIPed rods for LPBF IN718 similar to what was provided in LPBF CM247LC as outlined in Section 3.4, could provide significant insight and allow comparative behaviours in the form of macrocracking and SPT performances to be analysed and interpreted. Additionally, the manufacturing of these builds at the same time on the same machines would have been preferable in order to minimise any process and build-to-build variation.

References

[1] Rolls-Royce plc., The Jet Engine, 5th Edition, Derby, 1996.

[2] "Civil Aerospace - Business Aviation," Rolls-Royce plc., [Online]. Available: https://www.rolls-royce.com/products-and-services/civil-aerospace.aspx#/business-aviation. [Accessed 01 01 2020].

[3] Rolls-Royce plc., "Gas turbine technology - Introduction to a jet engine".

[4] N. Crumpsty, "Jet Propulsion: a simple guide to the aerodynamic and thermodynamic design and performance of jet engines," *The Aeronautical Journal*, vol. 102, no. 1016, p. 330, 1998.

[5] M. Boyce, Gas Turbine Engine Handbook 4th Edition, Butterworth-Heinemann, 2011.

[6] R. Flack, Fundamentals of Jet Propulsion with Applications, Cambridge University Press, 2005.

[7] Y. Cengel, M. Boles and M. Kanoglu, Thermodynamics: an engineering approach, New York: McGraw-Hill Education, 2019.

[8] P. Spittle, "Gas turbine technology," *Physics Education,* vol. 38, no. 6, 2003.

[9] R. Reed, The Superalloys: Fundamentals and Applications, Cambridge University Press, 2009.

[10] N. Miktinutalapati, "Materials for Gas Turbines - An Overview," in *Advanced in Gas Turbine Technology,* InTech, 2011.

[11] T. Rutherford, "Air transport statistics," House of Commons Library, 2011.

[12] Department for Transport, "UK Air Passenger Demand and CO2 Forecasts," 2009.

[13] X. Sun, S. Wandelt, C. Zheng and A. Zhang, "COVID-19 pandemic and air transportation: Successfully navigating the paper hurricane," *Journal of Air Transport Management,* vol. 94, 2021.

[14] Advisory Council for Aviation Research and Innovation in Europe, "FlightPath 2050 Goals - Protecting the environment and the energy supply," [Online]. Available: https://www.acare4europe.org/sria/flightpath-2050-goals/protecting-environment-and-energy-supply-0. [Accessed 01 01 2020].

[15] T. Pollock, "Nickel-Based Superalloys for Advanced Turbine Engines: Chemistry, Microstructure, and Properties," *Journal of Propulsion and Power,* vol. 22, no. 2, 2006.

[16] M. Perrut, P. Caron, M. Thomas and A. Couret, "High temperature materials for aerospace applications: Ni-based superalloy and γ-TiAl alloys," *Comptes Rendus Physique,* vol. 19, no. 8, pp. 657-671, 2018.

[17] A. Nowotnik, K. Kubicak, J. Sieniawski, P. Rokicki, P. Pedrak and G. Mrowka-Nowotnik, "Development of nickel based superalloys for advanced turbine engines," *Materials Science Forum,* Vols. 783-786, pp. 2491-2496, 2014.

[18] A. Buch, Pure metals properties: A scientific and technical handbook, ASM International, 1999.

[19] R. Kozar, A. Suzuki, W. Milligan, J. Schirra, M. Savage and T. Pollock, “Strengthening Mechanisms in Polycrystalline Multimodal Nickel-Base Superalloys,” *Metallurgical and Materials Transcations A,* vol. 40, no. 7, pp. 1588-1603, 2009.

[20] S. Milenkovic, I. Sabirov and J. Llorca, “Effect of the cooling rate on microstructure and hardness of MAR-M247 Ni-based superalloy,” *Materials Letters,* vol. 73, pp. 216-219, 2012.

[21] M. Donachie and S. Donachie, Superalloys: A Technical Guide, 2nd Edition, ASM International, 2002.

[22] R. Schafrik and R. Sprague, “Saga of Gas Turbine Materials, Part III,” *Advanced Materials & Processes,* vol. 162, no. 5, 2004.

[23] J. Wahl and K. Harris, “Advanced Ni-Base Superalloys For Small Gas Turbines,” *The Canadian Journal of Metallurgy and Materials Science,* vol. 50, no. 3, pp. 207-214, 2011.

[24] D. Furrer and H. Fecht, “Ni-based superalloys for turbine discs,” *The Journal of the Minerals, Metals & Materials Society,* vol. 51, no. 1, pp. 14-17, 1999.

[25] M. Brown, T. Fric, T. Johnson and A. Kolman, “Combustion liner for gas tubrine formed of cast nickel-based superalloy”. United States Patent US7540156B2, 2005.

[26] P. Caron and T. Khan, “Evolution of Ni-based superalloys for single crystal gas turbine blade applications,” *Aerospace Science and Technology,* vol. 3, no. 8, pp. 513-523, 1999.

[27] A. Jena and M. Chaturvedi, “The role of alloying elements in the design of nickel-base superalloys,” *Journal of Materials Science,* vol. 19, no. 10, pp. 3121-3139, 1984.

[28] G. Gessinger, Powder Metallurgy of Superalloys 1st Edition, Butterworth-Heinemann, 1984.

[29] M. Durand-Charre, The Microstructure of Superalloys, Amsterdam: Gordon and Breach Science Publishers, 1997.

[30] R. Cozar and A. Pineau, “Morphology of y' and y" precipitates and thermal stability of inconel 718 type alloys,” *Metallurgical and Materials Transactions B,* vol. 4, pp. 47-59, 1973.

[31] D. Collins, B. Conduit, H. Stone, M. Hardy, G. Conduit and R. Mitchell, “Grain growth behaviour during near-γ′ solvus thermal exposures in a polycrystalline nickel-base superalloy,” *Acta Materialia,* vol. 61, no. 9, pp. 3378-3391, 2013.

[32] M. Jackson and R. Reed, “Heat treatment of UDIMET 720Li: the effect of microstructure on properties,” *Materials Science and Engineering: A,* vol. 259, no. 1, pp. 85-97, 1999.

[33] S. Tin, T. Pollock and W. King, “Carbon Additions and Grain Defect Formation in High Refractory Nickel-Base Single Crystal Superalloys,” in *9th International Symposium on Superalloys*, Warrendale, 2000.

[34] Q. Chen, N. Jones and D. Knowles, “The microstructures of base/modified RR2072 SX superalloys and their effects on creep properties at elevated temperatures,” *Acta Materialia,* vol. 50, no. 5, pp. 1095-1112, 2002.

[35] E. Cutler, A. Wasson and G. Fuchs, “Effect of minor alloying additions on the carbide morphology in a single crystal Ni-base superalloy,” *Scripta Materialia,* vol. 58, no. 2, pp. 146-149, 2008.

[36] R. Reed, M. Jackson and Y. Na, “Characterization and modeling of the precipitation of the sigma phase in UDIMET 720 and UDIMET 720L,” *Metallurgical and Materials Transactions A,* vol. 30, pp. 521-533, 1999.

[37] H. Bor, C. Ma and C. Chao, “The influence of Mg on creep properties and fracture behaviors of Mar-M247 superalloy under 1255 K/200 MPa,” *Metallurgical and Materials Transactions A,* vol. 31, pp. 1365-1373, 2000.

[38] C. Sims, N. Stoloff and W. Hagel, Superalloys II: High-Temperature Materials for Aerospace and Industrial Power, john Wiley & Sons, 1987.

[39] A. Cladera, B. Weber, C. Leinenbach, S. M. Czaderski and M. Motavalli, “Iron-based shape memory alloys for civil engineering structures: An overview,” *Construction and Building Materials,* vol. 63, pp. 281-293, 2014.

[40] J. Brooks and P. Bridges, “Metallurgical Stability of Inconel Alloy 718,” in *Sixth International Symposium on Superalloys*, Warrendale, 1988.

[41] A. Devayx, L. Naze, R. Molins, A. Pineau, A. Organista, J. Geudou, J. Uginet and P. Heritier, “Gamma double prime precipitation kinetic in Alloy 718,” *Materials Science and Engineering: A,* vol. 486, no. 1-2, pp. 117-122, 2008.

[42] S. Azadian, L. Wei and R. Warren, “Delta phase precipitation in Inconel 718,” *Materials Characterization,* vol. 53, no. 1, pp. 7-16, 2004.

[43] A. Sinha, “Topologically close-packed structures of transition metal alloys,” *Progress in Materials Science,* vol. 15, no. 2, pp. 81-185, 1972.

[44] H. Xiao, S. Li, X. Han, J. Mazumder and L. Song, “Laves phase control of Inconel 718 alloy using quasi-continuous-wave laser additive manufacturing,” *Materials & Design,* vol. 122, pp. 330-339, 2017.

[45] F. Petit, G. Meier, M. Gell, C. Kartovich, R. Brickmel, W. Kent and J. Radovich, “Oxidation and Hot Corrosion of Superalloys,” in *5th International Symposium on Superalloys*, Champion, 1984.

[46] J. Stringer, “High-temperature corrosion of superalloys,” *Materials Science and Technology,* vol. 3, no. 7, pp. 482-493, 1987.

[47] W. Johnson, J. Doherty, B. Kear and A. Giamei, “Confirmation of sulfur embrittlement in nickel alloys,” *Scripta Metallurgica,* vol. 8, no. 8, pp. 971-974, 1974.

[48] J. Doherty, A. Giamei and B. Kear, “The importance of grain boundary morphology and cohesion on intergranular strength,” *The Canadian Journal of Metallurgy and Materials Science,* vol. 13, no. 1, pp. 229-236, 1974.

[49] K. Harris, G. Erickson and R. Schwer, “MAR M 247 Derivations - CM 247 LC DS Alloy and CMSX Single Crystal Alloys: Properties & Performance,” in *5th International Symposium on Superalloys*, Champion, 1984.

[50] G. Erickson, K. Harris and R. Schwer, “Directionally Solidified DS CM 247 LC—Optimized Mechanical Properties Resulting From Extensive γ′ Solutioning,” in *International Gas Turbine Conference and Exhibit*, Houston, 1985.

[51] A. Kim, B. Choi, S. Seo, D. Kim and C. Jo, “Influence of heat treatment on microstructure and tensile properties of conventionally cast and directionally solidified superalloy CM247LC,” *Materials Letters*, vol. 62, no. 6-7, pp. 1110-1113, 2008.

[52] “Review of INCONEL 718 Alloy: Its History, Properties, Processing and Developing Substitutes,” *Journal of Materials Engineering*, vol. 2, no. 8, pp. 92-100, 2012.

[53] A. Lingenfelter, “Welding of Inconel Alloy 718: A Historical Overview,” *Superalloy 718 - Metallurgy and Applications*, pp. 673-683, 1969.

[54] E. Acka and A. Gursel, “A Review on Superalloys and IN718 Nickel-Based INCONEL Superalloy,” *Periodicals of Engineering and Natural Sciences*, vol. 3, no. 1, 2015.

[55] A. Thomas, M. El-Wahabi, J. Cabrera and J. Prado, “High temperature deformation of Inconel 718,” *Journal of Materials Processing Technology*, vol. 177, pp. 469-472, 2006.

[56] S. Kalluri, K. Rao, G. Halford and M. Mcgaw, “Deformation and Damage Mechanisms in Inconel 718 Superalloy,” in *Superalloys 718, 625, 705 and Various Derivatives*, 1994.

[57] N. El-Bagoury, M. Hessien, M. Alsawat, M. Mahmoud, A. Alanazi and N. Alshanbari, “Optimization of Microstructure and Mechanical Properties of Hipped Inconel 718 by Various Heat Treatment Processes,” *Metallography, Microstructure, and Analysis*, vol. 8, pp. 642-655, 2019.

[58] M. Khan, A. Sheikh and B. Al-Shaer, Evolution of Metal Casting Technologies - A Historical Perspective, SpringerBriefs in Applied Sciences and Technology, 2016, pp. 1-43.

[59] J. Campbell, Complete Casting Handbook, Butterworth-Heinemann, 2015.

[60] American Foundry Society, *Cencus of World Casting Production Global Casting Production Expands*, Modern Casting, 2017.

[61] A. Mouritz, “Production and casting of aerospace metals,” in *Introduction to Aerospace Materials*, Woodhead Publishing, 2012, pp. 128-153.

[62] C. Ammen, The Complete Handbook of Sand Casting, McGraw Hill Professional, 1979.

[63] A. Kaye and A. Street, Die Casting Metallurgy - 1st Edition, Butterworth-Heinemann, 1982.

[64] P. Beeley and R. Smart, Investment Casting, Maney Publishing, 2008.

[65] C. Briant, “Preparation of Clean Superalloys,” in *Impurities in Engineering Materials*, New York, Taylor & Francis, 1999, pp. 18-41.

[66] Q. Bai, J. Lin, G. Tian, J. Zou and T. Dean, “Review and Analysis of Powder Prior Boundary (PPB) Formation in Powder Metallurgy Processes for Nickel-based Superalloys,” *Journal of Powder Metallurgy & Mining*, vol. 4, no. 1, 2015.

[67] "ASTM F2792-12a, Standard Terminology for Additive Manufacturing Technologies," ASTM International, West Conshohocken, 2015.

[68] P. Calvert, "Freeform Fabrication," in *Encyclopedia of Materials: Science and Technology (Second Edition)*, Pergramon Press, 2001, pp. 3340-3347.

[69] J. Giannatsis and V. Dedoussis, "Additive fabrication technologies applied to medicine and health care: A review," *The International Journal of Advanced Manufacturing Technology,* vol. 40, pp. 116-127, 2009.

[70] S. Murphy and A. Atala, "3D bioprinting of tissues and organs," *Nature Biotechnology,* vol. 32, pp. 773-785, 2014.

[71] S. Joshi and A. Sheikh, "3D printing in aerospace and its long-term sustainability," *Virtual and Physical Prototyping,* vol. 4, pp. 1-11, 2015.

[72] M. Yakout, M. Elbestawi and S. Veldhuis, "A Review of Metal Additive Manufacturing Technologies," *Solid State Phenomena,* vol. 278, pp. 1-14, 2018.

[73] A. Dass and A. Moridi, "State of the Art in Directed Energy Deposition: From Additive Manufacturing to Materials Design," *Materials,* vol. 9, no. 7, 2019.

[74] N. Crunchley, H. Li, G. Baxter, C. Heason and P. Bowen, "Microstructure and Texture of Ti-6Al-4V Direct Laser Deposits," in *13th World Conference on Titanium*, 2016.

[75] I. Chang and Y. Zhao, Advances in Powder Metallurgy - Properties, Processing and Applications, Woodhead Publishing, 2013.

[76] W. King, A. Anderson, R. Ferencz, N. Hodghe, C. Kamath, S. Khairallah and A. Rubenchik, "Laser powder bed fusion additive manufacturing of metals; physics, computational, and materials challenges," *Applied Physics Reviews,* vol. 2, no. 4, 2015.

[77] J. Boswell, "Development of Aero Engine Component Manufacturing using Laser Additive Manufacturing," MERLIN Final Report, 2014.

[78] P. Gokuldoss, S. Kolla and J. Eckert, "Additive Manufacturing Processes: Selective Laser Melting, Electron Beam Melting and Binder Jetting - Selection Guidelines," *Materials,* vol. 10, no. 6, 2017.

[79] F. Azam, A. Rani, A. Altaf, T. Rao and H. Zaharin, "An In-Depth Review on Direct Additive Manufacturing of Metals," in *IOP Conference Series: Materials Science and Engineering*, 2018.

[80] T. Debroy, H. Wei, J. Zuback, T. Mukherjee, J. Elmer, J. Milewski, A. Beese, A. Wilson-Heid, A. De and W. Zhang, "Additive manufacturing of metallic components - Process, structure and properties," *Progress in Materials Science,* vol. 92, pp. 112-224, 2018.

[81] L. Murr, S. Gaytan, D. Ramirez, E. Martinez, J. Hernandez, K. Amato, P. Shindo, F. Medina and R. Wicker, "Metal Fabrication by Additive Manufacturing Using Laser and Electron Beam Melting Technologies," *Journal of Materials Science & Technology,* vol. 28, no. 1, pp. 1-14, 2012.

[82] T. Wohlers and T. Gornet, "History of additive manufacturing," Wohlers Associates Inc, 2016.

[83] H. Gong, K. Rafi, H. Gu, T. Starr and B. Stucker, "Analysis of defect generation in Ti-6Al-4V parts made using powder bed fusion additive manufacturing processes," *Additive Manufacturing,* Vols. 1-4, pp. 87-98, 2014.

[84] J. Dilip, G. Ram, T. Starr and B. Stucker, "Selective laser melting of HY100 steel: Process parameters, microstructure and mechanical properties," *Additive Manufacturing,* vol. 13, pp. 49-60, 2017.

[85] K. Prashanth, S. Scudnie, T. Maity, J. Das and J. Eckert, "Is the energy density a reliable parameter for materials synthesis by selective laser melting?," *Materials Research Letters,* vol. 5, no. 6, pp. 386-390, 2017.

[86] U. Bertoli, A. Wolfer, M. Matthews, J. Delplanque and J. Schoenung, "On the limitations of Volumetric Energy Density as a design parameter for Selective Laser Melting," *Materials & Design,* vol. 113, pp. 331-340, 2017.

[87] J. Ion, H. Shercliff and M. Ashby, "Diagrams for Laser Materials Processing," *Acta Materialia,* vol. 40, no. 7, pp. 1539-1551, 1992.

[88] M. Thomas, G. Baxter and I. Todd, "Normalised model-based processing diagrams for additive layer manufacture of engineering alloys," *Acta Materialia,* vol. 108, pp. 26-35, 2016.

[89] U. Bertoli, G. Guss, S. Wu, M. Matthews and J. Schoenung, "In-situ characterization of laser-powder interaction and cooling rates through high-speed imaging of powder bed fusion additive manufacturing," *Materials & Design,* vol. 135, pp. 385-396, 2017.

[90] M. Attallah, R. Jennings, X. Wang and L. Carter, "Additive manufacturing of Ni-based superalloys: The outstanding issues," *MRS Bulletin,* vol. 41, no. 10, pp. 758-764, 2016.

[91] L. Carter, K. Essa and M. Attallah, "Optimisation of selective laser melting for a high temperature Ni-superalloy," *Rapid Prototyping Journal,* vol. 21, no. 4, pp. 423-432.

[92] L. Carter, X. Wang, N. Read, R. Khan, M. Aristizabal and K. Essa, "Process optimisation of selective laser melting using energy density model for nickel based superalloys," *Materials Science and Technology,* vol. 32, no. 7, 2015.

[93] W. Huang, Z. Wang, J. Yang, H. Yang and X. Zeng, "Effects of process parameters and heat treatments on the microstructure and mechanical properties of selective laser melted Inconel 718," in *Proceedings of the 29th Annual International Solid Freeform Fabrication Symposium,* Austin, 2018.

[94] P. Kumar, J. Farah, J. Akram, C. Teng, J. Ginn and M. Misra, "Influence of laser processing parameters on porosity in Inconel 718 during additive manufacturing," *The International Journal of Advanced Manufacturing Technology,* vol. 103, pp. 1497-1507, 2019.

[95] S. Kou, "Welding Metallurgy, 2nd Edition," *MRS Bulletin,* vol. 28, no. 9, 2003.

[96] L. Thijs, F. Verhaeghe, T. Craeghs, J. Humbeeck and J. Kruth, "A study of the microstructural evolution during selective laser melting of Ti-6Al-4V," *Acta Materialia,* vol. 89, no. 9, pp. 3303-3312, 2010.

[97] G. Dinda, A. Dasgupta and J. Mazumder, "Evolution of microstructure in laser deposited Al-11.28%Si alloy," *Surface and Coatings Technology,* vol. 206, no. 8-9, pp. 2152-2160, 2012.

[98] L. Thijs, K. Kempen, J. Kruth, Humbeeck and J, "Fine-structured aluminium products with controllable texture by selective laser melting of pre-alloyed AlSi10Mg powder," *Acta Materialia,* vol. 61, no. 5, pp. 1809-1819, 2013.

[99] Marshall Space Flight Center, "Specification for Control and Quantification of Laser Powder Bed Fusion Mteallurgical Processes," Alabama, 2017.

[100] J. White, N. Read, R. Ward, R. Mellor and M. Attallah, "Prediction of melt pool profiles for selective laser melting of AlSi10Mg alloy," in *Proceedings of Materials Science and Technology Conference and Exhibition*, Pittsburgh, 2014.

[101] H. Gong, H. Z. K. Gu, J. Dilip, D. Pal, B. Stucker, D. Christiansen, J. Beuth and J. Lewandowski, "Melt Pool Characterization of Selective Laser Melting of Ti-6AL=4V Pre-alloyed Powder," in *25th Annual International Solid Freeform Fabrication Symposium*, Austin, 2014.

[102] Q. Guo, C. Zhao, M. Qu, L. Xiong, L. Escano, S. Hojjatzadeh, N. Parab, K. Fezzaa, W. Everhart, T. Sun and L. Chen, "In-situ characterization and quantification of melt pool variation under constant input energy densiy in laser powder bed fusion additive manufacturing process," *Additive Manufacturing,* vol. 28, pp. 600-609, 2019.

[103] A. Philo, S. Mehraban, M. Holmes, S. Sillars, C. Sutcliffe, J. Sienz, S. Brown and P. Lavery, "A pragmatic continuum level model for the prediction of the onset of keyholing in laser powder bed fusion," *The International Journal of Advanced Manufacturing technology,* vol. 101, pp. 697-714, 2019.

[104] W. King, H. Barth, V. Castillo, G. Gallegos, J. Gibbs, D. Hahn, C. Kamath and A. Rubenchik, "Observation of keyhole-mode laser melting in laser powder-bed fusion additive manufacturing," *Journal of Materials Processing Technology,* vol. 214, no. 12, pp. 2915-2925, 2014.

[105] P. Karimi, E. Sadeghi, D. Deng, J. Andersson and P. Nylen, "Influence of build layout and orientation on microstructural characteristics of electron beam melted Alloy 718," *International Journal of Advanced Manufacturing Technology,* vol. 99, pp. 2903-2913, 2018.

[106] L. Carter, M. Attallah and R. Reed, "Laser Powder Bed Fabrication of Nickel-Base Superalloys: Influence of Parameters; Characterisation, Quantification and Mitigation of Cracking," in *The 12th International Symposium on Superalloys*, Champion, 2012.

[107] O. Ojo, "Intergranular liquation cracking in heat affected zone of a welded nickel based superalloy in as cast condition," *Materials Science and Technology,* vol. 23, no. 10, pp. 1149-1155, 2007.

[108] Y. Chen, F. Lu, K. Zhang, P. Nie, S. Hosseini, K. Feng, Z. Li and P. Chu, "Investigation of dendritic growth and liquation cracking in laser melting deposited Inconel 718 at different laser input angles," *Materials & Design,* vol. 105, pp. 133-141, 2016.

[109] P. Mercelis and J. Kruth, "Residual stresses in selective laser sintering and selective laser melting," *Rapid Prototyping Journal,* vol. 12, no. 5, pp. 254-265, 2006.

[110] G. Lewis and E. Schlienger, "Practical considerations and capabilities for laser asissted direct metal deposition," *Materials & Design,* vol. 21, no. 4, pp. 417-423, 2000.

[111] C. Brice, B. Rosenberger, S. Sankaran, K. Tamiger, B. Woods and R. Nasserrafi, "Chemistry Control in Electron Beam Deposited Titanium Alloys," *Materials Science Forum,* Vols. 618-619, pp. 155-158, 2009.

[112] C. Brice, R. Shenoy, M. Kral and K. Buchannan, "Precipitation behaviour of aluminum alloy 2139 fabricated using additive manufacturing," *Materials Science and Engineering: A,* vol. 648, pp. 9-14, 2015.

[113] T. Debroy and S. David, "Physical processes in fusion welding," *Reviews of Modern Physics,* vol. 67, no. 1, pp. 85-112, 1995.

[114] S. Gaytan, L. Murr, F. Medine, E. Martinez, M. Lopez and R. Wicker, "Advanced metal powder based manufacturing of complex components by electron beam melting," *Materials Technology - Advanced Performance Materials,* vol. 24, no. 3, 2009.

[115] ISO6892-2:2018, "Metallic materials — Tensile testing — Part 2: Method of test at elevated temperature," ISO, 2018.

[116] ISO204:2018, "Metallic materials — Uniaxial creep testing in tension — Method of test," ISO, 2018.

[117] J. Plocher and A. Panesar, "Review on design and structural optimisation in additive manufacturing: Towards next-generation lightweight structures," *Materials & Design,* vol. 183, 2019.

[118] J. Booth, J. Alperovich, P. Chawla, J. Ma, T. Reid and K. Ramani, "The Design for Additive Manufacturing Worksheet," *Journal of Mechanical Design,* vol. 139, no. 10, 2017.

[119] A. Alfaify, M. Saleh, F. Abdullah and A. Al-Ahmari, "Design for Additive Manufacturing: A Systematic Review," *Sustainability,* vol. 12, no. 19, 2020.

[120] T. Vilaro, C. Colin, J. Bartout, L. Naze and M. Sennour, "Microstructural and mechanical approaches of the selective laser melting process applied to a nickel-base superalloy," *Materials Science and Engineering: A,* vol. 534, pp. 446-451, 2012.

[121] P. Hosemann, "Small-scale mechanical testing on nuclear materials: bridging the experimental length-scale gap," *Scripta Materialia,* vol. 143, pp. 161-168, 2018.

[122] M. Manahan, A. Argon and O. Harling, "The development of a miniaturized disk bend test for the determination of postirradation mechanical properties," *Journal of Nuclear Materials,* vol. 104, pp. 1545-1550, 1981.

[123] M. Manahan, "A New Postirradiation Mechanical Behaviour Test - The Miniaturized Disk Bend Test," *Nuclear Technology,* vol. 63, no. 2, pp. 295-315, 1983.

[124] J. Parker and J. James, "Disc-bend creep deformation behaviour of 1/2Cr1/2Mo1/4V low alloy steel," in *Creep and Fracture of Engineering Materials and Structures: Proceedings of the Fifth International Conference,* Swansea, 1993.

[125] L. Zhao, H. Jing, L. Xu, Y. Han, J. Xiu and Y. Qiao, "Evaluating of creep property of distinct zones in P92 steel welded joint by small punch creep test," *Materials & Design,* vol. 47, pp. 677-686, 2013.

[126] B. Gulcimen and P. Hahner, "Determination of creep properties of a P91 weldment by small punch testing and a new evaluation approach," *Materials Science and Engineering: A,* vol. 588, pp. 125-131, 2013.

[127] B. Ule, T. Sustar, F. Dobes, K. Milicka, V. Bicego, S. Tettamanti, K. Maile, C. Schwarzkopf, M. Whelan, R. Kozlowski and J. Klaput, "Small punch test method assessment for the determination of the residual creep life of service exposed components: outcomes from an interlaboratory exercise," *Nuclear Engineering and Design,* vol. 192, no. 1, pp. 1-11, 1999.

[128] T. Izaki, T. Kobayashi, J. Kusumoto and A. Kanaya, "A creep life assessment method for boiler pipes using small punch creep test," *International Journal of Pressure Vessels and Piping,* vol. 86, no. 9, pp. 637-642, 2009.

[129] S. Jeffs, R. Lancaster and S. Davies, "Effect of Build Orientation and Post Processing of a Direct Laser Deposited Nickel Superalloy as Determined by the Small Punch Creep Test," *Key Engineering Materials,* vol. 734, pp. 128-136, 2017.

[130] R. Lancaster, G. Davies, H. Illsley, S. Jeffs and G. Baxter, "Structural Integrity of an Electron Beam Melted Titanium Alloy," *Materials,* vol. 9, no. 6, 2016.

[131] E3205-20, "Standard Test Method for Small Punch Testing of Metallic Materials," ASTM International, 2020.

[132] M. Bruchhausen, S. Holmstrom, I. Simonovski, J. Lapetite, S. Ripplinger and F. de Haan, "Recent developments in small punch testing: Tensile properties and DBTT," *Theoretical and Applied Fracture Mechanics,* vol. 86, pp. 2-10, 2016.

[133] J. Chica, P. Diez and M. Calzada, "A New Prediction Method for Ultimate Tensile Strength of Steel Alloys with Small Punch Test," *Materials,* vol. 11, no. 9, 2018.

[134] "Small Punch Testing - The Transition from a Cofe of Practice to a European Testing Standard," *Key Engineering Materials,* vol. 734, pp. 3-22, 2017.

[135] CEN Workshop Agreement CWA 15267, "European Code of Practise: Small Punch Test Method for Metallic Materials," CEN Members National Standards Body, 2007.

[136] C. Wen, T. Xu and K. Guan, "Correlation Factor Study of Small Punch Creep Test and Its Life Prediction," *Materials,* vol. 9, no. 10, 2016.

[137] S. Davies, R. Lancaster, S. Jeffs, R. Hurst and G. Baxter, "Small Punch Fatigue Testing of a Nickel Superalloy," in *5th International Small Sample Test Techniques Conference,* Swansea, 2018.

[138] R. Lancaster, S. Jeffs, H. Illsley, C. Argyrakis, R. Hurst and G. Baxter, "Development of a novel methodology to study fatigue properties using the small punch test," *Materials Science and Engineering: A,* vol. 748, pp. 21-29, 2019.

[139] C. Wen, T. Xu and K. Guan, "Correlation Factor Study of Small Punch Creep Test and Its Life Prediction," *Materials,* vol. 9, no. 10, 2016.

[140] I. Klevtsov, A. Dedov and A. Molodtsov, "Using of Small Punch Test for Determination of Tensile Properties for Power Plant Steels," in *6th International DAAAM Baltic Conference,* Tallinn, 2008.

[141] S. Norris and J. Parker, "Deformation process during disc bend loading," *Materials Science and Technology,* vol. 12, no. 2, 1996.

[142] T. Garcia, C. Rodriguez, F. Belzunce and C. Suarez, "Estimation of the mechanical properties of metallic materials by means of the small punch test," *Journal of Alloys and Compounds,* vol. 582, pp. 708-717, 2014.

[143] X. Mao and T. Takahashi, "Development of a further-miniturized specimen of 3mm diameter for tem disk (ø 3 mm) small punch tests," *Journal of Nuclear Materials,* vol. 150, no. 1, pp. 42-52, 1987.

[144] C. Rodriguez, J. Garcia, E. Cardenas and C. Betegon, "Mechanical properties characterization of heat-affected zone using the small punch test," *Welding Journal,* vol. 88, 2009.

[145] M. Contreras, C. Rodriguez, F. Belzunce and C. Betegon, "Use of small punch test to determine the ductile-to-brittle transition temperature of structural steels," *Fatigue and Fracture of Engineering Materials & Structures,* vol. 31, pp. 727-737, 2008.

[146] R. Lacalle, J. Garcia, J. Alvarez and F. Gutierrez-Solana, "Obtención mediante el ensayo small punch de las propiedades de tracción de materiales metálicos," *Anales de Mecanica de la Fractura 26,* vol. 2, 2009.

[147] R. Lacalle, J. Alvarez and F. Gutierrez-Solana, "Analysis of key factors for the interpretation fo small punch test results," *Fatigue & Fracture of Engineering Materials & Structures,* vol. 31, pp. 841-849, 2008.

[148] R. Hurst, "Where are we now with the European code of practice for small punch testing?," in *International Conference on Small Sample Test Techniques*, Ostrava, 2012.

[149] S. Davies, S. Jeffs, R. Lancaster and G. Baxter, "High Temperature Defrmation Mechanisms in a DLD Nickel Superalloy," *Materials,* vol. 10, no. 5, 2017.

[150] J. Chakrabarty, "A theory of stretch forming over hemispherical punch heads," *International Journal of Mechanical Sciences,* vol. 12, no. 4, pp. 315-325, 1970.

[151] S. Jeffs and R. Lancaster, "Elevated temperature creep deformation of a single crystal superalloy through the small punch creep method," *Materials Science and Engineering: A,* vol. 626, pp. 330-337, 2015.

[152] D. Blagoeva and R. Hurst, "Application of the CEN (European Committee for Standardization) small punch creep testing code of practice to a representative repair welded P91 pipe," *Materials Science and Engineering: A,* Vols. 510-511, pp. 219-223, 2009.

[153] R. Lancaster, W. Harrison and G. Norton, "An analysis of small punch creep behaviour in the γ titanium aluminide Ti-45Al-2Mn-2Nb," *Materials Science and Engineering: A,* vol. 626, pp. 263-274, 2015.

[154] Z. Abdullah, V. Gray, M. Whittaker and K. Perkins, "A Critical Analysis of the Conventionally Employed Creep Lifing Methods," *Materials,* vol. 7, no. 5, pp. 3371-3398, 2014.

[155] P. Dymacek, "Recent developments in small punch testing: applications at elevated temperatures," *Theoretical and Applied Fracture Mechanics,* vol. 86, pp. 25-33, 2016.

[156] D. Andres, R. Lacalle and J. Alvarez, "Creep property evaluation of light alloys by means of the Small Punch test: Creep master curves," *Materials & Design,* vol. 96, pp. 122-130, 2016.

[157] M. Whittaker, V. Gray and W. Harrison, "A Modern Philosophy for Creep Lifing in Engineering Alloys," in *Creep,* Intech Open, 2018.

[158] S. Jeffs, R. Lancaster and T. Garcia, "Creep lifing methodologies applied to a single crystal superalloy by use of small scale test techniques," *Materials Science and Engineering: A,* vol. 636, pp. 529-535, 2015.

[159] S. Davies, S. Jeffs, M. Coleman and R. Lancaster, "Effects of heat treatment on microstructure and creep properties of a laser powder bed fused nickel superalloy," *Materials & Design,* vol. 159, pp. 39-46, 2018.

[160] R. Evans and M. Evans, "Numerical modelling of small disc creep test," *Materials Science and Technology,* vol. 22, no. 10, pp. 1155-1162, 2006.

[161] K. Kobayashi, I. Kajihara, H. Koyama and G. Stratford, "Deformation and Fracture Mode during Small Punch Creep Tests," *Journal of Solid Mechanics and Materials Engineering,* vol. 4, no. 1, pp. 75-86, 2010.

[162] R. Evans, "A constitutive model for the high-temperature creep of particle-hardened alloys based on the theta projection method," *The Royal Society Publishing,* vol. 456, no. 1996, 2000.

[163] R. Lancaster, H. Illsley, G. Davies, S. Jeffs and G. Baxter, "Modelling the small punch tensile bahviour of an aerospace alloy," *Materials Science and Technology,* vol. 33, no. 9, pp. 1065-1073, 2017.

[164] R. Hurst, R. Lancaster, S. Jeffs and M. Bache, "The contribution of small punch testing towards the development of materials for aero-engine applications," *Theoretical and Applied Fracture Mechanics,* vol. 86, pp. 69-77, 2016.

[165] Y. Li, J. Bushby and D. Dunstan, "The Hall-Petch effect as a manifestation fo the general size effect," *Proceedings of The Royal Society A,* vol. 472, no. 2190, 2016.

[166] K. Turba, R. Hurst and P. Hahner, "Anisotropic mechanical properties of the MA956 ODS steel characterized by the small punch testing technique," *Journal of Nuclear Materials,* vol. 428, no. 1-3, pp. 76-81, 2012.

[167] T. Vilaro, C. Colin, J. Bartout, L. Naze and S. M, "Microstructural and mechanical approaches of the selective laser melting process applied to a nickel-base superalloy," *Materials Science and Engineering: A,* vol. 534, pp. 446-451, 2012.

[168] H. Illsley, R. Lancaster, S. Jeffs and G. Baxter, "Small Punch Testing of Electron Beam Melted (EBM) Ti-6Al-4V," in *Proceedings of the 13th World Conference on Titanium,* San Diego, 2016.

[169] G. Erickson, K. Harris and R. Schwer, "DS CM247 LC Characteristic Properties with Optimized Solutioning Techniques," in *Gas Turbine Conference and Exhibit,* Houston, 1985.

[170] W. Sames, F. List, S. Pannala, R. Dehoff and B. S, "The metallurgy and processing science of metal additive manufacturing," *International Materials Reviews,* vol. 61, no. 5, pp. 315-360, 2016.

[171] O. Adegoke, J. Andersson, H. Brodin and R. Pederson, “Influence of Laser Powder Bed Fusion Process Parameters on Voids, Cracks, and Microhardness of Nickel-based Superalloy 247LC,” *Materials,* vol. 13, no. 17, 2020.

[172] C. Zhang, W. Hu, C. Liu, Y. Zhao, J. Shang and Z. Wen, “Effects of low- to medium-angle grain boundaries on creep properties of superalloy,” *Materials Science and Technology,* vol. 34, no. 10, pp. 1176-1187, 2018.

[173] Y. Huang and T. Langdon, “The evolution of delta-phase in superplastic Inconel 718 alloy,” *Journal of Materials Science,* vol. 42, pp. 421-427, 2007.

[174] F. Cruz Gallo, L. Azevedo, C. Labre, L. Araujo, J. Dille and L. Almeida, “Correlation between grain boundary character and δ-phase precipitation in nickel-based superalloy 718,” *Journal of Materials Research and Technology,* vol. 9, no. 2, pp. 1801-1808, 2020.

[175] V. Beaubois, J. Huez, S. Coste, O. Brucelle and J. Lacaze, “Short term precipitation kinetics of delta phase in strain free Inconel 718 alloy,” *Materials Science and technology,* vol. 20, no. 8, 2004.

[176] H. Illsley, R. Lancaster, R. Hurst, S. Jeffs and B. G, “Mechanical Property Characterisation of Electron Beam Melted (EBM) Ti-6Al-4V via Small Punch Tensile Testing,” *Key Engineering Materials,* vol. 734, pp. 51-60, 2017.

[177] A. Spierings, M. Voegtlin, T. Bauer and K. Wegener, “Powder flowability characterisation methodology for powder-bed-based metal additive manufacturing,” *Progress in Additive Manufacturing,* vol. 1, pp. 9-20, 2016.

[178] S. Brika, M. Letenneur, C. Dion and V. Brailovski, “Influence of particle morphology and size distribution on the powder flowability and laser powder bed fusion manufacturability of Ti-6Al-4V alloy,” *Additive Manufacturing,* vol. 31, 2020.